Errata

Page

107 A sentence is added after equation (4.27):
The assumption is really that the outlet pip has been ignored and the film is flat to the centre and of thickness equal to the minimum.

125 Equation (4.66): $\delta_o(t)$ must be replaced by $\delta_{sc}(t)$ as $\dot{\delta}_{sc} = \dot{\delta}_o$.

126 Equation (4.71): the second term on the numerator is $\alpha \kappa'(\alpha'+1)K_1\dot{\delta}_{sc}^2(t)$

191 Equation (7.10): $\dot{\bar{h}}_i = \dfrac{\dot{h}_i}{\tau h_o}$

192 Equation (7.15): $\bar{P} = \dfrac{P}{\delta_o}$

196 3 lines above equation (7.38): $h_i = h_o - S_i$

220 Equation (7.79): = sign is missing.

226 Reference 8, line 2 reads: "Mechanical Vibrations".

242 Equation (A2.6): (1) numerator term $h_i^{-\frac{1}{2}}$ is missing.

(2) A factor of 2 in the denominator is missing.

INFLUENCE OF VIBRATIONS ON THE OIL FILM IN CONCENTRATED CONTACTS

by

Homayoon Rahnejat
BSc, MSc, DIC

A Thesis submitted for the Degree of

DOCTOR OF PHILOSOPHY

OF THE

UNIVERSITY OF LONDON

January 1984

Department of Mechanical Engineering
Imperial College of Science and Technology
University of London

ABSTRACT

The thesis investigates the vibration characteristics of gears and roller bearings when they are treated as bodies in concentrated contact, both with and without a lubricant film.

The investigation covers examples where the oil film between contiguous bodies is iso-viscous, piezo-viscous and EHD and is subjected to a combined rolling and squeeze action. The undistorted geometry includes finite line contacts (to simulate spur gears and roller bearings) and point contacts (to simulate ball bearings).

The system response is analysed both in the time and frequency domains, the latter using 'Fast Fourier Transforms' (FFT) and 'Phase Plane Representation' (PPR) as appropriate.

The analysis employs the solution to the generalized Reynolds equation which includes an approximation for the effect of squeeze velocity at the contacting surfaces.

The dynamic response of a rigid (non-bending) shaft supported by two deep-grooved ball bearings is then studied using the above theory both under dry and lubricated conditions. The time history of the shaft's centre-line movement and its frequency composition are found under various input loading functions such as a step function, a sinusoidal input caused by the shaft's out-of-roundness and surface waviness. The effect of varying the number of rolling elements, clearance and interference fit, and the shaft out-of-balance are also investigated.

When the model simulates two discs in line contact with rolling-squeezing motion, the latter being caused by a sinusoidal forcing function, the degree of damping is found to be frequency dependent. Under a short duration pulse forcing function, the oil film rapidly recovers to its initial steady state value after a few oscillations.

When the model simulates deep-groove ball bearings, the dominant natural frequency depends on number of balls, degree of radial interference and the load supported. When lubricant is present, there is an oscillatory decay in response to the step function input applied to the shaft. When there is a forcing function created by the shaft out-of-balance, the shaft centre locus is affected by its rpm, the magnitude of out-of-balance force and the ball-pass frequency.

To the memory of my mother

ACKNOWLEDGEMENTS

I would like to express my deepest gratitude to Dr. Ramsey Gohar for suggesting this research project and for his enthusiastic supervision.

Sincere thanks are also due to my parents for their continual encouragement and financial support. I would like to especially thank my wife, Patricia, for her technical assistance as well as the understanding and encouragement that she extended during this research.

Thanks are also due to Dr. P.B. MacPherson for his assistance in providing funds and to Dr. R. Curr for his useful advice. The help rendered by Miss M. Anvar in presenting some of the figures is greatly appreciated, as is the cooperation of Mr G. Tindall of Reprographics and Miss E.M. Archer, the Mechanical Engineering Librarian.

For access even at odd and unofficial hours of the day to Imperial College Computing facilities, I am indebted to Mr. A. Spirling, the Computing Manager.

My thanks go to Mrs. E.A. Hall and Mrs. D. Abeysekera for the excellent typing.

CONTENTS

LIST OF FIGURES

NOTATION FOR CHAPTER 1

b : contact length

C : a constant

C_1 : a constant of integration

C_2 : a constant of integration

f : surface tractive force per unit length

F : surface total tractive force

h : lubricant film thickness

h^* : h/R

h_o : lubricant central film thickness

h_o^* : h_o/R

$\dot{h}_o$: dh_o/dt

h_a : lubricant film thickness at $P = P_{max}$

h_e : lubricant film thickness at exit

$\bar{h}_e$: h_e/h_o

L : b

n : a constant

p : iso-viscous pressure

p^* : dimensionless iso-viscous pressure

P_{max} : maximum pressure

P^*_{max} : maximum dimensionless pressure

q : piezo-viscous pressure

r : radius of rolling elements

R : reduced radius of two rolling counterformal elements

T : surface traction

U : speed of entraining motion

ΔU : speed of sliding motion

ΔU^* : $\Delta U/U$

V : longitudinal flow speed (in y-direction)

W : integrated pressure distribution (load carrying capacity)

$\overline{W}$: dimensionless load

W_s : normal squeeze velocity

W_s^* : W_s/U

x : direction of induced entraining motion

$\overline{x}$: dimensionless position vector in direction of entraining motion

x_a : $x = x_a$ at $P = P_{max}$

$\overline{x}_a$: $\overline{x} = \overline{x}_a$ at $P^* = P^*_{max}$

x_e : position of film rupture (exit)

$\overline{x}_e$: $\overline{x} = \overline{x}_e$ at $P^* = dP^*/d\overline{x} = 0$

x_i : inlet position

$\overline{x}_i$: dimensionless vector corresponding to the position of inlet

y : longitudinal direction

z : direction of normal motion

α : piezo-viscosity index

η : viscosity

η_o : pressure-independent viscosity

η_q : pressure-dependent viscosity

Subscripts

0 : relating to mid-contact

$1,2$: corresponding to upper and lower surfaces, respectively

NOTATION FOR CHAPTER 2

b	:	contact length
dt	:	small time interval
f	:	frequency
F	:	forcing function
F_{max}	:	amplitude of forcing function
g	:	acceleration due to gravity
h	:	lubricant film thickness
$\dot{h}$	:	dh/dt
$\ddot{h}$	:	d^2h/dt^2
h^*	:	h/R
h_o	:	lubricant central film thickness
$\dot{h}_o$	:	dh_o/dt
$\ddot{h}_o$	:	d^2h_o/dt^2
h_m	:	mean steady-state lubricant film thickness
m	:	mass of rolling element
P	:	pressure
P_{max}	:	maximum pressure
q	:	piezo-viscous pressure
Q	:	steady applied load magnitude
R	:	reduced radius of rolling counterformal elements
t	:	time
U	:	speed of entraining motion
$\overline{U}$	:	$(U\,\eta_o\,\alpha)/R$
W	:	instantaneous integrated pressure distribution
$\overline{W}$	:	dimensionless instantaneous load carrying capacity
$W_{rolling}$	:	integrated pressure distribution due to rolling effect
$W_{squeezing}$	:	integrated pressure distribution due to normal motion

$w_{upstroke}$	:	$w_{rolling}$
w_s	:	squeeze velocity
w_s^*	:	w_s/U
$w_{s_{max}}$	:	maximum squeeze velocity
$\overline{x}_a$	:	dimensionless position vector corresponding to the position $P^* = P^*_{max}$
z	:	dynamic displacement of the element's geometric centre
z_{max}	:	maximum displacement
$\dot{z}$	:	dz/dt (squeeze velocity)
$\dot{z}_{max}$	:	maximum squeeze velocity (steady-state)
$\dot{z}_{min}$	:	minimum squeeze velocity (steady-state)
$\ddot{z}$	:	d^2z/dt^2
α	:	piezo-viscosity index
ε	:	a limit of numerical accuracy
η_o	:	pressure independent viscosity

Subscripts

i	:	time index
j	:	iteration index

NOTATION FOR CHAPTER 3

E_1	:	modulus of elasticity of the rolling element
E_r	:	$(1 - \nu_1^2)/(\pi E_1)$
G^*	:	material parameter, α/E_r
h	:	film thickness
h^*	:	h/R
$h^*(\overline{x},\overline{y})$	:	dimensionless lubricant film thickness at $(\overline{x},\overline{y})$
$\overline{h}_g(\overline{x},\overline{y})$	:	separation of the surfaces in their undeformed state at $(\overline{x},\overline{y})$
k	:	coefficient of W_s^* in the squeeze form factor
P	:	reduced pressure
P^*	:	dimensionless reduced pressure
q	:	actual hydrodynamic pressure
q^*	:	$1/G^* \ (1 - e^{-G^*P^*})$
R	:	reduced radius of rolling discs
U	:	rolling speed
W	:	integrated pressure distribution
W^*	:	$(W E_r)/R^2$
W_s	:	normal squeeze velocity
W_s^*	:	W_s/U
x	:	longitudinal direction
$\overline{x}$	:	x/R
y	:	direction of induced entraining motion
$\overline{y}$	:	y/R
α	:	piezo-viscosity
α_1	:	$(\partial h/\partial t)/(\partial_{ho}/\partial t)$
$\overline{\delta}(0,0)$	:	dimensionless central contact deflection
$\overline{\delta}(\overline{x},\overline{y})$	:	dimensionless contact deflection at $(\overline{x},\overline{y})$
η	:	viscosity

η_0 : pressure independent viscosity

η^* : $e^{G^*P^*}$

ρ : density

$\overline{\rho}$: $(1 + 0.6P^*)/(E_r + 1.7P^*)$

ν_1 : Poisson's ratio

Subscripts

0 : relating to mid-contact

1 : relating to the upper disc

2 : relating to the lower disc

NOTATION FOR CHAPTER 4

E	:	modulus of elasticity
E'	:	$1/E' = \frac{1}{2}\{(1-\nu_1^2)/E_1 + (1-\nu_2^2)/E_2\}$
$\tilde{E}$	:	E'
E_r	:	$(1-\nu_1^2)/(\pi E_1)$
e_p^*	:	contact ellipticity ratio
F	:	applied normal force
G^*	:	material parameter
h	:	oil film thickness
$\dot{h}$	:	$\partial h/\partial t$
h^*	:	h/R
L	:	contact length
m	:	mass of the oscillating member
$P_\ell(x)$	:	axial profile
$P_r(y)$	:	lateral profile
R	:	reduced radius of counterformal rolling discs
S	:	amplitude of lubricant film oscillations
$\dot{S}$	:	$dS/dt = \partial h/\partial t$ (since uniform surface deformation rate is assumed)
$\ddot{S}$	:	d^2S/dt^2, local surface acceleration
t	:	time
U	:	rolling speed
W	:	integrated pressure distribution
$\dot{W}$	:	rate of change of load
W^*	:	$(W E_r)/R^2$
W_s^*	:	W_s/U
x	:	longitudinal direction
y	:	direction of entraining motion
z	:	dynamic displacement of the element's centre

$\dot{z}$: dz/dt

$\ddot{z}$: d^2z/dt^2, centreline acceleration

α : piezo-viscosity

α_1 : power index of h in the load equation for point contacts

α' : power index of h in the load equation for finite line contacts

β : coefficient of $\dot{S}$ in the load equation for point contacts

β' : coefficient of $\dot{S}$ in the load equation for finite line contacts

Subscripts

0 : relating to mid-contact

1 : relating to the upper surface

2 : relating to the lower surface

min : position of 'minimum exit'

sc : 'side constriction'

NOTATION FOR CHAPTER 5

a	:	modal amplitude contribution
dt	:	time interval
f	:	response frequency
N	:	number of data points
S	:	time series relating to oil film oscillations
t	:	time
V	:	computational 'Butterfly'
X, Y	:	shortened sequences relating to the initial time series
z	:	time series relating to the centre line oscillations
ω	:	forcing frequency

Subscripts

K	:	relating to the Discrete Fourier transform
n	:	relating to natural frequency
r	:	relating to discrete time series

NOTATION FOR CHAPTER 6

a : half length of the major axis in the elliptical contact

b : half length of the minor axis in the elliptical contact

e_p^* : a/b

F : applied normal force

f : response frequency

g : acceleration due to free fall

K : load-deflection constant of proportionality

M : mass of heavy rigid shaft

m : number of balls employed

m_s : mass of the shaft (as used in reference [5])

n : power index of the deflection term

w : radial load per ball

R : radius of curvature of the rolling surface

T : period of limit cycle

t : time

U : displacement

$U(x)$: potential energy

X , Y : amplitudes of oscillation in two degrees of freedom motion

x , y : degrees of freedom

$\dot{x} , \dot{y}$: rates of change of displacement in respective degrees of freedom

$\ddot{x} , \ddot{y}$: accelerative terms in respective degrees of freedom

α , β : coefficients relating to the contact conformity

γ : $2\pi/m$

Δ : static deflection

δ : radial deflection per ball

ε : a specified limit of accuracy

θ : $\phi + i\gamma$

λ : coefficient relating to the contact conformity

ϕ : turning angle of the cage

ψ : an angle describing the contact condition

ω : angular speed of the rolling surface

Ω : system dominant response frequency

Subscripts

o : relating to the initial conditions

1 : relating to the inner raceway

2 : relating to the rolling element

CF : complementary function

h : housing

i : rolling element index number

ir : a radial property of the rolling element

j : iteration index

k : time index

m : relating to the number of balls employed

r : shaft relative to housing

s : shaft

Superscripts

$\hat{}$: corresponding to the maximum amplitude

$'$: defining the radius of curvature of the contacting surface in the lateral direction to the direction of induced rolling motion

NOTATION FOR CHAPTER 7

A : The term containing the EHD squeeze film damping

B : The term containing the hydrodynamic squeeze film damping

C : Clearance

c : See notations for Appendix A1

C_{iso} : $2\sqrt{c}\, U^*$

d : Logarithmic decrement

dt : Small time interval

E_r : $\dfrac{1-\nu_1^2}{\pi E_1}$

e : Eccentricity

f : Frequency

G^* : Material's parameter

h : Film thickness

$\dot{h}$: Squeeze velocity

K : $\dfrac{W}{\delta^{3/2}}$

K' : Time independent constant in the equation of EHD integrated pressure distribution

K_r : $(.25)^{\alpha} \cdot K'$

ℓ : Shaft perimeter

M : Mass of shaft

m : Number of balls

m_{ball} : Mass of ball

n : number of waves

$\bar{P}'$: $\dfrac{W_o}{M\tau^2\delta_o}$

Q : Step gravity load

R : The reduced radius

r : $X\cos\theta + Y\sin\theta$

S : Small dynamic displacement of the oil surface

$\dot{S}$: Squeeze velocity

t : time

U : Rolling speed

U^* $\dfrac{U\eta_o E_r}{R}$

W : Load per ball

X, Y : Movements of the shaft centre

x, y : Cartesian frames of reference

α' : Power index of h in the equation of EHD integrated pressure distribution

α'_1 : $\dfrac{2\alpha'+5}{2}$

β : $\dfrac{132}{U}$

γ : Radial distance between two successive balls

Δ : Static deflection of the shaft

δ : Radial deflection

ε : Limit of accuracy

θ : Ball's radial position with respect to $+x$-axis

θ' : Radial position on the wavy shaft periphery

λ : $\dfrac{67 \cdot 7}{U}$

λ_1 : Wavelength of the shaft's wavy surface

ρ : Radial interference

ψ_1 : $\dfrac{K'}{W_o h_o^{\alpha'}}$

ψ_2 : $\dfrac{C_{iso}}{W_o h_o^{\frac{1}{2}}}$

ψ_3 : $\dfrac{K\delta_o^{\nu}}{W_o} = 1$

ϕ : Shaft's angular displacement

ν : Power index of δ in $W = K\delta^{\nu}$

ω : Radial frequency

ξ : Damping factor

<u>Subscripts</u>

0 : Relating to the initial conditions

1 : Relating to the shaft

b : Corresponding to the ball-pass frequency

c : Corresponding to the cage

i : A radial position

j : Iteration index

K : Time index

ℓ_1 : A limit of the EHD action

ℓ_2 : A limit of the hydrodynamic action

max : Indicating the maximum value

min : Indicating the minimum value

x, y : Providing a property along the x, y directions

<u>Superscripts</u>

• : The first differential

•• : The second differential

* : Denoting a dimensionless variable

– : Indicating a normalised variable

NOTATION FOR CHAPTER 8

h	:	Film thickness
P_r	:	Profile
t	:	Time
W	:	Load (integrated pressure distribution)
W_s	:	Squeeze velocity
x, y	:	Cartesian frames of reference

Subscripts

0	:	Relating to mid-contact

Superscripts

	:	Denoting the first derivative, $\frac{\partial}{\partial t}$

NOTATION FOR APPENDIX A1

B_o	:	.75
c	:	A function of R_x and R_y
C_{iso}	:	$2\sqrt{c}\ U^*$
h	:	Film thickness
K	:	A constant = $-\dfrac{1}{2(1+R)}$
K_{c_1}	:	A time independent constant
P	:	Pressure
R	:	Reduced radius
U	:	Rolling speed
t	:	Time
W	:	Integrated pressure (Load per ball)
W_s	:	Squeeze velocity
λ	:	$67.7/U$
$\bar{\lambda}$	:	$\lambda \tau h_o$
ϕ	:	$\tan^{-1}\bar{y}$

Subscripts

0	:	Relating to initial conditions
i	:	A radial property
RL	:	A rolling parameter
SQ	:	A squeeze effect term
x, y	:	Corresponding to a component in x or y directions

Superscripts

*	:	Corresponding to a dimensionless parameter
–	:	Indicating a normalised variable

NOTATION FOR APPENDIX A2

B_o : .75

C_2, C_3 : Constants defining the hyperbolic load function

h : Film thickness

$\dot{h}$: Squeeze velocity

S : Small oil film oscillations

δ : Deflection

λ : $\frac{67.7}{U}$

ν : Power index of deflection = 3/2

ψ_2 : A function, see Notation for Chapter 7

Subscripts

co : At the change - over point to hyperbolic regime

i : A radial property

ℓ_2 : A limiting property of the hydrodynamic regime

Superscripts

$\cdot$: Relating to the first differential, $\frac{\partial}{\partial t}$

$\cdot\cdot$: Relating to the second differential, $\frac{\partial^2}{\partial t^2}$

$-$: A normalised variable

CHAPTER 1

HYDRODYNAMIC LUBRICATION

1.1 INTRODUCTION

The purpose of lubrication is to ensure the presence of a lubricant film of sufficient thickness between two surfaces sliding past each other. This lubricant film can then be sheared without causing damage to the adjacent sliding surfaces. This type of lubrication, applicable to journal and thrust bearings, is regarded as full hydrodynamic lubrication. Some early studies of a lubricated shaft and bearing operating under fully hydrodynamic conditions were carried out by Von Pauli [1] in 1849 and by Hirn [2] in 1854. Petroff [3] analysed the work of Hirn in some detail in 1883. Tower [4] showed that there were considerable pressures generated in rolling elements under full hydrodynamic contact conditions. His work was mathematically analysed by Reynolds [5] in 1886. Reynolds illustrated that a converging wedge-shaped film generated an oil pressure distribution. All the subsequent lubrication theory investigated by many authors is founded on the work of Reynolds.

The Reynolds equation of hydrodynamics, called after him, is based on a number of assumptions which are listed below:

(a) The body forces, such as gravitational or magnetic forces, are neglected. This assumption is generally true for lubrication with non-conducting fluids.

(b) As the lubricant film is considered to be very thin, the pressures generated are constant throughout its thickness.

(c) The curvatures of the rolling surfaces are considered large compared to the thickness of the lubricant film. Therefore, the surface velocities need not be taken as varying in direction.

(d) There is no slip at the boundaries of the rolling elements and the outermost adjacent lubricant layer.

(e) The lubricant is Newtonian.

(f) The flow is considered to be laminar.

(g) The inertia of the fluid can be neglected.

(h) The viscosity is assumed to be constant through the thickness of the lubricant film. This assumption is rather crude but has been adopted for simplification of the mathematical modelling.

The Reynolds equation of hydrodynamic pressures in one dimension can be derived by considering the equilibrium of a small element [6]. The corresponding equation in two dimensions is then established by simple extension of this theory. The full Reynolds equation in all dimensions makes use of the principle of fluid continuity [6,7]. For an incompressible fluid, the Reynolds full equation in all dimensions is:

$$\frac{\partial}{\partial x}\left(\frac{h^3}{\eta}\frac{\partial P}{\partial x}\right) + \frac{\partial}{\partial y}\left(\frac{h^3}{\eta}\frac{\partial P}{\partial y}\right)$$

$$= 6\left\{\frac{\partial}{\partial x}\left(U_1 + U_2\right) h + \frac{\partial}{\partial y}\left(V_1 + V_2\right) h + 2\left(W_{s1} - W_{s2}\right)\right\} \tag{1.1}$$

The terms on the right hand side may be considered as 'flow' terms and those on the left hand side indicate the 'resistance to flow' (see Figure 1.1).

There are two main assumptions generally used to obtain an approximate solution to the Reynolds equation. These assumptions, when implemented, result in a simplification in the mathematics of the problem, thus lending themselves to a rough solution of the pressures. Therefore, either an infinitely long bearing or an infinitely short bearing approximation is employed. In the former case, any terms containing $\partial P/\partial y$ are neglected,

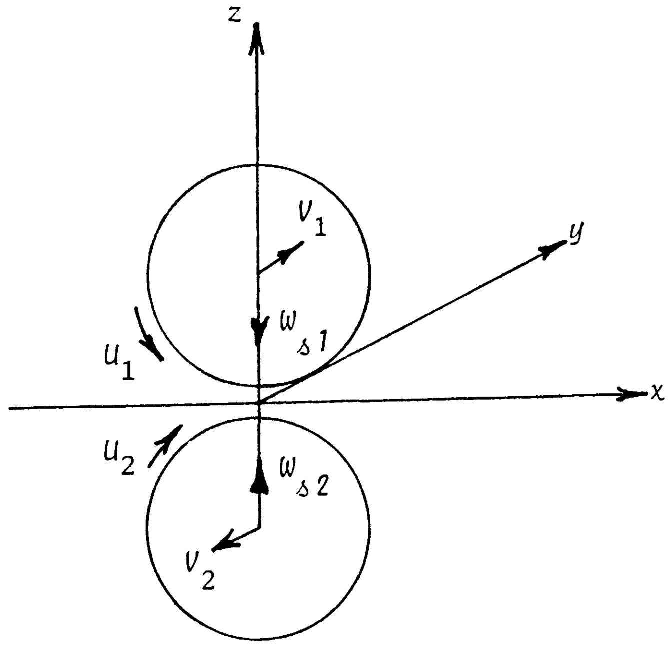

Fig 1.1 Physical representation of general Reynolds equation

effectively terminating the flow in the y-direction. In the latter case, the equation is simplified such that it merely contains the oil flow term in the direction of motion.

Several authors have solved the steady-state problem and compared their findings with the experimental measurements of the film thickness in two disc machines. The problem of lubricated lightly loaded cylinders in combined rolling, sliding and normal motion, where an iso-viscous lubricant is employed, has been considered in a non-steady-state solution by Dowson, Markho and Jones [8]. They concluded that a dimensionless parameter can be used to involve the 'normal' and 'entraining' motion to describe the performance characteristics of the bearing. Sasaki, Mori and Okino [9] also achieved an isothermal solution for lubricated rigid cylinders subjected to sinusoidal loading conditions. This solution was developed for a Bingham plastic which, at high speeds, would behave as a Newtonian lubricant. Finally, Pinkus and Sternlicht [10] have carried out a detailed analysis of squeeze film effects using iso-viscous and piezo-viscous lubricants.

1.2 ISO-VISCOUS PRESSURE DISTRIBUTION

The full Reynolds equation can be simplified using an infinitely long bearing assumption where there is no side leakage (i.e. $V_1 = V_2 = 0$, $\partial P/\partial y = 0$) (see Figure 1.2):

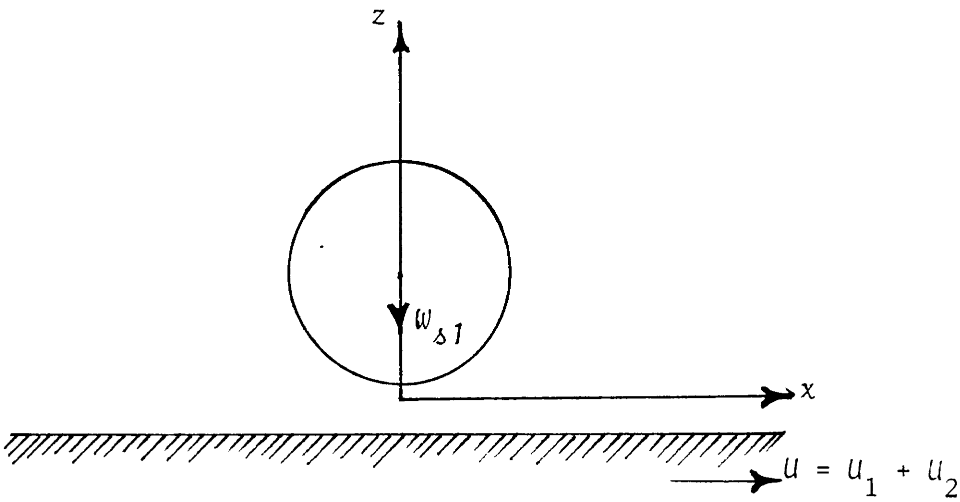

Fig 1.2 Physical representation of simplified Iso-viscous model

$$\frac{\partial}{\partial x}\left(\frac{h^3}{\eta}\frac{\partial P}{\partial x}\right) = 6\left\{\frac{\partial}{\partial x}(U_1 + U_2)\,h + 2(W_{s1} - W_{s2})\right\} \tag{1.2}$$

Furthermore, for an iso-viscous lubricant, the viscosity $\eta = \eta_0$ is pressure independent. Hence:

$$\frac{\partial}{\partial x}\left(h^3\frac{\partial P}{\partial x}\right) = 6\eta_0\left\{\frac{\partial}{\partial x}(U_1 + U_2)\,h + 2(W_{s1} - W_{s2})\right\} \tag{1.3}$$

Now, let $U = U_1 + U_2$ and $W_s = W_{s1} - W_{s2}$. Therefore:

$$\frac{\partial}{\partial x}\left(h^3\frac{\partial P}{\partial x}\right) = 6\,U\,\eta_0\frac{\partial h}{\partial x} + 12\,W_s\,\eta_0 \tag{1.4}$$

Integrating equation (1.4) with respect to x to obtain the pressure gradient in the lubricant:

$$h^3\frac{dP}{dx} = 6\,U\,\eta_0\,h + 12\,W_s\,\eta_0\,x + C1 \tag{1.5}$$

The constant of integration, $C1$, can be evaluated using the initial condition:

$$\frac{dP}{dx} = 0 \quad \text{at} \quad x = -x_a \tag{1.6}$$

where: $P = P_{max}$ and $h = h_a$

Implementing this condition:

$$C1 = -6U\eta_o h_a + 12W_s x_a \eta_o \tag{1.7}$$

and:
$$\frac{dP}{dx} = \frac{6U\eta_o(h - h_a)}{h^3} + \frac{12W_s\eta_o(x + x_a)}{h^3} \tag{1.8}$$

Now, let the film thickness assume a parabolic variation in the direction of flow [7]:

$$h = h_o\left(1 + \frac{x^2}{2Rh_o}\right) \tag{1.9}$$

where R is the 'reduced radius' of the two rolling elements:

$$R = \frac{r_1 r_2}{r_1 + r_2} \tag{1.10}$$

Substituting for h in the equation of the pressure gradient (1.8):

$$\frac{dP}{dx} = \frac{6\eta_o}{h_o^3\,(1 + (x^2/2Rh_o))^3}\left\{\frac{U}{2R}(x^2 - x_a^2) + 2W_s(x + x_a)\right\} \tag{1.11}$$

Equation (1.11) can be solved numerically by employing the dimensionless groups below:

$$\tan \bar{x} = \frac{x}{\sqrt{2 R h_o}}$$

$$\tan \bar{x}_a = \frac{x_a}{\sqrt{2 R h_o}}$$

$$P^* = \frac{h_o^{3/2}\, P}{6\, U\, \eta_o\, (2R)^{1/2}} \tag{1.12}$$

$$W_s^* = \frac{W_s}{U}$$

$$h_o^* = \frac{h_o}{R}$$

Thus: $$dx = \sqrt{2 R h_o}\, \sec^2 \bar{x}\, d\bar{x}$$

(1.13)

and: $$d\bar{x}_a = 0$$

Implementing these substitutions:

$$\frac{dP^*}{d\bar{x}} = \Big\{\sin^2 \bar{x} \cos^2 \bar{x} - \tan^2 \bar{x}_a \cos^4 \bar{x}$$

$$+ \frac{4W_s^*}{\sqrt{2h_o^*}} (\sin \bar{x} \cos^3 \bar{x} + \tan \bar{x}_a \cos^4 \bar{x})\Big\} \tag{1.14}$$

Integrating both sides of equation (1.14) with respect to $\bar{x}$:

$$P^* = \frac{1}{8}\bar{x} - \frac{1}{32} \sin 4\bar{x} - \tan^2 \bar{x}_a \left(\frac{3}{8}\bar{x} + \frac{1}{4}\sin 2\bar{x} + \frac{1}{32}\sin 4\bar{x}\right)$$

$$+ \frac{4W_s^*}{\sqrt{2h_o^*}} \Big\{- \frac{3}{32} - \frac{1}{8}\cos 2\bar{x} - \frac{1}{32}\cos 4\bar{x} + \tan \bar{x}_a$$

$$\left(\frac{3}{8}\bar{x} + \frac{1}{4}\sin 2\bar{x} + \frac{1}{32}\sin 4\bar{x}\right)\Big\} + C2 \tag{1.15}$$

Assuming a fully flooded inlet, the constant of integration, $C2$, can be evaluated using the boundary condition:

$$P = 0 \quad \text{at} \quad x = -\infty \tag{1.16}$$

In terms of dimensionless variables:

$$P^* = 0 \quad \text{at} \quad \bar{x} = -\frac{\pi}{2} \tag{1.17}$$

Therefore: $$C2 = \frac{\pi}{16}\left(1 - 3\tan^2\bar{x}_a + \frac{12W_s^*}{\sqrt{2h_o^*}}\tan\bar{x}_a\right) \tag{1.18}$$

Substituting $C2$ into equation (1.15), the final expression for the pressure distribution in terms of dimensionless quantities is obtained:

$$\begin{aligned} P^* = {} & \frac{1}{8}\bar{x} - \frac{1}{32}\sin 4\bar{x} - \tan^2\bar{x}_a\left(\frac{3}{8}\bar{x} + \frac{1}{4}\sin 2\bar{x} + \frac{1}{32}\sin 4\bar{x}\right) \\ & + \frac{4W_s^*}{\sqrt{2h_o^*}}\left\{-\frac{3}{32} - \frac{1}{8}\cos 2\bar{x} - \frac{1}{32}\cos 4\bar{x} + \tan\bar{x}_a \right. \\ & \left. \left(\frac{3}{8}\bar{x} + \frac{1}{4}\sin 2\bar{x} + \frac{1}{32}\sin 4\bar{x}\right)\right\} \\ & + \frac{\pi}{16}\left\{1 - 3\tan^2\bar{x}_a + \frac{12W_s^*}{\sqrt{2h_o^*}}\tan\bar{x}_a\right\} \end{aligned} \tag{1.19}$$

It is evident that the pressure distribution depends on the value of $\bar{x}_a$. In the case of pure rolling elements, the equation (1.19) reduces to equation (1.20) below, where $W_s^* = 0$:

$$\begin{aligned} P^* = {} & \frac{1}{8}\bar{x} - \frac{1}{32}\sin 4\bar{x} - \tan^2\bar{x}_a\left(\frac{3}{8}\bar{x} + \frac{1}{4}\sin 2\bar{x} + \frac{1}{32}\sin 4\bar{x}\right) \\ & + \frac{\pi}{16}\left(1 - 3\tan^2\bar{x}_a\right) \end{aligned} \tag{1.20}$$

The value of $\bar{x}_a$ can be established by applying an additional condition. Assuming a fully flooded outlet:

$$P^* = 0 \quad \text{at} \quad \bar{x} = + \frac{\pi}{2} \tag{1.21}$$

Therefore: $$\tan \bar{x}_a = \left\{- \frac{12W_s^*}{\sqrt{2h_o^*}} \pm \sqrt{\frac{72W_s^{*2}}{h_o^*} + 12}\right\}/-6 \tag{1.22}$$

When $W_s^* = 0$, the value of $\bar{x} = -\bar{x}_a$ which corresponds to the peak pressure at $P^* = P^*_{max}$, $dP^*/d\bar{x} = 0$. The value of $\tan \bar{x}_a = \pm 1/\sqrt{3}$, which is the Sommerfeld condition. It can also be seen that if $72W_s^{*2}/h_o^* >> 12$, then $\tan \bar{x}_a \doteqdot 0$, which is at the position of pure squeeze effect.

The numerical results obtained for dimensionless pressures for given W_s^* values are illustrated in Figure 1.3. Here, the negative pressures calculated are discarded as the fluids cannot support these pressures. It can be observed that as W_s^* increases negatively (i.e. larger velocity of normal approach), the pressure distribution increases in magnitude and the maximum pressure approaches the position of $\bar{x} = 0$ (i.e. position due to pure normal approach). When $W_s^* = 0$, the pressure distribution is that of half Sommerfeld, where $\tan \bar{x}_a = -1/\sqrt{3}$. The analysis already discussed was also adopted by Sasaki, et al. [9]. This condition, however, fails to satisfy the continuity of mass flow and thus, at the outlet, a cavitation boundary condition must be adopted. For this purpose, it is usual to employ the Reynolds or Swift-Stieber boundary conditions. In such a case, both the pressure and its gradient return to zero at the point of film rupture:

$$P = \frac{dP}{dx} = 0 \quad \text{at} \quad x = x_e \tag{1.23}$$

To alter the equation (1.19) to suit the new boundary conditions, let $dP/dx = 0$ at $x = x_e$, rather than $x = -x_a$. Therefore, simply replace $\bar{x}_a$

by $-\overline{x}_e$:

$$p^* = \frac{1}{8}\,\overline{x} - \frac{1}{32}\sin 4\overline{x} - \tan^2\overline{x}_e\,\left(\frac{3}{8}\,\overline{x} + \frac{1}{4}\sin 2\overline{x} + \frac{1}{32}\sin 4\overline{x}\right)$$

$$+ \frac{4W_s^*}{\sqrt{2h_0^*}}\left\{-\frac{3}{32} - \frac{1}{8}\cos 2\overline{x} - \frac{1}{32}\cos 4\overline{x} - \tan\overline{x}_e\right.$$

$$\left.\left(\frac{3}{8}\,\overline{x} + \frac{1}{4}\sin 2\overline{x} + \frac{1}{32}\sin 4\overline{x}\right)\right\}$$

$$+ \frac{\pi}{16}\left\{1 - 3\tan^2\overline{x}_e - \frac{12W_s^*}{\sqrt{2h_0^*}}\tan\overline{x}_e\right\} \qquad (1.24)$$

Now, the pressure distribution is dependent on the position of the oil film rupture, $\overline{x}_e$. Values of $\overline{x}_e$ can be determined for any particular set of values of W_s^* and h_0^* by applying the other half of the condition (1.23):

$$\frac{1}{8}\,\overline{x}_e - \frac{1}{32}\sin 4\overline{x}_e - \tan^2\overline{x}_e\,\left(\frac{3}{8}\,\overline{x}_e + \frac{1}{4}\sin 2\overline{x}_e + \frac{1}{32}\sin 4\overline{x}_e\right)$$

$$+ \frac{4W_s^*}{\sqrt{2h_0^*}}\left\{-\frac{3}{32} - \frac{1}{8}\cos 2\overline{x}_e - \frac{1}{32}\cos 4\overline{x}_e \mp \tan\overline{x}_e\right.$$

$$\left.\left(\frac{3}{8}\,\overline{x}_e + \frac{1}{4}\sin 2\overline{x}_e + \frac{1}{4}\sin 4\overline{x}_e\right)\right\} + \frac{\pi}{16}\left(1 - 3\tan^2\overline{x}_e \mp \frac{12W_s^*}{\sqrt{2h_0^*}}\tan\overline{x}_e\right) = 0 \qquad (1.25)$$

Equation (1.25) yields the value of $\overline{x}_e$. The position of maximum pressure, $\overline{x}_a$, can also be found from (1.25) by letting $\overline{x}_e = \overline{x}_a$ and using the lower sign conventions. The boundary condition corresponding to the inlet is used for both these alternative methods.

The numerical solution of the pressure distribution using the Reynolds condition yields the results illustrated in Figure 1.4 for varying squeeze-roll speed ratio, W_s^*. It can be observed from these results that the position of the film rupture and the position of maximum pressure are equi-distant from the line $\overline{x} = 0$, when the elements are purely rolling

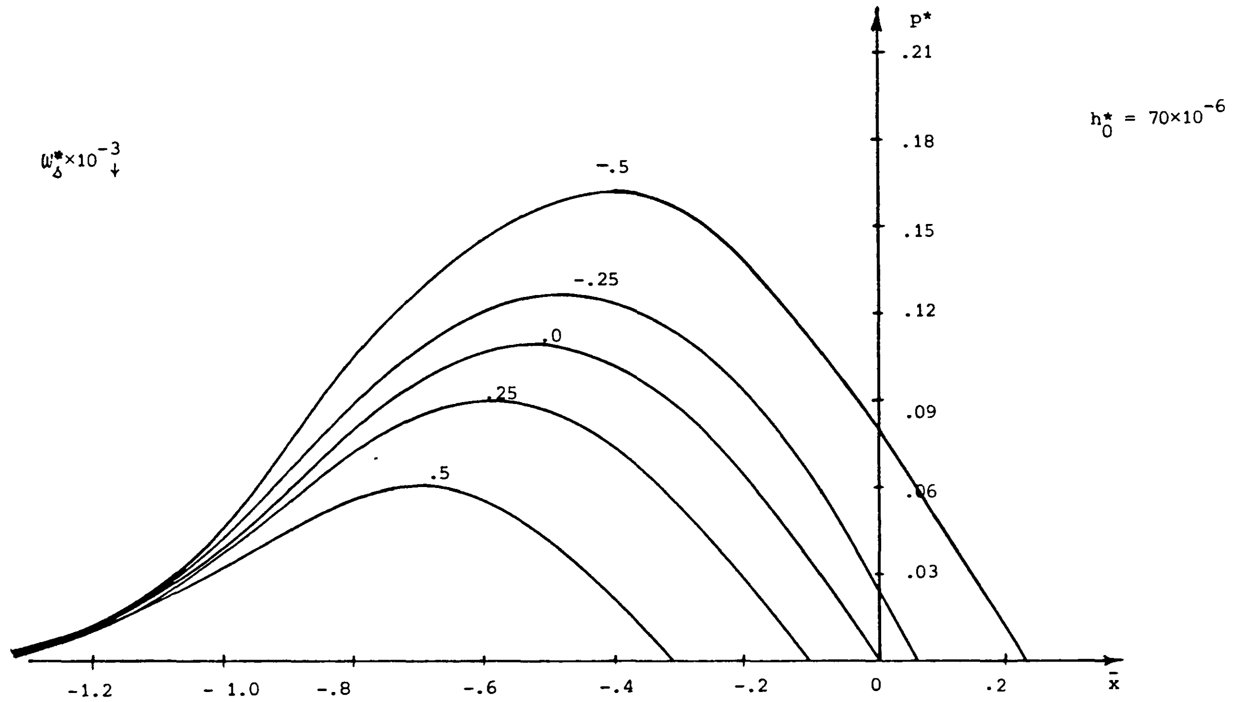

Fig 1.3 Dimensionless Iso-Viscous Pressure Distribution (combined Half Sommerfeld condition and squeeze effect)

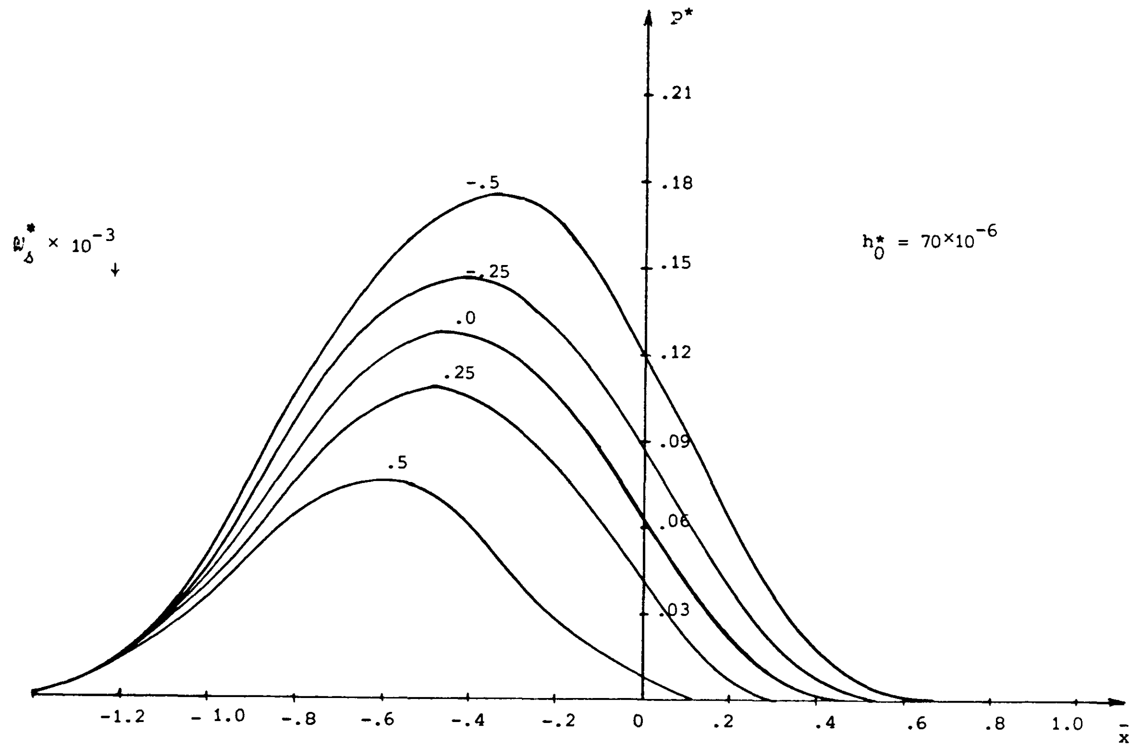

Fig 1.4 Dimensionless Iso-Viscous Pressure Distribution (combined Reynolds condition and squeeze effect)

[10]:

$$|\bar{x}_e| = |\bar{x}_a| \tag{1.26}$$

As the value of W_s^* increases negatively, the value of $|\bar{x}_e|$ increases and the corresponding value of $|\bar{x}_a|$ decreases. Also, the corresponding maximum pressure increases in magnitude. For the same value of W_s^*, the maximum pressure using the Reynolds boundary condition is greater than that yielded by the Sommerfeld boundary condition. Furthermore, the areas under the corresponding pressure distributions exhibit a greater instantaneous load carrying capacity for the pressure distribution relating to the Reynolds boundary condition.

1.3 INSTANTANEOUS LOAD CARRYING CAPACITY

The pressure distributions of Figures 1.3 and 1.4 are based upon the infinitely long bearing assumption. The area under the pressure distribution curve is the load carried by the lubricant per unit length:

$$\frac{W}{L} = \int_{x_i}^{x_e} P \, dx \tag{1.27}$$

The limits of this integral depend on the initial boundary conditions used. For purely rolling elements, the Sommerfeld condition is applicable, where $x_i = -\infty$ and $x_e = 0$. However, to simulate vibrational chatter in rolling element contacts, one or both elements are made to undergo normal motion. Therefore, the pressure limit at exit (i.e. x_e) varies as the squeeze speed, W_s, changes. The equation (1.27) is converted in terms of dimensionless parameters using the groupings given by equation (1.12), hence:

$$\frac{W\, h_o}{12\, b\, U\, \eta_o\, R} = \int_{\bar{x}_i}^{\bar{x}_e} P^* \sec^2 \bar{x} \, d\bar{x} \tag{1.28}$$

Let $\overline{W} = (W h_0)/(12 b U \eta_0 R)$ and integrate equation (1.28) with respect to $\overline{x}$ by replacing for P^* from equation (1.19), hence:

$$\overline{W} = \frac{1}{6} [\cos \overline{x}]_{\overline{x}_i}^{\overline{x}_e} - \frac{W_s^*}{4\sqrt{2h_0^*}} [\overline{x}]_{\overline{x}_i}^{\overline{x}_e} \tag{1.29}$$

The cosine term indicates the contribution of the rolling term and the remaining term is due to the effect of normal loading (i.e. squeeze effect). Therefore, for a crude but simple solution, a superposition idea can be adopted where, for the former term, the limits of integral are:

$$\overline{x}_i = -\frac{\pi}{2} \quad \text{and} \quad \overline{x}_e = 0$$

and for the latter term:

$$\overline{x}_i = -\frac{\pi}{2} \quad \text{and} \quad \overline{x}_e = +\frac{\pi}{2}$$

Implementing the limits of integration:

$$\overline{W} = \frac{1}{6} - \frac{\pi W_s^*}{4\sqrt{2h_0^*}} \tag{1.30}$$

When $W_s^* = 0$, the integrated pressure distribution yields the load due to the half Sommerfeld condition:

$$\overline{W} = \frac{1}{6} \tag{1.31}$$

Thus, using the grouping $\overline{W} = (W h_0)/(12 b U \eta_0 R)$:

$$W = \frac{2 b U \eta_0 R}{h_0} \tag{1.32}$$

and for equation (1.30):

$$W = \frac{2\,b\,U\,\eta_o\,R}{h_o} - \frac{3\,\pi\,b\,U\,\eta_o\,R\,W_s^*}{\sqrt{2h_o^*}} \tag{1.33}$$

Replacing for $W_s^* = W_s/U$ and let $W_s = dh_o/dt = \dot{h}_o$, equation (1.33) becomes:

$$W = \frac{2\,b\,U\,\eta_o\,R}{h_o} - \frac{3\,\pi\,b\,\eta_o\,R^{3/2}\,\dot{h}_o}{\sqrt{2}\,h_o^{3/2}} \tag{1.34}$$

where $\dot{h}_o < 0$ for normally approaching elements. A similar superposition assumption may be employed for normally departing elements. However, if the effects of suction and cavitation are to be neglected, the limits of the second term are:

$$\bar{x}_i = -\frac{\pi}{2} \quad \text{and} \quad \bar{x}_e = 0$$

Therefore, the load carried by the iso-viscous lubricant when the elements are subjected to departing motion (i.e. load relieving) is:

$$W = \frac{2\,b\,U\,\eta_o\,R}{h_o} - \frac{3\,\pi\,b\,\eta_o\,R^{3/2}\,\dot{h}_o}{2\sqrt{2}\,h_o^{3/2}} \tag{1.35}$$

where $\dot{h}_o > 0$ for normally departing elements. If the contribution due to pure rolling of elements is based upon the Reynolds condition, the term P^* in equation (1.28) is replaced from equation (1.24). Furthermore, the limits of integral for the rolling term are:

$$\bar{x}_i = -\frac{\pi}{2} \quad \text{and} \quad \bar{x}_e = \tan^{-1}(0.475129)$$

where $\bar{x}_e$ is the position of the oil film rupture for pure rolling effect. The instantaneous load carrying capacity is marginally increased in comparison to the combined half Sommerfeld and squeeze effect. By simple superposition:

$$W = \frac{2.8\, b\, U\, \eta_0\, R}{h_0} - \frac{3\pi\, b\, \eta_0\, R^{3/2}\, \dot{h}_0}{\sqrt{2}\, h_0^{3/2}} \tag{1.36}$$

where $\dot{h}_0 < 0$ for normally approaching rolling elements. For normally departing rolling contacts:

$$W = \frac{2.8\, b\, U\, \eta_0\, R}{h_0} - \frac{3\pi\, b\, \eta_0\, R^{3/2}\, \dot{h}_0}{2\sqrt{2}\, h_0^{3/2}} \tag{1.37}$$

where $\dot{h}_0 > 0$. The extent of inaccuracy due to superposition assumption is determined by comparing the results of expressions (1.34), (1.35), (1.36) and (1.37) with the appropriate numerically integrated pressure distributions using Simpson's rule. It is observed that the maximum percentage errors are about 10%. The error is greatest at higher values of squeeze velocity.

1.4 SURFACE TRACTION

It is of interest to obtain the values of tractive forces generated on the surfaces of two rolling elements due to the oil film pressure distribution and the sliding condition. For rolling and sliding elements, the contribution of the sliding motion is dominant and its effect plays an important rôle on the wear characteristics of the contacting elements. Some authors have investigated sliding friction by theoretical [11] and experimental [12] methods under various contacting conditions and lubricant properties. The shear stresses caused by surface traction contribute effectively in the phenomenon of scuffing of rolling elements such as gears or discs in 'disc machine' operation.

The lower and upper surfaces are considered to be at $z = 0$ and $z = h$.

The viscous stresses on these surfaces are [8]:

$$\tau_{1,2} = \pm \frac{h}{2} \frac{dP}{dx} + \eta_o \frac{(U_1 - U_2)}{h} \tag{1.38}$$

where indices *1* and *2* correspond to the upper and lower surfaces, respectively. Since the long bearing assumption is used, the friction force (i.e. surface traction) is:

$$\delta_{1,2} = \frac{F_{1,2}}{b} \tag{1.39}$$

where b represents the contact length. Thus:

$$\delta_{1,2} = \int_{x_i}^{x_e} \{\pm \frac{h}{2} \frac{dP}{dx} + \eta_o \frac{(U_1 - U_2)}{h}\} \, dx + \eta_o \, (U_1 - U_2) \, h_e \int_{x_e}^{x_o} \frac{dx}{h^2} \tag{1.40}$$

Equation (1.40) may be represented non-dimensionally using the substitutions listed in equation (1.12) and the groupings given below:

$$\Delta U^* = \frac{\Delta U}{U} \quad , \quad \text{where } \Delta U = U_1 - U_2$$

$$\delta^*_{1,2} = \frac{\delta_{1,2}}{U \, \eta_o} \tag{1.41}$$

$$\bar{h}_e = \frac{h_e}{h_o}$$

Therefore:

$$\delta^*_{1,2} = \pm \frac{6}{\sqrt{2h^*_o}} \int_{\bar{x}_i}^{\bar{x}_e} \sec^2 \bar{x} \, dP^* + \sqrt{2} \, \frac{\Delta U^*}{\sqrt{h^*_o}} \int_{\bar{x}_i}^{\bar{x}_e} d\bar{x}$$

$$+ \sqrt{2} \, \frac{\Delta U^* \, \bar{h}_e}{\sqrt{h^*_o}} \int_{\bar{x}_e}^{\bar{x}_o} \frac{d\bar{x}}{\sec^2 \bar{x}} \tag{1.42}$$

1.5 PIEZO-VISCOUS LUBRICANTS

It should be noted that in lubricated contacts of rolling elements, the pressures generated have a profound effect on the viscosity of the lubricant employed. In other words, an iso-viscous assumption for the lubricant film is extremely crude. Therefore, the dependence of oil viscosity on pressures generated are formulated by various models, each of which describe in an approximate manner a particular group of lubricants. For naphthenic oils:

$$\eta_{\dot{q}} = \eta_o \, e^{\alpha q} \tag{1.43}$$

where η_q is the viscosity at pressure q, η_o the atmospheric pressure viscosity, and α the 'piezo-viscosity' constant. For the more common paraffinic oils, the relationship is:

$$\eta_q = \eta_o \, (1 + C\, q)^n \tag{1.44}$$

where C and n are constants. Now, consider the Reynolds equation in one dimension. The pressure gradient is:

$$\frac{dq}{dx} = 6\, U \eta \, \frac{h - h_a}{h^3} \tag{1.45}$$

The viscosity term η is then replaced from equation (1.43):

$$e^{-\alpha q} \frac{dq}{dx} = 6\, U \eta_o \, \frac{h - h_a}{h^3} \tag{1.46}$$

Integrating the left hand side leads to:

$$- \frac{e^{-\alpha q}}{\alpha} + C_1 \tag{1.47}$$

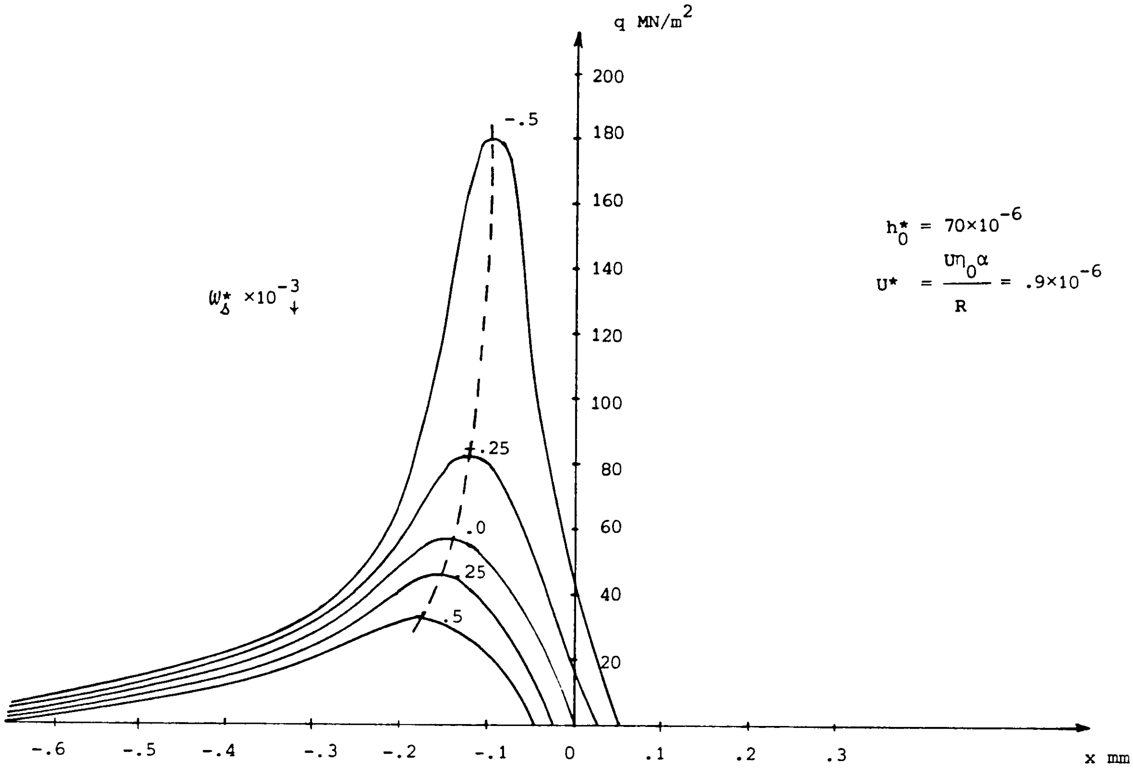

Fig 1.5 Actual Piezo-viscous Pressure Distribution (Combined Half Sommerfeld condition and squeeze effect)

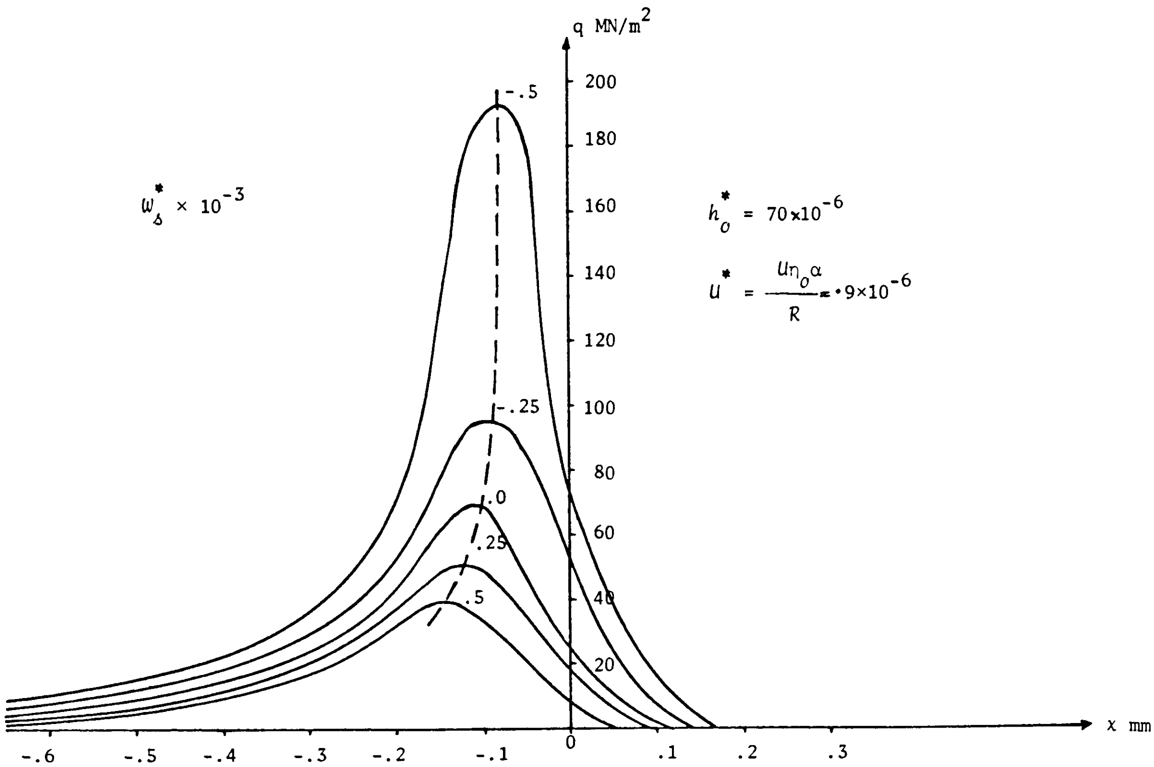

Fig 1.6 Actual Piezo-viscous pressure distribution (combined Reynolds condition and squeeze effect)

The constant must be selected such that when the piezo-viscous pressure, q, tends to zero, the whole term diminishes. Thus:

$$C_1 = \frac{1}{\alpha} \tag{1.48}$$

Therefore, the left hand side of equation (1.46) becomes:

$$P = \frac{1 - e^{-\alpha q}}{\alpha} \tag{1.49}$$

where P is known as the reduced pressure (i.e. the constant viscosity case) which is the iso-viscous pressure term.

Therefore, to solve the Reynolds equation using a piezo-viscous lubricant, the reduced pressure distribution (i.e. the iso-viscous pressure distribution) is initially calculated and those elements which satisfy the mathematical restriction $\alpha P_{max} < 1$ are considered to yield feasible results. This mathematical restriction effectively establishes a 'limiting film thickness', below which the subsequent pressures obtained are considered to be excessive and deemed unacceptable. The actual hydrodynamic pressure distribution is then evaluated using equation (1.49) (see Figures 1.5 and 1.6).

1.6 REFERENCES

[1] VON PAULI, F.A.
"Uber den Widerstand der Zapfenreibung",
Kunst und Gewerbeblatt des Polytechnischen Verein des Königreich Bayern, 1849.

[2] HIRN, G.A.
"Sur les Principaux Phénomènes que Présentent des Frottements Mediat et sur les Diverses Manières de Déterminer la Valeur Mécanique des Matières au Graissage des Machines",
Bull. de la Soc. Ind. de Mulhouse, 1854.

[3] PETROFF, N.P.
"Friction in Machines and the Effect of the Lubricant",
Inzhenernii Zhurnal, St Petersburg, 1883 (in Russian).

[4] TOWER, B.
"First Report on Friction Experiments",
Proc. Inst. Mech. Engrs., November 1883.

[5] REYNOLDS, O.
"On the Theory of Lubrication and its Application to Mr Beauchamp Tower's Experiments Including an Experimental Determination of the Viscosity of Olive Oil",
Phil. Trans., 1886.

[6] ROBERTSON, W.G., and CAMERON, A.
"On the Derivation of Reynolds' Equation",
Scientific Lubrication, 1962.

[7] CAMERON, A.
"The Principles of Lubrication",
Longmans Green & Company Limited, 1966.

[8] DOWSON, D., MARKHO, P.H., and JONES, D.A.
"The Lubrication of Lightly Loaded Cylinders in Combined Rolling, Sliding and Normal Motion",
Trans. ASME, J. Lubrication Technology, 1976.

[9] SASAKI, T., MORI, H., and OKINO, N.
"Fluid Lubrication Theory of Roller Bearings",
Trans. ASME, J. Basic Engineering, 1962.

[10] PINKUS, O., and STERNLICHT, B.
"Theory of Hydrodynamic Lubrication",
McGraw-Hill Book Company, Inc., New York, 1961.

[11] CROOK, A.W.
"The Lubrication of Rollers - Part III",
Phil. Trans. R. Soc., 1961.

[12] THORP, N., and GOHAR, R.

"Elastohydrodynamic Sliding Friction in a Low Modulus Point Contact",

J. Mech. Eng. Sci., 1973.

CHAPTER 2

INFLUENCE OF VIBRATIONS ON HYDRODYNAMIC LUBRICATION

2.1 INTRODUCTION

Rolling elements are usually subjected to fluctuating loads. An interesting extension to the numerical solution of Chapter 1 can be contemplated where the lubricating film is subjected to a cyclic forcing condition. Sasaki, Mori and Okino [1] have solved this problem for lubricated rigid cylinders under sinusoidal normal motion. Dowson, Markho and Jones [2] have compared the time average load carrying capacities of lubricating films subjected to sinusoidal motion with the corresponding steady-state load carrying capacities. They concluded that when sinusoidal normal motion is superimposed upon 'entraining' motion of two lightly loaded cylinders, a substantial increase in the nett load carrying capacity is encountered.

Rohde, Whicker and Booker [3] have also investigated the dynamic responses of squeeze films to fluctuating loads. They considered rigid, elastic and viscoelastic plates' response to a prescribed indenter motion and prescribed loadings. They noted that the transient behaviour decays more rapidly as the stiffness is increased. The pressure distribution also decays in the same manner as the temperature distribution in a transient heat conduction problem decays after the sources are turned off. This characteristic was concluded to be entirely due to the deformation rate effect which is often neglected in elastohydrodynamic problems. When the plates were assumed to be elastic, the response resembled a damped oscillation (see Figure 2.1). This behaviour was explained as follows [3]: "As the load is reduced, the pressures are reduced, and hence the time rate of change of deformation becomes negative and acts as a source term on the right hand side of the Reynolds equation". However,

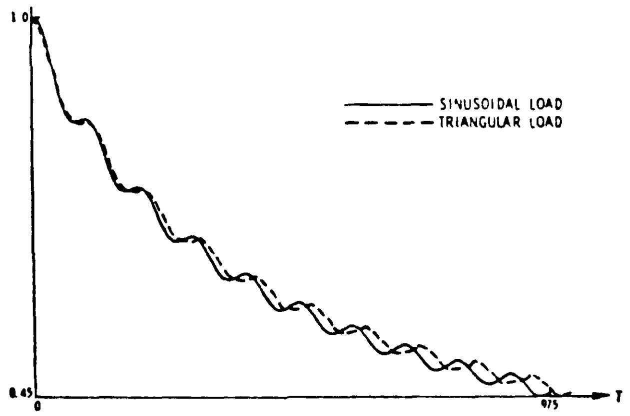

Film thickness versus T, elastic solid, E = 34480 kPa

Fig 2.1

θ = flow direction

ω = time base

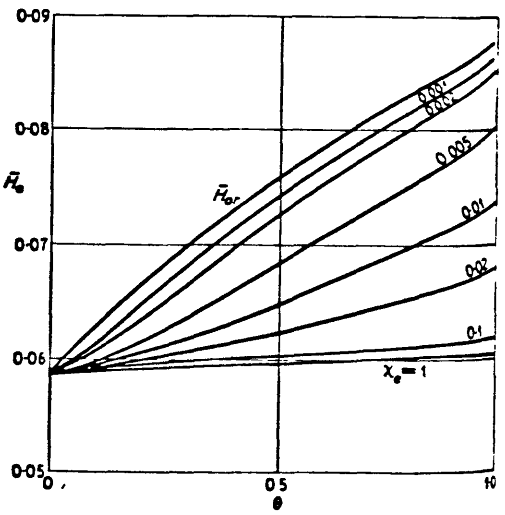

$b = 2.$
$\chi_r = 10.$
Different values of χ_e.

Fig 2.2

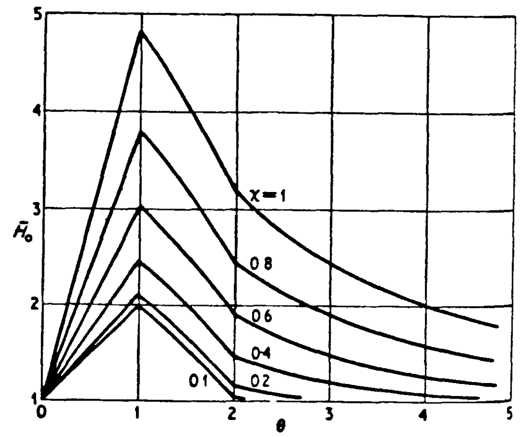

$A = 1$ for $\theta < 0$ and $\theta > 2$.
$A = 1+\theta$ for $0 < \theta < 1$.
$A = 1-\theta$ for $1 < \theta < 2$.
Variation of χ

Fig 2.3

$$X_e = \frac{\omega}{u} \sqrt{\frac{P_0 R}{E}}$$

X_e, is a number describing the damping phenomenon under Elastohydrodynamic condition

$$X = \omega R \sqrt{\frac{\eta_0}{U P_0}}$$

X, is a number describing the viscous damping under Hydrodynamic condition it was concluded that the response could not undergo a steady-state periodic form. Such characteristics in fact offer explanations to the manner of operation of certain systems, such as human joints, in a pure squeeze type motion without apparent load reversals.

Vichard [4] has examined the phenomenon of viscous damping, both under hydrodynamic and elastohydrodynamic contact conditions. The principal governing variables, such as load, temperature, radius of curvature and squeeze speed, were varied in turn in a time-dependent manner and their effects were investigated. It was established that the damping phenomenon due to normally approaching motion has a more vigorous effect under elastohydrodynamic contact conditions (see Figures 2.2 and 2.3).

Taylor and Kumar [5] have considered the numerical integration for prediction of dynamic response of squeeze film damper systems. They employed a planar rotor carried in a squeeze film damper with linear centering springs (see Figure 2.4). The fluid forces were obtained from the Ocvirk short bearing integrals and the governing differential equations were expressed in polar coordinates. The rotating unbalance was presented as a function of speed and a numerical integration technique was used to solve for transient response and the frequency response (see Figures 2.5 and 2.6). Initial eccentricity and eccentric velocity applications were found to be less important and, generally, the steady-state solution with lower eccentricity appeared to be more stable with a larger domain of convergence.

2.2 ROLLING ELEMENTS UNDER ROLLING AND NORMAL SINUSOIDAL MOTION

The first stage in a general time-dependent solution of bearings under fluctuating normal loads is to assume a cyclic forcing function. A sinusoidal loading condition may be considered to simplify the numerical

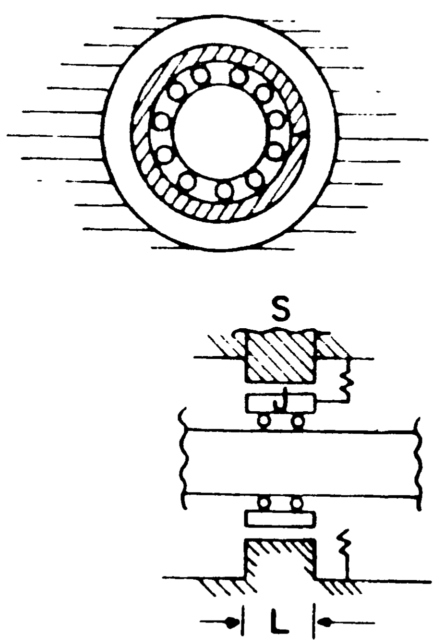

Squeeze film damper

Fig 2.4

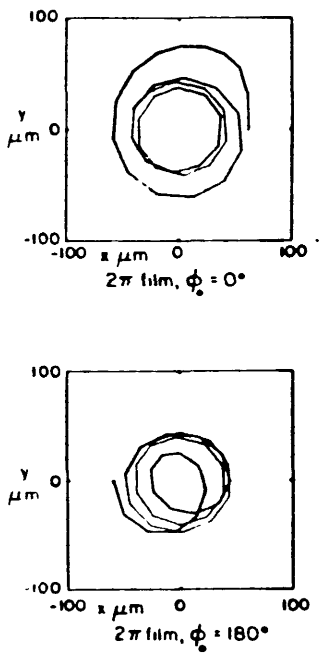

Transient response, e_e = 60 μm, $\dot{e}_e$ = 0.m/s
$\dot{\phi}_e$ = 1200 μ, rad/s, ω = 12,000 rev/min

Fig 2.5

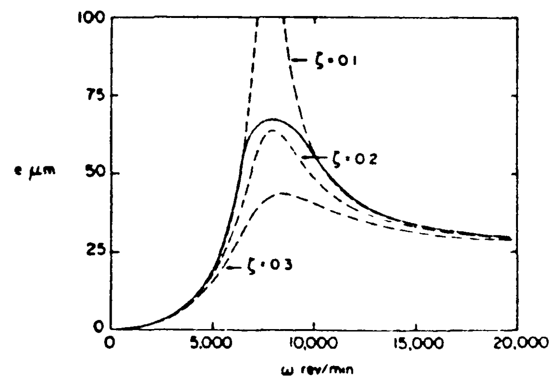

Unbalance speed response, 2π film

Fig 2.6

e = radial shaft displacement

ω = shaft speed

Ø = angular position

ζ = damping factor

solution of this problem. Furthermore, one may assume a cyclic harmonic response in normal motion. This characteristic behaviour for the lubricant has been adopted by several authors [1,2], where the lubricant undergoes steady-state harmonic response about a mean steady-state oil film thickness. The resulting pressure distribution during one cycle of loading can be determined, which leads to the evaluation of time-averaged load carrying capacity [2].

Let h_m be the mean steady-state lubricant film thickness. Therefore, the lubricant film response is governed by equation (2.1) below (see Figure 2.7):

$$h(t) = h_m + z_{max} \cos 2\pi f t \tag{2.1}$$

The squeeze velocity is defined as:

$$W_s(t) = \frac{dh(t)}{dt} = - 2\pi f z_{max} \sin 2\pi f t \tag{2.2}$$

The cosine variation for the lubricant film is adopted so that, initially, the squeeze velocity is zero and the bearing undergoes purely rolling motion with a thickness of $h_m + z_{max}$.

Now, let $W_{s_{max}} = 2\pi f z_{max}$, hence:

$$W_s(t) = - W_{s_{max}} \sin 2\pi f t \tag{2.3}$$

The squeeze-roll speed ratio, W_s^*, is therefore a time-dependent variable:

$$W_s^*(t) = \frac{W_s(t)}{U} = - \frac{W_{s_{max}}}{U} \sin 2\pi f t \tag{2.4}$$

and:
$$h^*(t) = \frac{h(t)}{R} = \frac{h_m + z_{max} \cos 2\pi f t}{R} \tag{2.5}$$

Therefore, if the extent (i.e. the amplitude) of the normal motion, z_{max}, and the frequency of sinusoidal normal forced vibration, δ, are selected, the variables $W_s^*(t)$ and $h^*(t)$ can be evaluated which, in turn, leads to the solution of the equation (1.19), yielding the instantaneous pressure distribution in the contacting region. Figure 2.8 illustrates changing dimensionless pressure distribution during the application of one cycle of forced normal vibration. The negative pressures generated due to sub-ambient conditions are discarded since cavitated lubricant layers under suction cannot withstand these pressures. There is one pressure distribution curve (i.e. the half Sommerfeld condition) which represents the instances of pure entraining motion. To distinguish between various instantaneous pressure distribution curves at pure rolling instances, one can re-dimensionalise using the groupingsof equation (1.12).

The position of maximum pressure for all pure rolling cases is at $\tan \bar{x}_a = -1/\sqrt{3}$. On the upward stroke (i.e. departing surfaces; $W_s^* > 0$), the locus of maxima passes through points where $\tan \bar{x}_a < -1/\sqrt{3}$. However, on the downstroke motion (i.e. normally approaching surfaces; $W_s^* < 0$), the maxima tend towards the pressure axis, where $0 > \tan \bar{x}_a > -1/\sqrt{3}$ (see Figure 2.8). This trend is because of the progressively more dominant rôle that the squeeze effect has on the pressure distribution.

2.3 ROLLING ELEMENTS SUBJECTED TO SINUSOIDAL NORMAL LOADS

A more general numerical solution is to apply the forcing function and obtain the lubricant response as a time-dependent variable. By applying this method, the transient non-harmonic and the subsequent steady-state harmonic responses of the lubricant can be evaluated. For a simple solution, the presence of an iso-viscous lubricant may be assumed. Furthermore, study of changing film thickness is of interest, especially at the position of the minimum film thickness, where the probability of

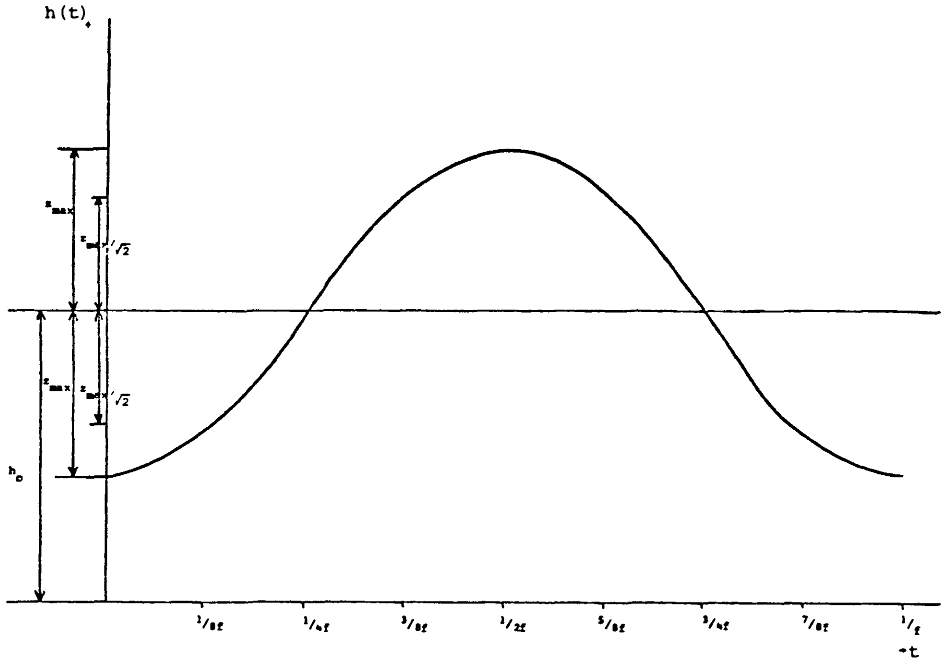

Fig.2.7 Minimum Film Thickness Variation due to Squeeze Effect

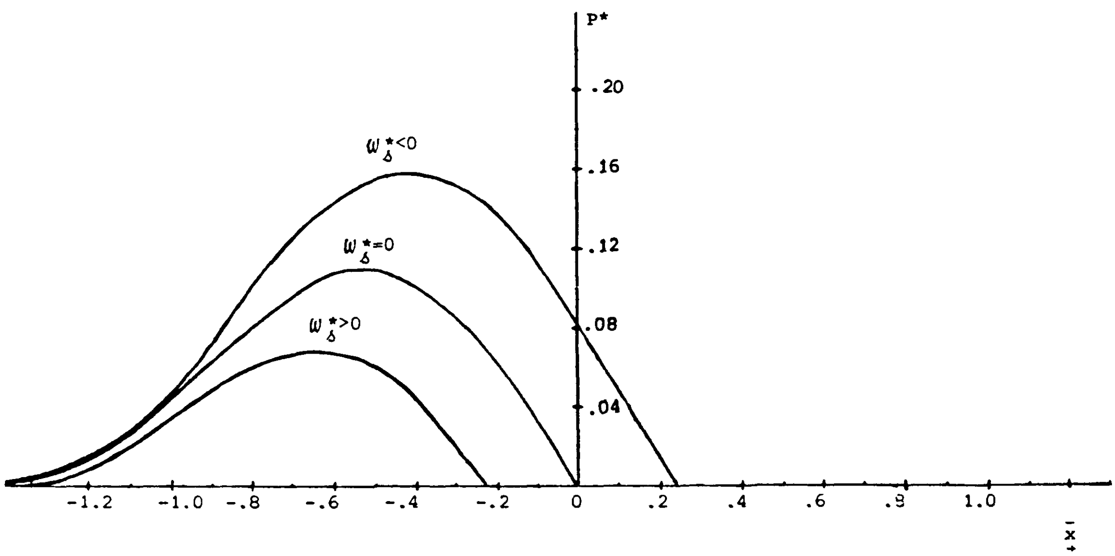

Fig 2.8 Dimensionless Iso-Viscous Pressure Distribution

the lubricant seizure is greatest. Such an occurrence gives an insight to the probable cause of scuffing in gears and rolling elements in general. The integration of equation (1.19) yields the load carried by the lubricant film. For purely rolling elements, the load is given by [6,7]:

$$W = \frac{2\,b\,U\,\eta_0\,R}{h_0} \tag{2.6}$$

When these rolling elements are subjected to normal loading such that they undergo normal approach (see Chapter 1):

$$W \doteq \frac{2\,b\,U\,\eta_0\,R}{h_0} - \frac{3\,\pi\,b\,\eta_0\,R^{3/2}\,\dot{h}_0}{\sqrt{2}\,h_0^{\,3/2}} \tag{2.7}$$

The equation (2.7) is obtained by an analytical integration of equation (1.19), incorporating a superposition approximation where:

$$W = W_{rolling} + W_{squeezing} \tag{2.8}$$

This assumption has also been made by other authors to enable the integration by analytical means and is not an absolutely accurate approximation. The varying minimum film thickness due to a cyclic forcing function, $F(t)$, is:

$$h(t) = h_0 + z(t) \tag{2.9}$$

where $z(t)$ is the dynamic displacement of the minimum film thickness due to the implementation of the periodic forcing function. Thus:

$$\dot{h}(t) = \frac{dh(t)}{dt} = \dot{z}(t) = W_s \tag{2.10}$$

and:

$$\ddot{h}(t) = \frac{d^2h(t)}{dt} = \ddot{z}(t) \qquad (2.11)$$

The magnitude of h_0 can be fixed as the original oil film thickness in this initial value problem, where the periodic forced loading has not yet commenced (see Figure 2. 9). For equilibrium, when $F(t) = F_{max} \cos 2\pi f t$ and $t = 0$:

$$W - mg - (Q + F_{max}) = 0 \qquad (2.12)$$

where, for purely rolling elements:

$$W = \frac{2\, b\, U\, \eta_0\, R}{h_0}$$

Thus, the minimum oil film thickness under the fixed load of $Q + F_{max} + mg$ is:

$$h_0 = \frac{2\, b\, U\, \eta_0\, R}{(mg + Q + F_{max})} \qquad (2.13)$$

When the periodic loading is introduced to one of the two rolling elements, the loaded bearing may (see Figure 2.10):

(a) Approach the unloaded bearing (i.e. downstroke squeezing).

(b) Depart from the unloaded bearing (i.e. upstroke squeezing).

(a) Downstroke Squeezing

The dynamic equation of motion for the centre-line of the loaded cylinder is:

$$W(t) - (mg + Q + F_{max} \cos 2\pi f t) = m\, \ddot{z}(t) \qquad (2.14)$$

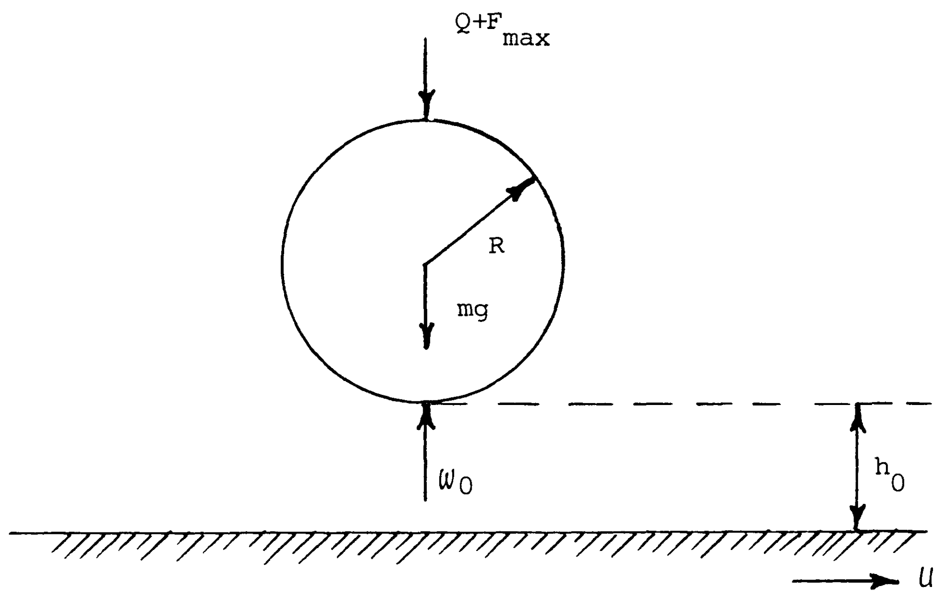

Fig 2.9 Physical representation of system's initial force balance

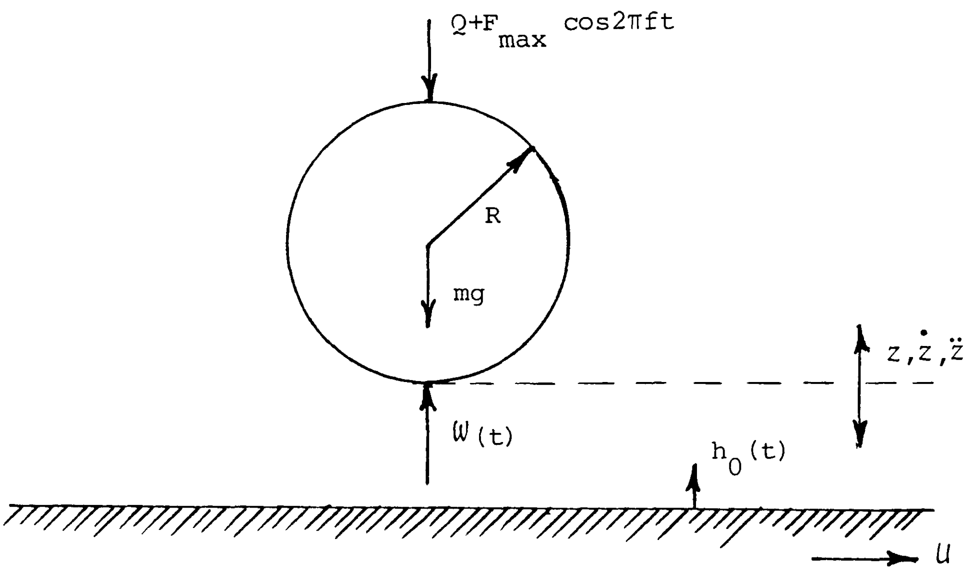

Fig 2.10 Physical representation of system dynamics

where $W(t)$ is given by equation (2.7). Equation (2.14) also describes the motion of the surface of the rolling element and the outermost adjacent iso-viscous lubricant layer. This is true since the rolling element's surface does not suffer any elastic deformation under hydrodynamic contact conditions.

(b) Upstroke Squeezing

Neglecting the effect of cavitation and suction due to any reduction in the magnitude of loading (i.e. assuming that the lubricant does not support negative pressures):

$$W_{upstroke} = W_{rolling} \tag{2.15}$$

Hence:

$$W(t)_{upstroke} = \frac{2\,b\,U\,\eta_o\,R}{h(t)} \tag{2.16}$$

2.4 NUMERICAL METHOD OF SOLUTION

Replacing for $W(t)$ in equation (2.14) from either equation (2.7) or (2.15), the resulting equation of forced vibration is of non-linear form. The solution to this pair of equations gives a complete picture of the minimum oil film thickness response to the applied forcing function, which is achieved using the "average acceleration method" [6].

The dynamic displacement, $z_{i,j}$, is calculated using:

$$z_{i,j} = z_{i-1} + 2\dot{z}_{i-1}\frac{dt}{3} + \ddot{z}_{i-1}\frac{dt^2}{6} + \dot{z}_{i,j}\frac{dt}{3} \tag{2.17}$$

for $i > 1$, $j \geqslant 1$, where i indicates the time interval, j the iteration index, and dt is the fixed interval of time during which the average acceleration is assumed. Accuracy of the solution is ensured by selecting a very small value for dt, usually in the region of one tenth of a millisecond.

For $i = 1$:

$$z_{1,j} = z_0 + 2\dot{z}_0 \frac{dt}{3} + \ddot{z}_0 \frac{dt}{6} + \dot{z}_{1,j} \frac{dt}{3} \tag{2.18}$$

where z_0, $\dot{z}_0$ and $\ddot{z}_0$ are the initial conditions at:

$$h(t) = h_0 \quad , \quad t = 0 \tag{2.19}$$

and:

$$\dot{z}_{i,j} = \dot{z}_{i-1} + \ddot{z}_{i-1} \frac{dt}{2} + \ddot{z}_{i,j-1} \frac{dt}{2} \tag{2.20}$$

for $i > 1$, $j \geqslant 1$. If the value of squeezing velocity, $\dot{z}_{i,j} < 0$, then the contacting surfaces are normally approaching:

$$\ddot{z}(i,j) = \frac{2\,b\,U\,\eta_0\,R}{m\,\{h_0 + z_{i,j}\}} - \frac{3\,\pi\,b\,\eta_0\,R^{3/2}\,\dot{z}_{i,j}}{\sqrt{2}\,m\,\{h_0 + z_{i,j}\}^{3\ 2}} - \frac{Q + F_{max}\cos 2\pi f\, t_i}{m} - g \tag{2.21}$$

and if $\dot{z}_{i,j} \geqslant 0$, then:

$$\ddot{z}_{i,j} = \frac{2\,b\,U\,\eta_0\,R}{m\,\{h_0 + z_{i,j}\}} - \frac{Q + F_{max}\cos 2\pi f\, t_i}{m} - g \tag{2.22}$$

The governing equations of motion (2.21) and (2.22) are used in conjunction with equations (2.17) and (2.20) in an iterative marching procedure to yield the values of $z_{i,j}$, $\dot{z}_{i,j}$ and $\ddot{z}_{i,j}$ for time $t = t_i$ and $F(t_i) = Q + F_{max}\cos 2\pi f\, t_i$, when:

$$|z_{i,j} - z_{i,j-1}| \leqslant \varepsilon \tag{2.23}$$

where ε is the specified accuracy required.

The iterative procedure is commenced using the initial conditions below:

$$z_0 = \dot{z}_0 = 0 \ , \ F_0 = Q + F_{max} \ , \ h(t) = h_0$$

$$\ddot{z}_0 = \frac{2\,b\,U\,\eta_0\,R}{m\,h_0} - \frac{Q + F_{max}}{m} - g$$

$$\dot{z}_{1,j} = \dot{z}_0 + \ddot{z}_0\,dt \quad \text{for} \quad i = 1 \tag{2.24}$$

$$\dot{z}_{2,j} = \dot{z}_0 + 2\ddot{z}_0\,dt \quad \text{for} \quad i = 2$$

and: $$\dot{z}_{i,j} = \dot{z}_{i-2} + 2\ddot{z}_{i-1}\,dt \quad \text{for} \quad i > 2$$

2.5 ISO-VISCOUS RESULTS AND DISCUSSIONS

The response to a sinusoidal forcing of $F(t) = F_{max}\cos 2\pi f t$ is a harmonic steady-state lubricant film thickness, initially undergoing a non-harmonic state of transient (see Figure 2.11). This pattern of response illustrates that the assumption of a sinusoidal normal motion as a result of applied sinusoidal forcing function as adopted in equation (2.2) and by several authors [1,2] is not absolutely realistic. Furthermore, due to the non-linear characteristics of the lubricant, the response frequency is different to that of the applied forcing frequency.

Ideally, when the applied force is decreasing, the film thickness should be increasing and vice versa. Therefore, when $F(t) = F_{max}$, $h(t) = h_{min}$. However, the response as shown on Figure 2.11 does not follow this ideal pattern fully and exhibits a phase lag equivalent to 5/16th of the forcing cycle. This lag is due to the non-linear nature of the system and the presence of damping because of the viscoelastic property of the lubricant film.

To obtain a clearer picture of the lubricant response to periodic loading, the squeezing velocity $\dot{z}(t)$ and its derivative, the acceleration of the normally loaded bearing $\ddot{z}(t)$, are also plotted (see Figures 2.12 and 2.13). Both these variables also lag the periodic forcing function but with smaller phase margins. In fact, the acceleration leads the velocity which, in turn, leads the oil film response. This state of affairs conforms with the mathematical reality [6].

In the steady-state condition, whenever $\dot{z}(t) = \dot{z}_{max}$ or $\dot{z}(t) = \dot{z}_{min}$, its derivative $\ddot{z}(t) = d\dot{z}(t)/dt = 0$ and at any position where $d\ddot{z}(t)/dt = \dddot{z}(t) = 0$ (i.e. no jerk, maximum or minimum acceleration), $d^2\dot{z}(t)/dt^2$ also returns to zero, resulting in points of inflection on the squeezing velocity graph.

When $\dot{z}(t) < 0$ (i.e. normally approaching and rolling elements), equation (2.21) is used and the acceleration $\ddot{z}(t)$ tends to reverse the motion of the loaded cylinder because of an increase in the value of the damping force exerted by the lubricant film and the reduction in the value of the applied periodic force $F(t)$. In the upstroke motion when $\dot{z}(t) > 0$, the acceleration tends to reverse the motion only when the applied forcing function decreases (see equation (2.22)). In a pure squeeze type motion, when the 'entraining' velocity ceases to exist, there is no apparent load reversals [3].

In general, the iso-viscous lubricants have very low load carrying capacities. This fact can be verified by a gradual increase in the amplitude of the applied forcing. Figure 2.14 illustrates the oil film response for increased sinusoidal normal loading. A considerable

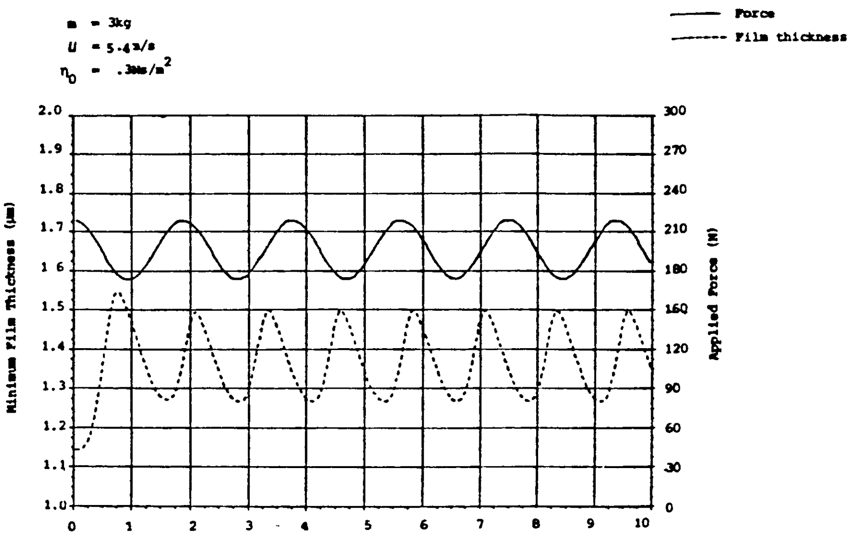

Fig 2.11 ISO-viscous lubricant response subjected to normal sinusoidal forcing

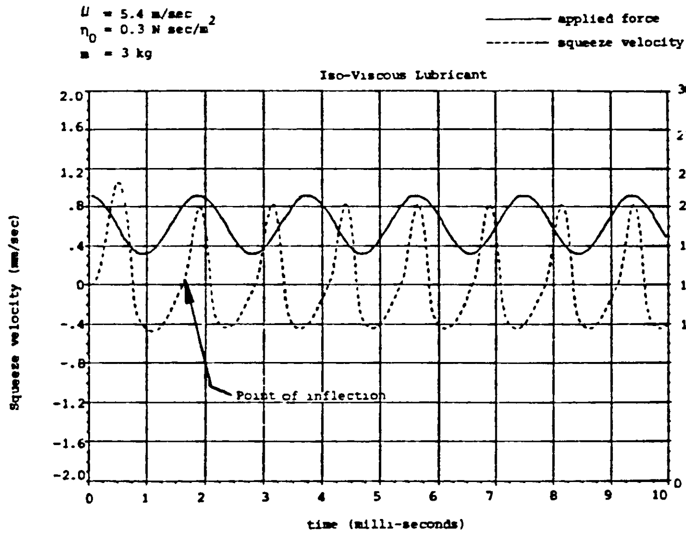

Fig 2.12 Time history of squeeze velocity under normal sinusoidal forcing

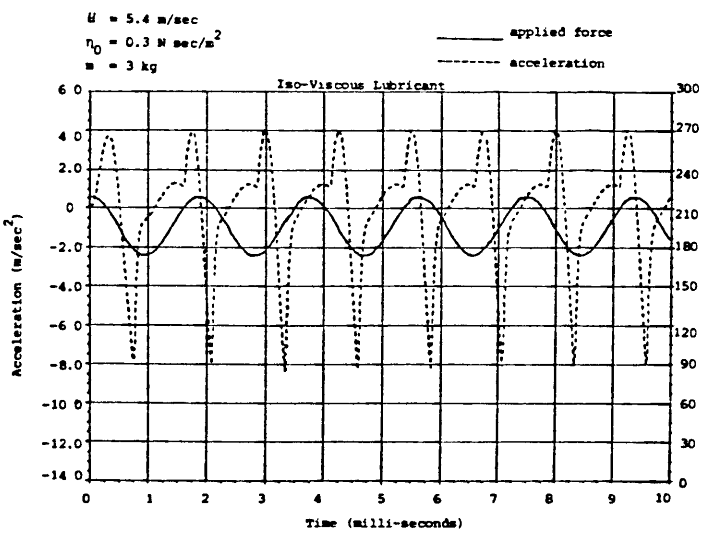

Fig 2.13 Time history of acceleration under normal sinusoidal forcing

reduction in the film thickness (i.e. 15% to 20%) can be observed. More noticeably, a plot of acceleration (see Figure 2.15), although exhibiting the same overall characteristics as before, manifests the occurrence of multiple turning points (i.e. beatings) which are due to an increase in the dynamical oil film instability. In fact, the survival of any finite oil film thickness at this magnitude of loading is merely due to the high speed of rolling assumed (i.e. 5.4 m/s). At lower speeds of rolling (i.e. larger W_s^* ratios), the iso-viscous lubricant ceases to exist at much lower loading magnitudes.

2.6 PIEZO-VISCOUS LUBRICANT UNDER SINUSOIDAL NORMAL LOADING

Because of the iso-viscous low load carrying capacity, the results obtained are far from reality. A piezo-viscous lubricant can be considered, where:

$$\eta = \eta_o \, e^{\alpha q} \tag{2.25}$$

The newly established pressure distribution, q, yields a higher film thickness and an increased load carrying capacity. The lubricant reaction, $W(t)$, at the position $h(t) = h_o$ (i.e. minimum (central) film thickness) is obtained by a regressional analysis of the results obtained for piezo-viscous integrated pressure distribution for two normally loaded rolling cylinders:

$$\overline{W}(t) = \frac{0.55\overline{U}^{7/4}}{h^*(t)^{5/2} \cdot e^{703 W_s^*(t)}} \tag{2.26}$$

where the non-dimensional groupings used are:

$$\overline{W}(t) = \frac{h(t)\, W(t)}{12\, b\, U\, \eta_o\, R} \quad , \qquad W_s^*(t) = \frac{W_s(t)}{U}$$

$$\overline{U} = \frac{U\, \eta_o\, \alpha}{R} \qquad \text{and} \qquad h^*(t) = \frac{h(t)}{R} \tag{2.27}$$

The dynamics governing equation of forced normal vibration of the centre of the loaded cylinder is:

$$W(t) - (mg + Q + F(t)) = m\,\ddot{z}(t) \tag{2.28}$$

where $W(t)$ and $F(t)$ also include their original values $W(0)$ and $F(0) = F_{max}$. Replacing from equation (2.27) into equation (2.26):

$$W(t) = \frac{6.6\, b\, U\, \eta_o\, \overline{U}^{7/4}}{h^*(t)^{7/2} \,.\, e^{703 W_s^*}} \tag{2.29}$$

where: $\quad h^*(t) = \dfrac{h(t)}{R} \quad , \quad W_s^* = \dfrac{\dot{z}(t)}{U}$

(2.30)

and: $\quad h(t) = h_o + z(t)$

To apply the average acceleration method to the piezo-viscous case, equations (2.17) and (2.20) are used, together with equation (2.31) below, if $\dot{z}(t) < 0$:

$$\ddot{z}_{i,j} = \frac{6.6\, b\, (U\, \eta_o)^{11/4}\, (R\, \alpha)^{7/4}}{m\, \{h_o + z_{i,j}\}^{7/2}\, e^{[(703/U)\dot{z}_{i,j}]}} - \frac{Q + F(t)}{m} - g \tag{2.31}$$

and if $\dot{z}(t) \geqslant 0$, simply modify equation (2.31) by letting the squeeze term $\dot{z}_{i,j} = 0$. This will ensure no negative squeezing effect. However, this assumption also leads to abrogation of the damping phenomenon in pure rolling and upstroke occasions. In such instances, the load reversal takes place as a result of a decrease in the magnitude of the forcing function.

The initial minimum oil film thickness, h_o, is calculated using equation (2.32) below:

$$W(0) - (mg + Q + F_{max}) = 0 \tag{2.32}$$

where the initial lubricant reaction, $W(0)$, is due to the entraining motion of the contacting bearings:

$$W(0) = \frac{6.6\, b\, U\, \eta_0\, \overline{U}^{7/4}}{h_0^{*7/2}} \tag{2.33}$$

Thus: $$h_0 = \left\{\frac{6.6b}{mg + Q + F_{max}}\right\}^{2/7} (U\,\eta_0)^{11/4}\,(R\,\alpha)^{1/2} \tag{2.34}$$

The initial conditions are given by equation (2.35):

$$z_0 = \dot{z}_0 = 0 \ , \quad F_0 = Q + F_{max} \ , \quad h(t) = h_0$$

and: $$\ddot{z}_0 = \frac{6.6\, b\, (U\,\eta_0)^{11/4}\,(R\,\alpha)^{1/2}}{m\, h_0^{7/2}} - \frac{Q + F_{max}}{m} - g \tag{2.35}$$

2.7 PIEZO-VISCOUS RESULTS AND DISCUSSIONS

The hydrodynamic lubricant response to a sinusoidal forcing function shows harmonic steady-state characteristics. Like the iso-viscous oil characteristics, the film response lags the forcing in the steady-state condition. A reduction in the magnitude of forcing results in an increase in the size of the minimum film thickness given a lag which is smaller than that experienced in the iso-viscous case (see Figure 2.16). A similar relationship between the acceleration and the squeezing velocity as that of the iso-viscous acceleration and velocity is observed (see Figures 2.17 and 2.18). However, the acceleration fluctuations in this case undergo larger rates of change. This fact is mainly because of the presence of a larger damping force in the piezo-viscous case when the

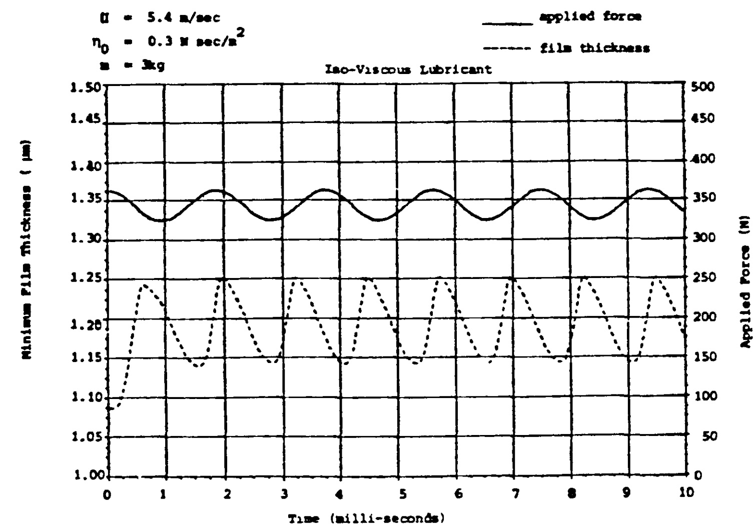

Fig 2.14 Iso-Viscous Lubricant response subjected to normal sinusoidal forcing

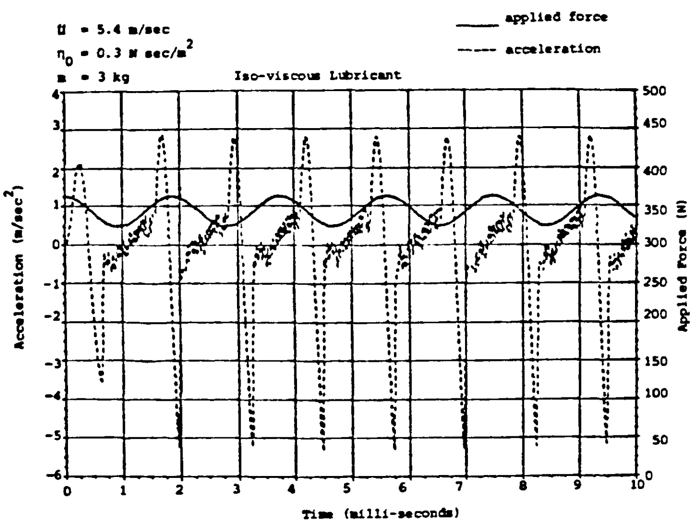

Fig 2 15 Time history of acceleration response corresponding to Fig 2.14

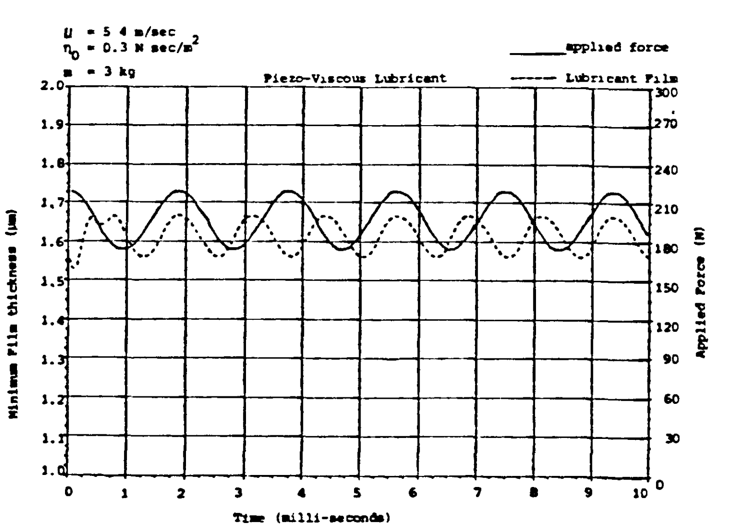

Fig 2.16 Time history of oil film response

downstroke squeezing is taking place. Thus, the magnitude and the variation of the squeezing velocity at the steady-state condition are somewhat larger than those for the iso-viscous lubricant under the same magnitudes of periodic loading. (Larger squeeze film effect).

The mean steady-state minimum film thickness is larger than that of the iso-viscous lubricant under the same loading condition. This indicates higher load carrying capacity. In the case of full hydrodynamic lubricated response, there is a limiting film thickness (i.e. critical film thickness) below which the governing condition is $\alpha P_{max} > 1$, where α is the piezo-viscosity and P_{max} is the highest elemental 'reduced pressure' in the 'reduced pressure distribution'.

In the steady-state condition, response fluctuations are considerably smaller in the piezo-viscous case, confirming the damper nature of the hydrodynamic response. If $\dot{z}(t) = 0$, the damping is removed and the governing equation of forced vibration of the loaded cylinder is that of a purely rolling cylinder with varying minimum film thickness. The steady-state response for this case exhibits an undamped periodic response (see Figure 2.19). The oil film thickness and its fluctuations are greater than that of the damped piezo-viscous oil film response, when $\dot{z}(t) < 0$. A comparison of Figures 2.16 and 2.19 illustrates the effect of damping exercised by the oil film opposing the normally approaching motion.

Like the iso-viscous lubricant, piezo-viscous oil has a limiting load carrying capacity above which the size of the film thickness falls below the critical film thickness, leading to the abrogation of the mathematical governing condition $\alpha P_{max} < 1$, where the 'reduced pressures' are of an acceptable magnitude. This limiting lubricant film thickness can be obtained from equation (2.7) where:

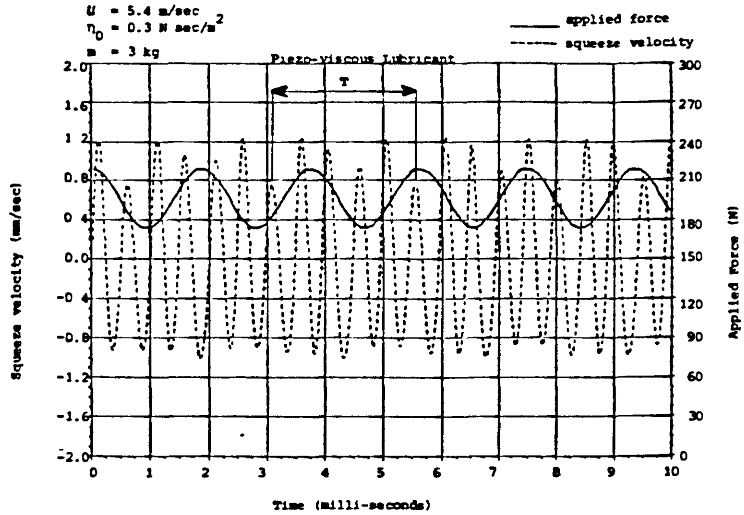

Fig 2.17 Time history of squeeze velocity

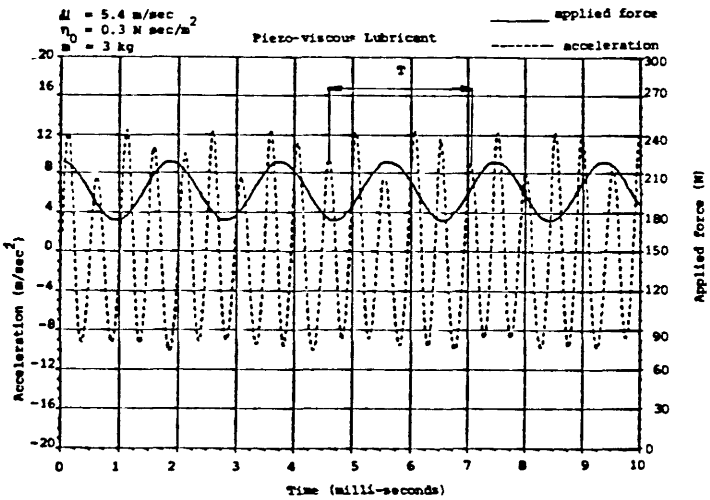

Fig 2.18 Time history of acceleration

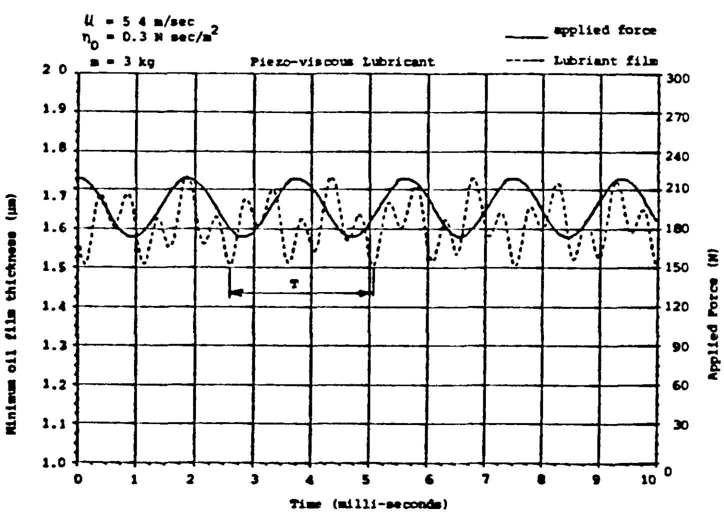

Fig 2.19 Time history of oil film response (undamped)

$$P = \frac{1 - e^{-\alpha q}}{\alpha} \tag{2.36}$$

2.8 REFERENCES

[1] SASAKI, T., MORI, H., and OKINO, N.
"Fluid Lubrication Theory of Roller Bearings",
Trans. ASME, J. Basic Engineering, 1962.

[2] DOWSON, D., MARKHO, P.H., and JONES, D.A.
"The Lubrication of Lightly Loaded Cylinders in Combined Rolling, Sliding and Normal Motion",
Trans. ASME, J. Lubrication Technology, 1976.

[3] ROHDE, S.M., WHICKER, D., and BOOKER, J.F.
"Elastohydrodynamic Squeeze Film Effects of Viscoelasticity and Fluctuating Load",
Trans. ASME, J. Lubrication Technology, 101 (1979) 74-80.

[4] VICHARD, J.P.
"Transient Effects in Lubrication of Hertzian Contacts",
J. Mech. Eng. Sci., 13(3) (1971) 173.

[5] TAYLOR, D.L., and KUMAR, B.R.K.
"Nonlinear Response of Short Squeeze Film Dampers",
Trans. ASME, J. Lubrication Technology, 102 (1980) 51-58.

[6] TIMOSHENKO, S., YOUNG, D.H., and WEAVER, Jnr, W.
"Vibration Problems in Engineering",
John Wiley & Sons, 4th edition, 1974.

CHAPTER 3

ELASTOHYDRODYNAMIC LUBRICATION

3.1 INTRODUCTION

When machine elements in counterformal lubricated contacts are subjected to high loads, the viscosity of the oil increases and the local surfaces undergo distortion. This condition is referred to as elastohydrodynamic lubrication. This concept of lubrication is restricted to point and line contacts where pressures generated are usually extremely high [1].

Most of the solutions for the point contact problem have been achieved only for moderate values of load and relatively low material parameters, representing glass against steel contacts [2,3,4]. A recent work embodies the inverse solution of the Reynolds equation. This provides the solutions of the point contact EHL at heavy loads [5]. Mostofi [4] included additional features in his solutions. One of these is the lubrication of helical Novikov (circular arc) gears when the direction of velocity vector is either coincident with the long axis of the static contact ellipse or skewed to it. Another special feature of his solution is the inclusion of the effect of squeeze velocity on EHL. This is an important factor. It can arise from transient and cyclic loads, causing the contacting surfaces to undergo considerable cyclic stresses due to change from the loaded to the unloaded zones [4,6]. It was concluded that if a downward squeeze velocity is present, the pressures are considerably higher than those resulting from the entraining motion of elements. As the squeeze-roll speed ratio increases more negatively (i.e. indicating a larger downward approach velocity), the peak pressure increases considerably and tends towards the pressure axis (see Figure 3.1).

Mostofi and Gohar [6] compared their oil film contours with the experimental results of Thorp [7], who used pure entraining motion, showing interference fringe contours under the same external conditions (see Figure 3.2). There was good agreement between theory and experiment.

The regression formula of reference [4] can be used as a design tool to approximate practical situations. This formula is of particular interest because it includes the effect of squeezing. The procedure applied by Mostofi [4] does not take into account the effect of directional flow θ on the material parameter G^* and the integrated pressure distribution W^*. Furthermore, a universal squeeze velocity vector is assumed to act across the contacting profiles. This approximation may be rather crude, especially when large squeeze-roll ratios are involved. Herrebrugh [8] defined a ratio:

$$\alpha_1 = \frac{\text{local velocity, } \partial h/\partial t}{\text{central velocity, } \partial h_0/\partial t}$$

He stated that the true normal velocity distribution can be obtained through a computing scheme based on successive approximations. The first approximation is provided in reference [8], illustrating the variation of normal velocity ratio α_1 with H^* (see Figure 3.3). It was concluded that under elastohydrodynamic conditions, a uniform normal velocity assumption may give an erroneous picture in the region of thin films. Mostofi's [4] approximation of the squeeze form in the regression formula is particularly inaccurate for higher values of normally approaching velocity. In this chapter, the governing parameters are regrouped to complement the new regression formula by the inclusion of a more accurate squeeze effect function.

The point contact condition occurs in many engineering applications, such as between balls and their races in ball bearings. The existence of

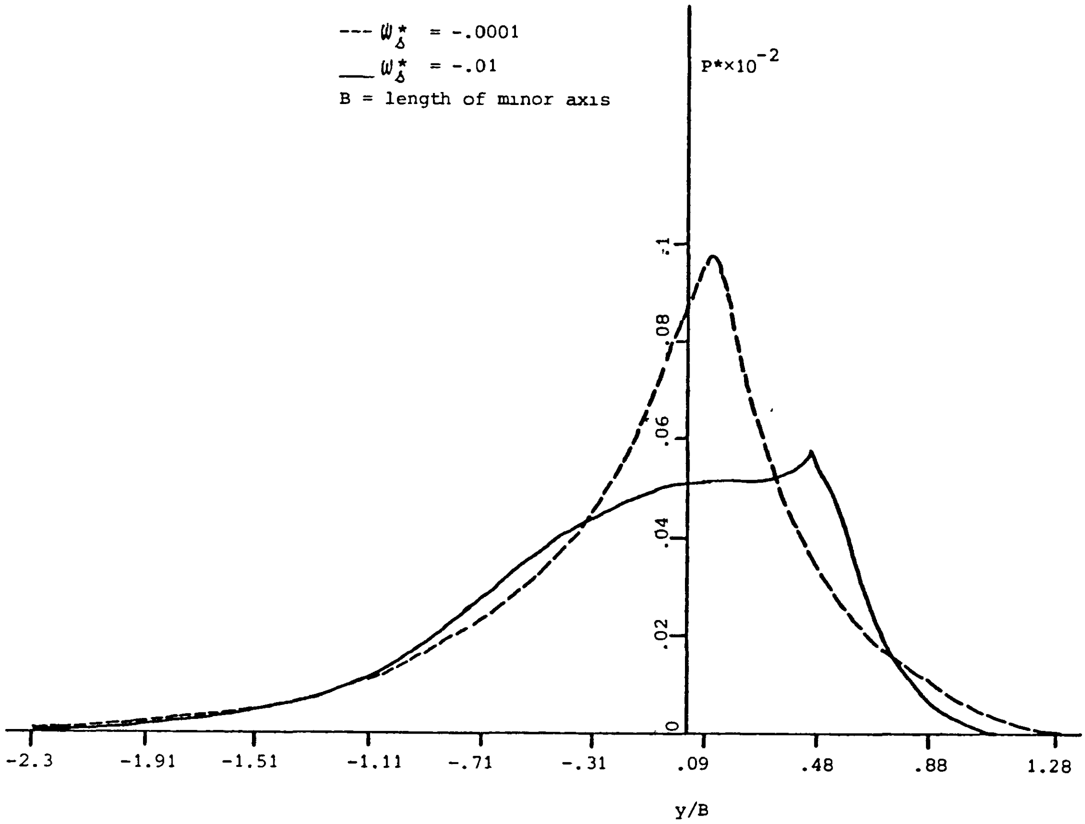

Fig 3.1 Point contact pressure distribution along the minor axis for various squeeze-roll speed ratios [ref 4]

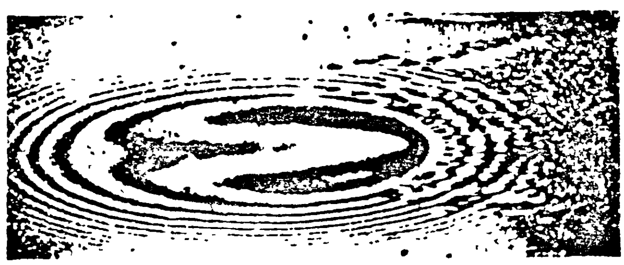

Fig 3.2 Interference fringe contours [ref 7] and the equivalent oil film contours [ref 6]

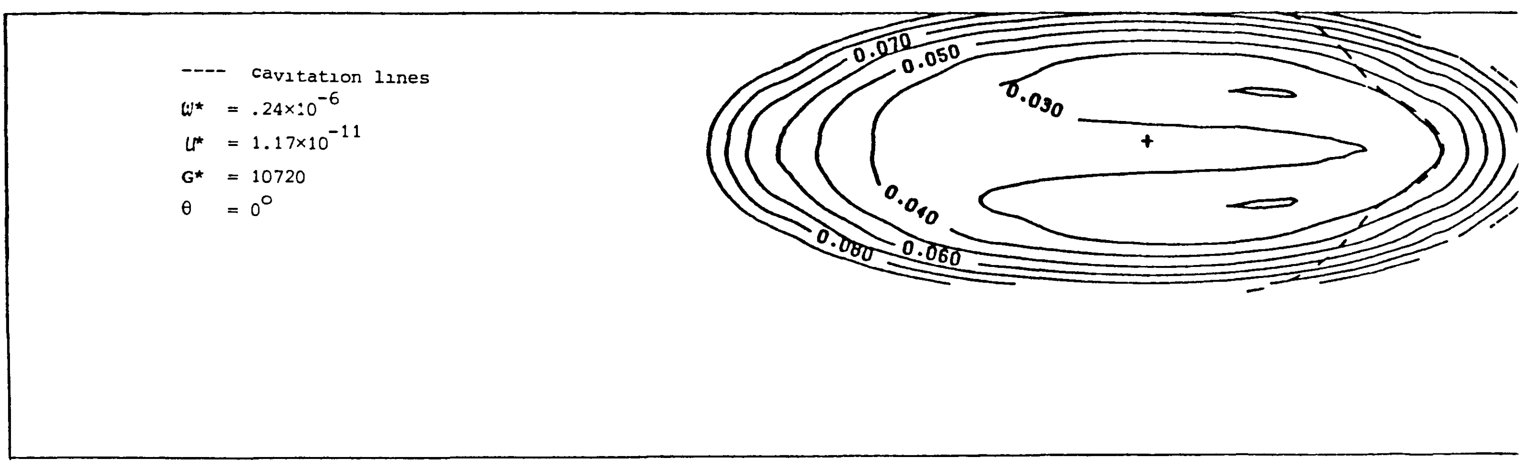

the EHL point contact condition has been proved experimentally by the absence of wear in precision ball bearings after an initial transition. When roller bearings are employed, the finite line contact condition takes place between the rollers and raceways. This condition is also observed between a pair of involute gear teeth in contact [9]. These elements are normally profiled near their ends to minimise the effect of edge stress concentrations. Several authors have solved the finite elastostatic line contact problem with its accompanying edge stress concentrations, reduced by suitably profiling the rollers [10,11,12†,13].

With the presence of a lubricant film, the EHL condition takes place under normal engineering loads. Solutions have been provided by several authors [1,2,3]. These all assume an infinitely long line contact between the two rolling bodies, thus making the problem one-dimensional. Hamrock and Dowson [2] have attempted to approximate the line contact problem by solving the point contact condition for an ellipticity ratio of 8. Other workers have made modifications to the infinite solution in order to approximate the finite line contacts [14,15]. Mostofi and Gohar [9] have presented a numerical solution to the two-dimensional EHL problem for finite line contacts. They concluded that, although the end closure effects and the outlet pressure gradient do not affect the film thickness along the central contact, the maximum edge stresses occur, accompanied by severe closure at the contact extremeties. These maximum stresses could be up to 1.5 times greater than the pressures generated at mid-contact.

Experimental work carried out by Bahadoran and Gohar [15] using the interference fringe pictures show that the minimum oil film occurs near the roller ends. The side constriction is observed to be dependent critically on the local geometry of the end closures. In fact, the edge film here is theoretically calculated to cause seizure. Such a phenomenon could be a contribution to scuffing failure (if there is sliding present)

---

† see publication at the end of Thesis

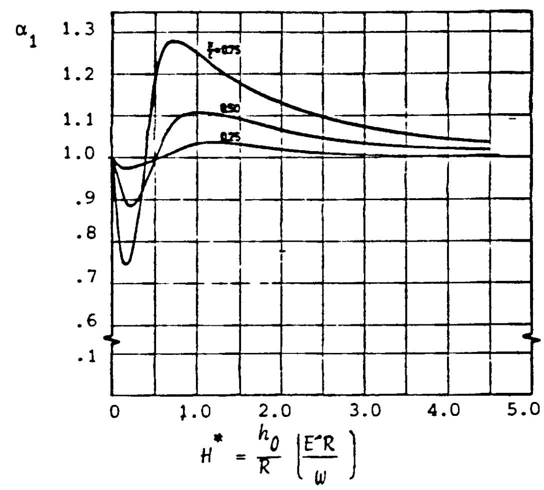

Fig 3.3 Squeeze velocity distribution in Elastohydrodynamic contacts [ref 8]

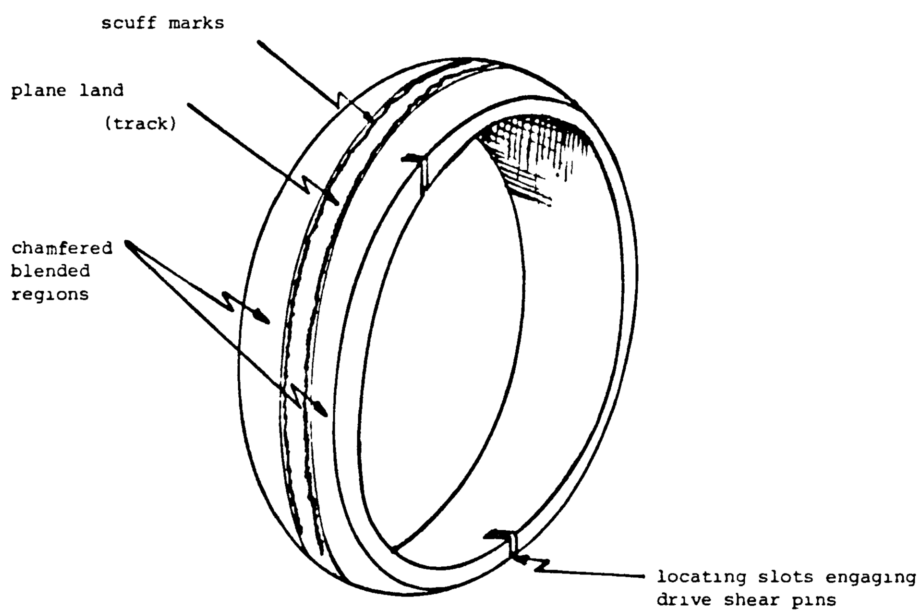

Fig 3.4 Illustration of scuffing failure near unblended regions

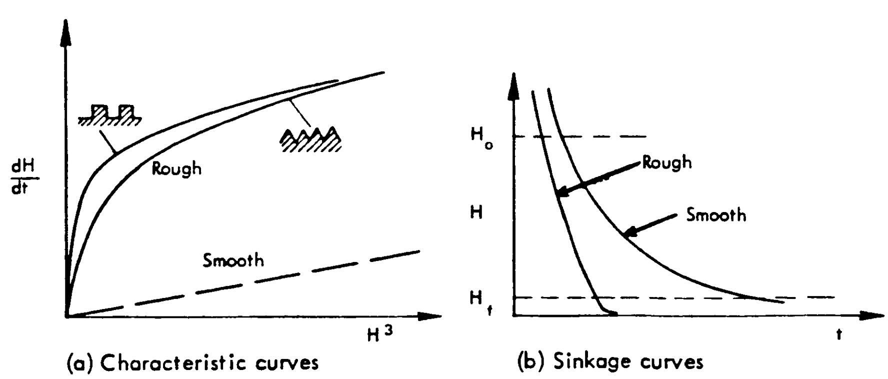

Fig 3.5 Squeeze film characteristics for rough and smooth surfaces. From Moore.

occurring near the unblended regions of a pair of contacting discs used in standard disc machines [16,17,18].

In Smith's [18] work, both discs were heat treated and finely ground to a mirror finish. One disc was lightly chamfered at 4° to provide a narrow 6 mm wide track across which the contact pressure distribution forms. Scuffing failure invariably occurs near the unblended edges of the track as demonstrated in Figure 3.4. Occasionally, the failure happens at mid-contact or only at one of the end extremeties. Scuffing at these regions may be due to uneven grinding of the track surface or a higher density of local asperity peaks protruding above the surface terrain. When the asperities are high (i.e. rough surfaces), loads are apt to provoke plastic deformation. However, even if the asperities are grossly deformed, they are usually retained after the removal of load [19]. Perhaps in the case of two rolling and sliding discs, asperity stress levels are purely plastic at first load application. However, during a running-in process, much of the plastic action would give way to elasticity [20]. Damage can then be caused by concentrated high loads generated in a small contact zone.

When a squeeze film is operated between surfaces of varying texture, different characteristics emerge as analysed by Moore [21] (see Figure 3.5). Smith [18] devised a series of experiments by varying the squeeze velocity between two rolling and sliding discs on a standard disc machine by means of a servo-valve attachment (see Figure 3.6). The idea was to establish a relationship between the input frequency and the load required to induce scuffing. Virtually similar results were observed for all the values of narrow band frequency range used (i.e. 0 to 60 Hz). The squeeze-roll speed ratio for this range is near enough to a pure entraining motion. It will be seen later in Chapter 4 that for this input frequency range, the lubricant responds with minimal damping force rather similar to undamped characteristics.

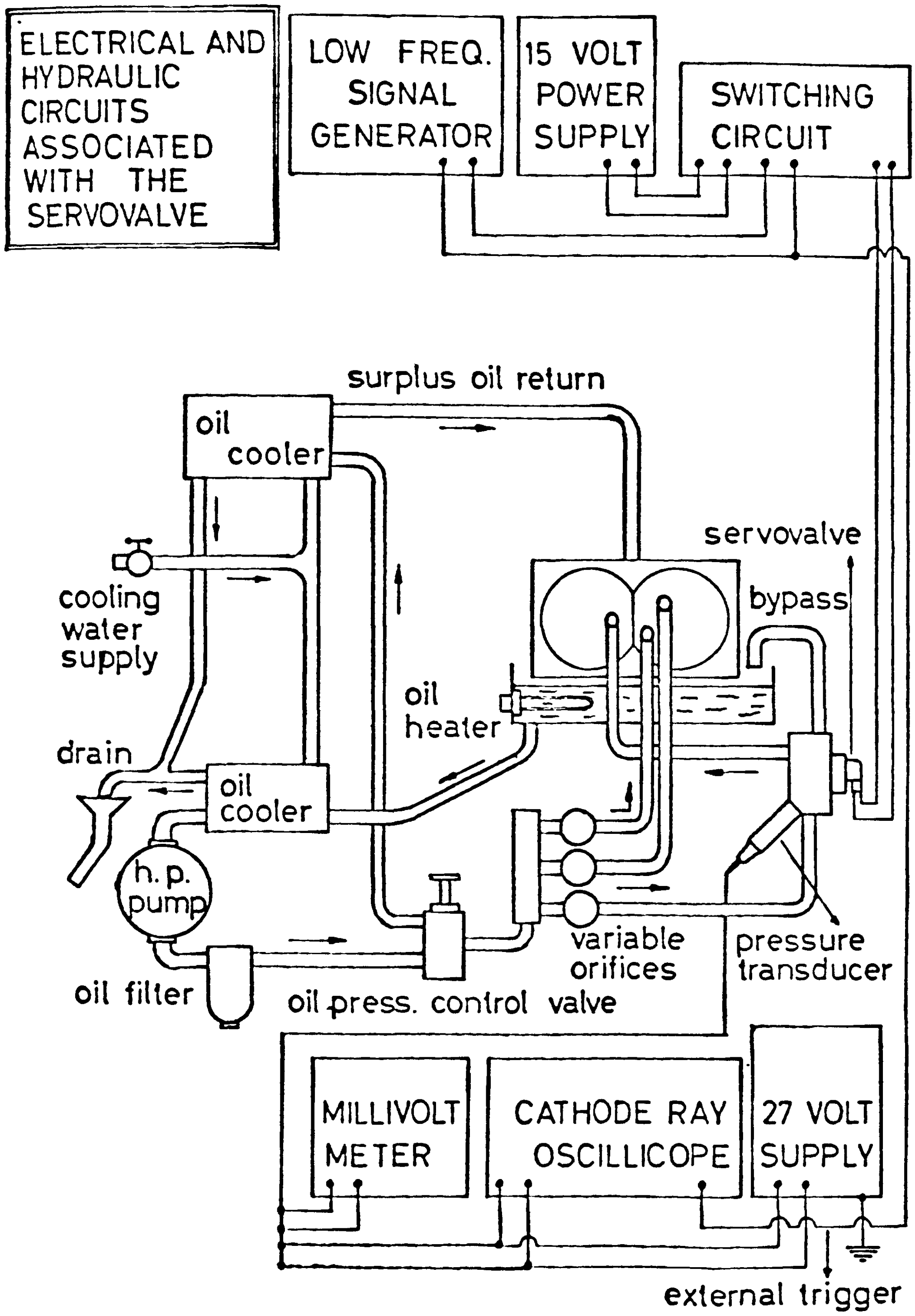

Fig 3.6 A Diagram of a Standard Disc Machine with Servo Valve attachment ref[18]

3.2 THEORY OF EHL CONTACTS UNDER SQUEEZE

For velocity induced flow in the transversal contact direction subjected to squeeze action, the Reynolds equation is:

$$\frac{\partial}{\partial x}\left[\frac{\rho\, h^3}{\eta}\frac{\partial P}{\partial x}\right] + \frac{\partial}{\partial y}\left[\frac{\rho\, h^3}{\eta}\frac{\partial P}{\partial y}\right] = 12\left\{U\frac{\partial(\rho h)}{\partial y} + W_s\right\} \tag{3.1}$$

where $U = (U_1 + U_2)/2$, the mean velocity in the y-direction

and $W_s = W_{s1} - W_{s2}$, the squeeze velocity in the direction of normal to the contacting surfaces

Equation (3.1) is made dimensionless by using the groups below:

$$\begin{aligned}
\bar{x} &= \frac{x}{R}\ , \quad \bar{y} = \frac{y}{R}\ , \\
h^* &= \frac{h}{R}\ , \quad R = \frac{r_1\, r_2}{r_1 + r_2} \quad \text{(the reduced radius)}\ , \\
P^* &= P\, E_r\ , \quad U^* = \frac{U\,\eta_0\, E_r}{R}\ , \\
G^* &= \frac{\alpha}{E_r}\ , \quad E_r = \frac{1 - \nu_1^{\,2}}{\pi\, E_1}\ , \\
W_s^* &= \frac{W_s}{U}\ , \quad \bar{\rho} = \frac{\rho}{\rho}\ , \quad W^* = \frac{W\, E_r}{R^2} \\
\text{and}\quad \eta &= \eta_0\, e^{\alpha P}
\end{aligned} \tag{3.2}$$

and the method of reduced pressures [22] is employed, where:

$$q = \frac{1}{\alpha}\left(1 - e^{-\alpha P}\right) \qquad \text{and} \qquad \eta^* = e^{G^* P^*}$$

Thus:

$$q^* = \frac{1}{G^*}(1 - e^{-G^*P^*}) \tag{3.3}$$

Therefore:

$$\frac{\partial}{\partial \overline{x}}\left[\overline{\rho}\, h^{*3} \frac{\partial q^*}{\partial \overline{y}}\right] + \frac{\partial}{\partial \overline{y}}\left[\overline{\rho}\, h^{*3} \frac{\partial q^*}{\partial \overline{y}}\right] = 12\ \{U^* \frac{\partial(\overline{\rho} h^*)}{\partial \overline{y}} + W^*_s\} \tag{3.4}$$

The variation of density with lubricant pressure is obtained from reference [3]:

$$\overline{\rho} = \frac{1 + 0.6P^*}{E_r + 1.7P^*} \tag{3.5}$$

3.3 LUBRICANT FILM THICKNESS

The EHL film thickness can be written as [9]:

$$h^*(\overline{x},\overline{y}) = [\overline{h}_g(\overline{x},\overline{y}) - (\overline{\delta}(0,0) - \overline{\delta}(\overline{x},\overline{y}))] + h^*_0 \tag{3.6}$$

where $\overline{h}_g$ is the separation of the surfaces in their undeformed state and the term $[-\overline{\delta}(0,0) + \overline{\delta}(\overline{x},\overline{y}) + \overline{h}_g]$ defines the elastic film shape. The variation of $\overline{h}_g$ depends on the axial profiling used. In this study, a crown profile is employed to relieve slightly the local geometry at the roller ends by an amount of the same order as the elastic deflection (see Figure 3.7). The region of pressure terminates very close to the commencement of the profiling and it is hoped that it does not rise sharply prior to this.

3.4 METHOD OF SOLUTION

A finite difference mesh is constructed to engulf the solution zone with regularly spaced elements in the direction of induced entraining

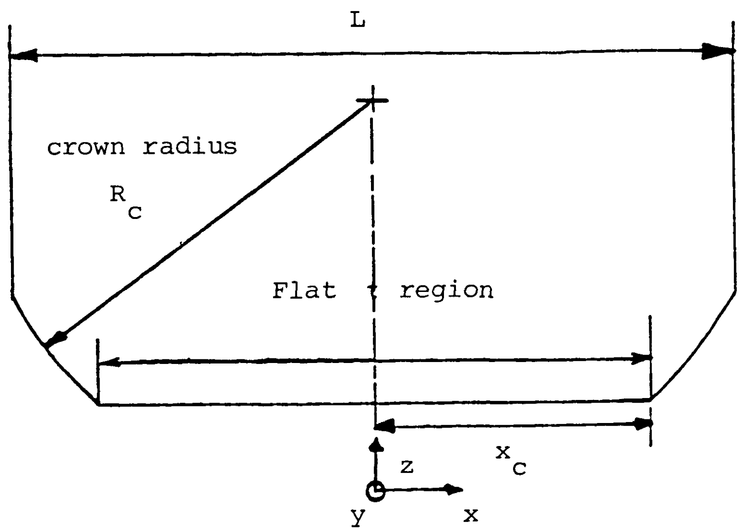

Fig 3.7 The crown profiled roller

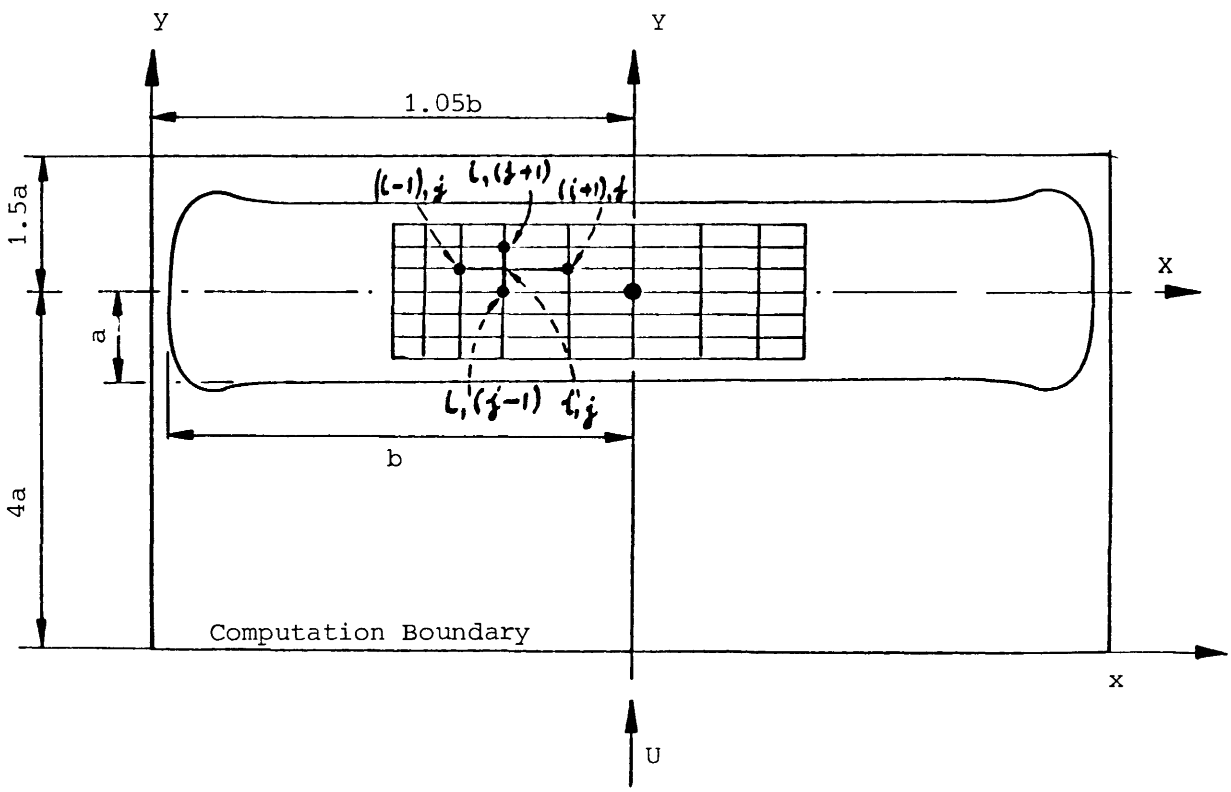

Fig 3.8 Irregular Mesh Construction [ref 9]

motion and irregularly spaced elements in the longitudinal direction [9] (see Figure 3.8). The spacing in the X-direction follows an arithmetic progression with the smaller elements at the contact extremeties. Therefore, the non-uniform grid assists the evaluation of high pressure gradients which are expected to occur due to the end closure effect near the roller ends.

3.5 RESULTS AND DISCUSSIONS

Figure 3.9 illustrates a typical film contour shape which is employed to exhibit the placement of various lubricant cross-sections [9]. The horizontal sections represent the lubricant layers in the direction of induced entraining motion and the vertical sections describe the oil film shape in the longitudinal directions. The mid-point A on section 1-1 corresponds to the film thickness, h_o^*. Point B represents the local minimum film thickness, h_e^* (i.e. the minimum exit oil film thickness). Point C is situated on the section 5-5 and is the end closure film, h_m^*, representing the absolute minimum film thickness. Section 4-4 corresponds to the side constriction, whilst section 3-3 describes the mid- longitudinal cut through the oil film contour.

Figure 3.10 shows two transverse pressure plots along the section 3-3 corresponding to two different squeeze velocity magnitudes. A tenfold increase in normal approach velocity hardly increases the peak pressures generated. The two remaining pressure distributions are taken from reference [9], one corresponding to pure entraining motion of elements under elastohydrodynamic conditions, and the other representing the elastostatic pressure distribution.

Figure 3.11 illustrates the pressures generated at the side constriction under the same governing conditions (along section 4-4). The lubricant undergoes a positive transverse pressure gradient due to an

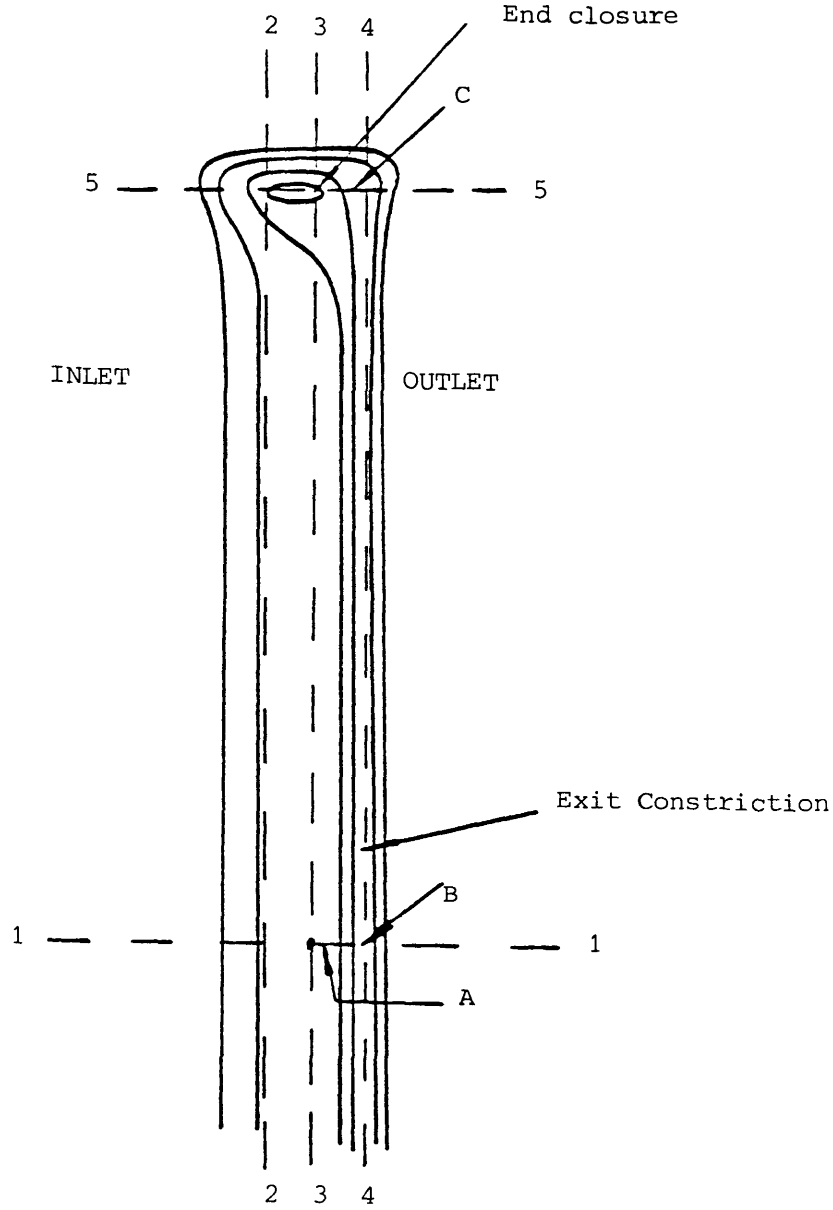

Fig 3.9 Typical guide contour [ref 9]

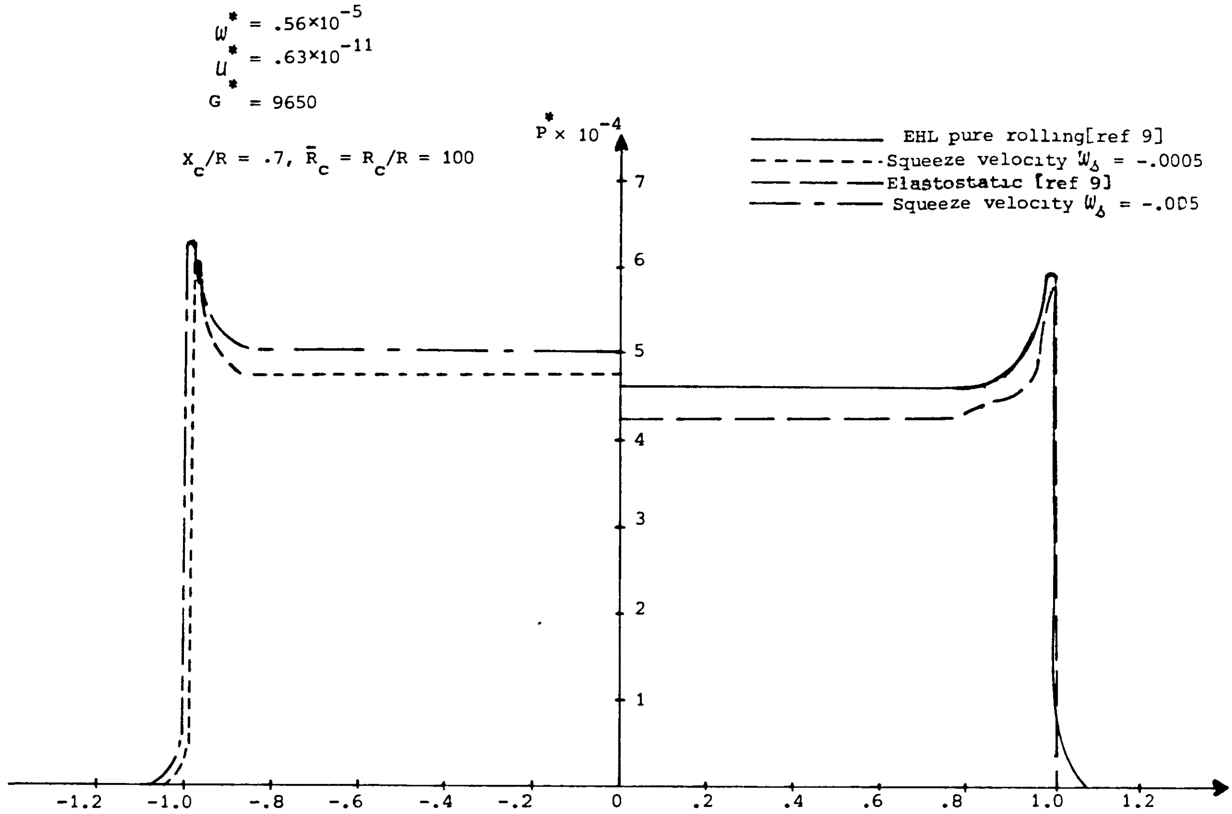

Fig 3.10 Pressure distribution along roller axial profile (section 3-3)

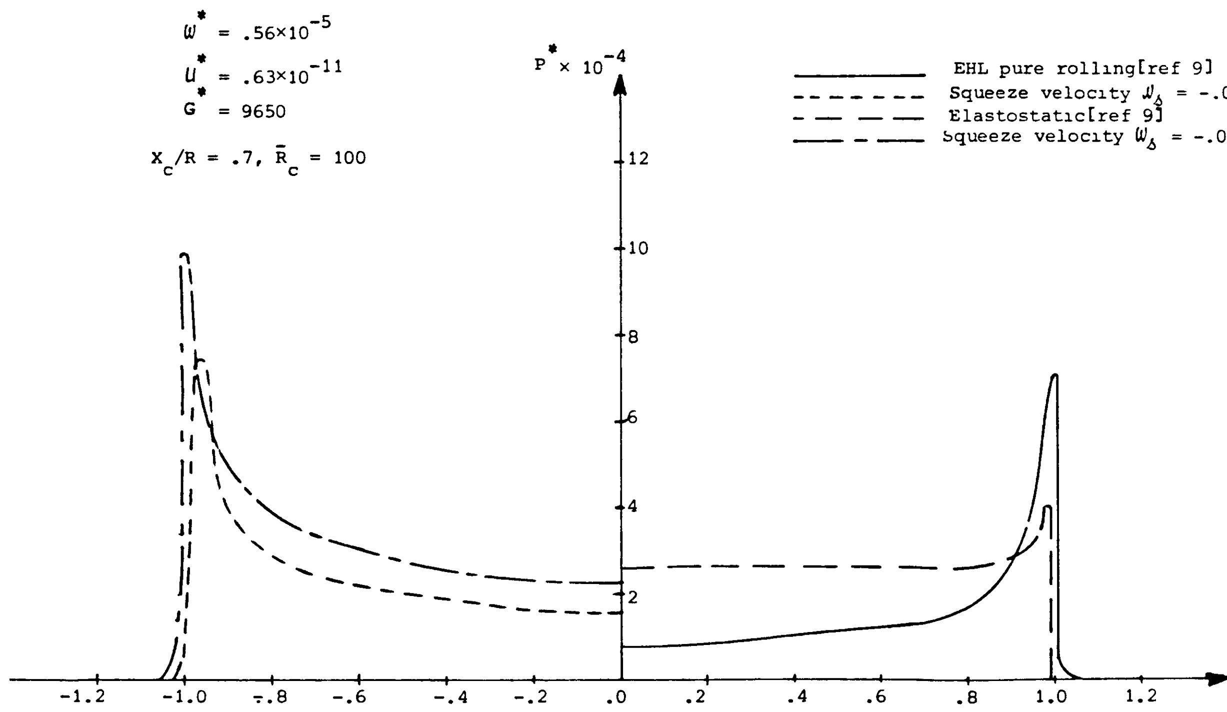

Fig 3.11 Pressure distribution along roller axial profile (section 4-4)

inward flow diffusion, which is not present at section 3-3. The pressure distributions for pure entraining motion and elastostatic conditions are again obtained from reference [9]. The accompanying edge stress concentrations are noticeably smaller in magnitude under elastostatic conditions. Mostofi and Gohar [9] suggested that it may seem advisable to cause deliberate starvation of the lubricant in roller bearings in order to keep the maximum pressures down to their elastostatic levels. The end closure is severely affected by an increase in the magnitude of the normal approach velocity, generating higher pressures near this region. This may be due to an even higher rate of inward flow diffusion.

Figure 3.12 illustrates two oil film shapes along section 3-3 corresponding to different squeeze velocity magnitudes and under the same load. Figure 3.13 shows the oil film profiles along section 4-4 under the same conditions. As expected, the lubricant thickness at exit constriction is thinner. The results demonstrate that under the same load, the oil film contours (on Figures 3.12 and 3.13) corresponding to a larger approach velocity exhibit higher oil film thicknesses.

The pressure distributions along section 5-5 are exhibited by Figure 3.14. The same external conditions prevail. The in-board section is taken from reference [9], representing the pressure distribution due to pure entraining motion with the outlet spike and at the same local load intensity. The corresponding parallel film shapes are illustrated in Figure 3.15, culminating in end closure.

3.6 SQUEEZE FORM FACTOR

The numerical regression formula found by Mostofi [4] (see Chapter 4) includes the effect of normal approach velocity. However, the formula has several shortcomings, not least of which is the assumption of a

$W^* = .56\times10^{-5}$

$U^* = .63\times10^{-11}$

$G^* = 9650$

$X_c/R = .7$

$\bar{R}_c = 100$

Note: for a constant load a thicker film is formed at higher value of W_s.

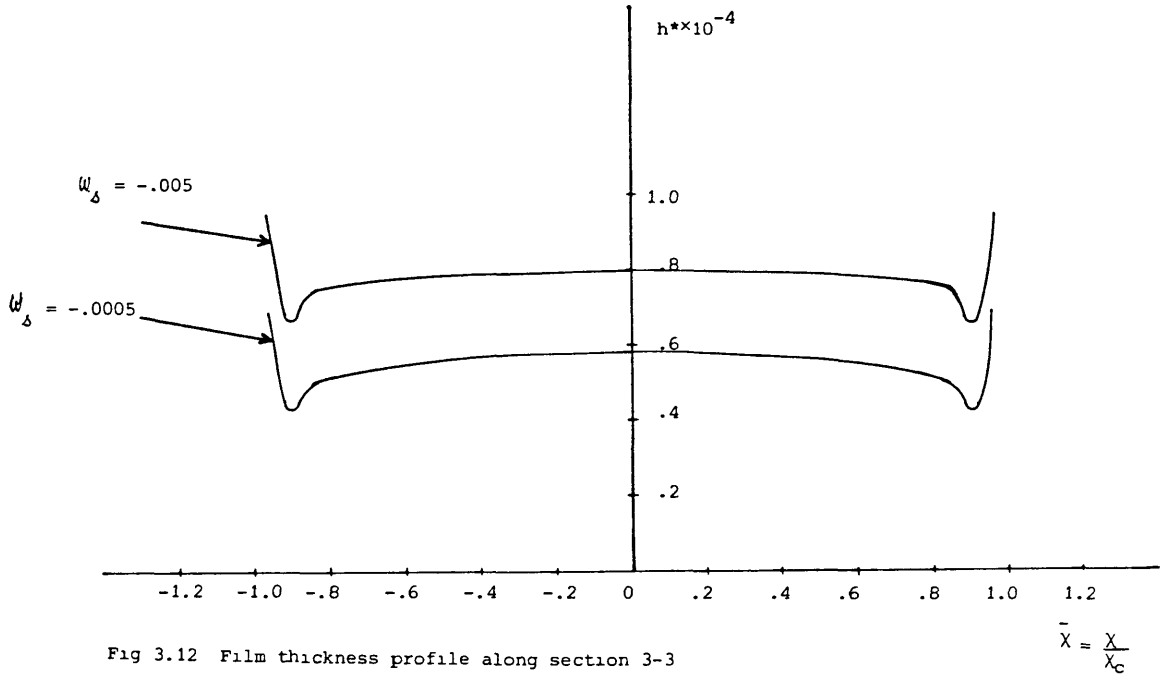

Fig 3.12 Film thickness profile along section 3-3

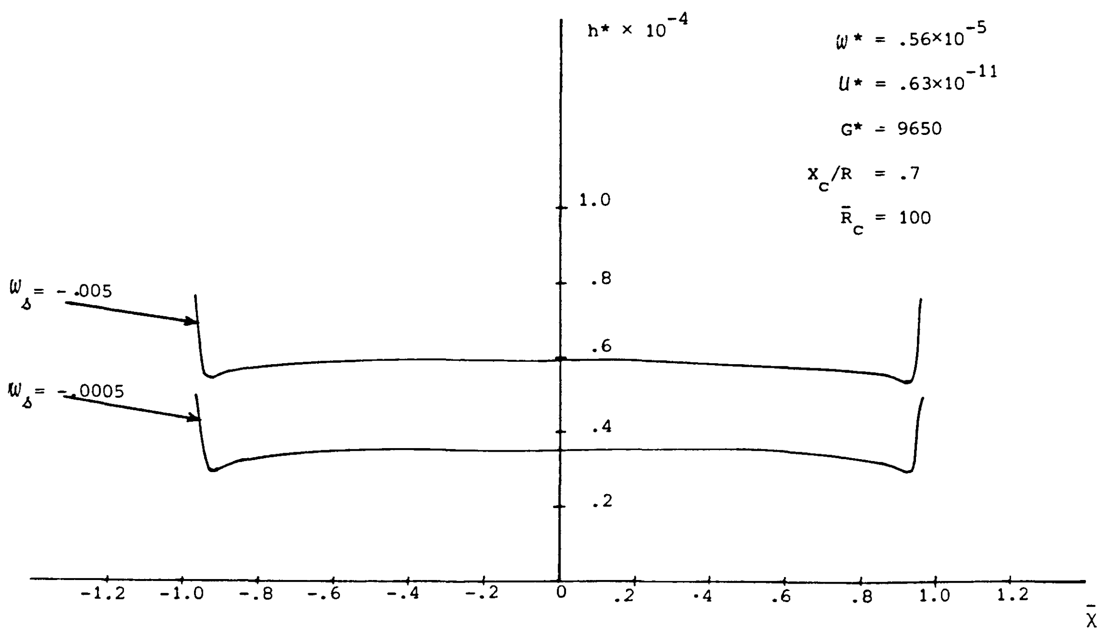

Fig 3.13 Film thickness profile along section 4-4

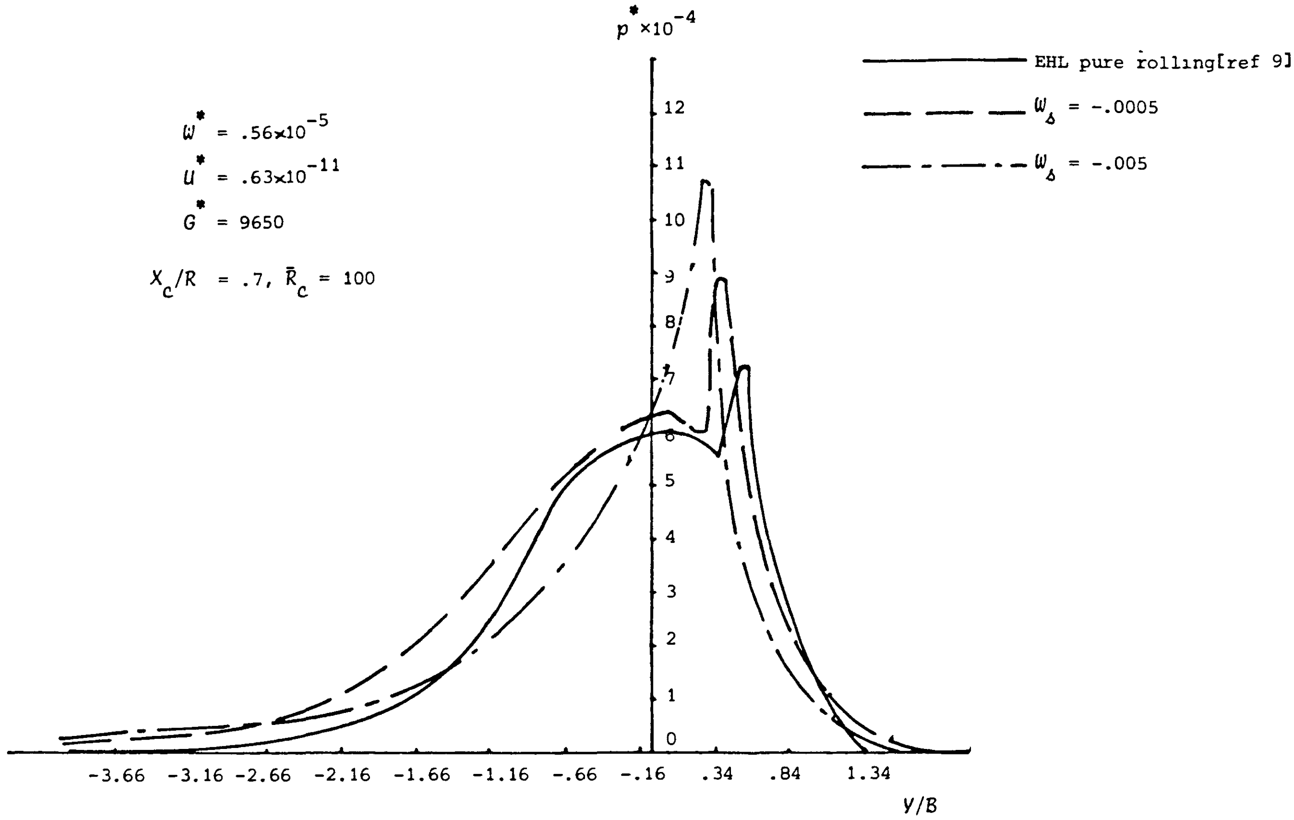

Fig 3.14 Pressure distribution in the direction of motion along section 5-5

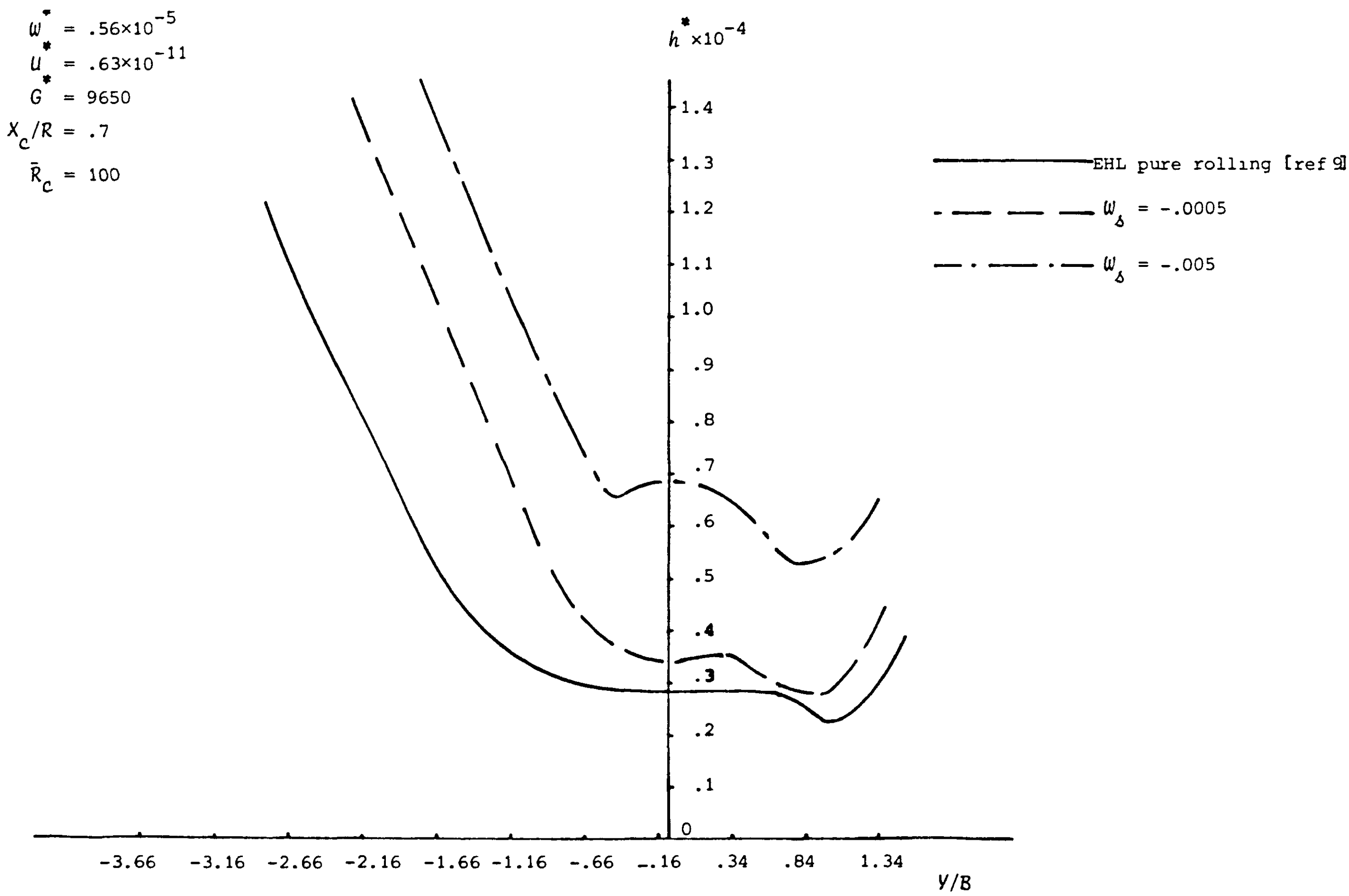

Fig 3.15 Film thickness profile along section 5-5

universal normal velocity profile across the contacting surfaces. Mostofi [4] assumed a squeeze factor of the form: $A e^{nW_s^*}$. The values of constants A and n were obtained by a regression analysis to establish the relationship between the normal approach velocity and the resulting film thickness at minimum exit (see Chapter 4). The values of these constants were:

$$A = 1.829 \times 10^{-5} \qquad , \qquad n = -123 \tag{3.7}$$

Figure 3.16 illustrates the inaccuracy between this form factor and the actual numerical results. In fact, as the magnitude of W_s^* increases, the percentage error widens (see Table 4.1, Chapter 4). A linear relationship can also be assumed, where:

$$h_m^* = C + m\, W_s^* \tag{3.8}$$

Using the same numerical results, these constants are evaluated:

$$C = 1.711 \times 10^{-5} \qquad , \qquad m = -3.889 \times 10^{-3} \tag{3.9}$$

This linear relationship is also demonstrated in Figure 3.16.

The effect of θ on the velocity parameter U^* was considered by Mostofi [4], but its influence on the load W^* and the material parameter G^* was neglected. Therefore, the formula is most accurate when describing the lubricant film behaviour in the y-direction (i.e. $\theta = \pi/2$). The problem is, however, overcome by a recent work presented by Mostofi and Gohar [5], who regrouped some of the governing parameters in a new regressional analysis, employing superior graphical approximations:

$$G^{*2} h_m^* = 3.51\,(U^* G^{*4})^{n'}\,(W^* G^{*3})^{m'}\,(1-.683e^{-.669e_p^*})\,(1-.559\cos^3\theta) \tag{3.10}$$

$$n' = .649 - .0875\cos^3\theta,\quad m' = .0865\cos^2\theta - .045.$$

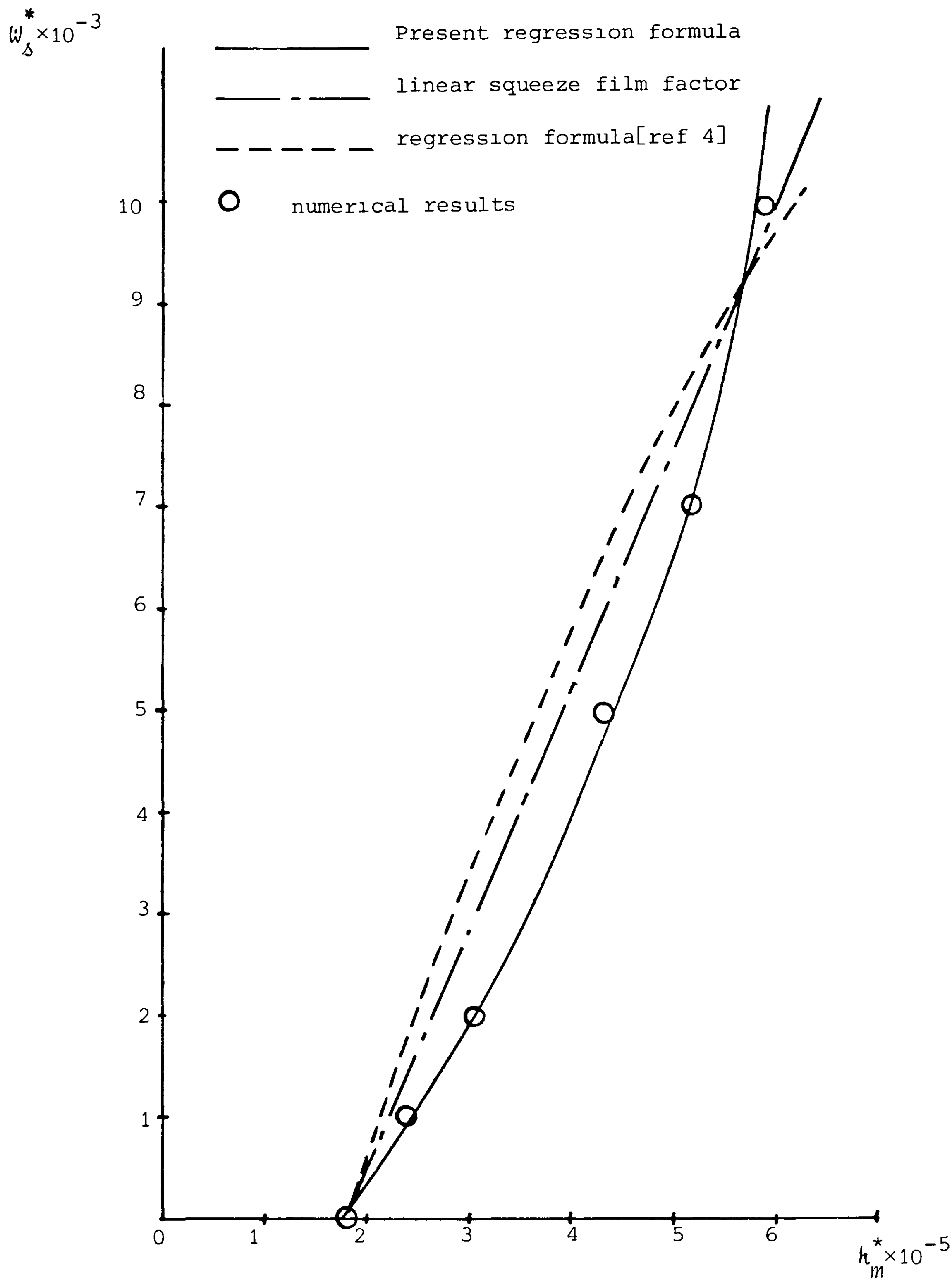

Fig 3.16 Illustration of behaviour of the appropriate regression formula

However, the influence of normal motion was not considered, which means that their equation cannot be employed to assess the dynamic characteristics of the lubricant film when subjected to normal fluctuating loads. Let:

$$h_m^* = a + b\, e^{kW_s^*} \tag{3.11}$$

where a, b and k are constants to be evaluated. Table 3.1 represents a brief selection of numerical data covering a large range of squeeze-roll speed ratios for two bodies under elastohydrodynamic point contact conditions.

TABLE 3.1

W_s^*	h_m^* ($\times 10^{-5}$)
-0.0001	1.75
-0.001	2.40
-0.01	5.60

Applying the results of Table 3.1 to equation (3.11) and eliminating the constants a and b (note: $0.0001k \doteqdot 0$):

$$\frac{1 - e^{+0.001k}}{e^{-0.0001k} - e^{-0.01k}} = 0.203 \tag{3.12}$$

The value of k is obtained by a numerical solution of equation (3.12) using the successive substitution method:

$$k = 132.0 \tag{3.13}$$

The values of constants a and b are then calculated using the data provided in Table 3.1 and equation (3.11):

$$a = 6.992 \times 10^{-5} \quad , \quad b = -5.242 \times 10^{-5} \tag{3.14}$$

Hence: $$h_m^* = 6.992 \times 10^{-5} - 5.242 \times 10^{-5}\, e^{132 W_s^*} \tag{3.15}$$

Figure 3.16 also illustrates the new fit achieved using equation (3.15). It can be observed that the squeeze factor resulting from this analysis conforms closer to the numerical output for a wider range of squeeze-roll speed ratios than that obtained in reference [4]. Therefore, the constant in the numerical formula of equation (3.10) is re-adjusted to include the new squeeze factor of: $1 - 0.75e^{132 W_s^*}$. Thus:

$$G^{*2} h_m^* = 14.04 (U^* G^{*4})^{.649} (W^* G^{*3})^{-.045} (1 - .683 e^{-.669 e_p^*}) (1 - .75 e^{132 W_s^*}) \tag{3.16}$$

where $\theta = \pi/2$, $n' = .649$ and $m' = -.045$

3.7 REFERENCES

[1] GRUBIN, A.N.

"Investigation of Scientific and Industrial Research",

Book 30, Central Scientific Research Institute for Technology and Mechanical Engineering, Moscow, 1949.

[2] HAMROCK, B.J., and DOWSON, D.

"Isothermal EHL Lubrication of Point Contacts",

Part 1: *Trans. ASME, J. Lubrication Technology*, Series F, 98 (1976) 223-229.

Part 2: *Trans. ASME, J. Lubrication Technology*, Series F, 98 (1976) 375-383.

Part 3: *Trans. ASME, J. Lubrication Technology*, Series F, 99 (1977) 264-274.

[3] DOWSON, D., and HIGGINSON, G.R.

"Elastohydrodynamic Lubrication",

Pergamon Press, SI edition, 1977.

[4] MOSTOFI, A.

"Oil Film Thickness and Pressure Distribution in Elastohydrodynamic Elliptical Contacts",

PhD Thesis, Imperial College of Science and Technology, University of London, September 1981.

[5] EVANS, H.P., and SNIDLE, R.W.

"The Elastohydrodynamic Lubrication of Point Contacts at Heavy Loads",

Proc. R. Soc. Lond., (1982) 183-199.

[6] MOSTOFI, A., and GOHAR, R.

"Oil Film Thickness and Pressure Distribution in Elastohydrodynamic Point Contacts", J. Mech. Eng. Sci. Vol 24, No.4, (1982) pp 173-182.

[7] THORP, N.
"Oil Film Thickness and Friction in Elliptical Contacts",
PhD Thesis, Imperial College of Science and Technology, University of London, 1972.

[8] HERREBRUGH, K.
"Elastohydrodynamic Squeeze Films Between Two Cylinders in Normal Approach",
Trans. ASME, J. Lubrication Technology, April 1970.

[9] MOSTOFI, A., and GOHAR, R.
"Elastohydrodynamic Lubrication of Finite Line Contacts",
Trans. ASME, J. Lubrication Technology, 1982.

[10] HEYDARI, M., and GOHAR, R.
"The Influence of Axial Profile on Pressure Distribution in Radially Loaded Rollers",
J. Mech. Eng. Sci., 21 (1979).

[11] JOHNS, P.M., and GOHAR, R.
"Roller Bearings Under Radial and Eccentric Loads",
Tribology International, June 1981.

[12] RAHNEJAT, H., and GOHAR, R.
"Design of Profiled Taper Roller Bearings",
Tribology International, December 1979.

[13] KANNEL, J.W.
"Comparison Between Predicted and Measured Axial Pressure Distribution Between Cylinders",
Trans. ASME, J. Lubrication Technology, 96 (1974).

[14] HOOKE, C.J.
"The EHL of Heavily Loaded Contacts",
J. Mech. Eng. Sci., 19 (1977).

[15] BAHADORAN, H., and GOHAR, R.

"End Closure in EHL Line Contact",

J. Mech. Eng. Sci., 16 (1974).

[16] MACPHERSON, P.B.

"Lubrication in Gear Scuffing and Pitting",

PhD Thesis, University of London, November 1971.

[17] MACPHERSON, P.B.

"Evaluation of 2497/Type A Oil as a Helicopter Gearbox Lubricant",

MOD Interim Report No. 1, Mechanical Transmission Laboratory,

Imperial College of Science and Technology, University of London,

May 1979.

[18] SMITH, A.G.D.

"The Effect of Vibrational Loading on Gear Scuffing",

PhD Thesis, University of London, October 1977.

[19] ENGEL, P.A.

"Impact Wear of Materials",

Elsevier Scientific Publishing Company, 1976.

[20] GREENWOOD, J.A.

"The area of contact between rough surfaces and flats",

Trans. ASME, J. Lubrication Technology, 89 (1967

[21] MOORE, D.F.

"Review of squeeze films"

Wear 8(1965) 245-263.

[22] RANGER, A.P., ETTLES, C.M.M., and CAMERON, A.

"The Solution of Point Contact EHL Problem",

Proc. R. Soc. Lond., 1975.

CHAPTER 4

ELASTOHYDRODYNAMIC CONTACTS UNDER OSCILLATING CONDITIONS

4.1 INTRODUCTION

It has been shown by a number of authors that a lubricant film of finite thickness forms in the concentrated contacts of rolling elements [1,2,3,4]. They have all discussed in some detail the surface distortion of the contacting bodies when sufficiently large loads are carried by the lubricant film to result in an increase in viscosity. These conditions take place invariably between rolling element and gear meshing contacts. Solutions to some practical applications, such as the meshing cycle in involute spur gears [5] and the rotational cycle in roller bearings [6], are already available. Adequate experimental work has been carried out to verify the existence of elastohydrodynamic contacts [7]. Absence of wear in precision bearing contacts or cessation of wear, after an initial transient period, provide proof of this argument [4].

In general, the numerical solutions for elastohydrodynamic point contacts are suitable for moderate values of load and low material parameter [3,4,8]. Therefore, the approximate formula obtained from numerical solutions are particularly adaptable to forecasting the lubricant film thickness in, for example, glass against steel contacts. However, experimental work carried out by Gohar [9] using sapphire, diamond and tungsten carbide indicates that these formulae possess scope for extrapolation of steel on steel contact conditions.

Dowson and Higginson [10] showed that for different values of Young's modulus, pressure viscosity index and peak pressure, the corresponding correlated single expression for contacting discs is:

$$\frac{h_{min}}{R} = \frac{(\alpha\,\tilde{E})^{0\cdot 6}\;((\eta_0\;U)/(\tilde{E}\;R))^{0\cdot 7}}{(W/(L\,\tilde{E}\,R))^{0\cdot 13}} \qquad (4.1)$$

where:

$$\frac{1}{\tilde{E}} = \frac{1}{2}\left\{\frac{1-\nu_1^2}{E_1} + \frac{1-\nu_2^2}{E_2}\right\} \tag{4.2}$$

and h_{min} is the minimum value of the oil film measured at the narrowest point of the diminishing gap. This equation yields results 25% lower than the Ertel-Grubin formula [1]:

$$\frac{h_o}{R} = \frac{1.18\ ((U\ \eta_o\ \alpha)/R)^{8/11}}{\{(1-\nu^2)\ W/(E\,L\,R)\}^{1/11}} \tag{4.3}$$

The latter expression describes the gap size in the inlet region only, disregarding the outlet conditions. Dowson and Higginson's [10] formula takes into account the "pip" at the end of the pressure distribution domain. The approximate Ertel-Grubin formula [1] (i.e. equation (4.3)) for contacting discs compares favourably with experimental results and has been used as a basis to obtain an approximate relationship by Archard and Kirk [11]:

$$\frac{h}{R} = 0.84\ ((\alpha\ \eta_o\ U)/R)^{0\cdot741}\ \left(\frac{E\ R^2}{W}\right)^{0\cdot074} \tag{4.4}$$

Archard and Cowking [12] also obtained a formula for the central film thickness. If the velocity vector is along the long axis of the ellipse:

$$h_o^* = 0.468U^{*0\cdot74}\ G^{*0\cdot74}\ W^{*-0\cdot074} \tag{4.5}$$

and if it is along the short axis of the ellipse:

$$h_o^* = 1.67U^{*0\cdot74}\ G^{*0\cdot74}\ W^{*-0\cdot074} \tag{4.6}$$

Hamrock and Dowson [13] have found formulae for the minimum and central film thicknesses:

$$h^*_o = 2.69U^{*0\cdot67} G^{*0\cdot53} W^{*-0\cdot067} (1 - 0.61e^{-0.73e^*_p}) \tag{4.7}$$

and:

$$h^*_{min} = 3.63U^{*0\cdot68} G^{*0\cdot49} W^{*-0\cdot073} (1 - 0.61e^{-0.73e^*_p}) \tag{4.8}$$

where the equations are converted to the symbols used here and the dimensionless groups used by the authors are as follows:

$$\begin{aligned} U^* &= \frac{U\ \eta_o}{E'\ R_x} \\ W^* &= \frac{W}{E'\ R_x^{\ 2}} \\ G^* &= E'\ \alpha \end{aligned} \tag{4.9}$$

and: $$e^*_p = \frac{a}{b} = 1.03\ (\frac{R_y}{R_x})^{0\cdot64}$$

Cheng [14] also represented the numerical results for the central film thickness along the long and the short axes of the ellipse by separate formulae; along the long axis:

$$h^*_o = 0.447U^{*0\cdot639} G^{*0\cdot639} W^{*-0\cdot028} \tag{4.10}$$

and along the short axis:

$$h^*_o = 1.33U^{*0\cdot738} G^{*0\cdot739} W^{*-0\cdot07} \tag{4.11}$$

Finally, Mostofi [4] obtained central and minimum film thickness formulae by independently varying each of the dimensionless groups whilst ensuring that the remaining groups were held constant. Mostofi obtained the formulae by using a regressional analysis of his numerical results. It included the effect of normal squeeze velocity, thus enabling these formulae to be employed in a numerical method studying the dynamical behaviour of the contact when subjected to periodic normal loads. These regression formulae are listed below:

$$h^*_{min} = 0.112U^{*(0.562+0.04\theta)}\, G^{*1.571\theta}\, W^{*-0.045}\, e^{-123W^*_s}\, e^{0.076e^*_p} \tag{4.12}$$

$$h^*_o = 0.073U^{*(0.484+0.068\theta)}\, G^{*0.439}\, W^{*0.004}\, e^{2.133\theta}\, e^{-123W^*_s}\, e^{0.025e^*_p} \tag{4.13}$$

It should be noted that these formulae assume a uniform squeeze velocity profile. This assumption leads to a possibly inaccurate solution of the problem. In fact, under strict EHD conditions, the squeeze velocity vector probably varies in magnitude along the contact, being dependent upon the local rate of change of film thickness and the local surface deformation rate (see also Chapter 3). Appropriate geometrical relationships are later derived between the movement of the bearings' centreline and the position of the minimum exit (see Section 4.2).

Furthermore, the regressional analysis in reference [4] has been carried out in full for $\theta = \pi/2$ (i.e. transversal flow direction), but only the effect of the rolling parameter U^* is known for various values of θ. It would have been advantageous to regroup the variables as studied by Thorp and Gohar [15] or establish the effect of θ upon W^* and G^* as well as U^*. This procedure has been carried out by Mostofi and Gohar [16] in a recent work (see Chapter 3).

In spite of all their shortcomings, equations (4.12) and (4.13) are probably reasonably accurate for an analysis of the gap variation when the flow is along the short axis (i.e. $\theta = \pi/2$) with low to moderate values of W^* and G^*.

4.2 INFLUENCE OF NORMAL APPROACH ON EHD POINT CONTACTS

The present work makes use of the regression formulae derived by Mostofi [4]. The range of parameters, the number of values taken for the purpose of regression analysis and the accuracy of these regressed results are given in Table 4.1 [4]. In an elastohydrodynamic contact, the contacting surfaces are subjected to elastic deflection. Therefore, the position of the minimum film thickness is not along the centre of the contact region. The study of the coherent lubricant film is of particular interest at the position of the minimum oil film thickness, where the probability of the oil film rupture is greatest. The time-dependent parameters are the instantaneous load carrying capacity, W (integrated pressure), the speed of normal motion, W_s, and the thickness of the oil film, h_{min}. Rearranging equation (4.12):

$$W^*(t) = \frac{K_n}{h^*_{min}(t)^{22.23}\, e^{\{2734.3W^*_s\}}} \qquad (4.14)$$

where K_n is the time-independent constant containing the remaining parameters:

$$K_n = (0.112)^{22.23}\, e^{\{34.92 + 1.69e^*_p\}}\, G^{*10.3}\, U^{*\{12.5+0.89\theta\}}$$

The dimensionless groups of Table 4.1 are given as follows:

TABLE 4.1

Dimensionless Group	Range	Number of Values	Maximum Percentage Error Between Regressed Results and the Numerical Values
U^*	$0.31 \times 10^{-11} \rightarrow 0.44 \times 10^{-10}$	10 for $\theta = \pi/2$ and 6 for $\theta = 0, \pi/6, \pi/3$	3.5% for h^*_{min} 5.8% for h^*_o
W^*	$0.12 \times 10^{-7} \rightarrow 0.56 \times 10^{-6}$	8	3.6% for h^*_{min} 5.9% for h^*_o
G^*	$0.57 \times 10^{4} \rightarrow 0.12 \times 10^{5}$	5	3.1% for h^*_{min} 5.3% for h^*_o
θ	$0 \rightarrow \pi/2$	11	16.0% for h^*_{min} 7.6% for h^*_o
e^*_p	$1.2 \rightarrow 5.34$	6	11.1% for h^*_{min} 9.8% for h^*_o
W^*_s	$-10^{-4} \rightarrow -10^{-2}$	11	22.6% for h^*_{min} 20.1% for h^*_o

$$G^* = \frac{\alpha}{E_r} \quad \text{where} \quad E_r = \frac{1 - \nu^2}{\pi E}$$

$$h^*_{min}(t) = \frac{h_{min}(t)}{R} \quad , \quad U^* = \frac{U \eta_o E_r}{R} \tag{4.15}$$

$$e^*_p = \frac{a}{b} \quad , \quad W^*_s(t) = \frac{W_s(t)}{U}$$

$$W^*(t) = \frac{E_r W(t)}{R^2}$$

and $h_{min}(t) = H_{min} + S_{min}(t)$, where H_{min} is the initial oil film thickness at $t = 0$. The rate of change of lubricant film thickness yields the normal approach velocity:

$$W_s = \frac{dh_{min}(t)}{dt} = \dot{h}_{min}(t) = \dot{S}_{min}(t) \tag{4.16}$$

Re-dimensionalising (4.14) using (4.15) and (4.16):

$$W(t) = \frac{K}{h_{min}(t)^{22.23} \, e^{\{(2734.3/U)\dot{S}_{min}(t)\}}} \tag{4.17}$$

where:

$$K = (0.112)^{22.23} \, e^{\{34.92\theta + 1.69 e^*_p\}} \, G^{*10.3} \, U^{*\{12.5 + 0.89\theta\}} \, \frac{R^{24.23}}{E_r}$$

and has the dimensions of $Nm^{22 \cdot 23}$.

The dynamic equation of a normally loaded rolling element is:

$$W(t) - \{mg + F(t)\} = m \ddot{z}(t) \tag{4.18}$$

where $\ddot{z}(t)$ is the normal acceleration of the centreline of the rolling element, and $W(t)$ and $F(t)$ also embody the original conditions $W(0)$ and $F(0)$ to fix the position of equilibrium. The movement of the outermost layer of the oil film at the position of minimum diminishing gap can be described in terms of the movement $z(t)$ of the centreline of the normally loaded element. For the central position of the pressure distribution domain, where $h(t) = h_0(t)$ (see Figure 4.1):

$$z(t) = H_0(t) + R \tag{4.19}$$

and:

$$h_0(t) = H_0(t) + \delta_0(t) \tag{4.20}$$

By simple elimination of $H_0(t)$:

$$z(t) = R + h_0(t) - \delta_0(t) \tag{4.21}$$

Thus:

$$\dot{z}(t) = \dot{h}_0(t) - \dot{\delta}_0(t) \tag{4.22}$$

and:

$$\ddot{z}(t) = \ddot{h}_0(t) - \ddot{\delta}_0(t) \tag{4.23}$$

but $h_0(t) = h_0(0) + S_0(t)$, where $h_0(0)$, as shown in Figure 4.1, is the original central film thickness due to a purely rolling contact. Hence:

$$\ddot{z}(t) = \ddot{S}_0(t) - \ddot{\delta}_0(t) \tag{4.24}$$

The lubricant reaction, $W(t)$, can be obtained for the central film thickness using equation (4.13). Employing equations (4.18) and (4.24), the lubricant response at $h(t) = h_0(t)$ can then be evaluated. However, it is more important to investigate the position of the minimum oil film thickness since it is subjected to higher pressures (see Figure 4.2):

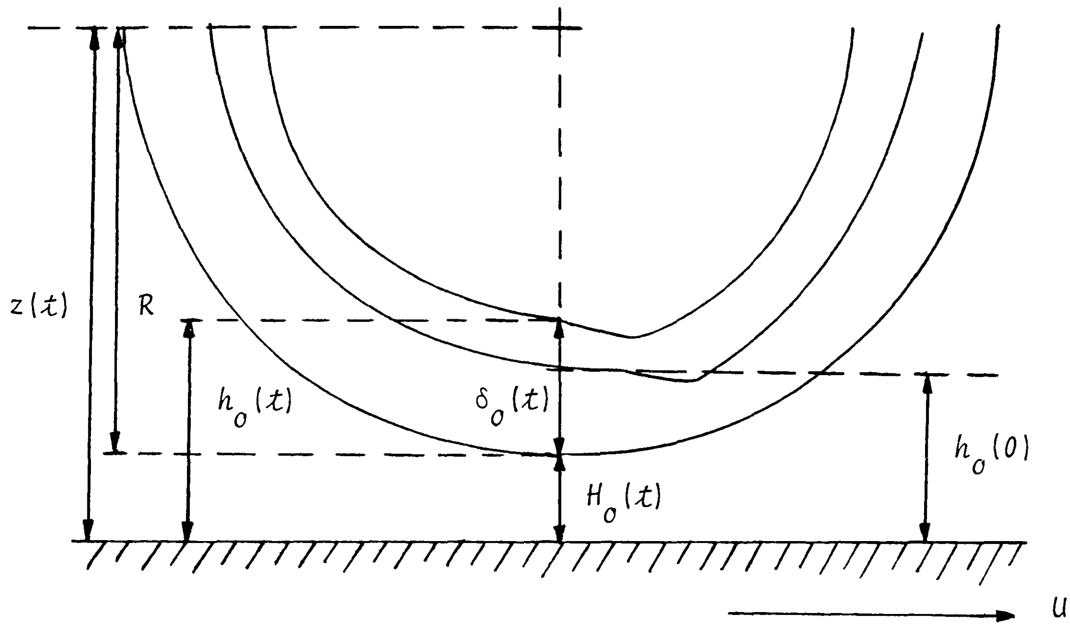

Fig 4.1 Geometrical consideration of an elliptical contact in normal motion

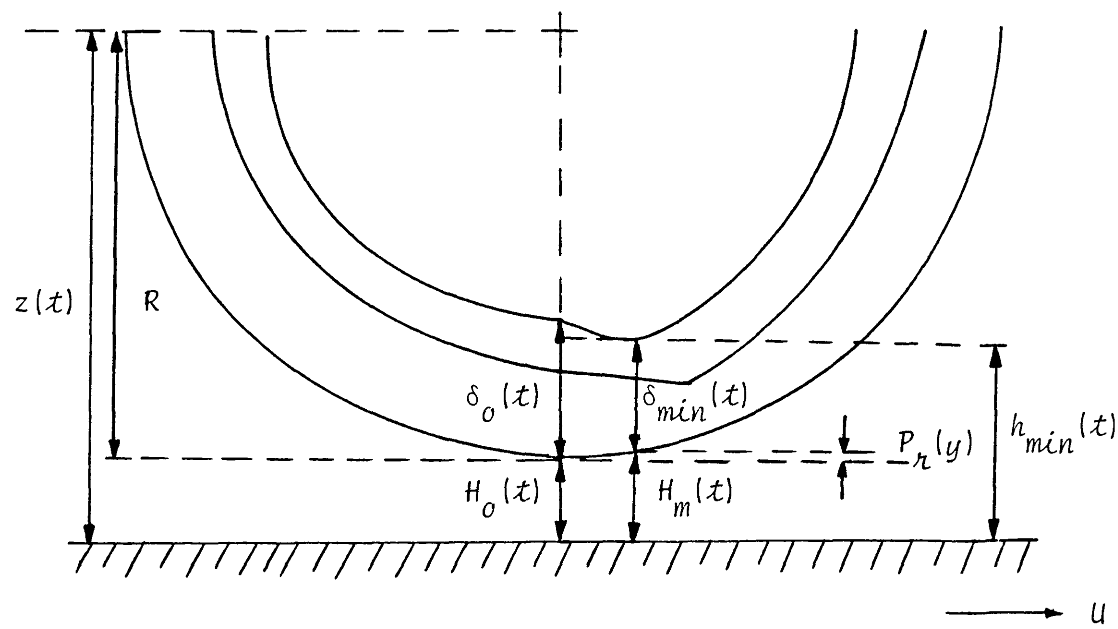

Fig 4.2 Geometrical consideration of an elliptical contact in normal motion

$$z(t) = H_m(t) + R - P_r(y) \tag{4.25}$$

and

$$H_m(t) = h_{min}(t) - \delta_{min}(t) \tag{4.26}$$

where $P_r(y)$ is the lateral profile of the bearing (i.e., in the direction of induced entraining motion). Now equation 4.13 for h_o^* cannot be easily used because of the positive index of W^*. So the equation 4.12 for h_{min}^* is employed which is the only one available (involving a squeeze term). In fig 4.2, if the deflections under the lubricant pressure distribution are assumed to be like those under a static contact, then:

$$\delta_o(t) = \delta_{min}(t) + P_r(y) \tag{4.27}$$

where $P_r(y_o) = 0$.

The assumption is really that the outlet pip has been ignored and the film is flat to the centre and of thickness equal to the minimum. Reference [4] shows that the ratio between the maximum and minimum film thickness is generally less than 0.75. Substituting from (4.27) into (4.26) yields:

$$H_m(t) = h_{min}(t) - \delta_0(t) + P_r(y) \; . \tag{4.28}$$

Eliminating $H_m(t)$ using (4.25) and (4.28) :

$$Z(t) = R + h_{min}(t) - \delta_o(t). \tag{4.29}$$

Using the above assumption, equation (4.29) indicates that the relationship between respective movements of the centre line and the corresponding movement of the distorted surface is now independent of the rolling elements' lateral profile. Furthermore :

$$\ddot{Z}(t) = \ddot{S}_{min}(t) - \ddot{\delta}_o(t) \tag{4.30}$$

The final forced vibration governing equation is:

$$W(t) - \{mg + F(t)\} = m\,\{\ddot{S}_{min}(t) - \ddot{\delta}_o(t)\} \qquad (4.31)$$

To solve this equation, a relationship between the central contact deflection, $\delta_o(t)$, and the integrated oil pressure distribution, $W(t)$, is to be assumed:

$$W(t) = K'\,\delta_o^{3/2}(t) \qquad (4.32)$$

The relationship above represents a dry contact condition where the lateral pressure distribution is elliptical (the longitudinal distribution is assumed to be constant). Under lubricated conditions, the elastic deflection varies within the contact domain (i.e. $\delta = \delta(x,y)$). The implication of using (4.32) is to consider:

δ_o (under lubricated conditions) = δ_o (under dry conditions), and that the central deflection, δ_o, is insensitive to any change in pressure distribution. When contacting discs are studied, $W(t)$ may approximate a finite line contact using (4.33) [17] and a large value for e_p^* (e_p^* = 10 for this analysis):

$$\delta_o(t) = K_1\,W(t) \qquad (4.33)$$

Therefore:

$$\ddot{\delta}_o(t) = K_1\,\ddot{W}(t) \qquad (4.34)$$

Replacing for $\ddot{\delta}_o(t)$ in equation (4.31) using equation (4.34):

$$W(t) - \{mg + F(t)\} = m\,\{\ddot{S}_{min}(t) - K_1\,\ddot{W}(t)\} \qquad (4.35)$$

This equation is then solved for $\ddot{S}_{min}(t)$ by employing a third order quasi linear numerical method. The 'average acceleration method' [18] is particularly suited to the solution of hydrodynamic and elastohydrodynamic concentrated contacts under fluctuating loads (see Chapter 2).

First, equation (4.17) is doubly differentiated to provide an expression for $\ddot{W}(t)$ in terms of the dynamic parameters describing the lubricant film behaviour (i.e. $S_{min}(t)$, $\dot{S}_{min}(t)$ and $\ddot{S}_{min}(t)$). Thus:

$$\dot{W}(t) = \frac{-\alpha_1 K \{\dot{S}_{min}(t) + \beta/(\alpha_1 U) \ddot{S}_{min}(t) h_{min}(t)\}}{h_{min}^{\alpha_1+1}(t) e^{\{(\beta/U)\dot{S}_{min}(t)\}}} \qquad (4.36)$$

and by subsequent differentiation:

$$\ddot{W}(t) = \alpha_1 K \{\frac{2\beta}{U} \ddot{S}_{min}(t) \dot{S}_{min}(t) h_{min}(t) - \ddot{S}_{min}(t) h_{min}(t)$$

$$- \frac{\beta}{\alpha_1 U} \dddot{S}_{min}(t) h^2_{min}(t) + (\alpha_1 + 1) \dot{S}^2_{min}(t)$$

$$+ \frac{\beta^2}{\alpha_1 U^2} \ddot{S}_{min}(t) h^2_{min}(t)\}/h_{min}^{\alpha_1+2}(t) e^{\{(\beta/U)\dot{S}_{min}(t)\}} \qquad (4.37)$$

where α_1 is the power index of the oil film in equation (4.17) (i.e. $\alpha_1 = 22.23$), and β is the coefficient of the $\dot{S}_{min}$ term in the exponential function (i.e. $\beta = 2734.3$). Equations (4.36) and (4.37) can now be used for any values of α_1 and β with the appropriate adjustment of constant K. Variables $h_{min}(t)$, $S_{min}(t)$ and $\dot{S}_{min}(t)$ represent very small quantities (see Chapter 2). Therefore, it is feasible to neglect third and higher order terms in equation (4.37). Thus:

$$\ddot{W}(t) = \frac{\alpha_1 K \{- \ddot{S}_{min}(t) h_{min}(t) + (\alpha_1 + 1) \dot{S}^2_{min}(t)\}}{h_{min}^{\alpha_1+2}(t) e^{\{(\beta/U)\dot{S}_{min}(t)\}}} \qquad (4.38)$$

4.3 INITIAL CONDITIONS (POINT CONTACT)

The initial conditions are (for purely rolling elements):

$$\text{at } t = 0 \;,\; h_{min}(t) = h_{min}(0) \;,\; \dot{S}_{min}(0) = 0 \tag{4.39}$$

Thus:
$$W(0) = \frac{K}{h_{min}^{\alpha_1}(0)} \tag{4.40}$$

Also:
$$W(0) - \{mg + F(0)\} = 0 \tag{4.41}$$

Using equations (4.40) and (4.41), the original minimum film thickness for purely rolling condition can be obtained:

$$h_{min}(0) = \left\{\frac{K}{mg + F(0)}\right\}^{1/\alpha_1} \tag{4.42}$$

The initial oil film surface acceleration is given by equation (4.43):

$$\ddot{S}_{min}(0) = \frac{h_{min}^{\alpha_1+1}(0)}{m\,\{h_{min}^{\alpha_1+1}(0) + \alpha_1\, K\, K_1\}} \cdot [W(0) - mg - F(0)] \tag{4.43}$$

where $\ddot{W}(0)$ used in (4.35) is the initial second rate of change of lubricant reaction:

$$\ddot{W}(0) = \frac{-\,\alpha_1\, K\, \ddot{S}_{min}(0)}{h_{min}^{\alpha_1+1}(0)} \qquad \text{where } \dot{S}_{min}(0) = 0 \tag{4.44}$$

4.4 THE GOVERNING EQUATION (POINT CONTACTS)

The governing equation of forced normal vibration of an elastohydrodynamic point contact is:

$$W(t) - mg - F(t) = m \{\ddot{S}_{min}(t) - (\alpha_1 K K_1 [- \ddot{S}_{min}(t) h_{min}(t) + (\alpha_1 + 1) \dot{S}^2_{min}(t)]) / h^{\alpha_1+2}_{min}(t) e^{\{(\beta/U)\dot{S}_{min}(t)\}}\} \quad (4.45)$$

The lubricant dynamic response to any periodic forcing function, $F(t)$, can be evaluated by simultaneous solution of equation (4.46) below with equations (2.17) and (2.20) using the average acceleration method. The initial conditions (4.39) to (4.44) are applied.

$$\ddot{S}_{min}(t) = \frac{\frac{1}{m}.h^{\alpha_1+2}_{min}(t)\, e^{\{(\frac{\beta}{U})\dot{S}_{min}(t)\}} . \{W(t)-mg-F(t)\} + \alpha_1(\alpha_1+1)\, \dot{S}^2_{min}(t)}{h_{min}(t)\, \{h^{\alpha_1+1}_{min}(t) . e^{\{(\beta/U)\dot{S}_{min}(t)\}} + \alpha_1 K K_1\}} \quad (4.46)$$

For pure entraining motion of elements or normally separating contacts, $\dot{S}_{min}(t) = 0$; hence:

$$\ddot{S}_{min}(t) = \frac{\{W(t) - mg - F(t)\}\, h^{\alpha_1+1}_{min}(t)}{m\, \{h^{\alpha_1+1}_{min}(t) + \alpha_1 K K_1\}} \quad (4.47)$$

4.5 RESULTS AND DISCUSSIONS (POINT CONTACTS)

When a normal periodic sinusoidal forcing function (i.e. $F(t) = F_{max} \cos 2\pi f t$) is applied to two rolling elements in an elastohydrodynamic point contact condition and the lubricant damping contribution is ignored, the undamped oil film response is observed to be harmonic under steady-state conditions (see Figure 4.3). The measured response frequency is notably different from the applied forcing frequency. This phenomenon is also observed under hydrodynamic conditions, although to a much lesser degree (see Chapter 2). Nevertheless, it is shown later that for certain values of applied forcing frequency, a condition of resonance is attained. Unlike the governing equations with iso-viscous and piezo-viscous lubricants, in EHL the applied forcing function is multiplied by non-linear terms containing the amplitude of the oil film response. Figures 4.4 and 4.5 show that a gradual increase in steady load merely results in a marginal decrease in the amplitude of the lubricant response. In fact, it can be observed that when the mean steady-state magnitude of the periodic load is increased twofold, the mean response characteristics of the film thickness indicate a decrease of 3%. In general, the response behaviour illustrates a slight ripple superimposed upon a mean steady lubricant film thickness. The apparent insensitivity shown by the lubricant to the applied loads is due to the low power index of W^* in equation (4.12) [4].

When the squeeze film term is included, the lubricant responds in a similar fashion to that already discussed when excited at lower forcing frequencies. However, at higher forcing frequencies, the squeeze film term provides a large damping force which counterbalances the normal motion and therefore the characteristic response is quite different (see Figure 4.6). At high applied frequency values (i.e. above 200 Hz), the response is an oscillatory decay (see Figure 4.6). The decaying transient response occurs because of the lubricant's increasing stiffness when subjected to increasing rates of compression under normal approach conditions. The pressure distribution also decays due to the deformation rate effect. The results obtained are generally in close agreement with the findings of Rohde, Whicker and Booker [19]. Rohde, et al. concluded that the response could not undergo a steady-state periodic form in a pure squeeze type motion. However, the inclusion of entraining motion in the present analysis allows for nett load reversals to take place.

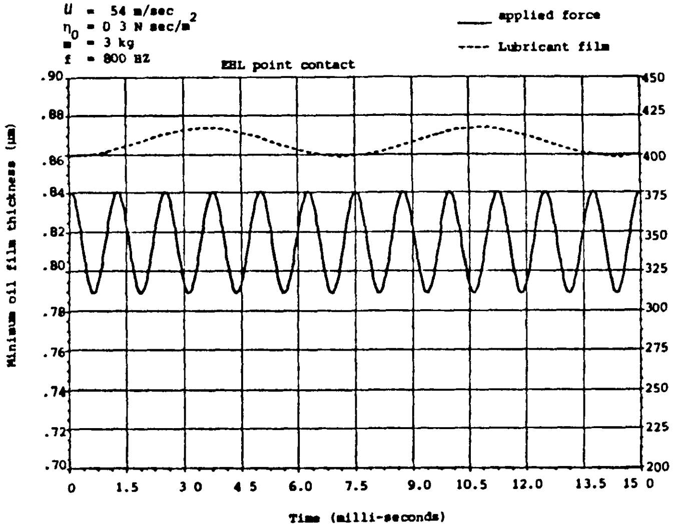

Fig 4.3 Undamped Lubricant time history (subjected to sinusoidal forcing)

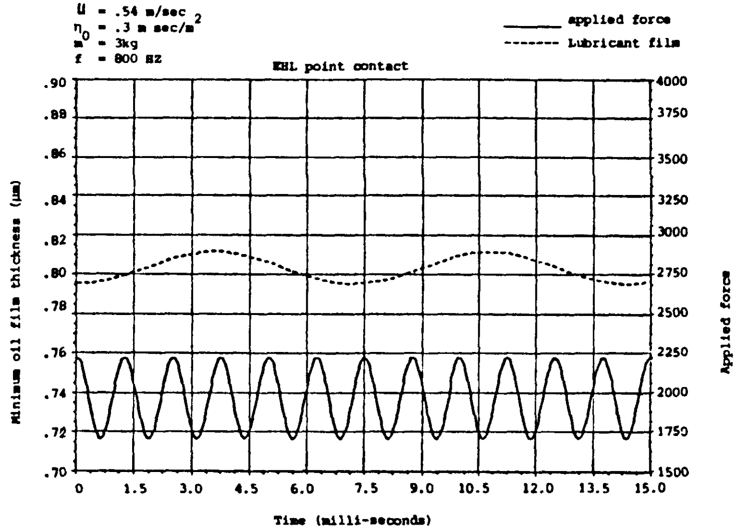

Fig 4.5 Undamped Lubricant time history

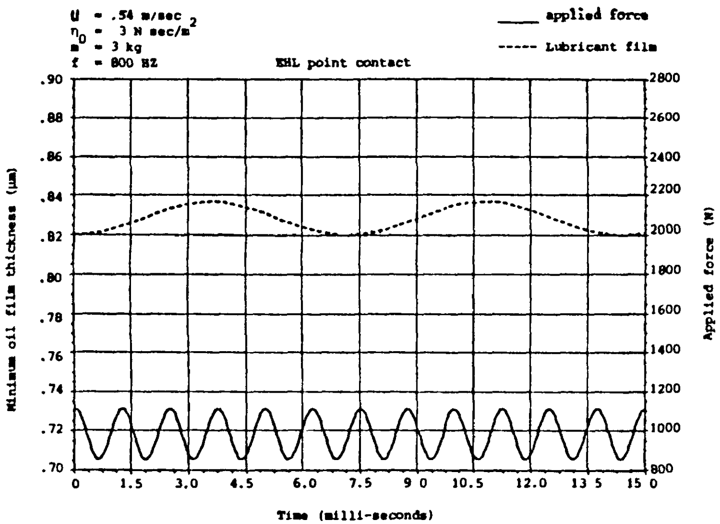

Fig 4.4 Undapmed Lubricant time history (subjected to sinosoidal forcing)

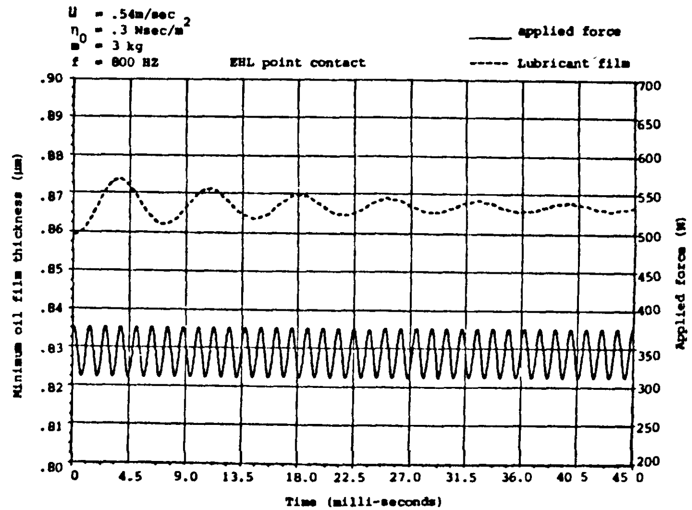

Fig 4.6 Damped Lubricant dynamic behaviour

The most unstable period of the lubricant film response occurs in the initial transient phase. When the contacting surfaces are assumed to be perfectly smooth, the elastohydrodynamic oil film response to a repetitive forcing function of fixed mean steady value seems unlikely to exhibit oil film seizure despite any increase in the amplitude of loading (see Figures 4.6 and 4.7). Under experimental conditions, a 'disc machine' is employed [20]. The amplitude of forcing is increased at fixed time intervals, leading to an initial sharp rise in the torque reading, indicating a reduction in the lubricant film thickness and an increase in the tractional forces at the discs' surfaces (see Figure 4.8). The subsequent torque relief after each load increment shows the lubricant film recovery as a result of the formation of low shear strength protective boundary layers forming at the mating surfaces. The torque trace history of Figure 4.8 is indicative of lubricant response characteristics which are not unlike those illustrated by the present theoretical model.

Figure 4.8 also illustrates the final oil film seizure, where purely metallic contact gives a sudden boost to rising contact friction, causing scuffing of the rolling contact surfaces. Scuffing damage takes place at localities with greatest concentrated load intensity. For theoretical comparison, it is therefore necessary to apply a periodic forcing function with increasing amplitude at given time intervals (see Figure 4.9). Periodically increased forcing amplitude merely delays the arrival of the steady-state condition and does not appear to have a drastic bearing on the amplitude of the lubricant film oscillations. (note: there is no sliding present in the model).

4.6 THE EFFECT OF EXCITATION FREQUENCY

The damped EHL minimum film thickness characteristics discussed so far were at a forcing frequency of 800 Hz. These characteristics are also observed at other excitation frequencies down to about 200 Hz (see Figures 4.10 and 4.11). The oil film behaviour differs when subjected to forcing frequencies below 200 Hz. When the excitation frequency is comparatively low (i.e. 10 to 50 Hz) the oil film response frequency is in closer agreement with it (see Figures 4.12 and 4.13). The lubricant response indicates a lightly damped system, not unlike that exhibited when the damping forces opposing the normal approaching motion were ignored. At higher forcing frequencies in the range 60 to 150 Hz, the oil film damped response frequency is almost coincident with it (see Figures 4.14 to 4.18). It should be noted that the damped response frequency referred to here is the dominant frequency, although the lubricant may respond with a multitude of frequencies because of its non-linear nature. For the same magnitude of loading, given this range of excitation frequencies, the oil film fluctuations tend to increase in amplitude as the forcing frequency approaches 120 to 140 Hz. Therefore, it is of interest to establish the range of frequencies at which a condition of resonance is attained.

For this purpose, a forcing function of large magnitude and short duration is applied (Dirac function, see Figure 4.19). The dominant damped response frequency is found to be within the range 130 to 140 Hz. At a given load, non-linear amplitude-frequency response characteristics may be observed for a number of values of excitation frequency. This is evidence of the non-linear behaviour of the lubricant. Such characteristics occur for hardening and softening springs under oscillating conditions. The extent of non-linearity of the lubricant response can be investigated by obtaining an amplitude-frequency graph. The numerical results obtained so far may be studied using spectral analysis. In Chapter 5, the fast Fourier transform method (FFT) is employed with this aim in mind.

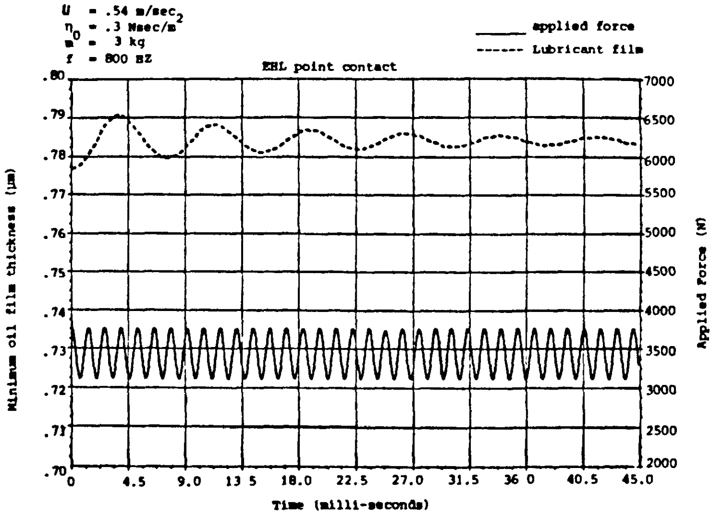

Fig 4.7 Damped Lubricant dynamic behaviour

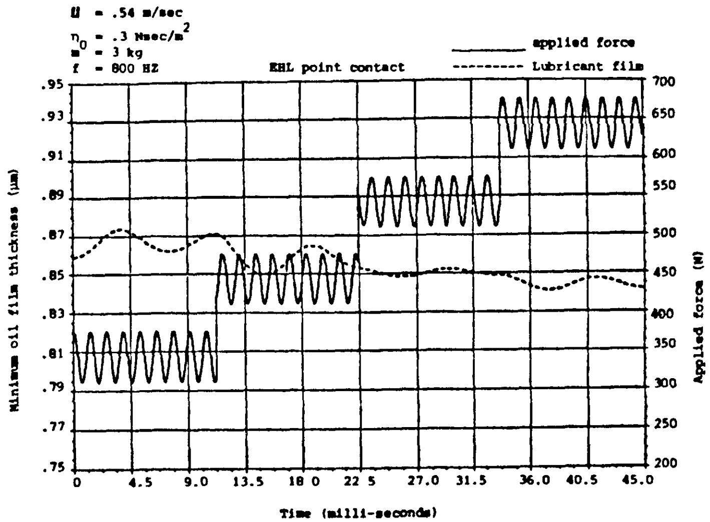

Fig 4 9 Damped lubricant dynamic behaviour subjected to sinusoidal forcing of increasing periodic magnitude

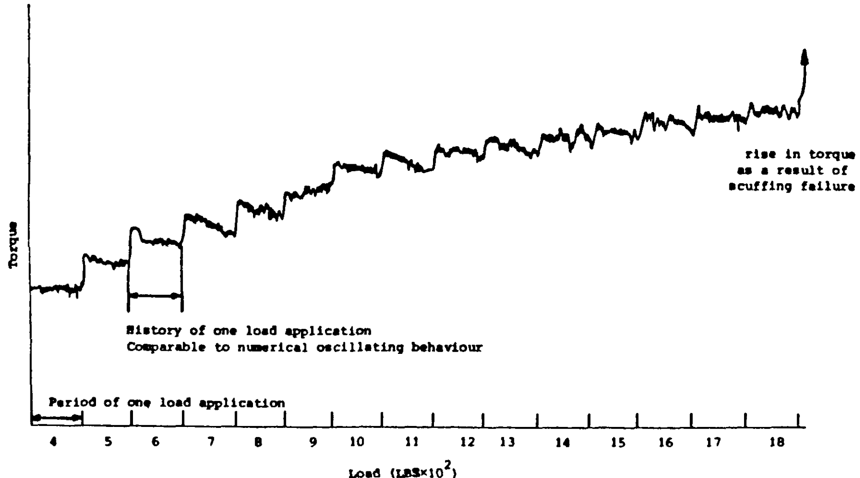

Fig 4.8 Scuffing Disc machine torque trace (for 80°C bulk oil temperature)

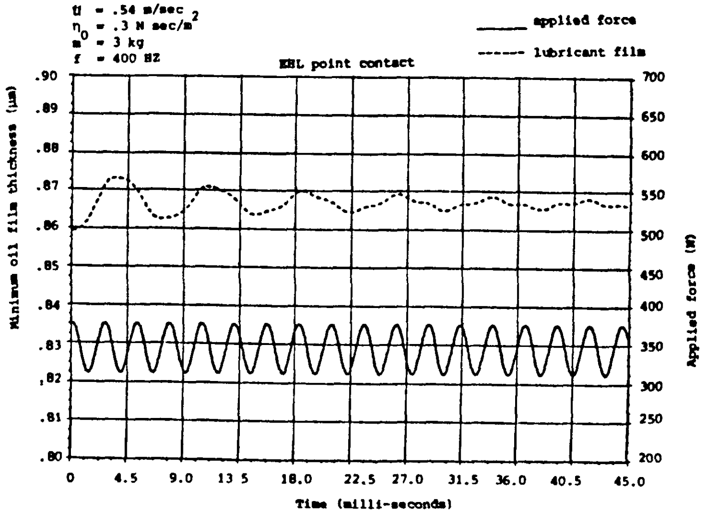

Fig 4.10 Damped Lubricant response subjected to sinusoidal forcing

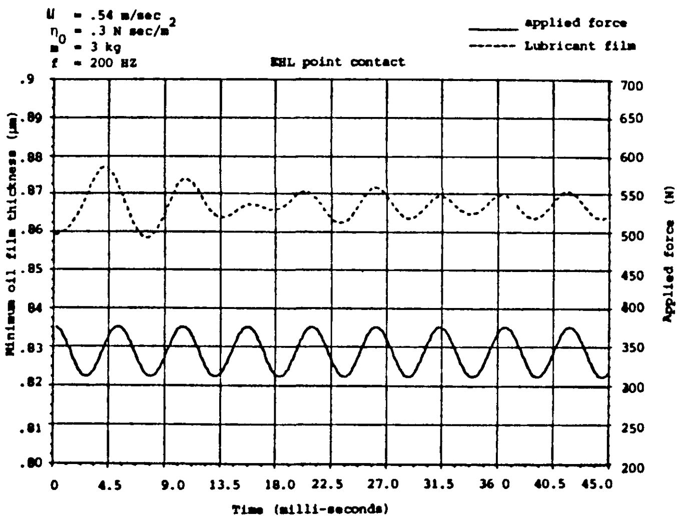

Fig 4.11 Damped Lubricant response subjected to sinusoidal forcing

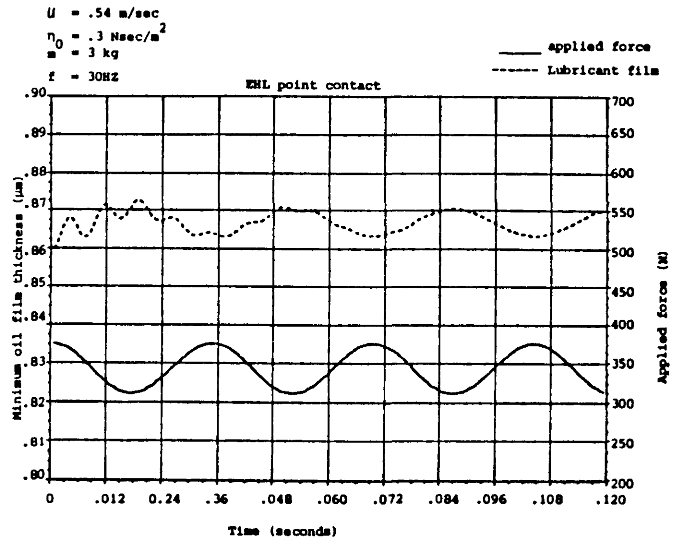

Fig 4.13 Damped Lubricant response subjected to sinusoidal forcing

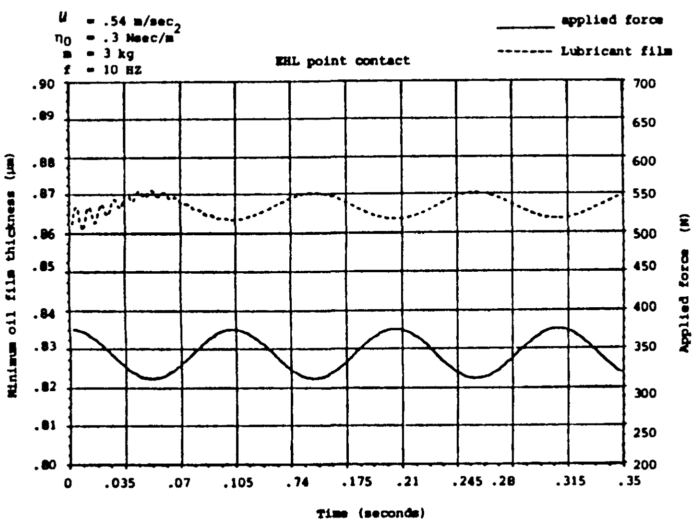

Fig 4.12 Damped lubricant response subjected to sinusoidal forcing

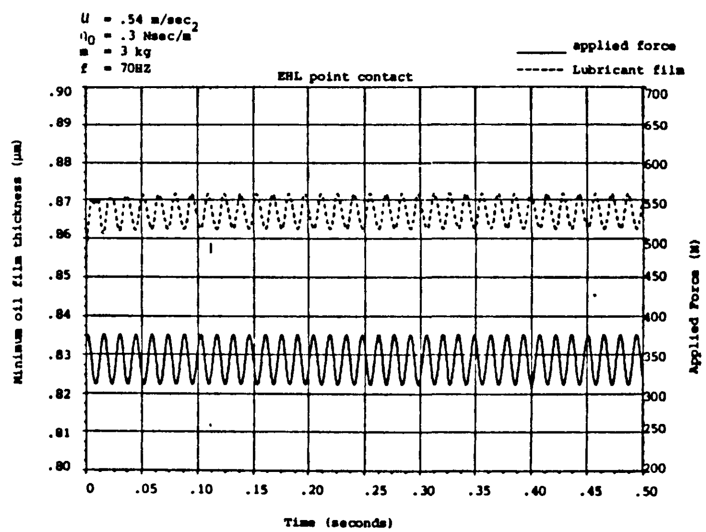

Fig 4.14 Damped lubricant response subjected to sinusoidal forcing

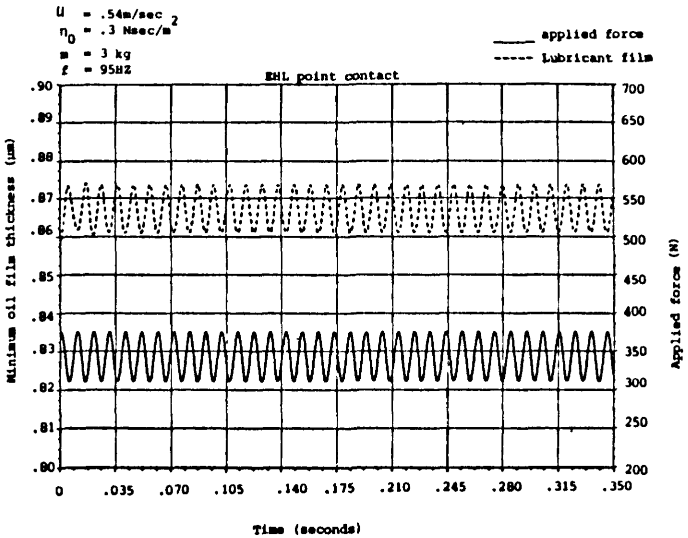

Fig 4.15 Damped lubricant response subjected to sinusoidal forcing

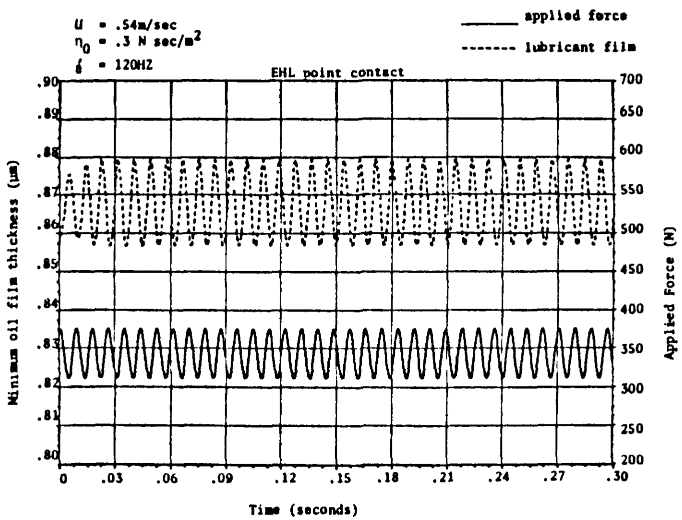

Fig 4.16 Damped lubricant response subjected to sinusoidal forcing

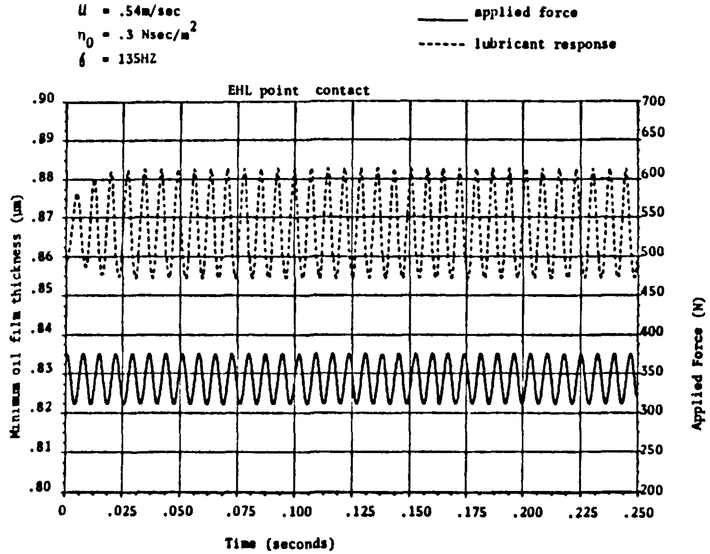

Fig 4.17 Damped lubricant response subjected to sinusoidal forcing

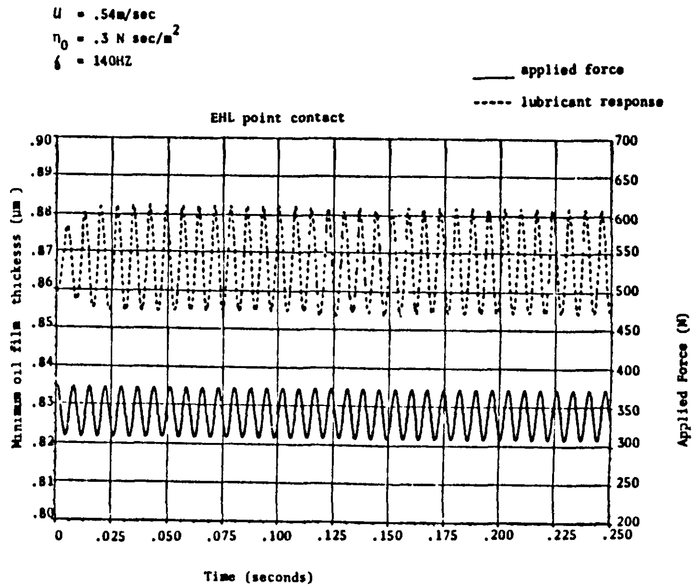

Fig 4.18 Damped lubricant response subjected to sinusoidal forcing

4.7 THE EFFECT OF ROLLING SPEED

It is important to realise that, like the squeeze velocity, the rolling speed variation has an important effect on the nature of the lubricant response. Higher values of rolling speed lead to larger film thicknesses which, in turn, result in a decrease in the stiffness of the oil film. This means there are various response frequencies at different rolling speeds.

All the results obtained so far were at a fixed combined rolling speed of 0.54 m/sec. A tenfold increase in the value of the combined rolling speed of mating elements to 5.4 m/sec yields a nearly fivefold increase in the steady value of the minimum film thickness at the steady-state condition (i.e. from $\simeq$ 0.8 μm to 4.1 μm).

If the EHD contact is considered transversely to the direction of induced entraining motion, the problem is of a finite line contact, where the minimum film occurs near unblended regions of the rolling element's axial profile. These regions are known as the exit or side constrictions (see Chapter 3). In these positions, the oil pressures and the subsequent stress concentration levels are larger than those on the centreline.

4.8 INFLUENCE OF NORMAL APPROACH ON EHD FINITE LINE CONTACTS

The numerical results of Chapter 3 are listed in Table 4.2. The range of parameters, the number of values taken for the purpose of regression analysis and the accuracy of these regressed results are provided in Table 4.2.

Using a log-log fit, approximate expressions describing the oil film thickness in terms of the dimensionless groups are obtained. For the central oil film thickness:

TABLE 4.2

Grouping	Range	Number of Values Taken	Maximum Difference Between Regressed and Numerical Results as a Percentage Difference	
			For $h^*_{\delta c}$	For h^*_o
G^*	$5700 \rightarrow 9650$	4	7.9	7.6
W^*_δ	$-0.005 \rightarrow 0$	5	32.6	5.8
W^*	$0.34 \times 10^{-6} \rightarrow 0.56 \times 10^{-5}$	6	13.1	4.7
U^*	$0.63 \times 10^{-11} \rightarrow 3.3 \times 10^{-11}$	8	12.5	2.5

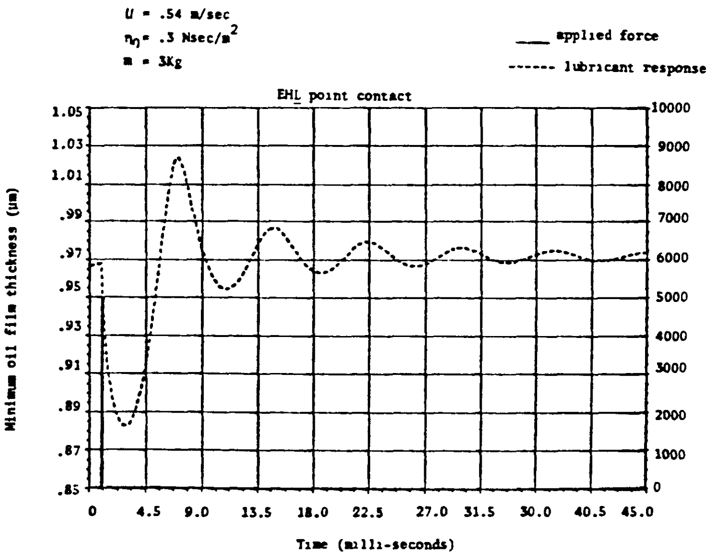

Fig 4.19 Dynamic lubricant response to the application of a Dirac function

$$h_o^* = 1.67G^{*0\cdot421}\,U^{*0\cdot541}\,W^{*0\cdot059}\,e^{-96.775W_s^*} \qquad (4.48)$$

and for the side constriction oil film thickness:

$$h_{sc}^* = 1150G^{*0\cdot406}\,U^{*0\cdot857}\,W^{*-0\cdot037}\,e^{-138.059W_s^*} \qquad (4.49)$$

The groups employed are similar to those used for the solution of the point contact problem (i.e. equation (4.15); see also Chapter 3). Also:

$$h_{sc}^* = \frac{h_{sc}}{R} \qquad (4.50)$$

The constant in expression (4.49) is considerably larger than that obtained for the central film thickness in equation (4.48) and the numerical formulae of Mostofi [4] (i.e. equations (4.12) and (4.13)). The reason for this is because of the higher power index of the rolling parameter, U^*. Figure 4.20 is a log-log plot of the film thickness, h^*, against U^* for various positions within the oil film contour (see Chapter 3). The slope selected for the side constriction leading to the calculation of the U^* power index includes the non-linear region of the plot.

To investigate the time-dependent behaviour of the film at the position of 'side constriction' when it is subjected to fluctuating periodic normal loads, the lubricant reaction force is found by rearranging equation (4.49):

$$W^*(t) = \frac{K_n'}{h_{sc}^{*27}(t)\; e^{\{3727.543W_s^*(t)\}}} \qquad (4.51)$$

where K_n' is the time-independent constant:

$$K'_n \;=\; (1150)^{27}\, G^{*10\cdot962}\, U^{*23\cdot139} \tag{4.52}$$

Substituting the dimensionless groups of (4.15) and (4.50) in equation (4.51):

$$W(t) \;=\; \frac{K'}{h_{sc}^{\alpha'}(t)\; e^{\{(\beta'/U)\dot{h}_{sc}(t)\}}} \tag{4.53}$$

where: $$K' \;=\; (1150)^{27}\, G^{*10\cdot962}\, U^{*23\cdot139}\, \frac{R^{29}}{E_r} \tag{4.54}$$

and has the units of Nm^{27}.

α' is the power index of the oil film thickness and β' is the coefficient of the squeeze velocity term, $\dot{h}_{sc}(t)$. Since:

$$h_{sc}(t) \;=\; h_{sc}(0) + S_{sc}(t) \tag{4.55}$$

Then: $$\dot{h}_{sc}(t) \;=\; \dot{S}_{sc}(t) \quad , \quad \text{(see Notation)} \tag{4.56}$$

Since the value of the 'side constriction' oil film is desired, the movement of the top of the lubricant film at this position should be described in terms of the movement of the centreline of the normally loaded rolling element.

Using Figure 4.21, the movement of the oil film at both the centre of the pressure distribution domain and the 'side constriction' can be found. For the former case:

$$z(t) \;=\; H_o(t) + R \tag{4.57}$$

and: $$h_o(t) \;=\; H_o(t) + \delta_o(t) \tag{4.58}$$

By elimination of $H_o(t)$:

$$z(t) = R + h_o(t) - \delta_o(t) \tag{4.59}$$

where: $$h_o(t) = h_o(0) + S_o(t) \tag{4.60}$$

Now, doubly differentiating (4.59) to replace for the centreline acceleration of the element in (4.18):

$$\ddot{z}(t) = \ddot{S}_o(t) - \ddot{\delta}_o(t) \tag{4.61}$$

For the position of the 'side constriction':

$$H_{sc}(t) = h_{sc}(t) - \delta_{sc}(t) \tag{4.62}$$

and: $$z(t) = R - P_\ell(x) + H_{sc}(t) \tag{4.63}$$

where $P_\ell(x)$ is the axial profile of the rolling element. Using the assumption outlined in page 107, the relationship between the deflection at the centre of the contact and the deflection at the position of 'side constriction' is:

$$\delta_o(t) = \delta_{sc}(t) + P_\ell(x) \tag{4.64}$$

since the profile at the central position, $P_\ell(x=0) = 0$. Substituting from equation (4.64) into equation (4.63):

$$H_{sc}(t) = h_{sc}(t) - \delta_o(t) + P_\ell(x) \tag{4.65}$$

By elimination of $H_{sc}(t)$ between equations (4.65) and (4.63):

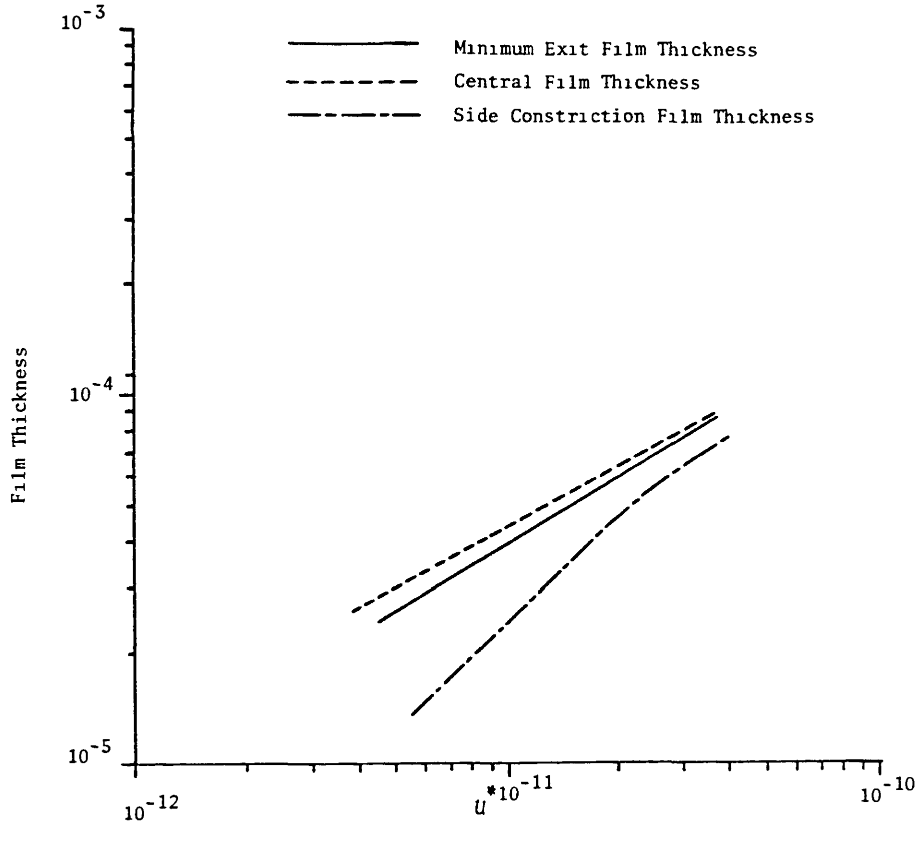

Fig 4.20 Film thickness variation with U^{*}

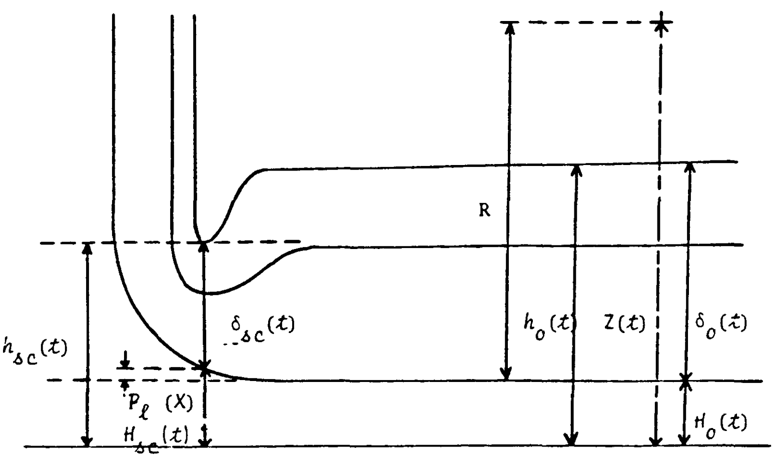

Figure 4.21 Geometrical consideration of a finite line contact under normal motion

$$z(t) = R + h_{sc}(t) - \delta_0(t) \tag{4.66}$$

Doubly differentiating equation (4.66) yields the acceleration of the centreline of the normally loaded rolling element in terms of the rate of change of lubricant squeezing effect and the rate of change of the local deformation gradient (i.e. $d\dot{\delta}_0(t)/dt$):

$$\ddot{z}(t) = \ddot{S}_{sc}(t) - \ddot{\delta}_0(t) \tag{4.67}$$

4.9 GOVERNING EQUATION (FINITE LINE CONTACT)

To obtain the dynamic governing equation of forced normal vibrations for the position of 'side constriction' in an EHD finite line contact problem, simply substitute for $\ddot{z}(t)$ from (4.67) into (4.18) and replace for $\ddot{\delta}_0(t)$ from (4.68) below:

$$\ddot{\delta}_0(t) = K_1\ \ddot{W}(t) \tag{4.68}$$

Therefore:

$$W(t) - \{mg + F(t)\} = m\ \{\ddot{S}_{sc}(t) - K_1\ \ddot{W}(t)\} \tag{4.69}$$

where $W(t)$ is given by equation (4.53) and $\ddot{W}(t)$, its second derivative, is calculated below by doubly differentiating equation (4.53) and neglecting the third and higher order terms:

$$\ddot{W}(t) = \frac{\alpha'\ K'\ \{-\ \ddot{S}_{sc}(t)\ h_{sc}(t) + (\alpha' + 1)\ \dot{S}^2_{sc}(t)\}}{h_{sc}^{\alpha'+2}(t)\ e^{\{(\beta'/U)\dot{S}_{sc}(t)\}}} \tag{4.70}$$

By simple manipulation of (4.69) and using equation (4.70):

$$\ddot{S}_{sc}(t) = \frac{\{W(t)-mg-F(t)\}.\left[\dfrac{h_{sc}^{\alpha'+2}(t)}{m}\; e^{\{\frac{\beta'}{U}\dot{S}_{sc}(t)\}}\right]+\alpha'(\alpha'+1)\,K_1\,\dot{S}_{sc}^{2}(t)}{h_{sc}(t).\left[h_{sc}^{\alpha'+1}(t)\; e^{\{(\beta'/U)\dot{S}_{sc}(t)\}} + \alpha'\,K'\,K_1\right]} \qquad (4.71)$$

4.10 INITIAL CONDITIONS (FINITE LINE CONTACT)

The dynamic behaviour of the lubricant film at the 'side constriction', subjected to periodic normal loads under an EHD finite line contact condition, can be assessed by a combined solution of equations (4.71), (2.17) and (2.20) implementing the appropriate initial conditions below:

$$\text{at } t = 0 \;, \quad h_{sc}(t) = h_{sc}(t{=}0) \;, \quad S_{sc}(t{=}0) = \dot{S}_{sc}(t{=}0) = 0 \qquad (4.72)$$

Therefore:

$$W(t{=}0) = \frac{K'}{h_{sc}^{\alpha'}(0)} \qquad (4.73)$$

The initial force balance is:

$$W(0) - \{mg + F(0)\} = 0 \qquad (4.74)$$

The original film thickness at 'side constriction' is:

$$h_{sc}(0) = \left\{\frac{K'}{mg + F(0)}\right\}^{1/\alpha'} \qquad (4.75)$$

The original lubricant surface acceleration is:

$$\ddot{S}_{sc}(0) = \frac{h_{sc}^{\alpha'+1}(0)\;[W(0) - mg - F(0)]}{m\,\{h_{sc}^{\alpha'+1}(0) + \alpha' K'\,K_1\}} \qquad (4.76)$$

4.11 RESULTS AND DISCUSSIONS (FINITE LINE CONTACTS)

Similar characteristics to those in Section 4.5 for EHD point contacts are observed. Under the EHD finite line contact condition, the position of interest is the 'side constriction'. For the same loading condition, the mean steady-state lubricant film thickness at the 'exit constriction' (see Figure 4.22) is nearly half that obtained for the minimum exit film under EHL elliptical contacts (see Figure 4.6). As for the case of EHL elliptical contacts, the side constriction film thickness also exhibits damped behaviour at higher forcing frequencies. Hence, as the value of the forcing frequency is reduced, the damped oscillatory behaviour ceases to exist (see Figures 4.23 and 4.24). At low values of excitation frequency (i.e. 10 to 50 Hz), lightly damped characteristics similar to a sinusoid are observed (see Figure 4.25).

The amplitude of the oil film oscillations increases markedly as the applied forcing frequency tends to coincide with the dominant response frequency. The range of excitation frequencies at which this resonant condition is attained is found to be 150 to 160 Hz (for the values of load, rolling speed and other governing parameters remaining constant). When a Dirac function is applied in the equation of motion of the EHL finite line contact condition (see Figure 4.26), the measured dominant response frequency is 150 Hz (i.e. a measure of natural frequency of the system). The approach to this resonant condition is best observed by progressively incrementing the applied excitation frequency (see Figures 4.27, 4.28 and 4.29).

The effect of rolling speed variation can be seen by comparing the response of the Figures 4.22, 4.30, 4.31 and 4.32. A tenfold increase in the magnitude of the rolling speed from 0.54 m/sec to 5.4 m/sec results in an approximate eightfold increase in the mean steady-state oil film thickness from 0.4885 μm to 3.515 μm. This increase is more than that

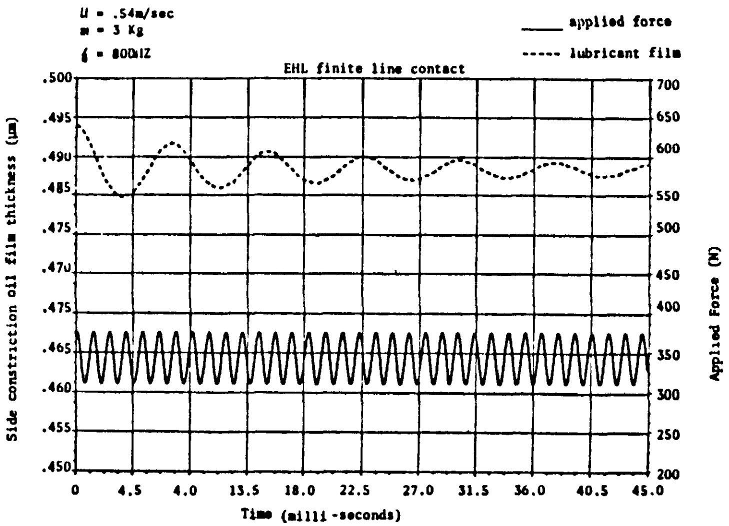

Fig 4.22 Damped lubricant dynamic response (sinusoidal forcing)

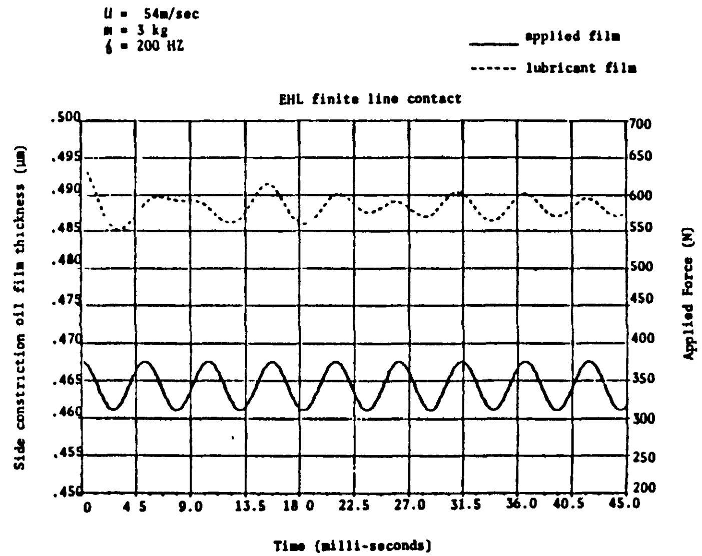

Fig 4.24 Damped lubricant dynamic response (sinusoidal forcing)

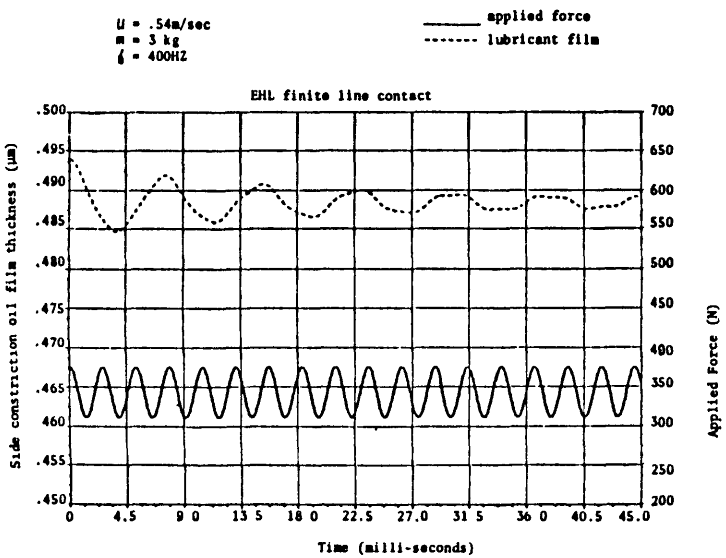

Fig 4.23 Damped lubricant dynamic response (sinusoidal forcing)

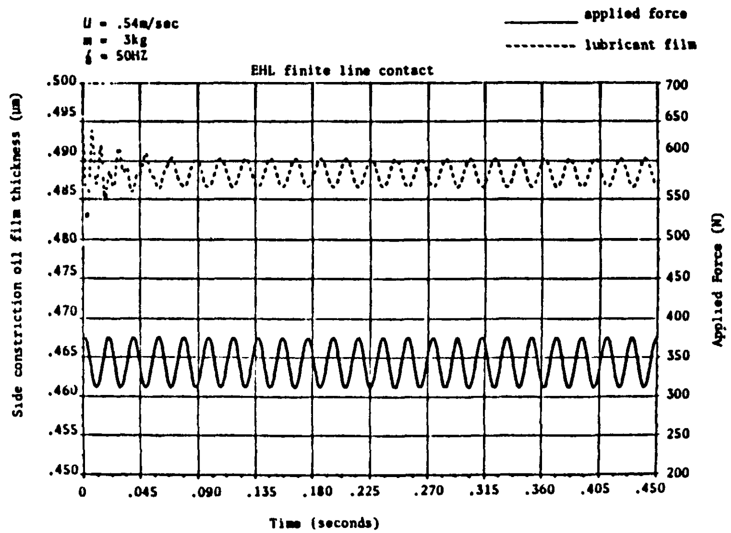

Fig 4.25 Damped lubricant dynamic response (sinusoidal forcing)

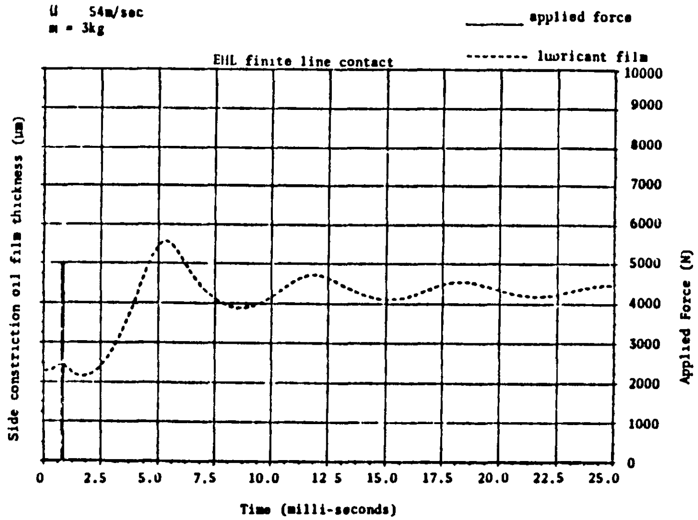

Fig. 4.26 Dynamic lubricant response to the application of a Dirac function

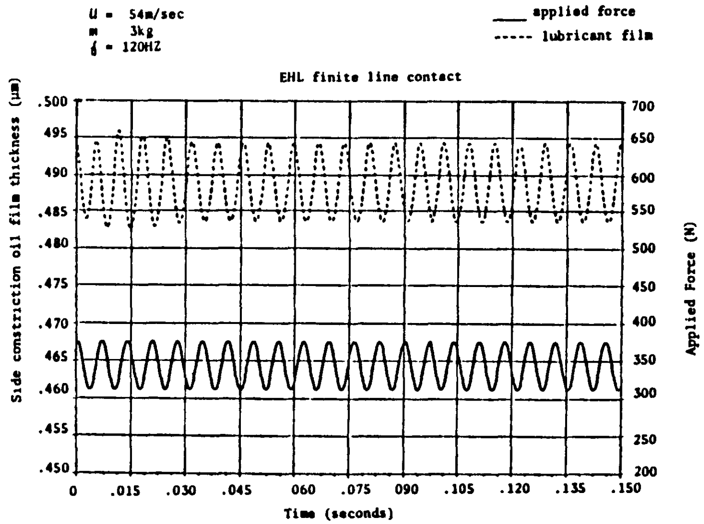

Fig 4.28 Damped lubricant dynamic response (sinusoidal forcing)

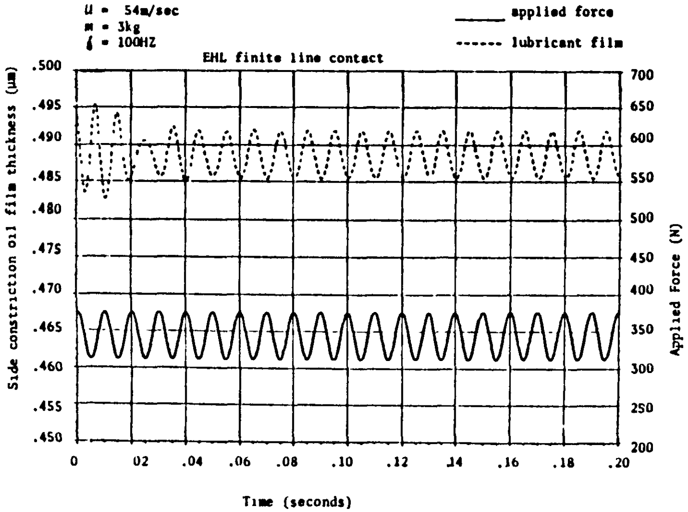

Fig 4 27 Damped lubricant dynamic response (sinusoidal forcing)

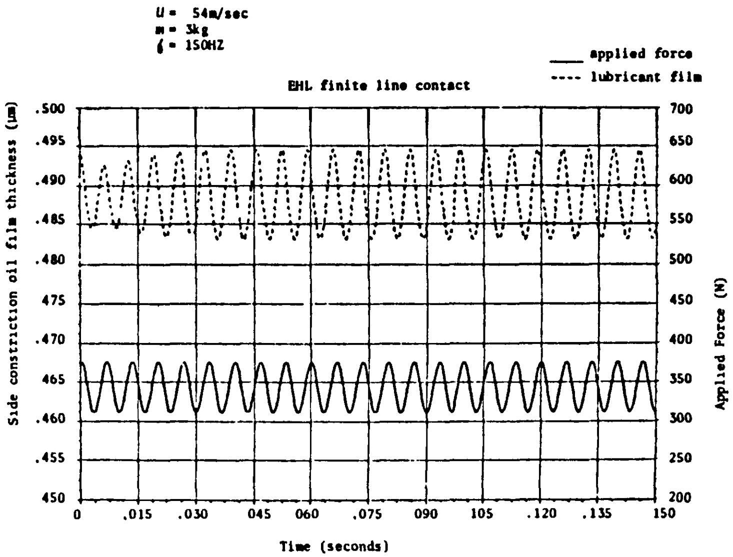

Fig 4 29 Damped lubricant dynamic response (sinusoidal forcing)

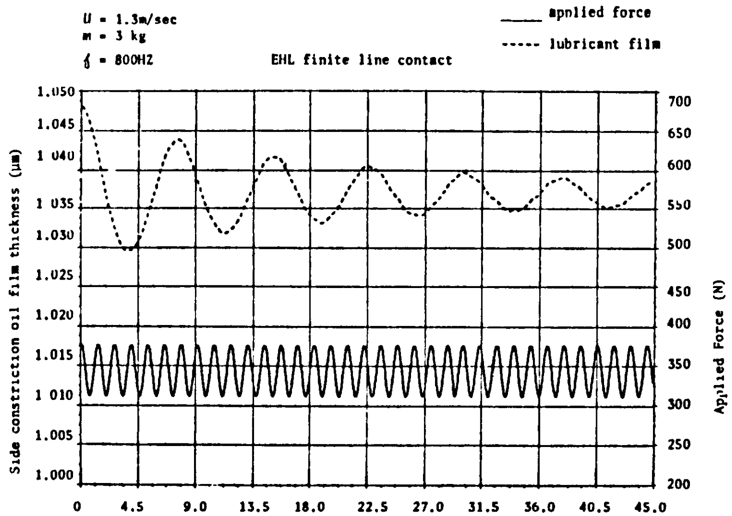

Fig 4.30 Damped lubricant time history(subjected to sinusoidal forcing)

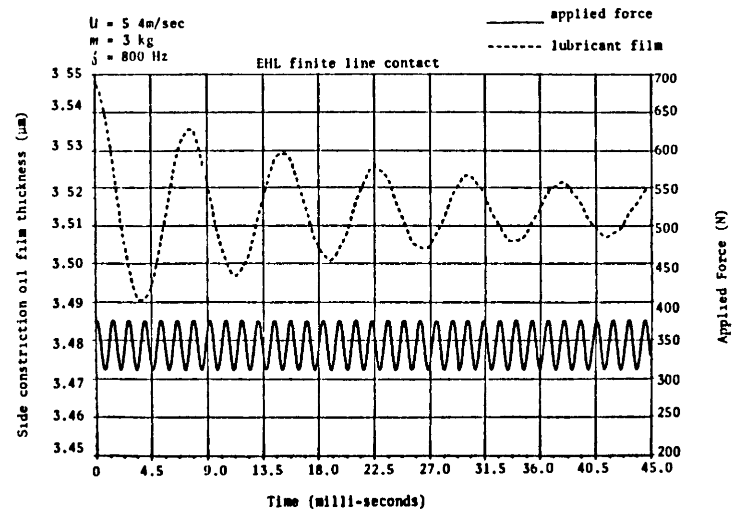

Fig 4.32 Damped lubricant time history (sinusoidal forcing)

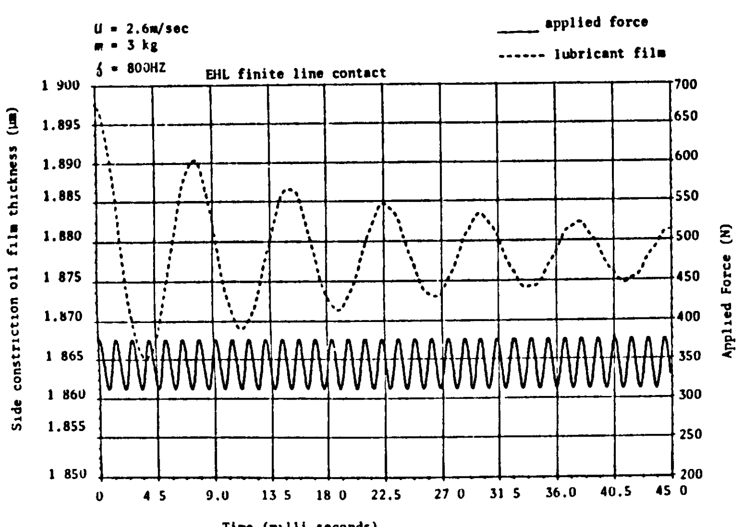

Fig 4 31 Damped lubricant time history (subjected to sinusoidal forcing)

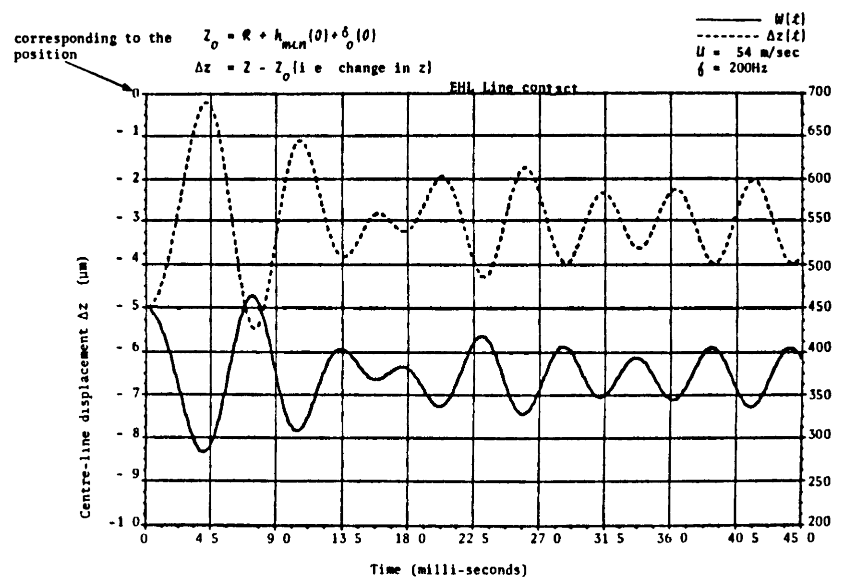

Fig 4 33 Time histories of centre-line movement and lubricant reaction observed for the minimum exit film thickness (in Section 4.7), since the index of U^* is 0.875.

In general, the finite line contact exhibits damper oil film behaviour and higher sensitivity to rolling speed variation than that of the point contact. These results are predictable if the line contact and elliptical contact load equations are compared (i.e. (4.51) and (4.17)).

4.12 CYCLIC STRESS UNDER OSCILLATING CONDITIONS

The present analysis indicates that the lubricant film is remarkably passive to any reasonable increase in the magnitude of loading and fairly sensitive to change of excitation frequency. Even when the forcing frequency coincides with the dominant response frequency, the extent of lubricant surface oscillations (superimposed upon a mean steady-state film thickness) is merely a ripple. The maximum fluctuations (i.e. $S(t)$) under any given condition do not exceed 6% to 8% of this steady-state oil film thickness. In fact, the lubricant tends to behave as a rigid layer appearing to pose a sizeable damping force when excited at higher frequencies. However, the adjacent elastic member is subjected to considerable rates of change of contact reaction (i.e. $\dot{W}(t) = dW(t)/dt$). Figure 4.33 illustrates the variation of $W(t)$ with time and the corresponding dynamic oscillations of the centreline of the rolling member (i.e. $z(t)$). These large roller centreline displacements are associated with high cyclic stress levels which act upon a small area. In a real system, fatigue failure might take place due to the concentrated action of these stresses on small areas of contact. Asperity interactions may also take place, even if the mean steady-state oil film thickness is several times greater than the composite surface roughness. The surface features can vary in height about ±3 times the composite surface roughness, and the oil film may vary about its calculated mean to a much lesser degree [21]. In fact, the spectrum of vibrations from a modern rolling element is continuous over all frequencies consisting of many resonant peaks. A mere handful of these are usually due to passing frequencies such as ring, cage or other contacting elements and fixtures [22].

4.13 WEAR CHARACTERISTICS

Gears and bearings are designed to function during the entire life of the machine of which they are a part. Regardless of proper design considerations, wear invariably does take place during the operation of these elements. Therefore, correct lubrication is deemed essential to minimise wear and increase the useful life of gear teeth and rolling element bearings. During manufacture, surfaces are very accurately generated and are developed as smooth as possible. Nevertheless, there are always microscopic surface irregularities which cause frictional resistance when asperity interactions take place. However, even with correct lubrication, under certain operating conditions, surface damage can result.

The major types of surface failure are pitting, abrasion, scuffing, scoring and flaking. Scuffing is definitely due to seizure of the surfaces under load. The thick wedge-type film gives way to a microscopically thin boundary layer which has low shear strength characteristics. Under abnormally severe operating conditions (for example, large slide-roll ratios or sizeable normal loads), excessive friction causes plastic flow of the top layers of the surfaces. In the case of counterformal contact of mating discs, scuffing failure occurs at the edges of the track (provided on one of the discs by lightly chamfering it (see Chapter 3)) [20]. Scoring is due to conditions not quite dependent upon lubrication. A rough surface finish or aggravated pitting produce sharp projections in the contact area. Asperity interactions may then extend beyond the lubricant film thickness and cause scratch furrows in the mating surfaces. Abrasion is another type of surface destruction caused by abrasive materials entering the contact zone (i.e. dirt and grit in the oil). In some cases, the abrasive agent may be metallic particles that have been pitted or scored from the contacting surfaces. Flaking, which is also referred to as spalling, is due to any physical condition that stresses the surface material beyond its fatigue limit. Under these conditions (for example, misalignment or excessive overload), localised stresses tend to form a wave of material which rolls ahead of the contact point. The theory that has been used in this thesis does not include any of the above phenomena. The model neither envisages changes in surface topography, nor does it yet discuss any fatigue that may occur. However, pitting phenomenon can be forecast where load is concentrated on local surface protrusions or hardspots. This produces heavy localised stresses which are repetitive in nature. The resulting sub-surface fatigue of the metal causes minute particles to break away, leaving small pits. The results obtained in the present analysis indicate the presence of these cyclic stresses (described in Section 4.12) under oscillating normal motion. The excitation is due to the application of periodic load and the response is frequency-dependent (see Sections 4.5 and 4.11). The incidence of pitting is greater at frequencies of 120 to 150 Hz, where the cyclic load on the surfaces has a larger amplitude (i.e. causes a larger film change). At these frequencies, there is sufficient time for the effect of applied periodic force to transmit to the lubricant film. At higher frequencies (above 200 Hz), contact stresses have smaller amplitude and the oil film is hardly affected by the applied normal load. A good analogy is to consider the suspension coil spring in a car to represent the rolling

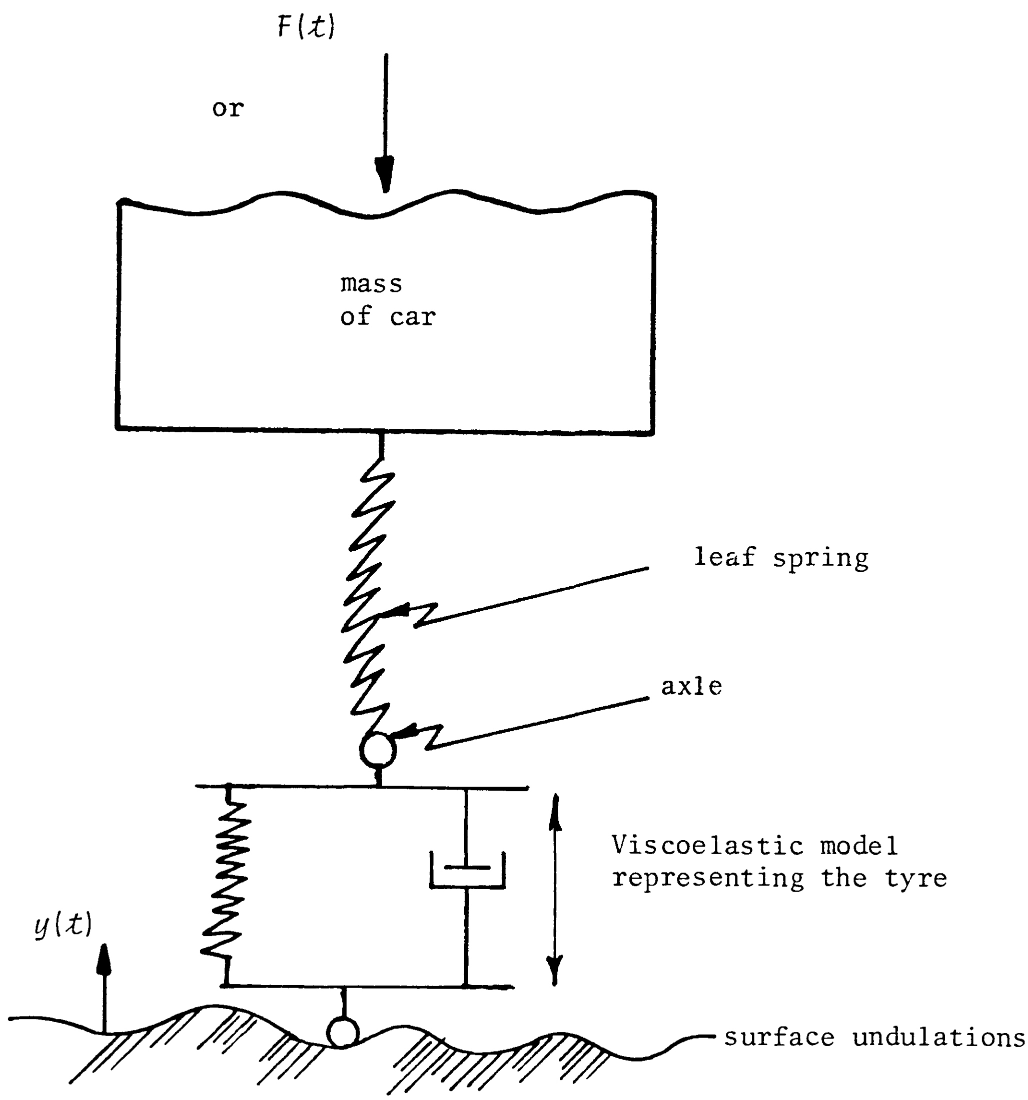

Fig 4.34 Wheel tyre and axle assembly

element and the much stiffer wheel tyre to simulate the lubricant film (see Figure 4.34). If a periodic force of low frequency is applied to the top of the coil, there is sufficient time for transmission of its effect to the axle. At a higher frequency, the coil tends to receive the full magnitude of the force with little or no transmission to the axle and the wheel tyre.

4.14 REFERENCES

[1] GRUBIN, A.N.
"Investigation of Scientific and Industrial Research",
Book 30, Central Scientific Research Institute for Technology and Mechanical Engineering, Moscow, 1949.

[2] DOWSON, D., and HIGGINSON, G.R.
"Elastohydrodynamic Lubrication",
Pergamon Press, SI edition, 1977.

[3] RANGER, A.P., ETTLES, C.M.M., and CAMERON, A.
"The Solution of Point Contact EHL Problem",
Proc. R. Soc. Lond., A346, 1975.

[4] MOSTOFI, A.
"Oil Film Thickness and Pressure Distribution in Elastohydrodynamic Elliptical Contacts",
PhD Thesis, Imperial College of Science and Technology, University of London, 1981.

[5] DOWSON, D., and HIGGINSON, G.R.
"A Theory of Involute Gear Lubrication",
Proceedings of Symposium on Gear Lubrication, Institute of Petroleum, 1966.

[6] DOWSON, D.
"Die Elastohydrodynamishe Schmierung Von Wälzlagern",
Maschinebau Technik, Jahrgang 18, Heft 2, 1969.

[7] WYMER, D.G.

"EHL of a Rolling Line Contact",

PhD Thesis, Imperial College of Science and Technology, University of London, 1972.

[8] BISWAS, S., and SNIDLE, R.W.

"EHL of Spherical Surfaces of Low Elastic Modulus",

Trans. ASME, J. Lubrication Technology, Series F, 98 (1976).

[9] GOHAR, R.

"Oil Film Thickness and Rolling Friction in EHL Point Contact",

Trans. ASME, J. Lubrication Technology, Series F, 93 (1971).

[10] DOWSON, D., and HIGGINSON, G.R.

"New Roller Bearing Lubrication Formula",

Engineering, 1961.

[11] ARCHARD, J.F., and KIRK, M.T.

"Lubrication at Point Contacts",

Proc. R. Soc. Lond., A ___ (1961).

[12] ARCHARD, J.F., and COWKING, E.W.

"EHL Lubrication at Point Contacts",

Proc. I. Mech. E., 180 (1965-66).

[13] HAMROCK, B.J., and DOWSON, D.

"Isothermal EHL Lubrication of Point Contacts",

Part 1: *Trans. ASME, J. Lubrication Technology*, Series F, 98 (1976) 223-229.

Part 2: *Trans. ASME, J. Lubrication Technology*, Series F, 98 (1976) 375-383.

Part 3: *Trans. ASME, J. Lubrication Technology*, Series F, 99 (1977) 264-274.

[14] CHENG, H.S.

"A Numerical Solution to the EHL Film Thickness in an Elliptical Contact",

Trans. ASME, J. Lubrication Technology, 92 (1970).

[15] THORP, N., and GOHAR, R.

"Oil Film Thickness and Shape for a Ball Sliding in a Grooved Raceway",

Trans. ASME, J. Lubrication Technology, July 1972.

[16] MOSTOFI, A., and GOHAR, R.

"Oil Film Thickness and Pressure Distribution in Elastohydrodynamic Point Contacts",

J. Mech. Eng. Sci. Vol 24, No 4, (1982) pp 173-182.

[17] JOHNS, P.M., and GOHAR, R.

"Roller Bearings Under Radial and Eccentric Loads",

Tribology International, June 1981.

[18] TIMOSHENKO, S., YOUNG, D.H., and WEAVER, Jnr, W.

"Vibration Problems in Engineering",

John Wiley & Sons, 4th edition, 1974.

[19] ROHDE, S.M., WHICKER, D., and BOOKER, J.F.

"Elastohydrodynamic Squeeze Film Effects of Viscoelasticity and Fluctuating Load",

Trans. ASME, J. Lubrication Technology, 101 (1979) 74-80.

[20] MACPHERSON, P.B.

"Lubrication in Gear Scuffing and Pitting",

PhD Thesis, Imperial College of Science and Technology, University of London, 1971.

[21] SAYLES, R.S., and POON, S.Y.

"Surface Topography and Rolling Element Vibrations",

Precision Engineering, 1981.

[22] POON, S.Y., and WARDLE, F.P.
"Running Quality of Rolling Bearings Assessed",
CME, April 1978.

CHAPTER 5

SPECTRAL COMPOSITION OF EHD RESPONSES

5.1 INTRODUCTION

In Chapter 4, it was discussed that whilst the oil film acts as a very stiff layer, the adjacent elastic member is considerably more responsive to changing external conditions†. It was also shown that changing the forcing frequency among these external parameters has the most prominent effect on the dynamic characteristics of both the lubricant and the elastic member. Because of the system's non-linear nature, a given value of forcing frequency tends to excite a particular number of response modes. Each mode can be considered as the interaction of two phases (i.e. a non-linear hardening spring and a non-linear softening spring), simulating the behaviour of the lubricant under squeezed and relieved conditions, respectively. The relative contribution of these two phases determines the modal characteristic response. For example, under the squeeze condition, the lubricant provides a considerable damping force when the forcing frequency is above 200 Hz and the lubricant response has an oscillatory decay. At low values of forcing frequency, the overall response appears to be in-phase harmonic. This is because most of the excited modes have a non-linear softening stiffness (i.e. have little damping).

The characteristics of hardening and softening springs have been extensively studied (see Figure 5.1) [1]. It was found that the response amplitude undergoes a sudden discontinuous jump near resonance. Duffing [2] made an exhaustive study of this phenomenon for a cubic spring. On

---

†Speed of entraining motion, magnitude of loading and the forcing frequency.

an amplitude-frequency plot, these areas of instability can be located (see Figure 5.2) [2]. It is, nevertheless, difficult to establish an amplitude-frequency relationship which describes the non-linear behaviour of the present model (detailed in Chapter 4). The time histories of both the lubricant film response and the local deformation of the adjacent elastic member are available (see results in Chapter 4). The numerical output provides historical samples at a series of regularly spaced times. These discrete series are referred to as 'discrete time series'. However, they are assumed to have been derived from a 'continuous time function' and represent a 'continuous time series'. For any given variable, 'time series' refers to a sequence of discrete numbers ordered in time, or the original continuous time sample from which the discrete series has been obtained [3]. The objectives of time series analysis are to determine the statistical characteristics of the original variable by manipulating the series of numerically obtained discrete numbers describing its behaviour. The obvious method is to estimate the appropriate correlation function and to establish the Fourier transform of it to obtain the required spectrum. The assumptions and approximations involved have been studied in detail elsewhere. This approach is nowadays referred to as 'classical' [4]. The fast Fourier transform (FFT) is an efficient way of calculating the Fourier transform of a time series, it being quicker and more accurate than the 'classical' approach.

The objective in this chapter is to obtain the frequency composition of the time series (i.e. time histories found in the previous chapter). The amplitude of oscillations (relating to either the lubricant response or the displacement of the elastic member) is considered to be made up of the contributions of the constituent harmonics. An amplitude-forcing frequency plot can be obtained by analysing the time series at each value of forcing frequency and establishing the amplitude contribution to the

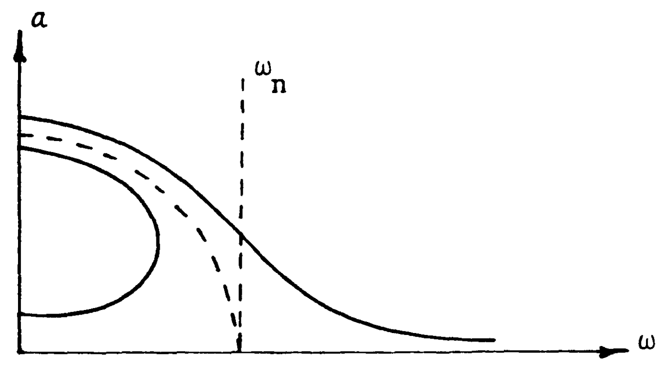

(a) Softening spring

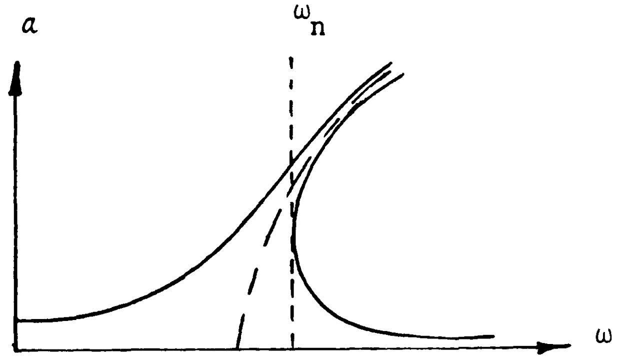

(b) Hardening spring

Fig 5.1 Dynamic characteristics of hardening and softening springs

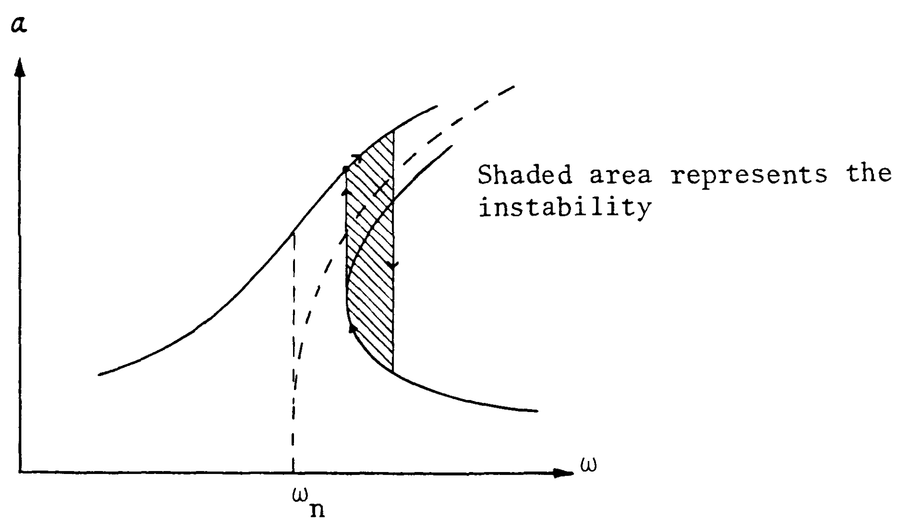

Fig 5.2 Dynamic instability exhibited on an amplitude-frequency plot (hardening spring)

overall response at this frequency (i.e. the contribution of the in-phase harmonic). The classical method applied to this problem is tedious, mainly due to the large number of time intervals that the model has to be used for, at various forcing frequencies, and the resulting large 'time series' which need to be analysed for spectral composition. Therefore, FFT lends itself favourably to a quicker analysis of this problem.

5.2 THE FAST FOURIER TRANSFORM

The displacement history of the elastic member (i.e. $z(t)$) was numerically obtained in the previous chapter at regularly spaced time intervals for any given forcing frequency. The sampling interval is dt and the discrete value of $z(t)$ at time $t = i\,dt$ is denoted by z_r. The sequence $\{z_r\}$, $r = 0, 1, 2, 3, \ldots, N-1$ is referred to as a 'discrete time series'. The 'discrete Fourier transform' (DFT) of the finite sequence $\{z_r\}$ is a new finite sequence $\{z_K\}$ and using the complex notation, it is defined as [3]:

$$z_K = \frac{1}{N} \sum_{r=0}^{N-1} z_r \, e^{-j(2\pi K r/N)} \qquad (5.1)$$

where $K = 0, 1, 2, 3, \ldots, N-1$. If the values of z_K are to be worked out by a direct approach, N multiplications of the form $z_r \, e^{-j(2\pi K r/N)}$ are required for each of the N values of z_K. Therefore, the total work of calculating the full sequence $\{z_K\}$ would require N^2 multiplications. However, the FFT works by partitioning the full sequence $\{z_K\}$ into a number of shorter sequences. Instead of calculating the DFT of the original sequence, only the DFT's of these shorter sequences are worked out. The FFT then combines these together to yield the full DFT of the sequence $\{z_r\}$. A considerable time-saving in the number of multiplications results which reduces the computer time allocation enormously and increases the accuracy by reducing the errors caused due to the truncation of products.

If N is an even number, the sequence $\{z_n\}$ is partitioned into two shorter sequences, $\{x_n\}$ and $\{y_n\}$, where:

$$\begin{aligned} x_n &= z_{2n+1} \\ y_n &= z_{2n} \\ n &= 0,\ 1,\ 2,\ 3,\ \ldots,\ (N/2)-1 \end{aligned} \tag{5.2}$$

The DFT's of these two shorter sequences are X_K and Y_K, where:

$$\begin{aligned} X_K &= \frac{1}{(N/2)} \sum_{n=0}^{(N/2)-1} x_n \, e^{-2j\pi Kn/(N/2)} \ ; \\ Y_K &= \frac{1}{(N/2)} \sum_{n=0}^{(N/2)-1} y_n \, e^{-2j\pi Kn/(N/2)} \ ; \\ K &= 0,\ 1,\ 2,\ 3,\ \ldots,\ (N/2)-1 \end{aligned} \tag{5.3}$$

The DFT of the original sequence $\{z_n\}$ can be obtained in terms of X_K and Y_K [3]:

$$z_K = \tfrac{1}{2}\{Y_K + X_K \, e^{-j(2\pi Kn/N)}\} \tag{5.4}$$

If the original number of samples, N, in the sequence $\{z_n\}$ is a power of 2, then the half sequences $\{x_n\}$ and $\{y_n\}$ may themselves be partitioned into quarter-sequences and so on, until each of the last sub-sequences contains a solitary term. The so-called computational 'butterfly' is thus obtained [3]:

$$z_K = \tfrac{1}{2}\{y_K + V^K x_K\}$$

$$z_{K+(N/2)} = \tfrac{1}{2}\{y_K - V^K x_K\} \tag{5.5}$$

$$K = 0,\ 1,\ 2,\ 3,\ \ldots,\ (N/2)-1$$

where the new complex variable, V, is:

$$V = e^{-j(2\pi/N)} \tag{5.6}$$

5.3 EHD spectral composition and discussions

The 'time histories' of the rolling element centre-line movement $Z(t)$ and the corresponding oil film oscillations $S(t)$ are investigated by the application of FFT. The system is non-linear in nature and a given applied forcing frequency excites a number of its response modes. The aim of this investigation is to analyse the frequency composition of the overall response up to a frequency of 1000HZ. Therefore, the amplitude contribution of each mode and its significance can be found. This process is somewhat laborious requiring a large number of samples to be investigated at various forcing frequencies. In practice, structures are often excited with "White Noise' containing many input frequencies. Therefore, it is argued technically that all the modes of vibration of the structure are excited. The analysis of the resulting 'time series' would reveal the amplitude contribution of each mode within an overall frequency envelope. The largest amplitude or range of amplitudes correspond to the input frequency or a bandwidth of frequencies where the most active and damaging modes of vibration are excited. However, numerical generation of a white noise function is impossible and either a step or a Dirac function may be employed to obtain the main part of the response envelope. Figure 5.3 illustrates the frequency composition of the centre-line movement under the point contact condition when subjected to either a Dirac or a step forcing function. The break up of the overall response amplitude to its constituent modal contributions indicate that the largest amplitude is at 135HZ (i.e. the Fundamental mode) with a small spike at 270HZ (i.e. the first harmonic). The spike at 270HZ is significant as it confirms the non-linear nature of the response.

To examine the oil film response characteristics a series of 'time histories' (for a line contact condition) are obtained where U = 1.3 m/sec and a sinusoidal forcing function of fixed magnitude with various forcing frequency, f (as in Chapter 4) is applied. At f = 50HZ (see fig 5.4) the fundamental mode contains the largest amplitude. There are small but significant contributions at the first and second harmonics (i.e., 100 and 150HZ). The same characteristics are observed at an input frequency 150HZ (see figure 5.5). When f = 250HZ the higher harmonics' contribution are negligible and instead there is considerable sub-harmonic response at f = 125HZ. Nevertheless, the largest amplitude still appears at the in-phase fundamental amplitude. At higher frequencies (i.e. f = 800HZ) the disturbing force excites a large motion at a frequency lower than or at a submultiple of the applied frequency (see Fig 5.7).

In general the findings of Chapter 4 are reinforced by this analysis. The lubricant filters out the higher input frequencies but the effect of the sub-harmonic vibrations are transmitted through to bear upon the adjacent elastic member. At lower forcing frequencies fundamental's effect is most damaging and its higher harmonics' contributions are significantly reduced by the lubricant's filtering effect.

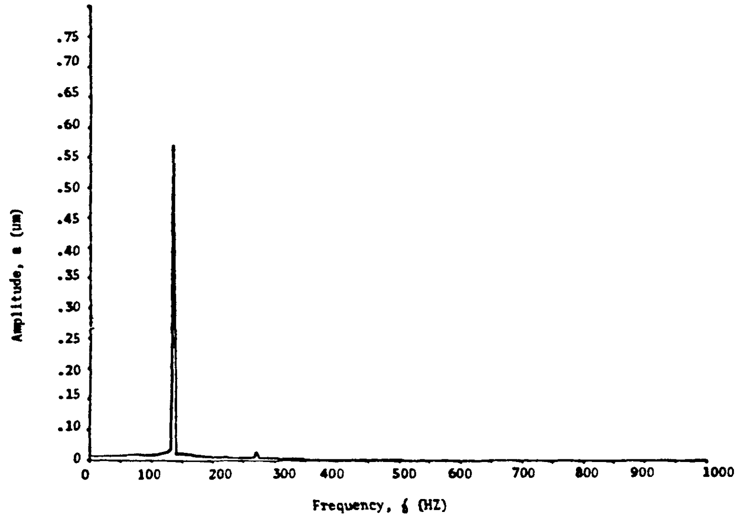

Fig 5.3 Frequency composition of centre-line oscillations

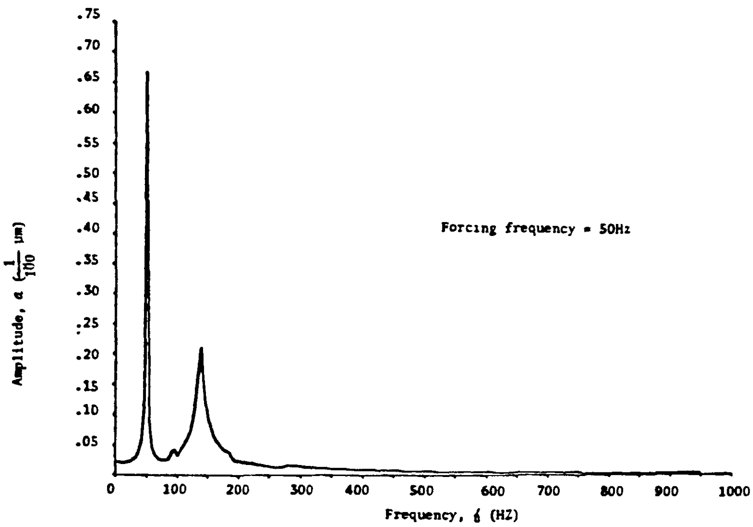

Fig 5.4 Oil film spectral composition

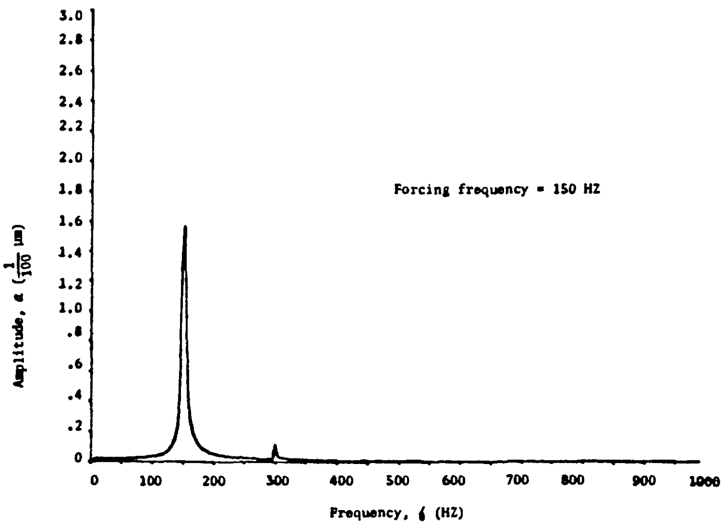

Fig 5.5 Oil film spectral composition

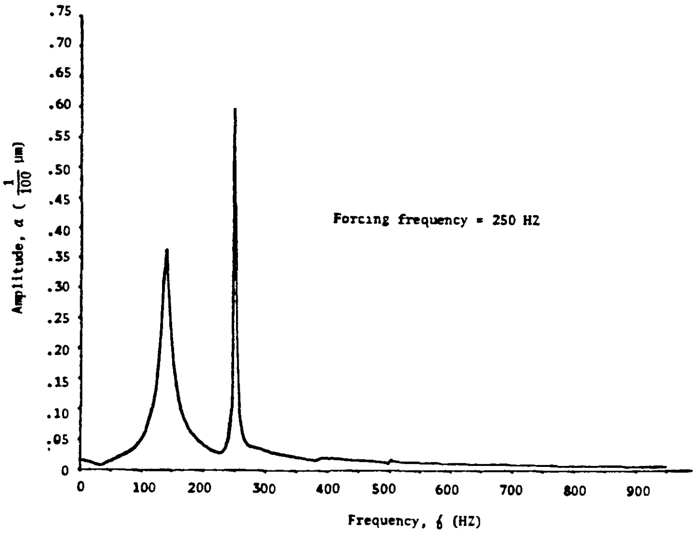

Fig 5 6 Oil film spectral composition

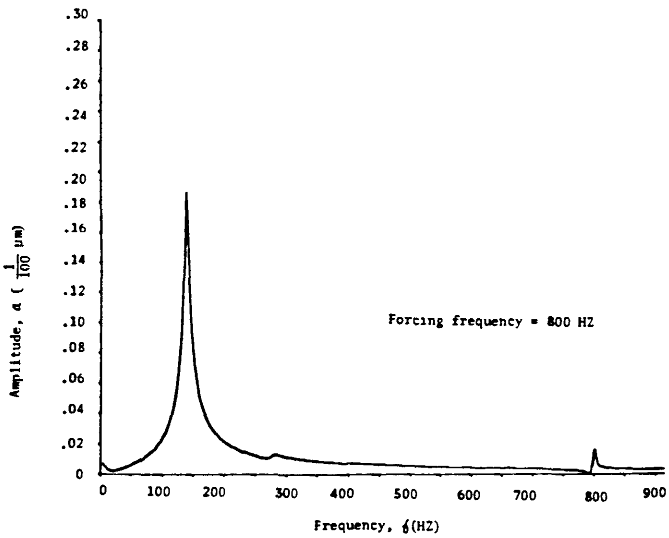

Fig 5.7 Oil film spectral composition

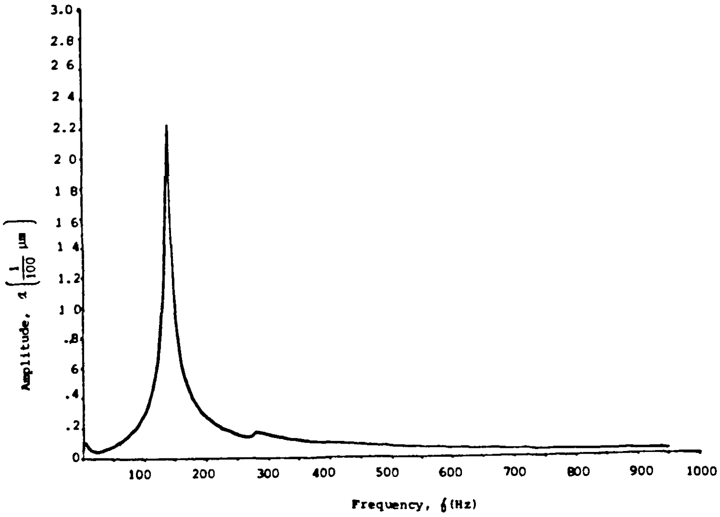

Fig 5 8 Oil film frequency envelope given a step input forcing function

These findings confirm the damper nature of the lubricant reaction at higher excitation frequencies and the analogy of the wheel-tyre axle assembly outlined in section 4.12. Furthermore, when either a Dirac or a step forcing function is used the response frequency envelope indicates much greater amplitude contributions at lower frequencies with the maximum at 150HZ (i.e., line contact resonating peak) (see figure 5.8). The line contact equation shows both greater damping and stiffer properties than that of the point contact.

5.4 References

[1] THOMSON, W.T.,
"Vibration theory and application",
George Allen and Unwin Ltd, 1976

[2] DUFFING, G.,
"Erzwungene Schwingungen bei Veränderlicher Eigenfrequenz",
F. Vieweg U. Sohn, 1918.

[3] NEWLAND, D.E.
"An introduction to random vibration and spectral analysis",
Longman Group Ltd, 1975.

[4] JENKINS, G.M., and WATTS, D.G.,
"Spectral analysis and its applications",
Holden-Day, San Francisco, 1968.

CHAPTER 6

ELASTIC VIBRATION OF BEARINGS

6.1 INTRODUCTION

It is of practical interest to establish an appropriate mathematical model for a shaft and bearing assembly. Such a model can be useful for a study of system vibrational problems.

The vibration of a bearing system is often due to geometrical inaccuracies caused in manufacture (like out-of-round), or damage to the bearing when in use. Even perfect bearings suffer vibration as a result of the applied radial loads, because the rolling elements undergo varying deflection in their orbital paths. The problem is further complicated because of rolling element contact spring non-linearity and that generally they are out-of-round and have wavy surfaces. In addition, the radial loading can be oscillatory, leading to excitation of the whole shaft/ bearing assembly.

Unfortunately, little or no research has been directed to a proper study of the bearing vibration, especially when lubricated contacts occur. Some work, however, has been carried out by various authors, notably of Russian origin [1,2], in the field of elastic vibration of bearings. Here, again, the damping behaviour of the contact is assumed to be hysteric due to the elastic bodies in the dry contact [1]. The characteristics of the shaft and housing have been widely and reliably researched and mathematical models established. The bearing characteristics, however, are much more difficult to predict. Nevertheless, the dearth of information on bearings is bridged by some experimental work. Elserman, et al. [3] examined taper roller bearings and pointed out that the damping due to tilting of the bearing could be more significant than the damping caused by radial motion. Honrath [4] also examined damping in the radial direction and found that it was significant, although he did not compute any physical values.

Walford and Stone [5] measured experimentally the dynamic radial stiffness of a pair of angular contact ball bearings under rotating conditions. They also assumed a simple model to represent their experimental rig (see Figure 6.1). The value of the bearing stiffness K is given by the ratio $-m_s \ddot{u}_s / u_r$, where $u_r = u_s - u_h$ (see Notation), and for steady-state sinusoidal excitation $\ddot{u}_r = -\omega^2 u_r$. Consideration of deflections and forces at every ball position under the conditions found in the experiments yielded an incremental stiffness of about 0.7 GN/m compared with 0.12 GN/m from the practical tests. The difference was argued to be due to the additional series stiffnesses at the interfaces between the races and the shaft and housing, respectively. If a coherent lubricant film was formed under their experimental conditions, its stiffness in series may be neglected since it was subjected to considerably smaller displacements. However, the effective stiffness of the bearing is dependent on a large number of factors, including some dynamic parameters, such as frequency of forced vibration, instantaneous applied radial load and the shaft rotational speed.† The stiffness characteristics of a linear model, as investigated by Matsubara [6] and in reference [5], are hardly affected by such dynamic parameters. A more realistic model is also suggested by Matsubara [6], where the Hertzian load-deflection behaviour of a ball bearing system without lubricant is approximated by a piece-wise linear fit (see Figure 6.2).

The magnitude of mechanical vibration and noise generated within machinery is influenced by damping. Vibration damping may occur externally through the supports and frame, or internally between the mating surfaces [1] (i.e. material hysteresis), fluid film friction or dry friction. Little is known of the amount of contribution of each of these phenomena.

---

†in unbalanced systems

Dareing and Johnson [7] used a disc machine to investigate the significance of lubricant film damping contribution . The details of the disc machine employed is provided by Carson and Johnson [8]. The source of excitation was a corrugated surface provided on one of the mating discs. Figure 6.3 illustrates a model of the equipment by a spring-mass system. The simplified model in reference [7] is shown in Figure 6.4. The contact surface non-linear spring follows the Hertzian load-deflection characteristics. The fluid film damping is simulated by a viscous damping model. The non-linear damping behaviour of the oil film cannot reasonably be approximated by linear damping characteristics, particularly under elastohydrodynamic conditions. The corrugations excited the spring-mass system in transverse motion as the discs rotated. The vibratory motion had a frequency of 120 cycles per revolution and was measured by an accelerometer and an analogue computer, ultimately providing the displacement history. The procedure was repeated both under dry and lubricated conditions. Various rotational speeds were employed to allow displacement amplitudes to be obtained for a range of frequencies. For a given contact load, the response characteristics of dry and lubricated contacts could be compared. It was concluded that lubrication film damping contributes significantly to the total damping of the system. Furthermore, the results indicated that at higher loads, the surface separation was slight or non-existent and the fluid damping was not as great. In fact, the fluid film damping was found to be more effective under conditions of severe vibration when surface separation is more apt to occur. These findings conform closely to the conclusions arrived at in Chapter 4, where an extremely non-linear model is used to represent two normally loaded rolling discs. The squeeze effect damping is shown to be very sensitive to the value of applied forcing frequency and remarkably passive to any increase in magnitude of loading.

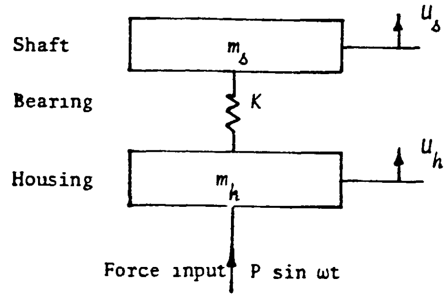

Fig 6.1 The simple model of reference [5]

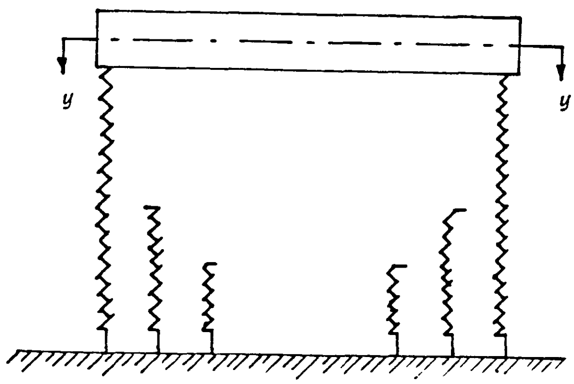

Fig 6.2 Piece wise linear model[ref 6]

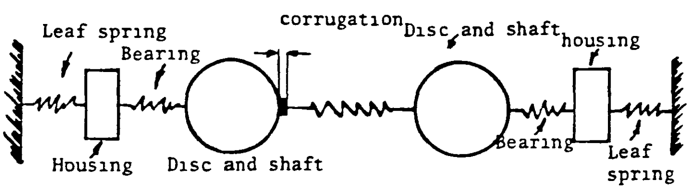

Fig 6.3 Equipment model [ref 7]

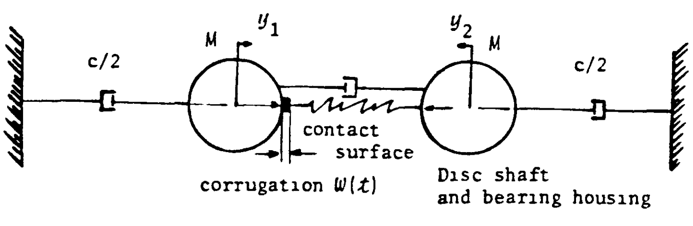

Fig 6.4 Simplified model [ref 7]

Gupta [9] presented the roller motion in cylindrical roller bearings in terms of the classical differential equations of motion. The roller/cage and race/cage interactions were simulated by either a metallic contact or some simple hydrodynamic treatment within the present framework of the theory of hydrodynamic lubrication. The switchover point from a hydrodynamic to a dry contact was defined by a critical film thickness. The motion was considered in two parts; one relating to the motion of the roller mass centre in an inertial frame of reference, and the other corresponding to the angular motion of the roller mass centre in a roller fixed coordinate frame. This formulation presented six degrees of freedom and could treat roller skew and other undesirable motions. The normal contact force was determined primarily by locating the geometric centre of the roller with respect to the interacting surface of the race, therefore resulting in the computation of the elastic deflection at the contact point. Knowing the deflection, the normal contact load was determined by either a Palmgren [10] or Lundberg [11] type of load-deflection relation for a line contact. The problem with the model is that it assumes no real form of damping since it only uses the conventional "long" or "short" bearing approximations for hydrodynamic reactions subjected only to pure induced entraining motion. The conclusions were presented in an accompanying article [12], mainly relating to the effects of roller misalignment. Gupta [12] argued that misalignment leads to roller skewing and, hence, careful consideration of roller/race clearance would be necessary in order to prevent excessive flange collisions. With a particular roller/flange clearance, skewing oscillations of the roller could be allowed. Elastohydrodynamic traction models were considered in determining the roller/race tractive forces and moments. The same author provided a similar model for the dynamic behaviour of a ball bearing system [13] and presented his findings in another accompanying article [14].

The present work primarily assumes a non-linear elastic model to represent a ball bearing system supporting a non-bending vibrating shaft. A two degrees of freedom system will be considered when subjected to radial loads. Furthermore, the model is expanded to include the effect of squeeze film damping present under elastohydrodynamic conditions (see Chapter 7).

6.2 NON-LINEAR ELASTIC MODEL

An angular radial ball bearing system is represented by an elastic model (see Figure 6.5). The total stiffness in the radial direction of each ball due to its interactions with the races is simulated by a non-linear rolling contact spring. The total restoring force at the point of contact of the ith rolling element with the inner and outer raceways, according to Hertz's [15] theory, is expressed as:

$$W_i = K\,\delta_i^{\,n} \tag{6.1}$$

where δ_i is the local deformation (i.e. mutual convergence of rings) in the direction of the ith rolling element, and K is the coefficient of proportionality. The projection of this restoring force on the line of action of the applied radial load on the bearing is (see Figure 6.6):

$$W_{x_i} = K\,\delta_i^{\,n}\cos\theta_i \tag{6.2}$$

and the projection of the load in the lateral direction is:

$$W_{y_i} = K\,\delta_i^{\,n}\sin\theta_i \tag{6.3}$$

where $\theta_i = \phi + i\gamma$ and is the angle between the lines of action of radial load and the radius passing through the geometric centre of the ith rolling element

$\phi = \omega_c t$ is the turning angle of the cage

and γ is the angular distance between the rolling bodies:

$$\gamma = \frac{2\pi}{m} \tag{6.4}$$

where m = the number of rolling bodies in the bearing, and $n = 3/2$ for ball reactions.

6.3 GEOMETRICAL CONSIDERATIONS AND EQUATIONS OF MOTION

If the centreline of the rigid shaft undergoes movements X and Y in a two degrees of freedom motion and the shaft is assumed to be perfectly concentric with the supporting bearing, the mutual convergence of rings (i.e. the total elastic deflection) in the radial direction of the ith rolling element is (see Figure 6.7):

$$2\delta_i = X \cos\theta_i + Y \sin\theta_i + 2\rho \tag{6.5}$$

where ρ is the extent of interference fit employed.

The equations of bearing vibration in two degrees of freedom motion are:

$$M\ddot{x} + \sum_{i=1}^{m} W_i \cos\theta_i = F(t) + Mg \tag{6.6}$$

and:

$$M\ddot{y} + \sum_{i=1}^{m} W_i \sin\theta_i = 0 \tag{6.7}$$

where $F(t)$ is the applied cyclic radial load, and M is the proportion of the mass of the rigid shaft held by one bearing support. It should be

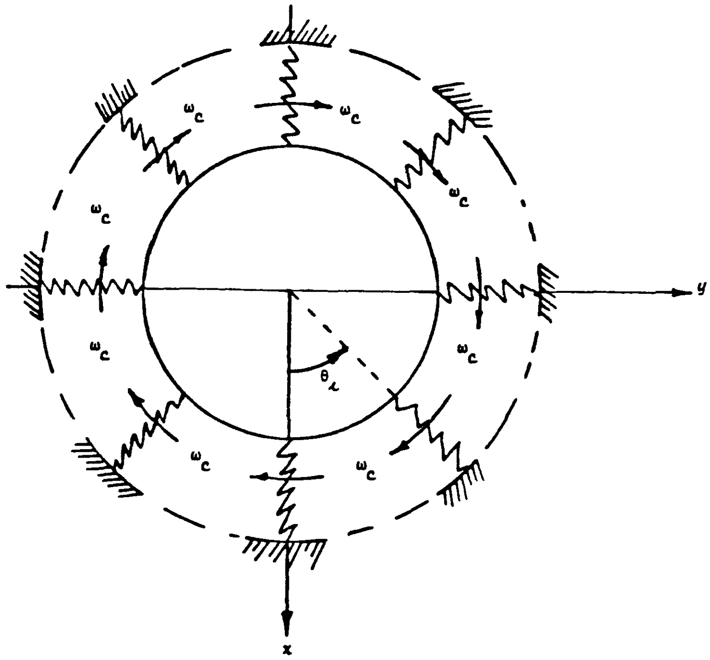

Fig 6.5 Non-linear elastic model

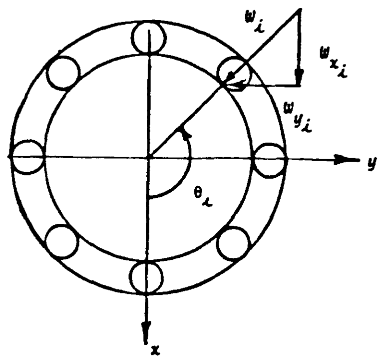

Fig 6.6 Model's restoring force considerations

The shaft is assumed to suffer all the radial deflections

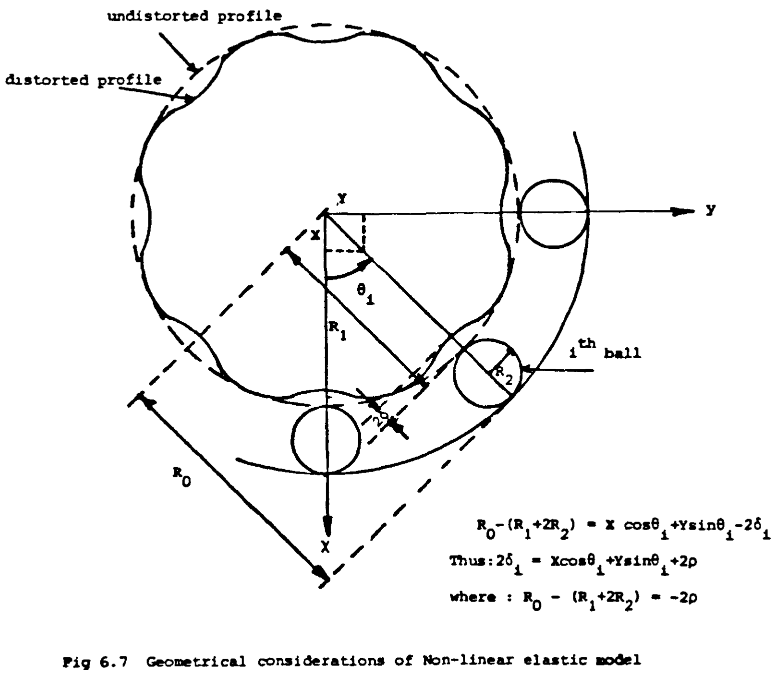

Fig 6.7 Geometrical considerations of Non-linear elastic model

noted that for simplicity, the mass of the rolling balls and the effect of inertia are ignored. If the masses of the rolling bodies are not neglected, the problem becomes one of $m+2$ degrees of freedom motion requiring discretisation of the contributing mass of the shaft in each of these degrees of freedom.

6.4 METHOD OF SOLUTION

The governing equations of motion in two degrees of freedom (i.e. equations (6.6) and (6.7)) are solved by an iterative marching procedure, incorporating the equations (6.1) and (6.5). This procedure employs a third-order quasi-linear method known as the 'average acceleration technique' [16], already described in earlier chapters. For simplicity, manufacturing imperfections of the inner and outer raceways and the rolling bodies are assumed to be negligible. To commence the iterations, it is necessary to establish initial conditions prior to the solution of the forced vibration of the system. Thus:

$$x_0 = y_0 = \dot{x}_0 = \dot{y}_0 = 0 \quad \text{at} \quad t = 0 \tag{6.8}$$

and:

$$2\delta_{0_i} = 2\rho \tag{6.9}$$

where $2\delta_{0_i}$ is the total initial elastic deformation in the radial direction of the ith rolling body caused by interference fitting. When the shaft is released from its pre-held position, its centreline undergoes initial accelerations in the x- and y-directions:

$$M\ddot{x}_0 + \sum_{i=1}^{m} W_{0_i} \cos\theta_{0_i} = Mg \tag{6.10}$$

and:

$$M\ddot{y}_0 + \sum_{i=1}^{m} W_{0_i} \sin\theta_{0_i} = 0 \tag{6.11}$$

where:

$$\theta_{o_i} = i\,\gamma = \frac{2\pi\, i}{m} \qquad \text{for } i = 1 \text{ to } m \tag{6.12}$$

Successive numerical integrations using the acceleration method results in the evaluation of x, $\dot{x}$, y and $\dot{y}$ by applying the initial conditions established:

$$\dot{x}_{1,j} = \dot{x}_o + \ddot{x}_o\, dt \tag{6.13}$$

$$\dot{x}_{2,j} = \dot{x}_o + 2\ddot{x}_o\, dt \tag{6.14}$$

and:

$$\dot{x}_{k,j} = \dot{x}_{k-2} + 2\ddot{x}_{k-1}\, dt \tag{6.15}$$

where k corresponds to the time interval, j is the iteration index, and dt is a fixed interval of time. Then:

$$x_{1,j} = x_o + 2\dot{x}_o \frac{dt}{3} + \ddot{x}_o \frac{dt^2}{6} + \dot{x}_{1,j} \frac{dt}{3} \tag{6.16}$$

$$x_{k,j} = x_{k-1} + 2\dot{x}_{k-1} \frac{dt}{3} + \ddot{x}_{k-1} \frac{dt^2}{6} + \dot{x}_{k,j} \frac{dt}{3} \tag{6.17}$$

Similar numerical integration expressions are used for $\dot{y}$ and y:

$$\dot{y}_{1,j} = \dot{y}_o + \ddot{y}_o\, dt \tag{6.18}$$

$$\dot{y}_{2,j} = \dot{y}_o + 2\ddot{y}_o\, dt \tag{6.19}$$

$$\dot{y}_{k,j} = \dot{y}_{k-2} + 2\ddot{y}_{k-1}\, dt \tag{6.20}$$

and:

$$y_{1,j} = y_o + 2\dot{y}_o \frac{dt}{3} + \ddot{y}_o \frac{dt^2}{6} + \dot{y}_{1,j} \frac{dt}{3} \tag{6.21}$$

$$y_{k,j} = y_{k-1} + 2\dot{y}_{k-1}\frac{dt}{3} + \ddot{y}_{k-1}\frac{dt^2}{6} + \dot{y}_{k.j}\frac{dt}{3} \tag{6.22}$$

The equation (6.5) is rearranged to calculate the values of δ_i for $i = 1$ to m at every ball position:

$$\delta_i = \tfrac{1}{2}\{x \cos \theta_i + y \sin \theta_i + 2\rho\} \tag{6.23}$$

The instantaneous contact reactions are obtained for each rolling body using equation (6.1) and the dynamic equations of motion (6.6) and (6.7) yield the acceleration of the centre of the rigid shaft in the x- and y-directions. The procedure is repeated over and over again within each suitably selected time step until the variables, such as $x = x(t)$, $y = y(t)$, etc., are calculated within a certain specified limit:

$$x_{k,j} - x_{k,j-1} \leqslant \varepsilon_x \tag{6.24}$$

$$y_{k,j} - y_{k,j-1} \leqslant \varepsilon_y \tag{6.25}$$

where ε_x and ε_y are the specified limits of accuracy.

It should be noted that two bodies in contact cannot exert tensile forces upon each other. Therefore, care is taken to ensure that no reactions constituting state of tension is generated within the computer procedure.

Prior to the use of the model, it is important to check the validity of the numerical method. The elastic model can be adopted for a system of shaft being supported by a number of linear rotating springs (see Figure 6.8). The power index of the load-deflection relation (i.e. n in equation (6.1)) may be equated to unity. The stiffness of the springs can be selected in such a way as to nearly describe the equivalent stiffness of a similar number of rolling elements within a certain range of ball deflections (see Figure 6.9). For a particular number of linear springs, the accuracy of the numerical results can be verified against the exact solution obtained analytically.

6.5 LINEAR ELASTIC MODEL

Let the number of springs be 4 (i.e. $m = 4$). The equations of motion for these rotating springs supporting a rigid shaft of mass M are:

$$M \ddot{x} + K \sum_{i=1}^{4} (x \cos \theta_i + y \sin \theta_i + 2\rho) \cos \theta_i = M g \tag{6.26}$$

$$M \ddot{y} + K \sum_{i=1}^{4} (x \cos \theta_i + y \sin \theta_i + 2\rho) \sin \theta_i = 0 \tag{6.27}$$

where ρ is defined as the radial deflection due to initial pre-tensioning. To solve the equations of motion, the trigonometric terms are first calculated:

$$\sum_{i=1}^{4} \cos^2 \theta_i = 2 \quad , \quad \sum_{i=1}^{4} \sin^2 \theta_i = 2$$
$$\sum_{i=1}^{4} \sin \theta_i \cos \theta_i = 0 \tag{6.28}$$

Therefore, the simplified equations of motion in two degrees of freedom motion are:

$$M \ddot{x} + 2K x = M g \tag{6.29}$$

$$M \ddot{y} + 2K y = 0 \tag{6.30}$$

The above equations can be generalised to include any number of rotating springs. Therefore:

$$M\ddot{x} + \frac{m}{2} K x = M g \tag{6.31}$$

$$M\ddot{y} + \frac{m}{2} K y = 0 \tag{6.32}$$

It can be observed that the motion of the system in the x- and y-directions are independent of the angular speed of the shaft. Furthermore, the linear relationship between the load and deflection results in constant effective stiffness throughout the cyclic rotation of the supporting system.

6.6 ANALYTICAL SOLUTION

Assuming 4 springs in static equilibrium, being pre-tensioned as shown in Figure 6.10, where Δ is the static deflection due to the mass of the shaft. T represents the pre-tension prior to releasing the shaft. Therefore:

$$M g = 2K \Delta \tag{6.33}$$

The dynamic displacement in the loaded direction is denoted by $x(t)$ and the oscillations in the transverse mode is represented by $y(t)$. $y(t)$ under this loading condition is virtually negligible. Thus:

$$M\ddot{x} + 2K(x - \Delta) = 0 \tag{6.34}$$

or:

$$M\ddot{x} + 2K x = 2K\Delta = M g \tag{6.35}$$

The particular integral solution is:

$$x_{PI} = \frac{M g}{2K} \tag{6.36}$$

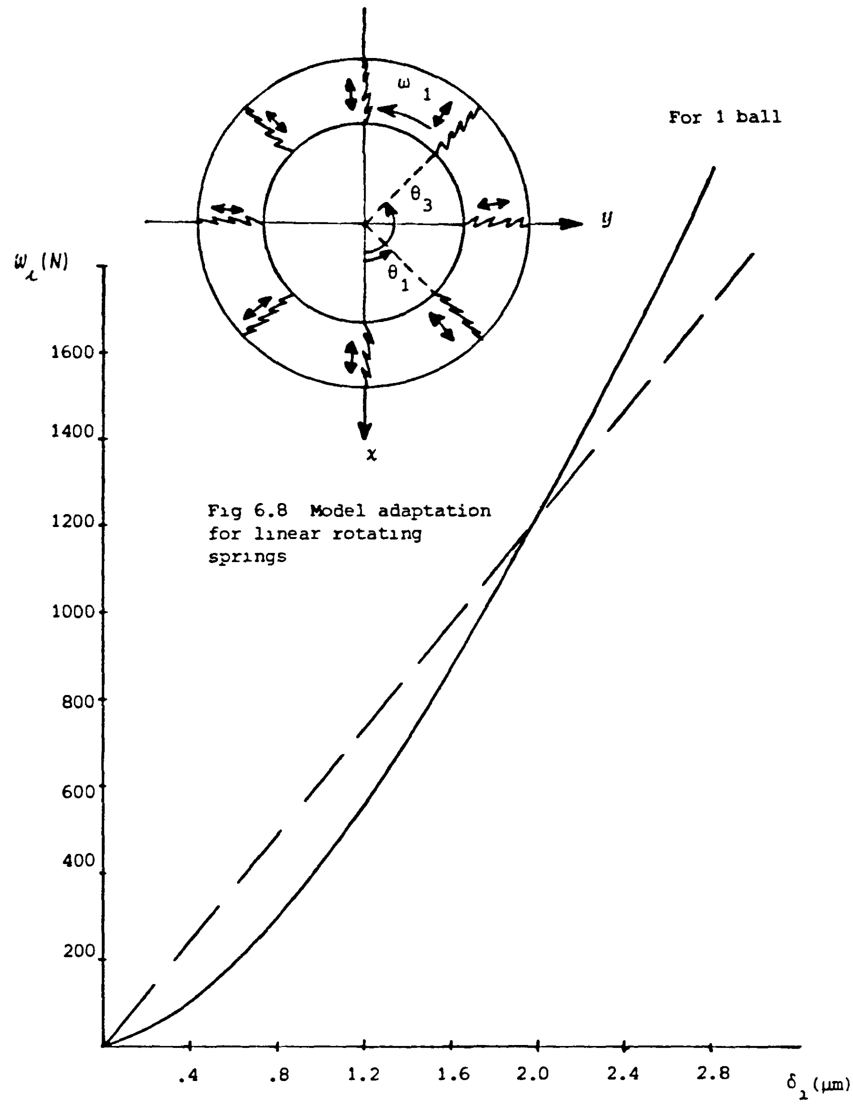

Fig 6.8 Model adaptation for linear rotating springs

Fig 6.9 Load versus deflection graph for a ball

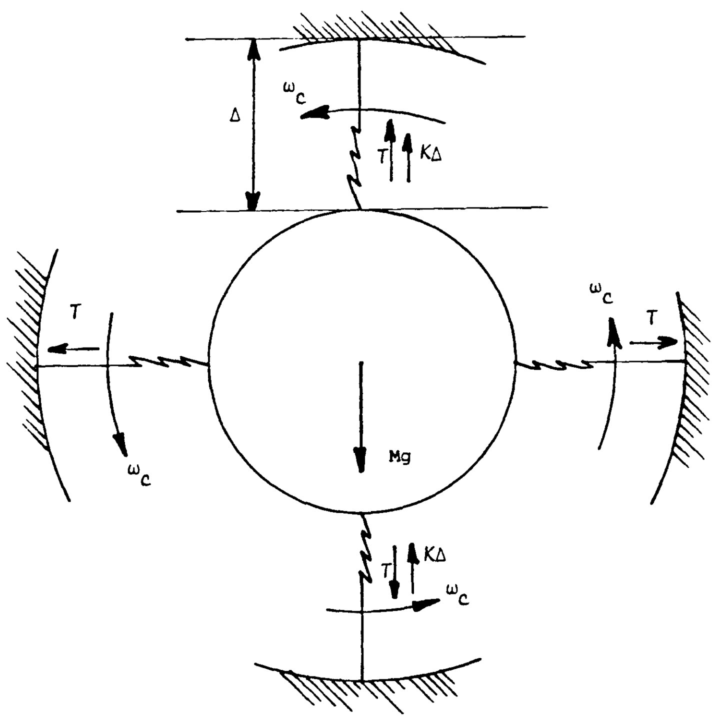

Fig 6.10 Four rotating pre-tensioned spring model

and the complementary function is:

$$x_{CF} = A \cos \Omega t + B \sin \Omega t \tag{6.37}$$

The general solution is:

$$x = x_{PI} + x_{CF} \tag{6.38}$$

and using the initial conditions:

$$x_0 = \dot{x}_0 = 0 \quad \text{at} \quad t = 0 \tag{6.39}$$

it yields: $$A = -\frac{M\,g}{2K} \quad \text{and} \quad B = 0 \tag{6.40}$$

Thus, the complete solution is obtained:

$$x(t) = \frac{M\,g}{2K}\{1 - \cos \Omega t\} \tag{6.41}$$

and its derivative is:

$$\dot{x}(t) = \frac{M\,g}{2K}\,\Omega \sin \Omega t \tag{6.42}$$

The peak amplitude is: $$\hat{x} = \frac{M\,g}{K} \tag{6.43}$$

The average response is: $$\frac{\hat{x}}{2} = \frac{M\,g}{2K} \tag{6.44}$$

The natural frequency of this undamped system is given by expression (6.45) below:

$$f = \frac{1}{2\pi}\sqrt{2K/M} \tag{6.45}$$

If the effective stiffness of the system $2K=28\,^{MN}/m$ and the bearing is made to support a heavy rigid shaft of 250. kg, the analytical results are listed below:

$$\text{The mass supported by one bearing} = 250 \text{ kg}$$

$$\hat{x} = 175.2\ \mu m \tag{6.46}$$

$$\text{and } \quad f = 53.3 \text{ Hz} = 3195.8 \text{ cpm}$$

6.7 NUMERICAL SOLUTION

The numerical solution as outlined in Section 6.5 (see Figure 6.11) yields the results as below:

$$\hat{x} = 172.5\ \mu m$$

(6.47)

$$\text{and:} \quad f = 53.33 \text{ Hz} = 3200 \text{ cpm}$$

The results obtained by the numerical method are in close agreement with the analytical solution above. The comparison of the respective results indicates small percentage errors:

on peak amplitude = 1.54%

on natural frequency = 0.13125%

The next step in using the numerical model is to design a shaft/bearing system which provides appropriate data for use in the numerical solution.

6.8 DESIGN OF A BALL BEARING SYSTEM

A single row deep-groove ball bearing system (see Figures 6.12 and 6.13) is designed in order that the applied load is endured by pure radial deflection of the balls. The specifications are as follows:

Bore	:	40 mm
Inner race diameter	:	50 mm
Pitch diameter	:	56.3 mm
Outer race diameter	:	75.4 mm
Ball diameter	:	12.7 mm
Outside diameter	:	83.7 mm
Width	:	23.4 mm

Therefore, the number of balls for a tightly packed arrangement is 14, and for a moderately packed selection is 12. The radii of curvature of the races are a design consideration dependent on the contact conformity required. For a 2% contact conformity, the radii of curvature are 6.48 mm. However, 2% conformity leads to a contact ellipticity ratio of 9.75. For a point contact condition, such as that experienced by a ball on an elastic half-space, it is desirable to obtain ellipticity ratio in the region of 3 to 5. It is advisable to adopt a design procedure as described in reference [17], where the combined radial deformation of both bodies is:

$$\delta_{ir} = \lambda \sqrt[3]{\frac{W_i^{\,2}}{K_c^{\,2}\, e}} \tag{6.48}$$

for i = 1 to m, where [17]:

$$e = \frac{4}{(1/R_1) + (1/R_1') + (1/R_2) + (1/R_2')} \tag{6.49}$$

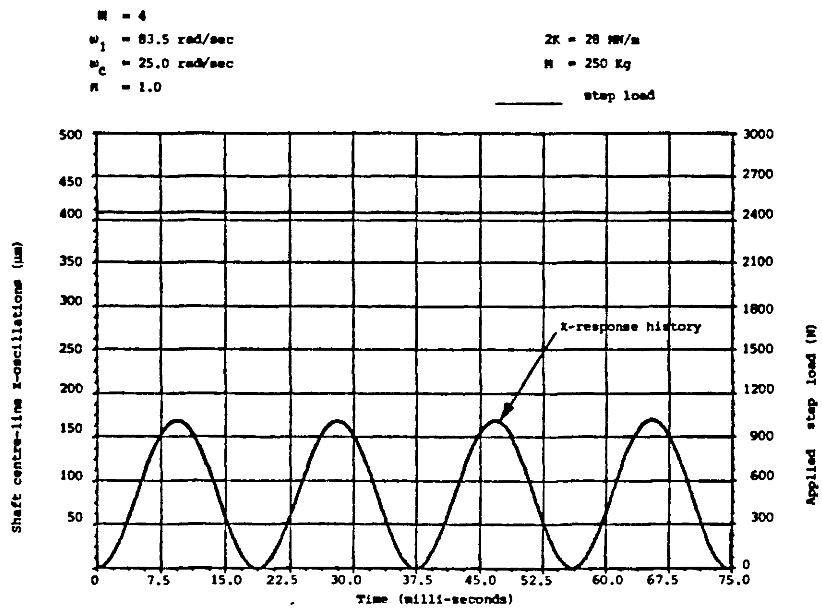

Fig 6.11 Numerically obtained time history of $x(t)$ (4 linear spring model)

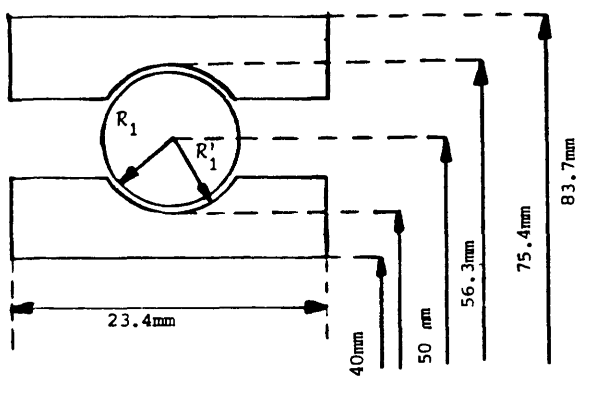

Fig 6.12 A single row deep-groove ball bearing system

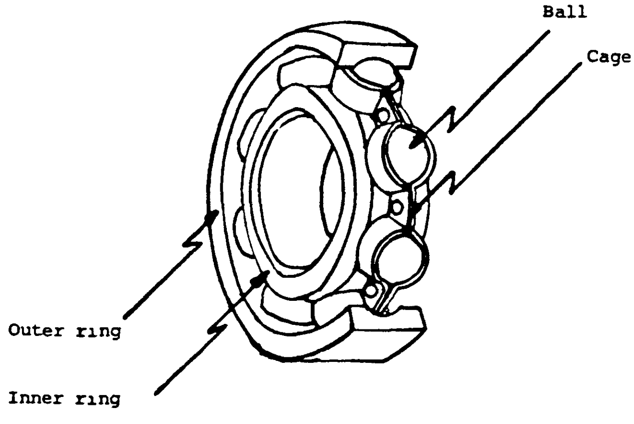

Fig 6.13 A single row deep-groove ball bearing system

R_1 and R_1' are the radii of curvature of the inner and outer raceways, respectively. R_2 and R_2' are the radii of curvature of the rolling body in the respective planes of contact (see Figure 6.14). For a ball, $R_2 = R_2'$. Care must be taken in the implementation of the sign convention for these radii when using equation (6.49). Furthermore, R_1 and R_1', as already described, depend on the desired contact conformity. The constant K_c in equation (6.44) reflects the elastic property of the contact and is given by reference [17] as:

$$K_c = \frac{8}{3} \frac{E_1 \; E_2}{E_2 \; (1 - \nu_1^2) + E_1 \; (1 - \nu_2^2)} \tag{6.50}$$

The contact dimensions per ball can be evaluated when the radial load per ball is found, using:

$$a_i = \alpha \sqrt[3]{\frac{W_i \; e}{K_c}} \tag{6.51}$$

$$b_i = \beta \sqrt[3]{\frac{W_i \; e}{K_c}} \tag{6.52}$$

$$\text{for } i = 1 \text{ to } m$$

where a_i and b_i are the half lengths of the major and minor axes of the elliptical contact area for each ball, respectively. The coefficients α, β and λ can be evaluated from an appropriate table relating the contact condition of the rolling bodies to an angle ψ, as described in reference [18]:

$$\psi = \text{arc} \; \frac{e}{4} \sqrt{\left(\frac{1}{R_1} - \frac{1}{R_1'}\right)^2 + \left(\frac{1}{R_2} - \frac{1}{R_2'}\right)^2 + 2\left(\frac{1}{R_1} - \frac{1}{R_1'}\right)\left(\frac{1}{R_2} - \frac{1}{R_2'}\right) \cos 2\phi} \tag{6.53}$$

where 2ϕ is the contact angle.

The table in reference [18] is provided below:

ψ	0^o	10^o	20^o	30^o	35^o	40^o	45^o	50^o
α	∞	6.612	3.778	2.731	2.397	2.136	1.926	1.754
β	0	0.319	0.408	0.493	0.530	0.567	0.604	0.641
λ	-	0.851	1.220	1.453	1.550	1,637	1.709	1.772

ψ	55^o	60^o	65^o	70^o	75^o	80^o	85^o	90^o
α	1.611	1.486	1.387	1.284	1.202	1.128	1.061	1.00
β	0.678	0.717	0.759	0.802	0.846	0.893	0.944	1.00
λ	1.828	1.875	1.912	1.944	1.967	1.985	1.996	2.00

Figure 6.15 illustrates the variations of α, β and λ with ψ. As it can be seen using equations (6.49), (6.51), (6.52) and (6.53), the essence of this design criterion is the contact conformity desired which establishes the radii of curvature of the raceways (i.e. R_1 and R_1'). For the present design, 7% contact conformity and a contact angle of $2\phi = 90°$ are selected. Thus:

$$\alpha = 1.5 \quad , \quad \beta = 0.5 \quad \text{and} \quad \lambda = 2.5 \tag{6.54}$$

Therefore, using equation (6.48), the relationship between the radial deflection per each rolling contact and the load in the radial direction of each ball is obtained:

$$W_i \doteq 13.509 \times 10^9 \, \delta_{ir}^{3/2} \tag{6.55}$$

The load-deflection constant of proportionality, K, can be obtained by

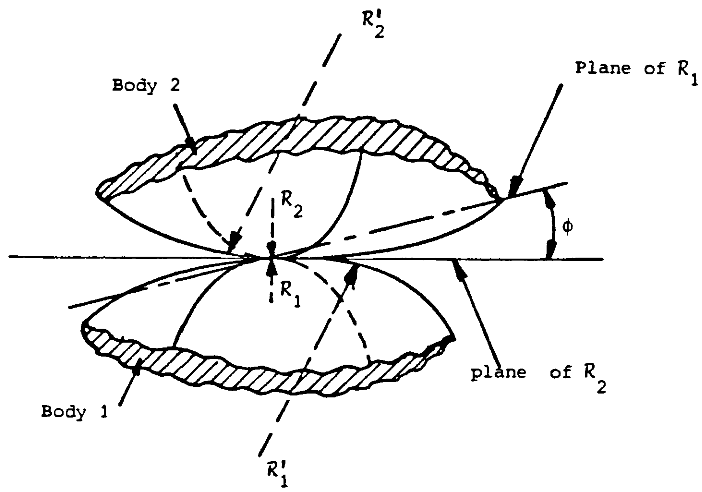

Fig 6.14 General case of two bodies in counterformal contact

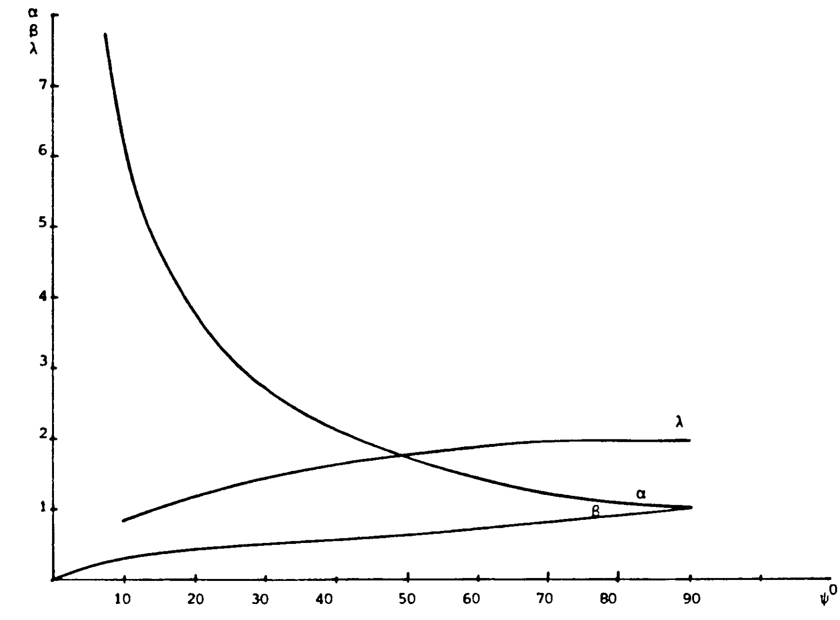

Fig 6.15 Variation of contact properties α β and λ with ψ

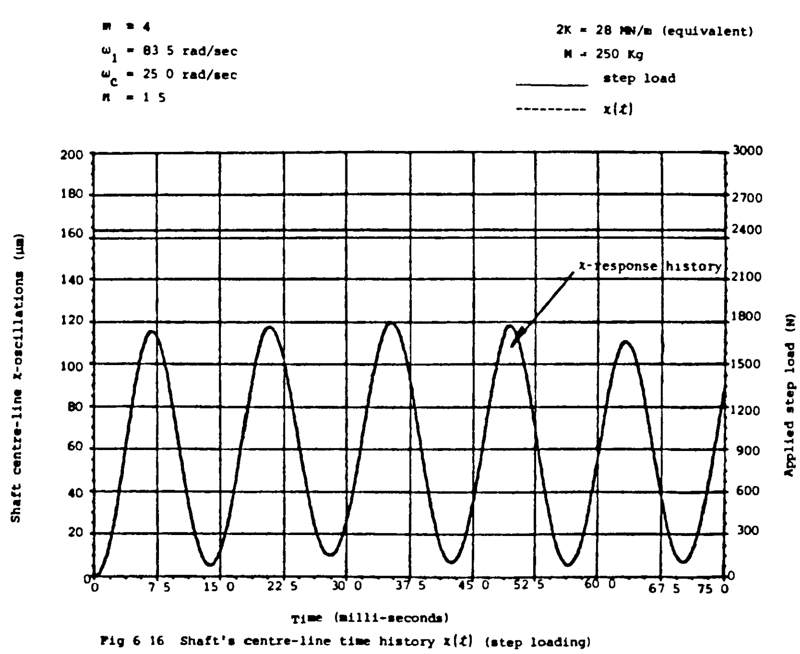

Fig 6 16 Shaft's centre-line time history x(t) (step loading) comparing equation (6.55) with equation (6.1):

$$K = 13.509 \text{ GN/m}^{3/2} \tag{6.56}$$

Also:

$$a_i \doteqdot 0.1157 \, W_i^{1/3} \tag{6.57}$$

$$b_i \doteqdot 0.0384 \, W_i^{1/3} \tag{6.58}$$

The ellipticity ratio, e_p^*, can be obtained for these contact conditions. This value is universal for all the contacts and throughout the cyclic rotation of the rolling bodies:

$$e_p^* = \frac{a_i}{b_i} = 3.0 \qquad \text{for } i = 1 \text{ to } m \tag{6.59}$$

6.9 NUMERICAL RESULTS AND DISCUSSIONS

For a 4 ball bearing system, the response in the direction of loading is illustrated by Figure 6.16. The extent of oscillations in the transverse direction (i.e. y-direction) is virtually negligible. When a ball bearing system replaces linear rolling springs, the maximum amplitude of the shaft oscillations decreases by 32% (see Figures 6.11 and 6.16). The natural frequency of the shaft supported by the non-linear support system is 4102.6 cpm. Therefore, the undamped natural frequency has increased by 22%. The measured response frequency is referred to as undamped since the hysteric damping exerted by the rolling bodies material contact is ignored. The comparisons between the linear and non-linear supporting systems discussed here are realistic since the balls are stiffer than springs, allow smaller oscillations and exhibit higher natural frequencies.

The system response depends on a number of design considerations, and the loading and running conditions:

(a) The contact conformity between the rolling surfaces.

(b) The number of balls.

(c) The magnitude of the load supported (i.e. weight of the heavy rigid shaft).

(d) The frequency of any applied periodic forcing function.

(e) The amount of preload (i.e. interference fitting or clearance between the rolling surfaces).

(f) The shaft's angular speed.

(g) Any eccentric loading or out-of-roundness.

The important response characteristics are:

i) The extent of the shaft's dynamic displacement.

ii) The radial deflections of the rolling balls.

iii) The response frequency and system instability.

First of all, the cage set angular speed, ω_c, is determined in such a way as to eliminate the effect of sliding at the rolling contact points. For a linear rolling speed variation (see Figure 6.17):

$$U_c = \omega_2 r_2 \qquad \text{where} \qquad 2\omega_2 r_2 = \omega_1 r_1 \tag{6.60}$$

and: $$\omega_c = \frac{U_c}{(r_1 + r_2)} = \frac{\omega_1 r_1}{2(r_1 + r_2)} \qquad \text{(see Figure 6.18)} \tag{6.61}$$

The simplest approach is to initially assume a fixed heavy load (e.g. a heavy rigid shaft) to be supported by the bearing. When clearance is

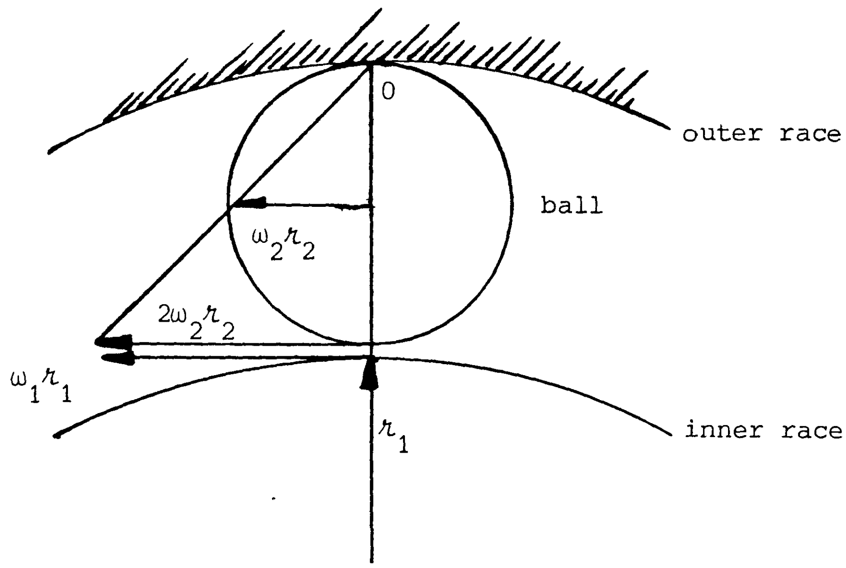

Fig 6.17 Illustration of ball and races angular motions

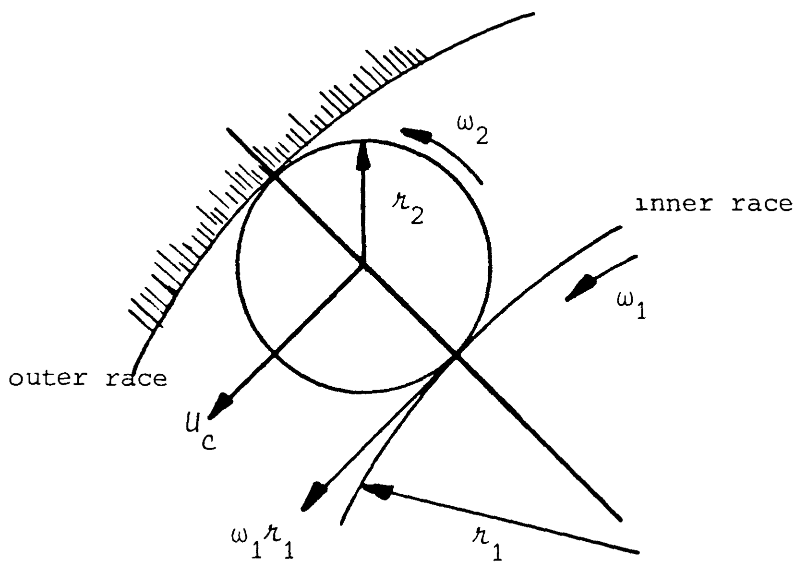

Fig 6.18 Illustration of ball and races angular motions

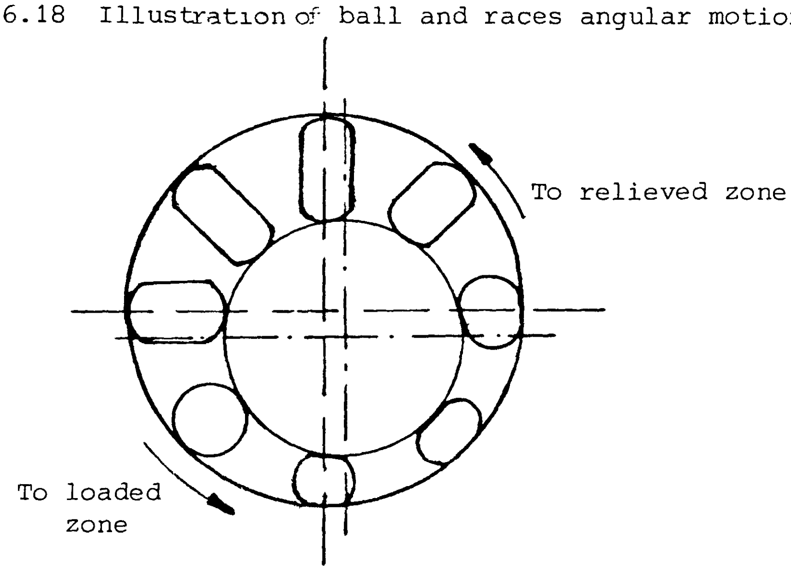

Fig 6.19 Loaded and unloaded regions of the bearing

provided in the region of the rolling interfaces, large dynamic displacements may occur in both degrees of freedom. This undesirable feature can be minimised or eliminated by introducing some degree of interference fitting. The extent of fit can be determined numerically by controlling the mutual separation of the races (i.e. negative deflections generated). The separation of rings corresponds to the relief experienced by the rolling bodies throughout their rotation in the unloaded region of the bearing (see Figure 6.19).

The effective stiffness of the support is dependent on the number of balls employed. Figures 6.20 to 6.24 illustrate the dynamic displacement of the shaft in the loaded radial direction (i.e. x-direction) for different numbers of balls. A comparison between these figures indicates that closer packed arrangements restrict the extent of oscillations more effectively. In addition, the system responds at higher frequencies when a larger number of balls are used. All the results are based upon an interference fit of 3 μm and the shaft angular speed of 62.8 rad/s, supporting a load of 1000 kg. In general, the system response is of a non-linear nature and since the time base as an independent variable appears only as a differential in the governing equations of motion, the system is autonomous. It is then permissible to shift the time origin without influencing the behaviour of the system. This offers the representation of the numerical results by the phase plane analysis [19, 20].

6.10 PHASE PLANE REPRESENTATION

The shaft's dynamic displacement, $x(t)$, is plotted against its derivative $\dot{x}(t)$ at small time intervals of dt. The procedure is repeated for a series of numerical outputs corresponding to a varying number of balls employed (see Figure 6.25). The elliptical shapes represent

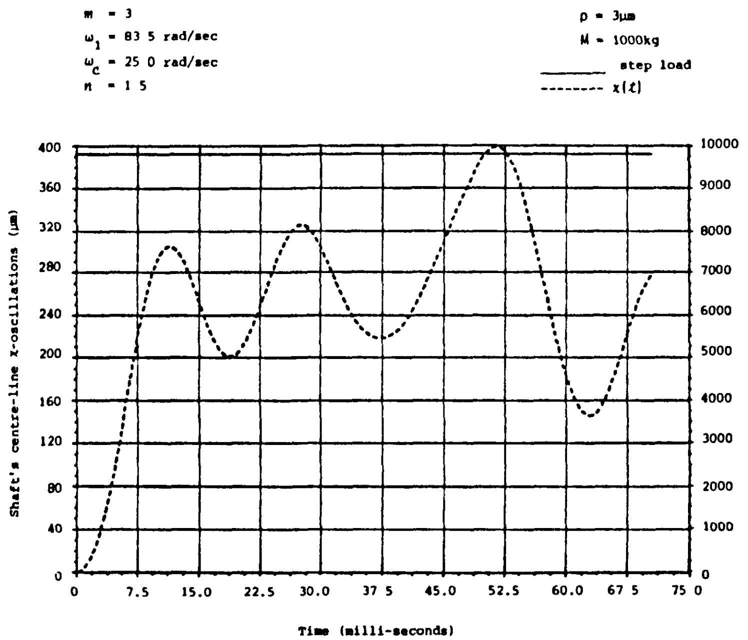

Fig 6 20 Shaft centre-line time history (subjected to step forcing function)

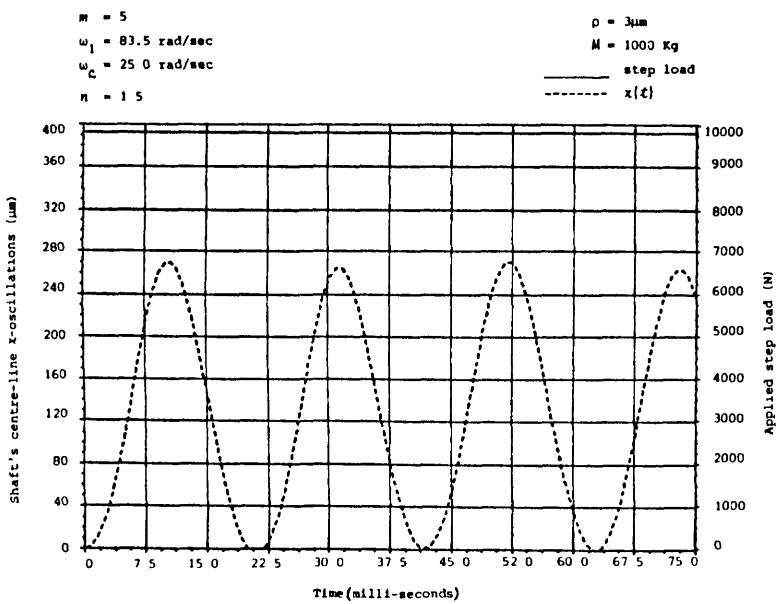

Fig 6 21 Shaft's centre-line time history (subjected to a step forcing function)

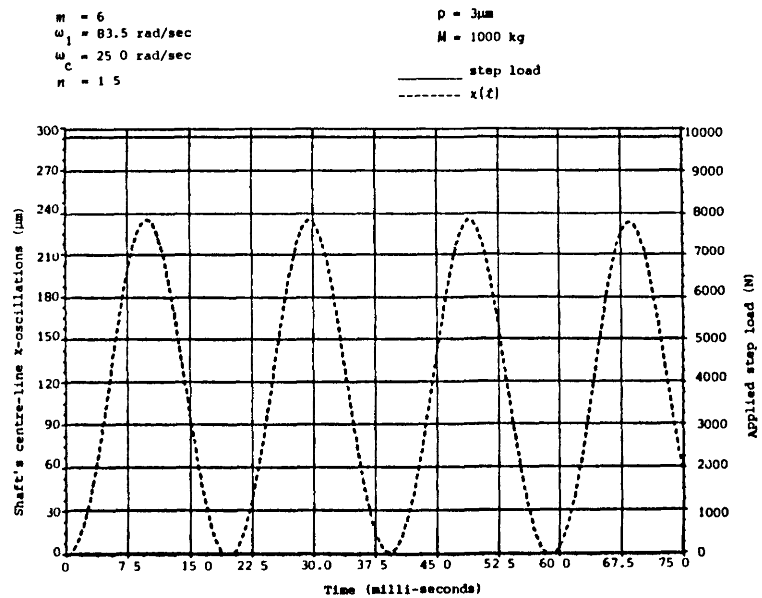

Fig 6.22 Shaft's centre-line time history (subjected to step forcing function)

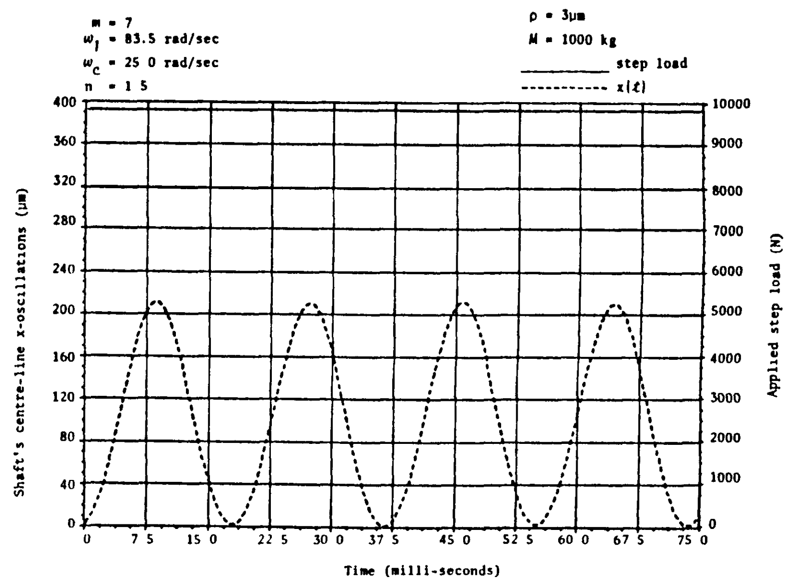

Fig 6 23 Shaft's centre-line time history (subjected to a step forcing function) conservative systems, since when $\dot{x}(t) = 0$ and $F(x(t)) \neq 0$ in the equation $M\ddot{x}(t) = -F(x(t))$ (i.e. equation (6.6)), the slope $d\dot{x}(t)/dx(t) = F(x(t))/\dot{x}(t)$ becomes infinite and the trajectories of the phase plane cross the x-axis at right angles. These phase plane trajectories are symmetrical about the x-axis and the deviation from a circular path trajectory indicates the non-linear behaviour of the response. The response of the bearing system is initiated with x_0 and $\dot{x}_0$, and the oscillations eventually reach a stable amplitude known as the limit cycle. As already illustrated by Figure 6.25, for a different number of balls, there is only one closed trajectory in each case, which is independent of the initial conditions. The initial conditions may be inside or outside the closed trajectory. The limit cycle occurs over one steady-state cycle, indicating that the nett energy input from the excitation is equal to the energy dissipated within the system.

For a periodic undamped motion, such as the example under consideration, the full period of oscillation is obtainable by describing the closed loop once. Thus:

$$T = \oint \frac{dx(t)}{\dot{x}(t)} \tag{6.62}$$

Let $U(x)$ be the potential energy of the system. The energy equation for the conservative system at any instant can be written as:

$$\tfrac{1}{2}\dot{x}^2 + U(x) = constant = E \tag{6.63}$$

where E is the total energy at that instant, and $U(x) = -\int_0^x F(x)\,dx$. For the phase plane trajectories obtained:

$$\frac{\dot{x}^2}{b_1^{\,2}} + \frac{(x - c_1)^2}{a_1^{\,2}} = 1 \tag{6.64}$$

where $2a_1$ is the length of the major axis, $2b_1$ is that corresponding to the minor axis, and c_1 represents the point where:

$$\frac{dU(x)}{dx} = \ddot{x} = 0 \tag{6.65}$$

The bearing possesses varying potential energy levels, dependent both on its number of balls and the instantaneous effective stiffness throughout the cyclic rotation (see Figure 6.25). Therefore, the points corresponding to $dU(x)/dx = \ddot{x} = 0$ are not coincident for the trajectories of Figure 6.25.

Because of the symmetric nature of each trajectory, the period of oscillations, T, can be evaluated in each case using equation (6.66):

$$T = 4 \int_{x=c_1}^{x=x_{max}} \frac{dx(t)}{\dot{x}(t)} \tag{6.66}$$

For an eight ball bearing (referring to Figure 6.25):

$$2a_1 = 2.02 \quad , \quad 2b_1 = 0.7 \quad , \quad c_1 = 1.05$$

Thus: $$\dot{x} \doteqdot 0.35 \quad \{1 - 0.98\ (x - 1.05)^2\}^{\frac{1}{2}} \tag{6.67}$$

Replacing for $\dot{x}$ in equation (6.66) using equation (6.67) and implementing the substitution: $\sin\theta_1 \doteqdot 0.989\,(x - 1.05)$, the full period of oscillations for an eight ball bearing is:

$$T_8 \doteqdot \frac{4}{0.35\ (0.989) \times 10^3} \int_{\theta_1=0}^{1.2514} d\theta_1 \tag{6.68}$$

The factor 10^3 in the denominator is essential in order to compensate for the difference between the scales chosen for the x and $\dot{x}$ axes. Hence,

T_8 = 14.62 milliseconds, which, incidentally, is the time obtained numerically for one complete traverse of the trajectory loop (i.e. the limit cycle). Thus, the undamped response frequency (i.e. the first natural frequency) is: $\Omega_8 = 1/T_8$ = 68.4 Hz. The same procedure is applied to the other trajectories and the results obtained are listed in Table 6.2.

TABLE 6.2

Number of Balls (m)	T_m (ms)	Ω_m (Hz)
5	22.13	45.18
6	17.53	57.00
7	15.49	64.55
8	14.62	68.40
12	9.93	100.93

When a closer packed arrangement is employed, the system dynamic stiffness undergoes smaller rates of change throughout the cyclic rotation of the bearing. The corresponding closed loop trajectory tends to a circular path (i.e. becomes less non-linear) and has a shorter limit cycle.

6.11 EFFECT OF LOADING ON NATURAL FREQUENCY

It is important to note that the bearing may respond with a number of frequencies, depending on a set of governing parameters, one of which being the load it is supporting. The dynamic stiffness is related to the elastic deflections the balls suffer. Taking the case of one ball, the stiffness due to a radial static load of W_i acting upon it is:

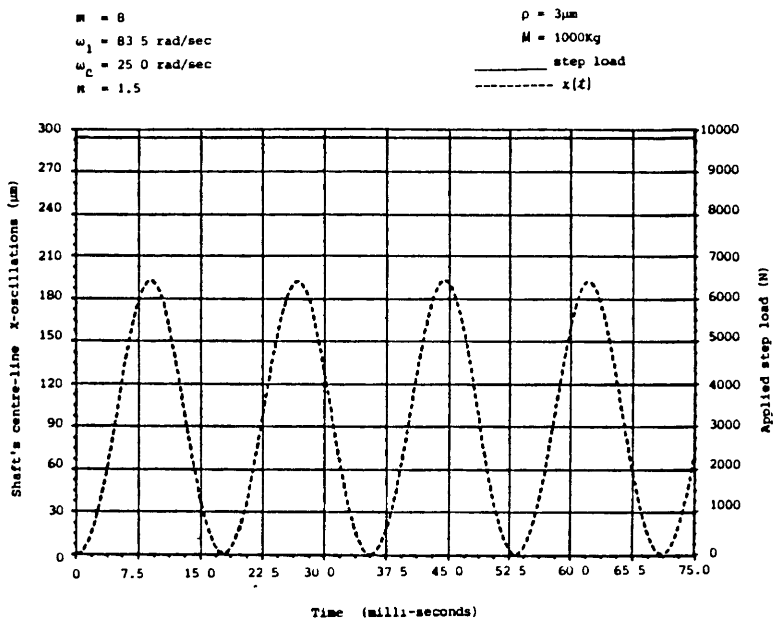

Fig 6 24 Shaft's centre-line history (subjected to step forcing function)

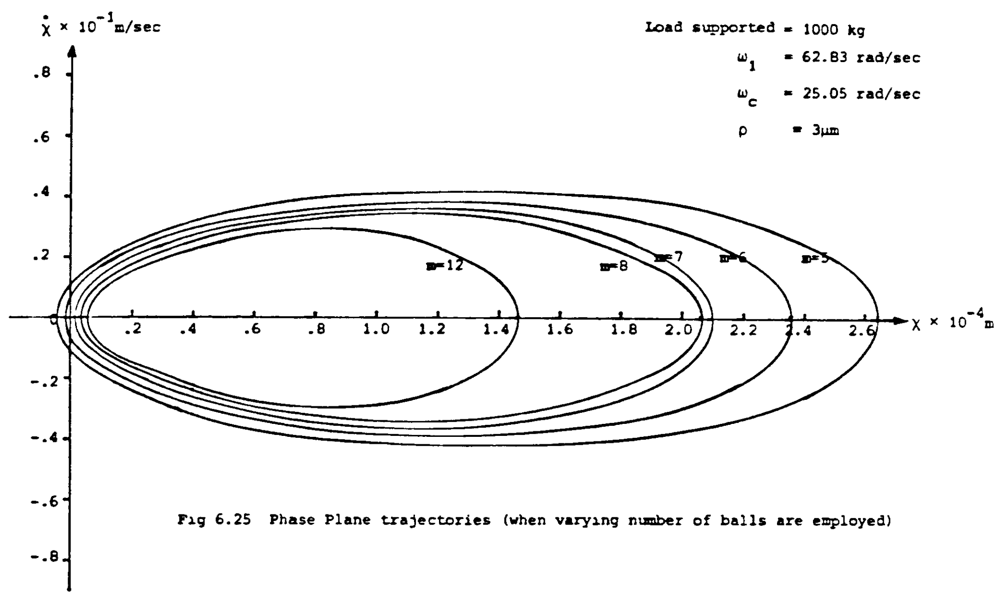

Fig 6.25 Phase Plane trajectories (when varying number of balls are employed)

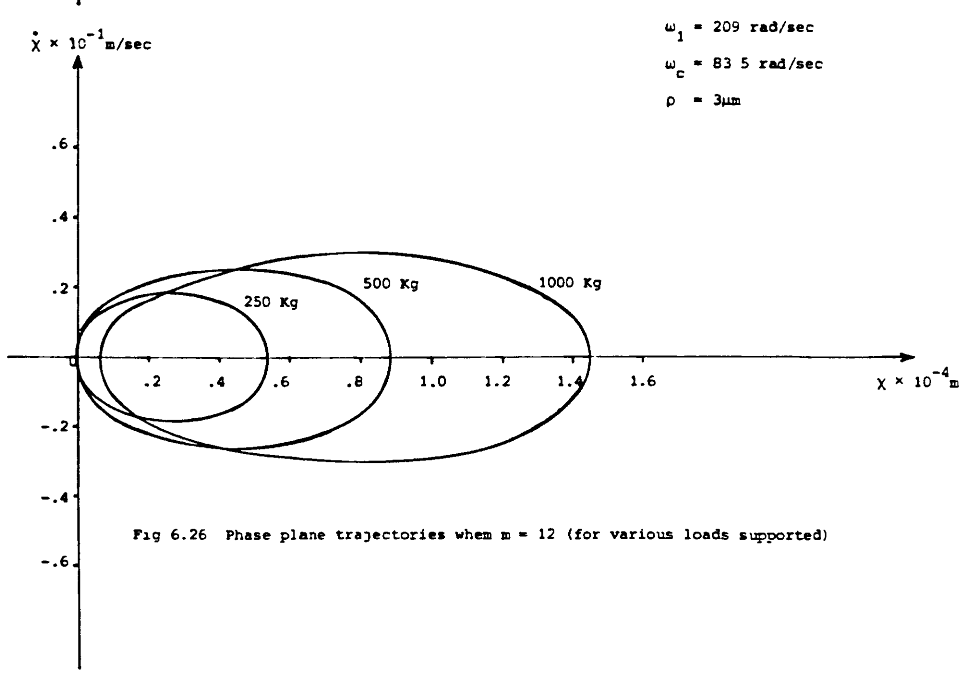

Fig 6.26 Phase plane trajectories whem m = 12 (for various loads supported)

$$\frac{dW_i}{d\delta_i} = \frac{3}{2} K \delta_i^{\frac{1}{2}} \tag{6.69}$$

Dynamically, the stiffness is determined by the rate of change of load $\dot{W}_i$ and the local radial deformation rate, $\dot{\delta}_i$:

$$\frac{dW_i}{d\delta_i} = \frac{dW_i}{dt} \cdot \frac{dt}{d\delta_i} = \frac{\dot{W}_i}{\dot{\delta}_i} \tag{6.70}$$

The instantaneous system dynamic stiffness is determined by the contribution of terms $\dot{W}_i/\dot{\delta}_i$ for $i = 1$ to m at any moment. Therefore, a family of trajectories is obtained as the applied load varies (see Fig 6.26).

6.12 OFF-CENTRE ROTATION

Off-centre or eccentric rotation occurs when the centre of rotation (i.e. geometric centre of the inner ring 0_1) does not coincide with the geometric centre of the shaft (i.e. 0) (see Fig 6.27).

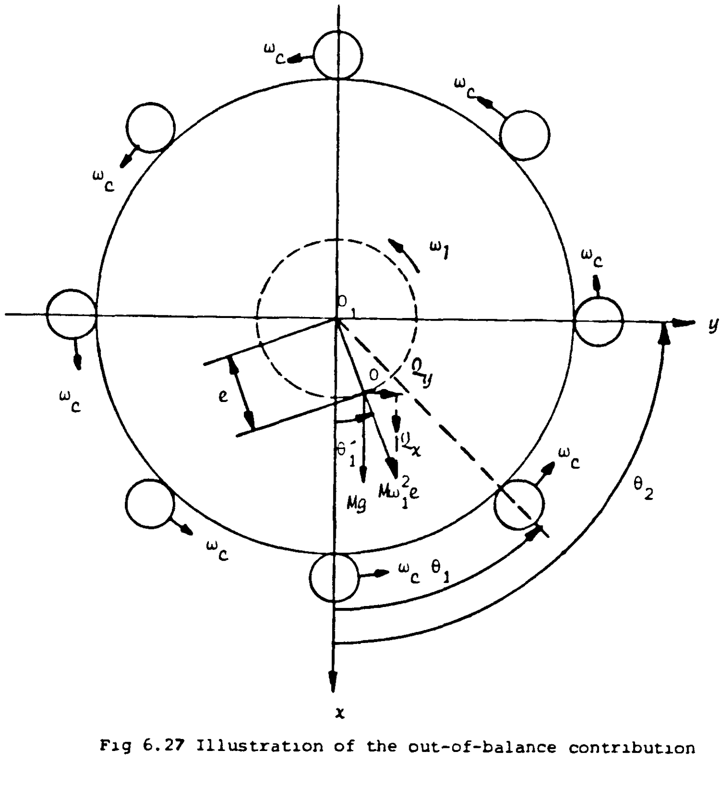

Fig 6.27 Illustration of the out-of-balance contribution

The distance 0 to 0_1 is denoted by e which is the eccentricity. The forces acting at point 0 consist of the weight of the shaft Mg and the centripetal force $M\omega_1^2 e$ in the direction of $0_1 0$. Therefore, the out-of-balance forces acting in x and y directions are:

$$Q_x = M\omega_1^2 \, e \, \cos\theta_1' \tag{6.71}$$

and

$$Q_y = M\omega_1^2 \, e \, \sin\theta_1' \tag{6.72}$$

where $\theta_1' = \omega_1 t$, is the angle turned through by the shaft from $t = 0$.

The equations of vibration in two degrees of freedom are :

$$M\ddot{x} + \sum_{i=1}^{m} W_i \cos\theta_i = M(g+\omega_1^2 \, e \, \cos\theta_1 t) \tag{6.73}$$

$$M\ddot{y} + \sum_{i=1}^{n} W_i \sin\theta_i = M\omega_1^2 e \sin\omega_1 t \quad . \tag{6.74}$$

The initial conditions are those outlined in Section 6.4.

Figure 6.28 shows the $(x-\dot{x})$ cycle at the steady-state condition. The time base as an independent variable appears explicitly on the right hand side (RHS) of the governing equations. Therefore, the system is not strictly autonomous. However, for a given time origin a unique $(x-\dot{x})$ cycle is obtained. The trajectory consists of two loops with point X common between them. The area between the loops corresponds to the system modulating response. This indicates that the system responds with two frequencies, one as a result of the shaft rotation and the other is due to the effect of the gravity load and stiffness characteristics of the bearing (i.e. natural frequency). If the system is perfectly balanced there is one response frequency which increases as the load carried is reduced (see Fig 6.26) . The shaft rotational speed hardly affects this limit cycle, when $e = 0$. If the springs were linear, there would be no effect at all (see Section 6.5). When the load is 250Kg the steady-state response frequency (natural frequency) is 195Hz. When $e > 0$ (i.e. unbalanced shaft rotation) the trajectory consists of a given number of loops. This occurs due to larger contact penetrations. At ω_1 = 209 rad/sec and M = 250Kg, the dominant response frequencies corresponding to the trajectory loops are 195Hz and 159HZ respectively (see Fig 6.28). The response frequency of 159Hz is the ball-pass frequency which is $m f_c$ where m = 12 and $f_c = \frac{\omega_c}{2\pi}$ = 13.2 rev/sec. These are infact two out of four major response frequencies generated by bearings. The other two correspond to ball to inner and outer raceways relative speeds which are due to geometrical inaccuracies of the raceways or unequal size balls. There are also generally many harmonics as well as vibration levels produced by the rolling surfaces' features.

The value of e is usually very small in precision engineering and the practical loads supported by the bearing are normally high. As a result of this the out-of-balance contribution is only significant when high rotational speeds are operating (i.e. the out-of-balance is proportional to ω_1^2). When e = 0, the movement in y - direction is insignificant and the locus of the shaft's centre movement (i.e. x versus y) is a very long and narrow ellipse with $y_{max} \geq \frac{1}{50} x_{max}$. When ω_1 = 209Hz and e = 25μm, the y - movement is more noticable such that $y_{max} \doteqdot \frac{1}{10} x_{max}$ (see Fig 6.29). The complete steady-state cycle commences from point 0 along OABC and returns to point 0 via CDEO. The parts of symmetrical locus where $x < 0$ correspond to comparatively large out-of-balance force contributions which overcome the effect of gravity load Mg. At 0 and C the acceleration $\ddot{x} = \pm g$ respectively with $\ddot{y} = 0$ at both these points. Furthermore, $\ddot{x} = g$ at the positions where the trajectory cuts the y-axis with $\ddot{y} = \omega_1^2 e$ along AB and $\ddot{y} = -\omega_1^2 e$ along BC. $\ddot{x} = -g$ at the points of intersection of the vertical at

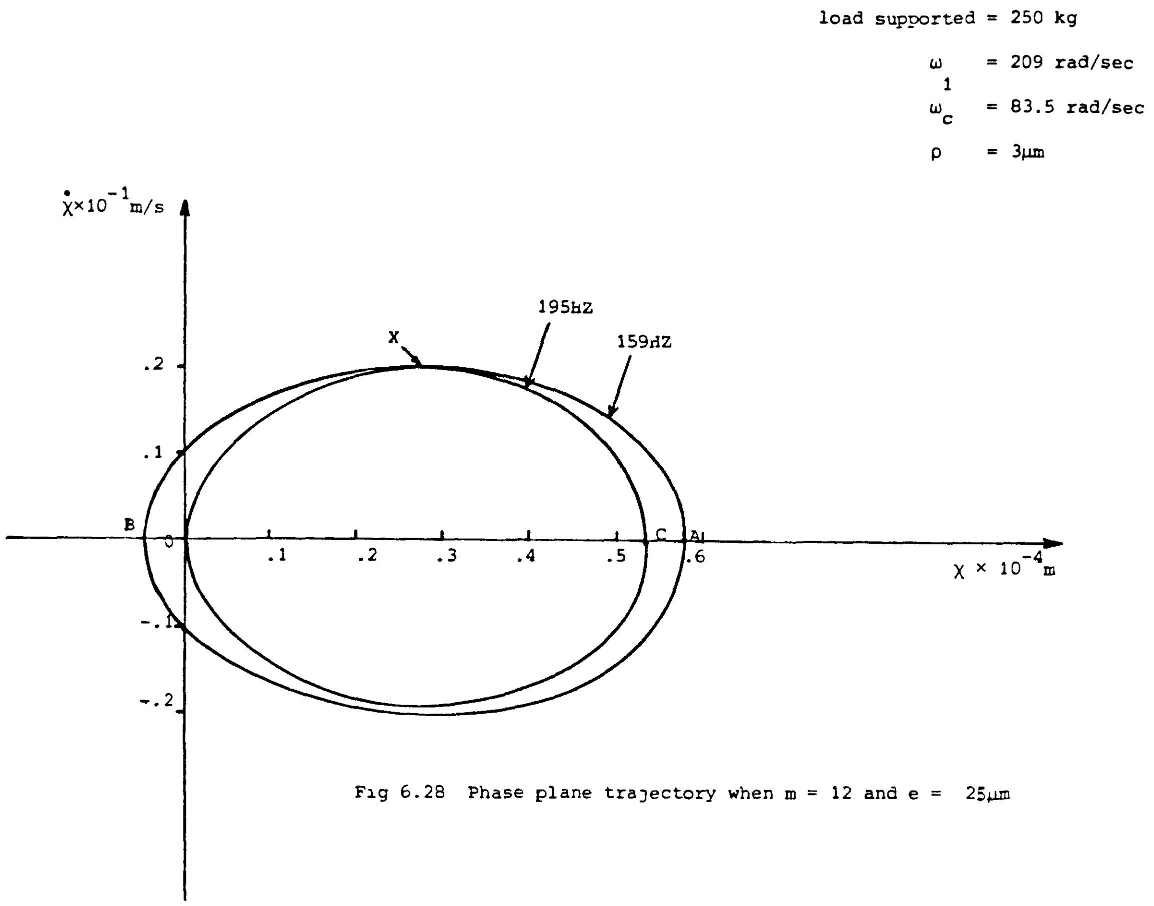

Fig 6.28 Phase plane trajectory when m = 12 and e = 25μm

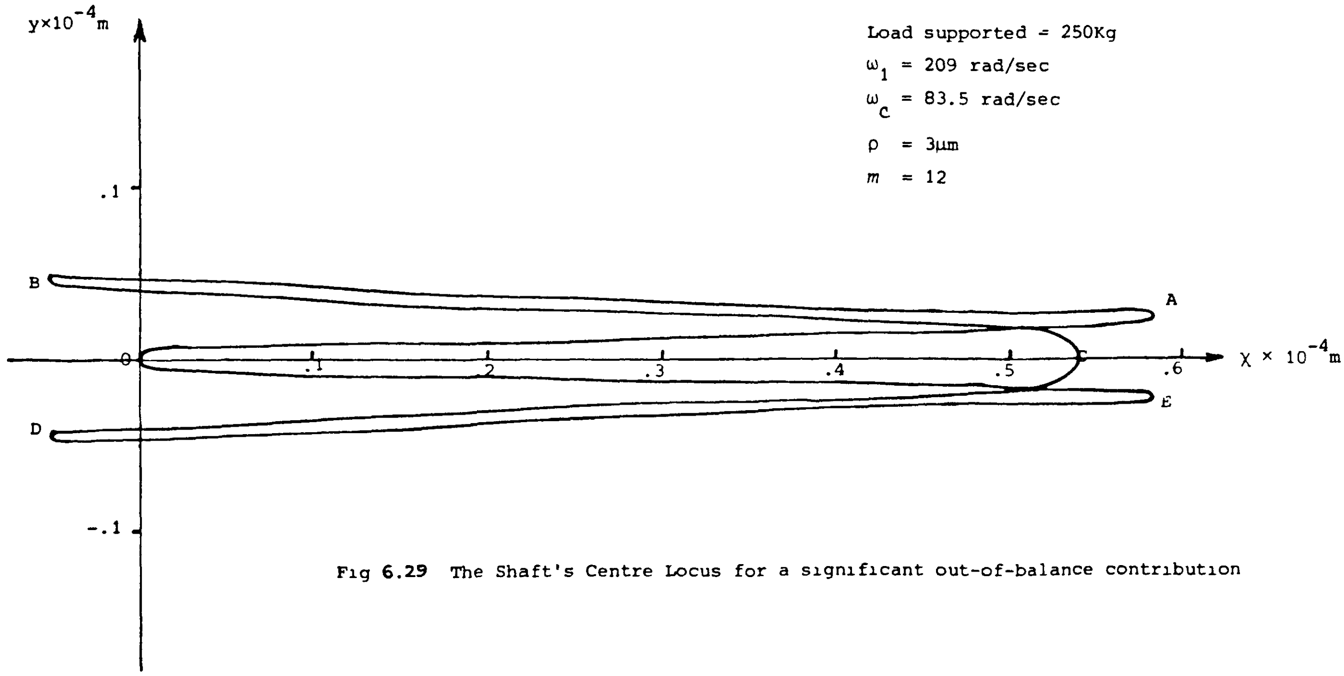

Fig 6.29 The Shaft's Centre Locus for a significant out-of-balance contribution

C and the cyclic trajectory ($\ddot{y} = \omega_1^2 e$ along OA and $\ddot{y} = -\omega_1^2 e$ along AB at these points).

The motion OA corresponds to the x-oscillations traversing the small loop of the $(x-\dot{x})$ cycle (see Fig 6.28) along OX and the larger loop along XA with $\ddot{x} = -g - \omega_1^2 e$ and $\ddot{y} = 0$ at point A. The path AB relates to the oscillations at the ball-pass frequency with $\ddot{x} = g + \omega_1^2 e$ and $\ddot{y} = 0$ at point B. The remaining part of the half cycle (i.e. BC) corresponds to the BXC on the $(x-\dot{x})$ cycle. Therefore, point X in Fig 6.28 is known as the changeover point where the oscillations' modulating behaviour is initiated. The area between the trajectory loops of the $(x-\dot{x})$ cycle is the modulating zone. The other half of the $(x-y)$ locus describes the same shape with the inverse y-oscillation characteristics. The period of one complete $(x-y)$ cycle corresponds to the rotating unbalance frequency ω_1.

Figure 6.30 shows the $(x-y)$ locus for the shaft speed of $\omega_1 = 1047$ rad/sec. The y-oscillations are of the same order as the x-movements since the out-of-balance force dominates the gravity load. The trajectory commences from point A along the path ABC. $\ddot{x} = 0$ and $\ddot{y} = -\omega_1^2 e$ at point B. The midway point along AB corresponds to the position where $x \doteq 17.5\mu m$ and $y \doteq 50\ \mu m$ and $\ddot{x} = g + \omega_1^2 e$, $\ddot{y} = 0$. Time to traverse the semi-loop ABC corresponds to the motion $A \rightarrow B \rightarrow A$ on the inner loop of the $(x-\dot{x})$ trajectory (see Fig 6.31). This time is $T = \frac{1}{f_b}$ where $f_b = 800$Hz and is the ball-pass frequency. Referring to Fig 6.30, the time to travel the entire trajectory corresponds to the period of the $(x-\dot{x})$ cycle which represents the unbalance frequency f_1.

In Fig 6.31 $\ddot{x} = \pm(g + \omega_1^2 e)$ at points E and E' respectively where E' corresponds to a point nearly at the mid-point of path FG in Fig 6.30. At H and H' (in Fig 6.31) $\ddot{x} = \pm g$ correspondingly where

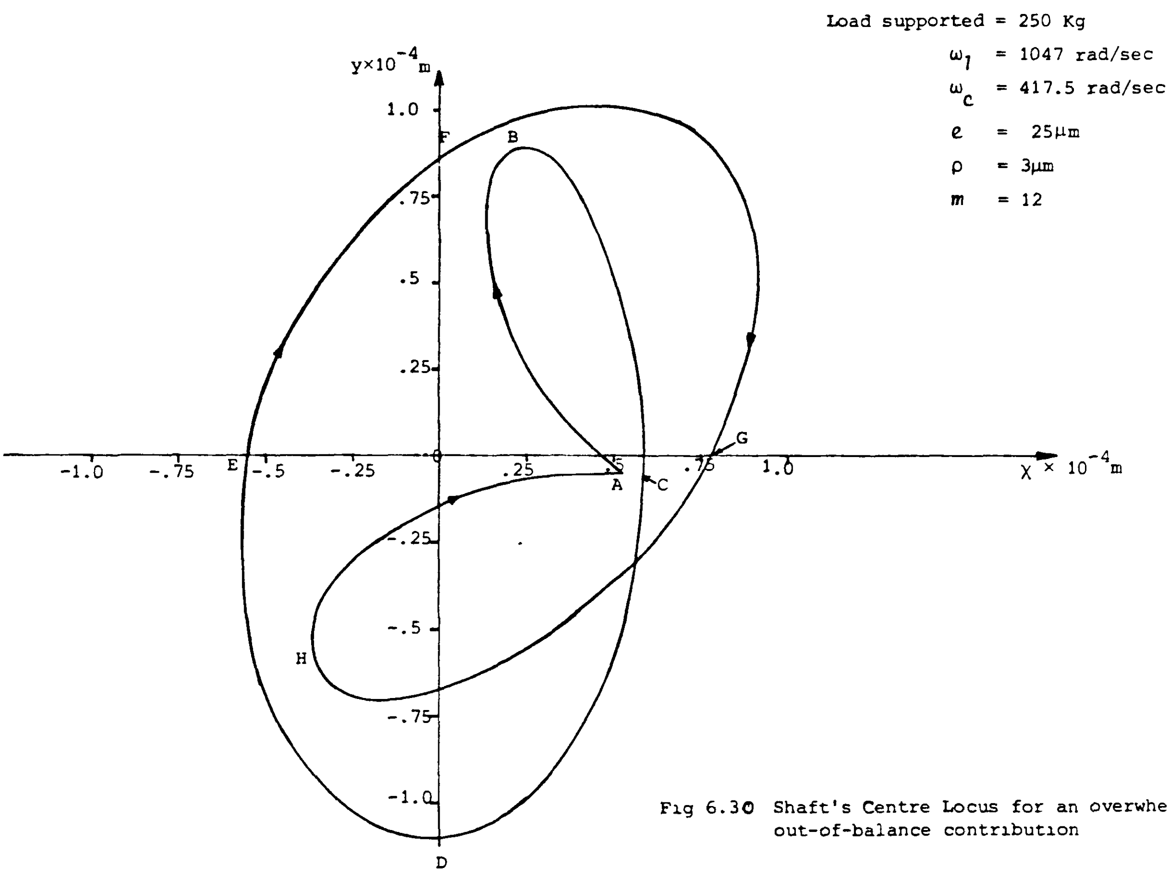

Fig 6.30 Shaft's Centre Locus for an overwhelming out-of-balance contribution

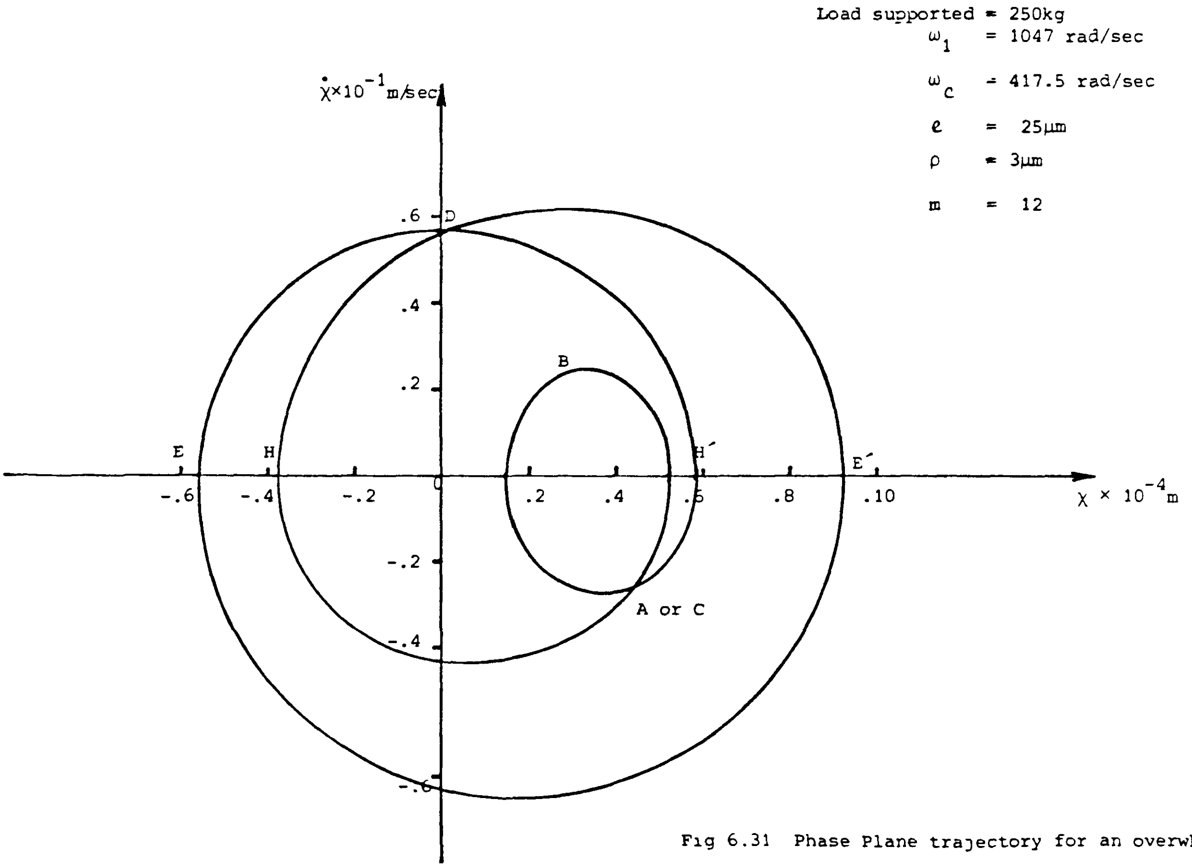

Fig 6.31 Phase Plane trajectory for an overwhelming out-of-balance contribution

H' is the point at the intersection of loop BC with the x-axis in Fig 6.30. The time to traverse the loop $AHDH'AB$ (in Fig 6.31) corresponds to the system natural frequency f_0.

6.13 REFERENCES

[1] RAGULSKIS, K.M., JURKAUSKAS, A.Yu., ATSTUPENAS, V.V., VITKUTE, A.Yu., and KULVEC, A.P.
"Vibration of Bearings",
Mintis Publishers, Vilnyus, 1974.

[2] NOVIKOV, L.Z.
"Ob uprugikh Kharakteristikakh radialno-upornogo Sharikovogo podshipnika" (On the Elastic Characteristics of Radial-Thrust Ball Bearings),
Izv. An. SSSR, OTN, Mekhanika i mashinosronerue, No. 3, 1964.

[3] ELSERMAN, M., HONGERLOOT, M., and SNOEYS, R.
"Damping in Taper Rolling Bearings",
Proc. 16th MTDR Conference, Manchester, 10-12 September 1975 (Macmillan, London), p. 223.

[4] HONRATH, K.
"Concerning the Stiffness of Machine Tool Spindles and Their Bearings",
Thesis submitted for Dicktor Ingenieur at the Technical University of Aachen, 1960.

[5] WALFORD, T.L.H., and STONE, B.J.
"The Measurement of the Radial Stiffness of Rolling Element Bearings Under Oscillating Conditions",
J. Mech. Eng. Sci., 1980.

[6] MATSUBARA, M.
"Vibrations of an Elastic Shaft Supported by Ball Bearings",
MSc Thesis, University of London, October 1982.

[7] DAREING, D.W., and JOHNSON, K.L.
"Fluid Film Damping of Rolling Contact Vibrations",
J. Mech. Eng. Sci., 1975.

[8] CARSON, R.M., and JOHNSON, K.L.
"Surface Corrugations Spontaneously Generated in a Rolling Contact Disc Machine",
Wear, 17 (1971) 59-72.

[9] GUPTA, P.K.
"Dynamics of Rolling Element Bearings. Part I: Cylindrical Roller Bearing Analysis",
Trans. ASME, J. Lubrication Technology, 101 (1979) 293-304.

[10] PALMGREN, A.
"Ball and Roller Bearing Engineering",
SKF Industries Incorporated, 3rd edition, 1959.

[11] LUNDBERG, G.
"Elastische Berührung Zweirer Halbraüme",
VDI Forschung, 10 (1939).

[12] GUPTA, P.K.
"Dynamics of Rolling Element Bearings. Part II: Cylindrical Roller Bearing Results",
Trans. ASME, J. Lubrication Technology, 101 (1979) 305-311.

[13] GUPTA, P.K.
"Dynamics of Rolling Element Bearings. Part III: Ball Bearing Analysis",
Trans. ASME, J. Lubrication Technology, 101 (1979) 312-318.

[14] GUPTA, P.K.
"Dynamics of Rolling Element Bearings. Part IV: Ball Bearing Results",
Trans. ASME, J. Lubrication Technology, 101 (1979) 319-326.

[15] HERTZ, H.
"Gesammelte Werke",
Volume 1, Leipzig, 1895.

[16] TIMOSHENKO, S., YOUNG, D.H., and WEAVER, Jnr, W.
"Vibration Problems in Engineering",
John Wiley & Sons, 4th edition, 1974.

[17] ROARK, R.J., and YOUNG, W.C.
"Formulas for Stress and Strain",
McGraw-Hill Kogakusha Limited, 5th edition, 1975.

[18] WHITEMORE, H.L., and PETRENKO, S.N.
"Friction and Carrying Capacity of Ball and Roller Bearings",
Tech. Paper Bur. Stand., No. 201, 1921.

[19] HAYASHI, C.
"Non-Linear Oscillations in Physical Systems",
McGraw-Hill Book Company, 1964.

[20] THOMSON, W.T.
"Vibration Theory and Applications",
George Allen and Unwin Limited, 1965.

CHAPTER 7

Elastohydrodynamic Vibration of Bearings

7.1 INTRODUCTION

The non-linear elastic model outlined in section 6.2 lacks any source of damping. However, Coulomb damping is present in metallic interactions of ball with races. This source of damping is greatest when surfaces slide past each other and is especially significant when surface irregularities interact within the contact areas [1]. Under these conditions vibrations can take place which are usually attributed to poor quality of the rolling surfaces or occasionally to an unstable cage [2]. Nevertheless, the variable compliance vibration occurs even if the rolling surfaces are perfect and the sliding action is minimised [3]. When bearings undergo radial or misaligning loads the instantaneous applied forces are supported by a few rolling elements which are travelling through the narrow loaded region. The mutual convergence of inner and outer rings depends on the radial elastic deflections at the rolling element-raceway contacts. As the rolling bodies change their radial position, the effective resisting dynamic stiffness is varied and the load distribution alters, producing a relative movement between the races.

In the absence of sliding action (as described in the nonlinear elastic model of chapter 6) there is no source of damping to control the extent of bearing oscillations.

In the model described in the following section lubricated contacts of perfect rolling surfaces are considered. The source of damping is generated by the lubricant film and its effect being somewhat frequency dependent [4] (see also chapter 4).

7.2 The Non-Linear Elastohydrodynamic Model

The EHD model is shown by Figure 7.1. The total stiffness in the radial direction of each ball is represented by its non-linear EHD interactions with the races. The radial restoring force at the point of contact of the ith rolling element is expressed by the integrated contact pressure distribution there as (see chapter 3†)

$$W_i = \frac{K'(1-A_i)^{\alpha'}}{h_i^{\alpha'}} + \frac{C_{iso}(1-B_i)^{\frac{1}{2}}}{h_i^{\frac{1}{2}}} \qquad (7.1)$$

where; $$A_i = A_o e^{\beta \dot{h}_i}, \quad \beta = \frac{132}{U}, \quad A_o = .75, \quad \alpha' = 22.23 \qquad (7.2)$$

$$B_i = B_o e^{\lambda \dot{h}_i}, \quad \lambda = \frac{67.7}{U}, \quad B_o = .75 \qquad (7.3)$$

and: $$K' = (14.04)^{22.23} U^{*14.44} G^{*10.3} (1 - .683\bar{e}^{.669}\, e_p^{*})^{22.23} \frac{R}{E_r}^{24.23} \qquad ..(7.4)$$

(the groups in 7.4 are explained in detail in Chapter 3)

$$C_{iso} = 2\sqrt{c}\; U^{*} \qquad (7.5)$$

(see Appendix A.1 for further details).

The equation (7.1) is used for all values of $\dot{h}_i$ (i.e. positive or negative corresponding to departing and approaching surfaces respectively). To obtain a continuous load regime throughout the cyclic rotation of each ball and to eliminate the generation of negative loads (i.e. tensile forces generated in unloaded regions) the equation (7.1)

---

† Equation 3.16 is arranged in terms of load to obtain the first term in equation 7.1. The second term is discussed in the Appendix A.1.

has been modified by adding another term. The first term gives the contribution of the elastohydrodynamic lubrication and the second corresponds to the hydrodynamic component (see Appendix A.1). Therefore, when a ball is travelling in a loaded region the effect of the first term is dominant, and when it is situated in an unloaded zone the contribution of the second term is greatest. All the local oil film thicknesses are measured in radial directions from a rigid fixed datum and the corresponding total radial defelection is allocated to the shaft (see fig. 7.2).

The equations of motion in two degrees of freedom can be established as was done in section 6.5 for the elastic model. However, the range of values generated within the numerical solution are found to be so diverse in magnitude (i.e. $10^{-134} \rightarrow 10^{+132}$) as to cause serious rounding off errors due to the truncation effects. To alleviate this problem a normalised solution is attempted in the main part of the programme, the results of which are denormalised at a later stage to obtain the real output.

7.3 Model Normalisation

The normalizing terms are:

$$\bar{x} = \frac{x}{\delta_o}, \quad \bar{y} = \frac{y}{\delta_o}$$
$$\bar{W}_i = \frac{W_i}{W_o}, \quad \bar{t} = \tau t \qquad (7.6)$$
$$\bar{\delta}_i = \frac{\delta_i}{\delta_o}, \quad \bar{h}_i = \frac{h_i}{h_o}$$

where δ_o is the initial universal deflection, W_o is the corresponding reaction (see initial conditions section 7.11) and τ is a normalising constant. Using the terms in (7.6) the equation (7.1) can be normalised to

$$\bar{W}_i = \psi_1 \left(\frac{1-\bar{A}_i}{\bar{h}_i}\right)^{\alpha'} + \psi_2 \left(\frac{1-\bar{B}_i}{\bar{h}_i}\right)^{\frac{1}{2}} \tag{7.7}$$

where:

$$\psi_1 = \frac{K'}{W_o h_o^{\alpha'}} \tag{7.8}$$

$$\psi_2 = \frac{C_{iso}}{W_o h_o^{\frac{1}{2}}} \tag{7.9}$$

and :

$$\bar{A}_i = A_o e^{\bar{\beta}\dot{\bar{h}}_i}, \quad \bar{\beta} = \beta \tau h_o$$

$$\bar{B}_i = B_o e^{\bar{\lambda}\dot{\bar{h}}_i}, \quad \bar{\lambda} = \lambda \tau h_o \tag{7.10}$$

$$\dot{\bar{h}}_i = \dot{h}_i / \tau h_o$$

7.4 Geometrical Considerations

The model assumes a total oil film of $2h_i$ and a total elastic deflection of $2\delta_i$ in the radial direction of the ith ball. The coefficient 2 refers to the ball contacts with the inner and outer raceways, both forming the same oil film and suffering an equal total contact deflection. Therefore, the mutual convergence of rings in the radial direction of the ith rolling body is given by $2(h_i - \delta_i)$. If the centreline of the shaft undergoes movements X and y with respect to the fixed cartesion frame of reference (x, y) then (see fig. 7.2).

$$R+2(h_i - \delta_i) = R+2C-r \tag{7.11}$$

$$r = X \cos\theta_i + y \sin\theta_i \tag{7.12}$$

and C is the extent of the initial clearance. If the bearing is initially radially preloaded such that there is an interference of ρ, then $C=-\rho$.

Hence: $$2\delta_i = 2(h_i + \rho) + x \cos \theta_i + y \sin \theta_i \tag{7.13}$$

and $$\theta_i = \phi + i\gamma \quad \text{(see section 6.2).}$$

Using the normalising terms of equation (7.6), for any movement x and y of the shaft centre the geometric equation is

$$2\,\bar{\delta}_i = 2\,(\bar{h}_o \bar{h}_i + \bar{\rho}) + \bar{x} \cos \theta_i + \bar{y} \sin \theta_i \tag{7.14}$$

where: $$\bar{h}_o = \frac{ho}{\delta_o} \quad \text{and} \quad \bar{\rho} = \left(\frac{\rho}{\delta_o}\right) \tag{7.15}$$

7.5 Equations of Motion

The projection of a radial load $\bar{W}_i$ in the x and y directions according to the cartesian frame of reference, are $\bar{W}_{x_i}$ and $\bar{W}_{y_i}$ respectively. (see fig. 7.3)

$$\bar{W}_x = \sum_{i=1}^{m} - \bar{W}_i \cos \Theta_i \tag{7.16}$$

$$\bar{W}_y = \sum_{i=1}^{m} - \bar{W}_i \sin \Theta_i \tag{7.17}$$

where $\bar{W}_i$ is given by equation (7.7) and m is the number of balls employed.

The equations of motion for two degrees of freedom are therefore:

$$\ddot{\bar{x}} = -\bar{P}' \left\{\bar{W}_x + \frac{Mg}{W_o}\right\} \tag{7.18}$$

$$\ddot{\bar{y}} = -\bar{P}' \left\{\bar{W}_y\right\} \tag{7.19}$$

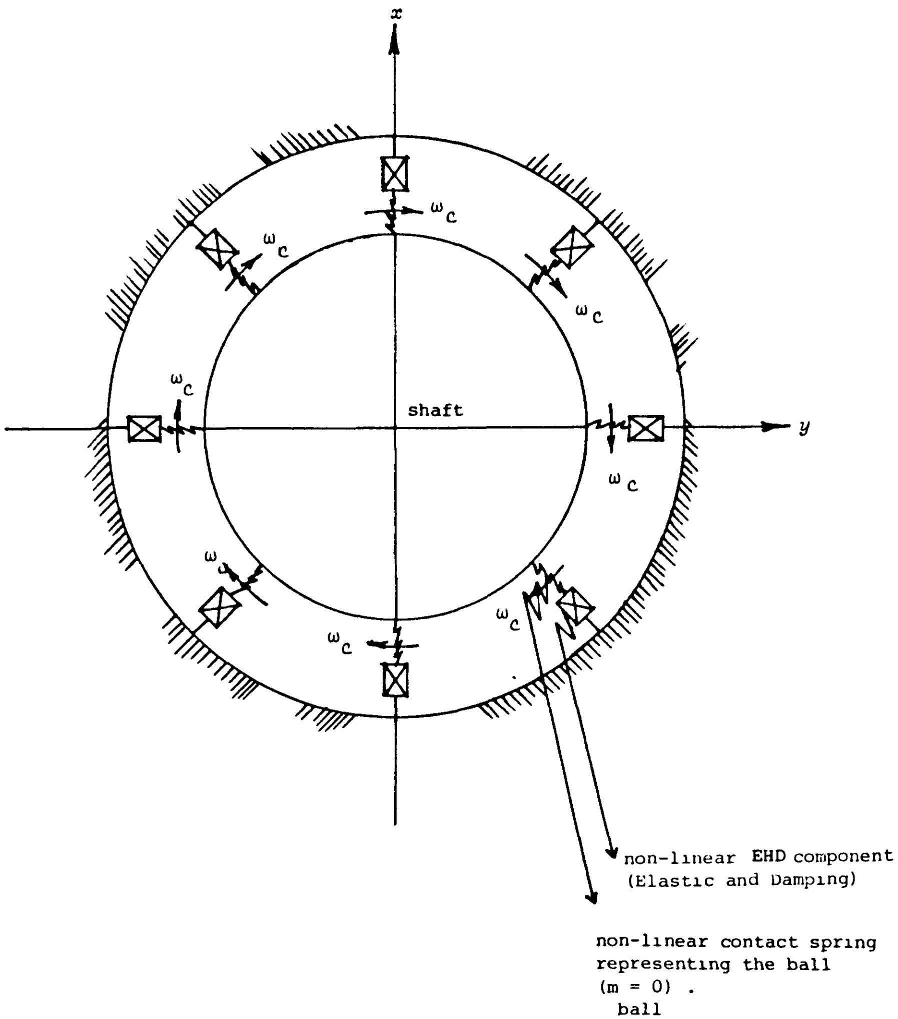

Fig 7.1 Non-linear Elastohydrodynamic model

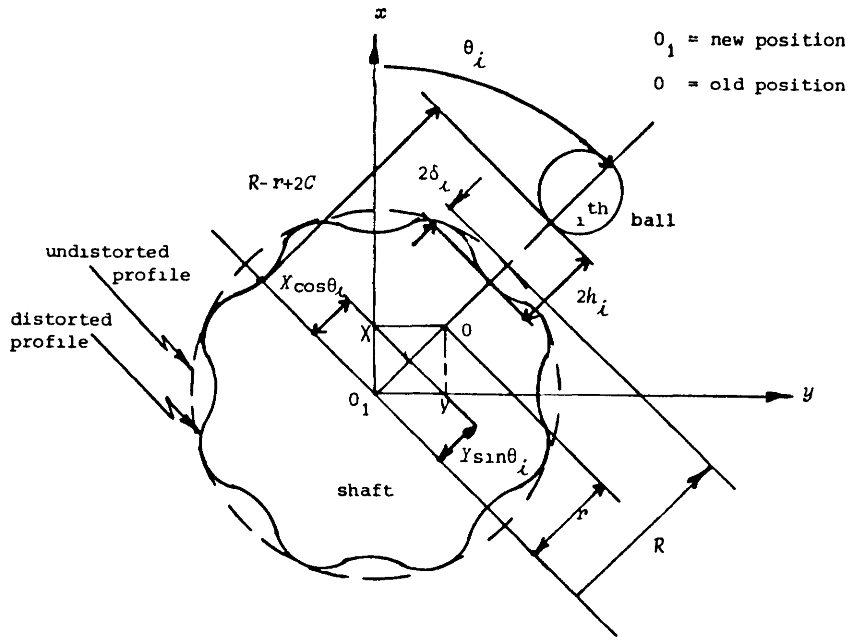

Fig 7.2 Geometrical considerations of the non-linear EHD model

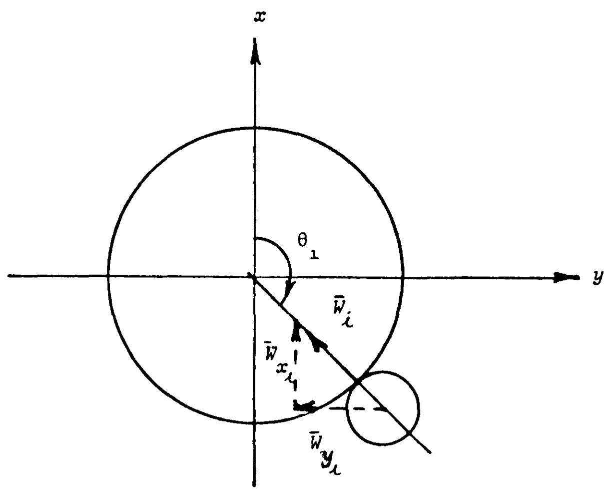

Fig 7.3 Model's restoring force considerations

where, $$\bar{P}' = \frac{W_o}{M\tau^2\delta_o} \tag{7.20}$$

and ; $$\ddot{\bar{x}} = \frac{\ddot{x}}{\delta_o\tau^2} \tag{7.21}$$

$$\ddot{\bar{y}} = \frac{\ddot{y}}{\delta_o\tau^2} \tag{7.22}$$

The value of τ is set for convenience such that

$$\bar{P}' = \frac{W_o}{M\tau^2\delta_o} = 1 \tag{7.23}$$

Therefore $$\tau = \{\frac{W_o}{M\delta_o}\}^{\frac{1}{2}} \tag{7.24}$$

7.6 CONTINUITY OF THE LOAD REGIME

As described in section 7.2 a continuous load regime for any ball is obtained as the inner race rotates. Figure 7.4 shows on a log scale the variation of $\bar{W}_i$ with $\dot{\bar{h}}_i$ for a series of values of $\bar{h}_i$. The values of $\bar{W}_i$ corresponding to $\dot{\bar{h}}_i < o$ represent increasing EHD contact conditions. The more $\dot{\bar{h}}_i > o$ the greater is the significance of the hydrodynamic contribution.

When $\dot{\bar{h}}_i > \dot{\bar{h}}_{\ell_1}$ the EHD component becomes negative and is then equated to zero so that the ith contacting zone is now subjected to a pure hydrodynamic regime (i.e. $\dot{\bar{h}}_{\ell_1} \leq \dot{\bar{h}}_i < \dot{\bar{h}}_{\ell_2}$). Furthermore, when $\dot{\bar{h}}_i \geq \dot{\bar{h}}_{\ell_2}$ the hydrodynamic load term also would become negative. To ensure continuity, a hyperbolic load variation† is considered to operate in this region. The limiting EHD and hydrodynamic oil film surface separation rates are:

$$\dot{\bar{h}}_{\ell_1} = -\frac{1}{\lambda}\ln B_0 \tag{7.25}$$

$$\dot{\bar{h}}_{\ell_2} = -\frac{1}{\beta}\ln A_0 \tag{7.26}$$

---

† see Appendix (A-2)

7.7 METHOD OF SOLUTION

The governing equations of motion in two degrees of freedom (i.e. equations 7.18 and 7.19) are solved by an iterative marching procedure which incorporates equations (7.7) and (7.14). The marching method is outlined in chapters 4 and 6 and is described fully in reference [5].

The dimensionless parameters in the model (i.e. the radial oil film thicknesses $\bar{h}_i$, the radial contact deflections $\bar{\delta}_i$, shaft centre line movements $\bar{x},\bar{y}$ etc) are calculated iteratively within a small time interval, $d\bar{t}$. At the beginning of each time interval the details relating to the movement of the shaft's centre line are calculated from its past history and from the other parameters of the model ($\bar{h}_i$, $\bar{\delta}_i$, $\dot{\bar{h}}_i$, $\dot{\bar{\delta}}_i$, etc). The new resulting centre movements ($\bar{x}$, $\bar{y}$) in turn initiate new rates of change in all the model parameters.

The movements (x,y) of the centre are given by equations 6.17 and 6.22 (see chapter 6). After normalisation we get

$$\bar{x}_{k,j} = \bar{x}_{k-1} + 2\,\dot{\bar{x}}_{k-1}\frac{d\bar{t}}{3} + \ddot{\bar{x}}_{k-1}\frac{d\bar{t}^2}{6} + \dot{\bar{x}}_{k,j}\frac{d\bar{t}}{3} \tag{7.27}$$

$$\bar{y}_{k,j} = \bar{y}_{k-1} + 2\dot{\bar{y}}_{k-1}\frac{d\bar{t}}{3} + \ddot{\bar{y}}_{k-1}\frac{d\bar{t}^2}{6} + \dot{\bar{y}}_{k,j}\frac{d\bar{t}}{3} \tag{7.28}$$

where $k>1$ and corresponds to the time interval, j is the iteration index and $d\bar{t} = \tau\, dt$ (7.29)

Similarly for $k=1$

$$\bar{x}_{1,j} = \bar{x}_o + 2\,\dot{\bar{x}}_o.\frac{d\bar{t}}{3} + \ddot{\bar{x}}_o.\frac{d\bar{t}^2}{6} + \dot{\bar{x}}_{1,j}.\frac{d\bar{t}}{3} \tag{7.30}$$

$$\bar{y}_{1,j} = \bar{y}_o + 2\dot{\bar{y}}_o.\frac{d\bar{t}}{3} + \ddot{\bar{y}}_o.\frac{d\bar{t}^2}{6} + \dot{\bar{x}}_{1,j}.\frac{d\bar{t}}{3} \tag{7.31}$$

The expressions for $\dot{\bar{x}}$ and $\dot{\bar{y}}$ can also be obtained by normalising the equations (6.13) through (6.21).

$$\dot{\bar{x}}_{1,j} = \dot{\bar{x}}_o + \ddot{\bar{x}}_o \, d\bar{t} \tag{7.32}$$

$$\dot{\bar{x}}_{2,j} = \dot{\bar{x}}_o + 2\ddot{\bar{x}}_o \, d\bar{t} \tag{7.33}$$

$$\dot{\bar{x}}_{k,j} = \dot{\bar{x}}_{k-2} + 2\ddot{\bar{x}}_{k-1} \, d\bar{t} \tag{7.34}$$

$$\dot{\bar{y}}_{1,j} = \dot{\bar{y}}_o + \ddot{\bar{y}}_o \, d\bar{t} \tag{7.35}$$

$$\dot{\bar{y}}_{2,j} = \dot{\bar{y}}_o + 2\ddot{\bar{y}}_o \, d\bar{t} \tag{7.36}$$

$$\dot{\bar{y}}_{k,j} = \dot{\bar{y}}_{k-2} + 2\ddot{\bar{y}}_{k-1} \, d\bar{t} \tag{7.37}$$

The oil film thickness in the radial direction of the *ith* ball is $h_i = h_o + \delta_i$ where h_o is the universal initial oil film thickness (see section 7.11) and S_i is the small dynamic variation of the oil film. In terms of the normalised variables

$$\bar{h}_{i,k,j} = 1 + \bar{S}_{i,k,j} \tag{7.38}$$

$$\bar{S}_{i,k,j} = \frac{S_{i,k,j}}{h_o} \tag{7.39}$$

The average acceleration method is also applied to find the variation of $\bar{S}_{i,k,j}$.

$$\bar{S}_{i,k,j} = \bar{S}_{i,k-1} + 2\dot{\bar{S}}_{i,k-1}\frac{d\bar{t}}{3} + \ddot{\bar{S}}_{i,k-1}\frac{d\bar{t}^2}{6} + S_{i,k,j}\frac{d\bar{t}}{3} \tag{7.40}$$

for $k>1$ and $\dot{\bar{S}}_i$ $(=\dot{\bar{h}}_i)$ terms represent the radial squeeze velocities operating on the top surface of the oil films $\bar{h}_i$. For $k=1$,

$$\bar{S}_{i,1,j} = \bar{S}_o + 2\,\dot{\bar{S}}_o \frac{d\bar{t}}{3} + \ddot{\bar{S}}_{io} \frac{d\bar{t}^2}{6} + \dot{\bar{S}}_{i,1,j} \frac{d\bar{t}}{3} \tag{7.41}$$

$\bar{S}_o$, $\dot{\bar{S}}_o$ and $\ddot{\bar{S}}_{io}$ are given in section 7.11.

The squeeze velocity terms are normalised using the same procedure applied to the centre movement.

$$\dot{\bar{S}}_{i,1,j} = \dot{\bar{S}}_o + \ddot{\bar{S}}_{io}\, d\bar{t} \tag{7.42}$$

$$\dot{\bar{S}}_{i,2,j} = \dot{\bar{S}}_o + 2\ddot{\bar{S}}_{io}\, d\bar{t} \tag{7.43}$$

$$\dot{\bar{S}}_{i,k,j} = \dot{\bar{S}}_{i,k-2} + 2\ddot{\bar{S}}_{i,k-1} d\bar{t} \tag{7.44}$$

The radial deflection of the ith contact is calculated using equation (7.14). In terms of the subscript notations used in this section;

$$2\bar{\delta}_{i,k,j} = 2(\bar{h}_o \bar{h}_{i,k,j} + \bar{\rho}) + \bar{x}_{i,k} \cos\theta_{i,k} + \bar{y}_{i,k} \sin\theta_{i,k} \tag{7.45}$$

The solution for k equal time steps of $d\bar{t}$ is achieved iteratively by marching through equations (7.18),(7.19) and(7.27) through (7.45). The convergence criterion is discussed in section 7.9.

If the values of $\ddot{\bar{S}}_i$ are known, then the remaining parameters can be obtained from the equations already discussed.

7.8 Formulation of $\ddot{\bar{S}}_i$ terms

As the rolling elements change their radial position, the resultant radial load distribution alters.

Therefore, in any radial direction, a relative movement occurs between the races. The rate of change of load in the radial direction of the i^{th} ball is given by equation 7.46 below (i.e. by differentiating equation 7.7 with respect to $\bar{t}$).

$$\dot{\bar{W}}_i = - \bar{h}_i^{-\alpha'_1} \cdot (1-\bar{B}_i)^{-\frac{1}{2}} \cdot \{\alpha'\psi_1(1-\bar{A}_i)^{\alpha'-1} \cdot (1-\bar{B}_i)^{\frac{1}{2}}\, \bar{h}^{3/2}\, [\beta\bar{A}_i\bar{h}_i\ddot{\bar{S}}_i + (1-\bar{A}_i)\dot{\bar{S}}_i]$$

$$+ \psi_2\bar{h}_i^{\alpha'+1}\, [\bar{\lambda}\bar{B}_i h_i\ddot{\bar{S}}_i + (1-\bar{B}_i)\dot{\bar{S}}_i]\} \qquad \ldots \quad (7.46)$$

where $\dot{\bar{W}}_i = \dfrac{d\bar{W}_i}{d\bar{t}} = \dfrac{\dot{W}_i}{W_0\tau}$, $\alpha'_1 = \dfrac{2\alpha'+5}{2}$ (7.47)

As in chapter 4, the load-deflection characteristic of a rolling element contact uses that given by Hertz [6] where;

$$W_i = K\delta_i^{\nu} \tag{7.48}$$

($\nu = 3/2$ for ball-race contacts).

In terms of normalised parameters:

$$\bar{W}_i = \frac{K\delta_0^{\nu}}{W_0} \cdot \bar{\delta}_i^{\nu} \tag{7.49}$$

and the ratio $\psi_3 = \dfrac{K\delta_0^{\nu}}{W_0} = 1$ (see section 7.11).

Thus:

$$\bar{W}_i = \bar{\delta}_i^{\nu} \tag{7.50}$$

Differentiating (7.50) with respect to $\bar{t}$ an alternative formula to that given by (7.46) results.

$$\dot{\bar{W}}_i = \nu\dot{\bar{\delta}}_i\, \bar{\delta}_i^{\nu-1} \tag{7.51}$$

Equating (7.46) and (7.51) an equation results from which the value of $\ddot{\bar{S}}_i$ can be obtained in terms of the system's remaining parameters

$$\ddot{\bar{S}}_i = - \frac{\bar{\sigma}_{2_i} + \bar{\sigma}_{3_i}}{\bar{\sigma}_{1_i}} \tag{7.52}$$

where:

$$\bar{\sigma}_{1_i} = \alpha'\bar{\beta}\psi_1\bar{A}_i(1-\bar{A}_i)^{\alpha'-1}\cdot(1-\bar{B}_i)^{\frac{1}{2}}\bar{h}_i + \bar{\lambda}\psi_2\bar{B}_i\bar{h}_i^{\alpha'+1} \tag{7.53}$$

$$\bar{\sigma}_{2_i} = \nu\bar{h}^{\alpha_1'-1}\cdot(1-\bar{B}_i)^{\frac{1}{2}}\,\dot{\bar{\delta}}_i\,\dot{\bar{\delta}}_i^{\nu-1} \tag{7.54}$$

$$\bar{\sigma}_{3_i} = \dot{\bar{S}}_i(1-\bar{B}_i)^{\frac{1}{2}}\cdot\{\alpha'\psi_1(1-\bar{A}_i)^{\alpha'}\bar{h}_i + \psi_2\bar{h}_i^{\alpha'}(1-\bar{B}_i)\}\;. \tag{7.55}$$

And

$$\dot{\bar{\delta}}_i = \bar{h}_0\,\dot{\bar{S}}_i + \tfrac{1}{2}\{\dot{\bar{x}}\cos\theta_i + \dot{\bar{y}}\sin\theta_i + \bar{\omega}_c[\bar{y}\cos\theta_i - \bar{x}\sin\theta_i]\} \quad \ldots \tag{7.56}$$

where $\dot{\bar{\delta}}_i$ is the rate of change of radial contact deflection.

$$\dot{\bar{\delta}}_i = \frac{d\bar{\delta}_i}{d\bar{t}} = \frac{\dot{\delta}_i}{\tau\delta_0} \tag{7.57}$$

$\bar{\omega}_c = \dfrac{\omega_c}{\tau}$ (ω_c is the case set angular velocity = $\dot{\theta}_i$ for all values of i).

The solution outlined here is general and can be applied to any rolling bearing problem as long as the integrated pressure distribution is approximated to the form of equation 7.1. The values of K, ν, α' and β must be defined for a given type of bearing and its respective contact geometry.

7.9 Convergence Criterion

Small changes in the radial oil film thicknesses can significantly alter the bearing's load distribution. Furthermore, this model is more non-linear than the model outlined in Chapter 6 mainly due to the damping characteristics of squeeze film elastohydrodynamics. When the non-linear elastic model is used the narrow loaded region is symmetrical about the line of action of the external force XX if there is no significant out-of-balance contribution (i.e. movement in the transverse direction y is negligible, see Chapter 6 and figure 7.5). The loaded region in the EHD model is asymetric since the $i-1^{th}$ element exerts a larger reaction than the $i+1^{th}$ element by the token that it has a thinner film thickness and a larger approaching squeeze velocity ($i-1^{th}$ element is carrying a squeezed time history whereas the $i+1^{th}$ element is just entering the squeezed zone). Therefore, a more accurate check on convergence can be employed than that used in Chapter 6 (i.e. equations 6.24 and 6.25). However, it is impossible to set a general criterion on the convergence of the local oil film thickness as this would require a substantial computing time allocation. Therefore, the criterion is based on the accelerations $\ddot{\bar{x}}$ and $\ddot{\bar{y}}$ which are sensitive to any small changes in the values of the radial restoring loads $\bar{W}_i$. Furthermore the average acceleration uses suitably small time steps of $d\bar{t}$ within which the average values of $\ddot{\bar{x}}$ and $\ddot{\bar{y}}$ are considered to be representative of them. Thus, changes between consecutive iterations of $\ddot{\bar{x}}$ and $\ddot{\bar{y}}$ in time steps of $d\bar{t}$ may be regarded as small, where :

$$\left(\frac{\ddot{\bar{x}}_{k,j} - \ddot{\bar{x}}_{k,j-1}}{\ddot{\bar{x}}_{k,j}}\right) \leq \varepsilon_x \qquad (7.58)$$

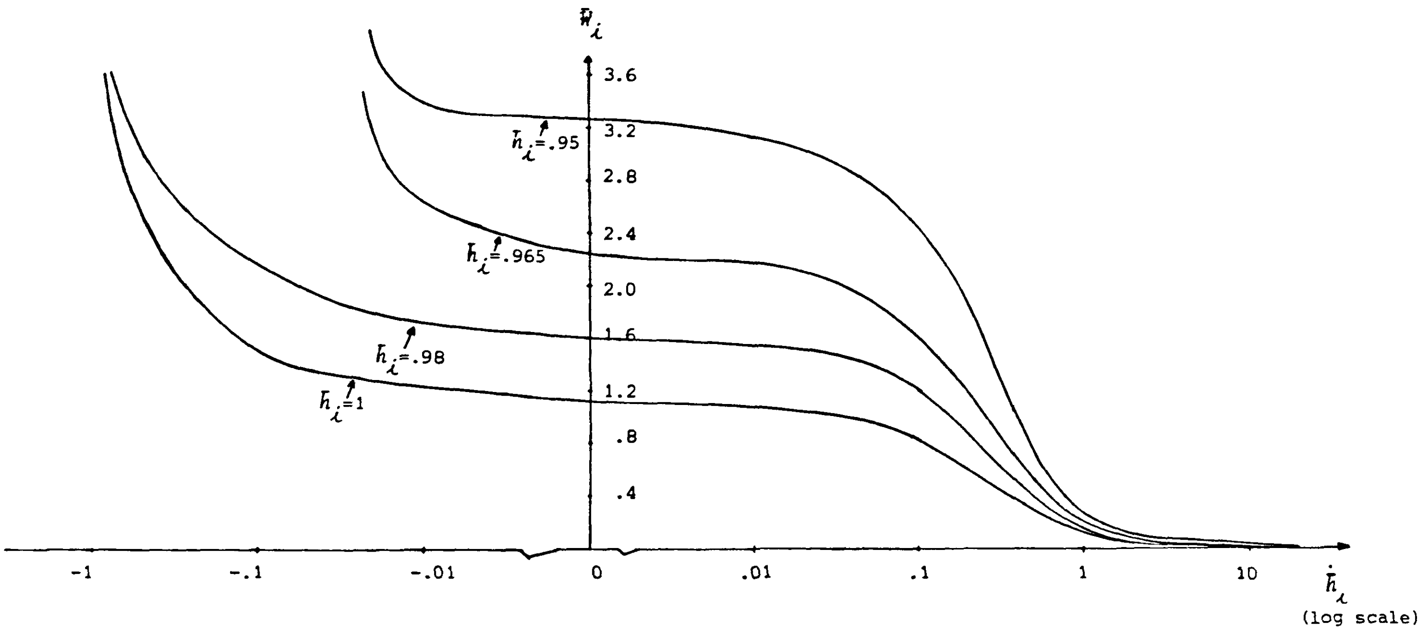

Fig 7.4 Continuous load regime throughout the cyclic rotation

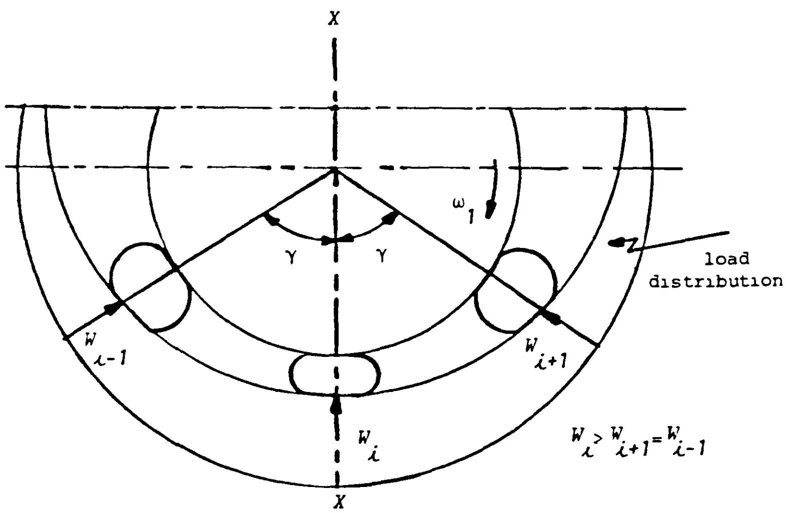

(a) Non-linear elastic model

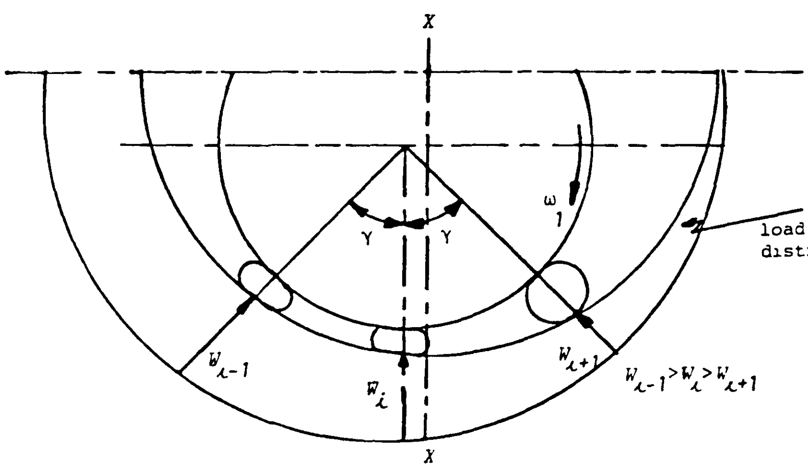

(b) Non-linear EHD model

Fig 7.5 Loaded region in a ball bearing system

$$\text{and;} \quad \left\{ \frac{\ddot{y}_{k,j} - \ddot{y}_{k,j-1}}{\ddot{y}} \right\} \leq \varepsilon_y \tag{7.59}$$

ε_x and ε_y are the specified limits of accuracy.

The model is found to iterate satisfactorily for ε_y and ε_y values down to 0.005 (i.e. 0.5% accuracy) and iterate for a considerable time as these limits are further reduced. The optimal range of values for dt is 0.01 - 0.005 milliseconds (ms). When dt is decreased further, longer computational time is required and when dt > 0.05 ms, inaccuracies creep into the solution as some vital time history of the model parameters are being lost. The criterion in Chapter 6 may also be employed . Here, the accuracy is somewhat load dependent. For low values of load both criteria are in agreement. At higher values of load (i.e. above 500 Kg) equations 6.24 and 6.25 introduce a maximum error of 5% when values of $\ddot{x}$ and $\ddot{y}$ are small.

7.10 The ball bearing system

The ball bearing system employed is described in Section 6.8. The shaft is rotated at speed ω_1 (rad/sec) and each ball gains an angular speed of ω_2. For no sliding to take place it follows that (see fig 6.17)

$$\omega_1 r_1 = 2\omega_2 r_2 \quad . \tag{7.60}$$

A uniform rolling speed distribution is assumed. The cage set rolling speed U_c is :

$$U_c = \omega_2 r_2 = \frac{\omega_1 r_1}{2} \quad . \tag{7.61}$$

This value is not to be confused with the speed of entraining motion in equation (7.2) which is:

$$U = u_1 + u_2 = \omega_1 r_1 = 2\omega_2 r_2 \quad . \tag{7.62}$$

The cage set angular speed ω_c can be determined in terms of ω_1 (as in Chapter 6).

$$\omega_c = \frac{\omega_1 r_1}{2(r_1+r_2)} \tag{7.63}$$

7.11 Initial Conditions

The shaft is initially held and the bearing is fitted with a radial interference ρ. Therefore, in the radial direction of the i^{th} ball the total elastic deflection is : $2\delta_{o_i} = 2\rho + 2h_{o_i}$. If the shaft is rotating with an angular velocity of ω_1, a lubricant film forms to fill the opening gaps at the rolling contact surfaces. Since the initial radial interference is universal for all the contacting elements, the initial lubricant thickness in the radial direction of all the rolling contacts is identical. Thus,

$$W_{o_i} = \frac{C_{iso}}{2h_{o_i}^{\frac{1}{2}}} + \frac{K_r}{h_{o_i}^{\alpha'}} \tag{7.64}$$

for all values of i.

where $K_r = (0.25)^{\alpha'} . K'$ and both terms indicate contribution due to pur entraining motion.

With sufficient interference EHD conditions result and the contribution of the hydrodynamic term diminishes.

Therefore:

$$W_{o_i} \doteq \frac{K_r}{h_o^{\alpha'}} \quad . \tag{7.65}$$

Also:

$$W_o = K\delta_o^{\nu} \ . \tag{7.66}$$

Hence the universial initial film thickness can be obtained by solution of equation 7.67 by successive substitutions.

$$(\rho + h_o)^{\nu} \, h_o^{\alpha'} = \frac{K_r}{K} \ . \tag{7.67}$$

However, if there is a radial clearance or $\rho = 0$ equation (7.67) cannot be used. For zero clearance or interference (i.e, $\rho = 0$):

$$\frac{K_r}{h_o^{\alpha'}} + \frac{C_{iso}}{h_o^{\frac{1}{2}}} = Kh_o^{\nu} \tag{7.68}$$

and again h_o can be obtained by successive substitution technique using the normalising groups of equation (7.6).

$$\bar{h}_o = 1 \quad , \quad \bar{W}_o = 1 \ . \tag{7.69}$$

The shaft's initial centre-line accelerations $\ddot{\bar{x}}_o$ and $\ddot{\bar{y}}_o$ are :

$$\ddot{\bar{x}}_o = \frac{W_o}{M\tau^2\delta_o} \cdot \left(\sum_{i=1}^{m} - \cos\theta_{o_i} - \frac{Mg}{W_o} \right) \tag{7.70}$$

$$\ddot{\bar{y}}_o = \frac{W_o}{M\tau^2\delta_o} \cdot \left(\sum_{i=1}^{m} - \sin\theta_{o_i} \right) \tag{7.71}$$

where in this solution $\dfrac{W_o}{M\tau^2\delta_o} = 1$.

Furthermore, when $t = o$:

$$\bar{\sigma}_{1_o} = \alpha'\bar{\beta}\psi_1\bar{A}_o(1-\bar{A}_o)^{\alpha'-1} \cdot (1-\bar{B}_o)^{\frac{1}{2}}\bar{h}_o^{3/2} + \bar{\lambda}\,\psi_2\bar{B}_o\bar{h}_o^{\alpha'+1} \tag{7.72}$$

$$\bar{\sigma}_{2_o} = \nu\bar{h}_o^{\alpha_1'-1} \cdot (1-\bar{B}_o)^{\frac{1}{2}}\dot{\bar{\delta}}_o\,\bar{\delta}_o^{\nu-1} \tag{7.73}$$

and

$$\bar{\sigma}_{3_o} = 0.0 \quad . \tag{7.74}$$

Thus:

$$\ddot{\bar{S}}_o = -\frac{\bar{\sigma}_{2_o}}{\bar{\sigma}_{1_o}} \tag{7.75}$$

7.12 Results of a step load application

When the bearing is lubricated squeeze film damping is introduced at each rolling contact. The system is therefore no longer conservative. Energy dissipation takes place in the form of work required to overcome the fluid damping as the balls traverse their orbital paths.

Figures 7.6 and 7.7 show the shaft's centre time histories in x and y directions respectively. The x-oscillations take place about the system static deflection position. The oscillatory decay indicates underdamped behaviour. The y-oscillations show a build up of a non-linear vibration to its final amplitude. Figure 7.8 depicts the phase plane trajectory (x-$\dot{x}$) forming an enclosed limit cycle at the steady-state condition. The transient decay is represented by the "logarithmic spiral" and the residual steady-state oscillations describe the enclosed elliptical path. The response frequency in both x and y directions corresponds to the damped natural frequency of the system at the limit cycle and is given by $\frac{1}{T}$ where T is the time to traverse the limit cycle once. When the step gravity load is Q = 500N and the radial interference is 5μm, for a twelve ball system this response frequency is 260Hz. The undamped natural

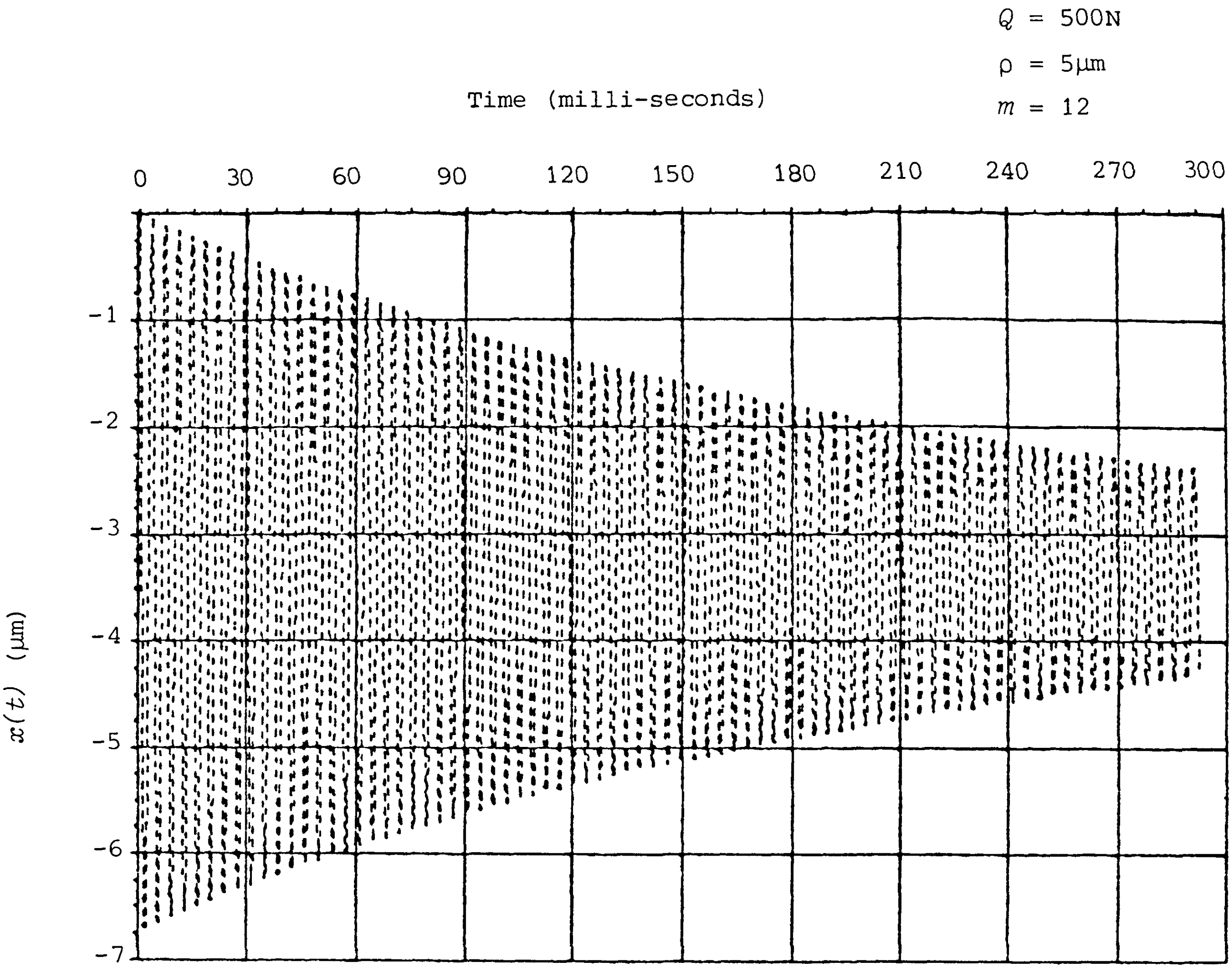

Fig 7.6 Shaft centre-line time history $x(t)$

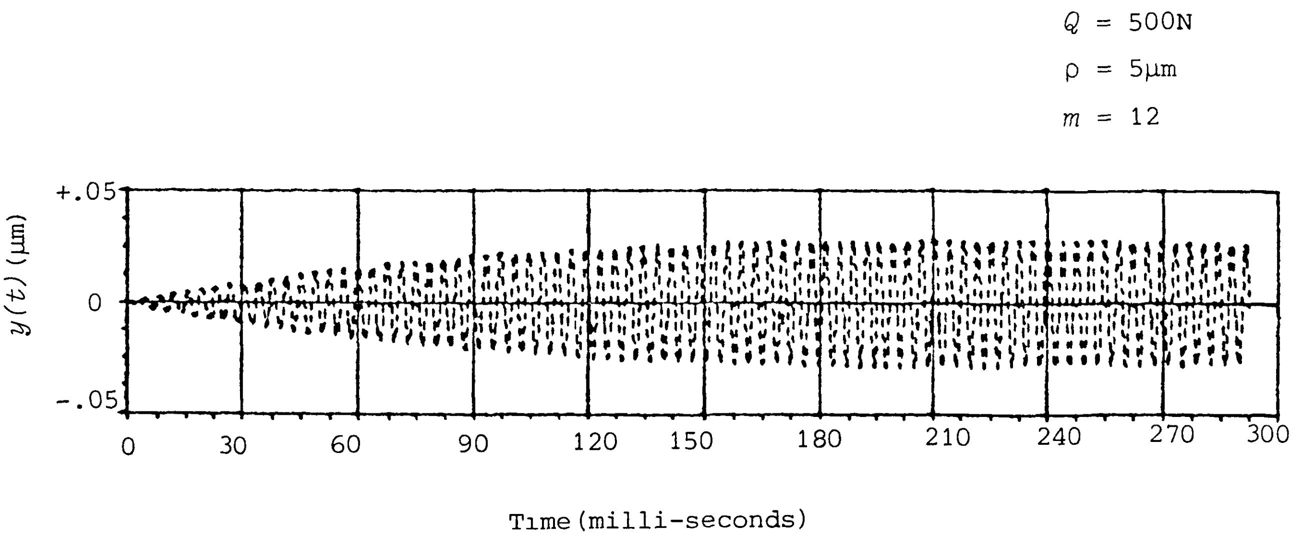

Fig 7.7 Shaft centre-line time history $y(t)$

frequency is obtained using an equivalent elastic model under the same step load, f = 264Hz. Therefore, the damped natural frequency is only marginally less than the undamped natural frequency. This is true of most engineering applications where $\xi \doteqdot 0.001-0.2$ [7].

The residual x and y oscillations occur because of self-excitation which appear to take place as a result of system's unstable state of equilibrium [8]. The equilibrium position is represented in Fig 7.9 (y-$\dot{y}$ phase plane) as the point where $\dot{y} = \dfrac{\partial y}{\partial t} = 0$ (and $x = \Delta$, the system static deflection) and is known as the unstable focus. However, the growth of the y-oscillations' amplitude falls off gradually and settles down to a practically constant value (i.e., a limit cycle). This processes is known as "stationary self-excited oscillations" and the system behaviour is quasi-linear [9].

Some energy is inevitably dissipated in all real vibratory systems. Therefore, every self-excited vibration has to possess a source of energy to compensate for the energy losses. Here, the energy source is the power input into the system which maintains the rotation. The amplitude of the y-oscillations is $y_{max} \doteqdot 0.025\mu m$ and that of the x-oscillations is $x_{max} \doteqdot 1.5\ \mu m$ about the system equilibrium point where $\Delta = 3.5\mu m$.

Both x and y waves have the same frequency but different amplitudes. Therefore, the shaft's centre locus describes an ellipse (see fig 7.10, y-axis scale is exaggerated). The skewed shape of the elliptical trajectory is due to a phase difference between the x and y time histories [10]. The phase difference is caused by the system non-linearity as well as the squeeze film damping action. In the elastic undamped model (outlined in Chapter 6), the (x-y) locus is an ellipse along the x-axis with the insignificant y-oscillations lagging behind the x-movements by 1/4 cycle. The inclination of the locus'

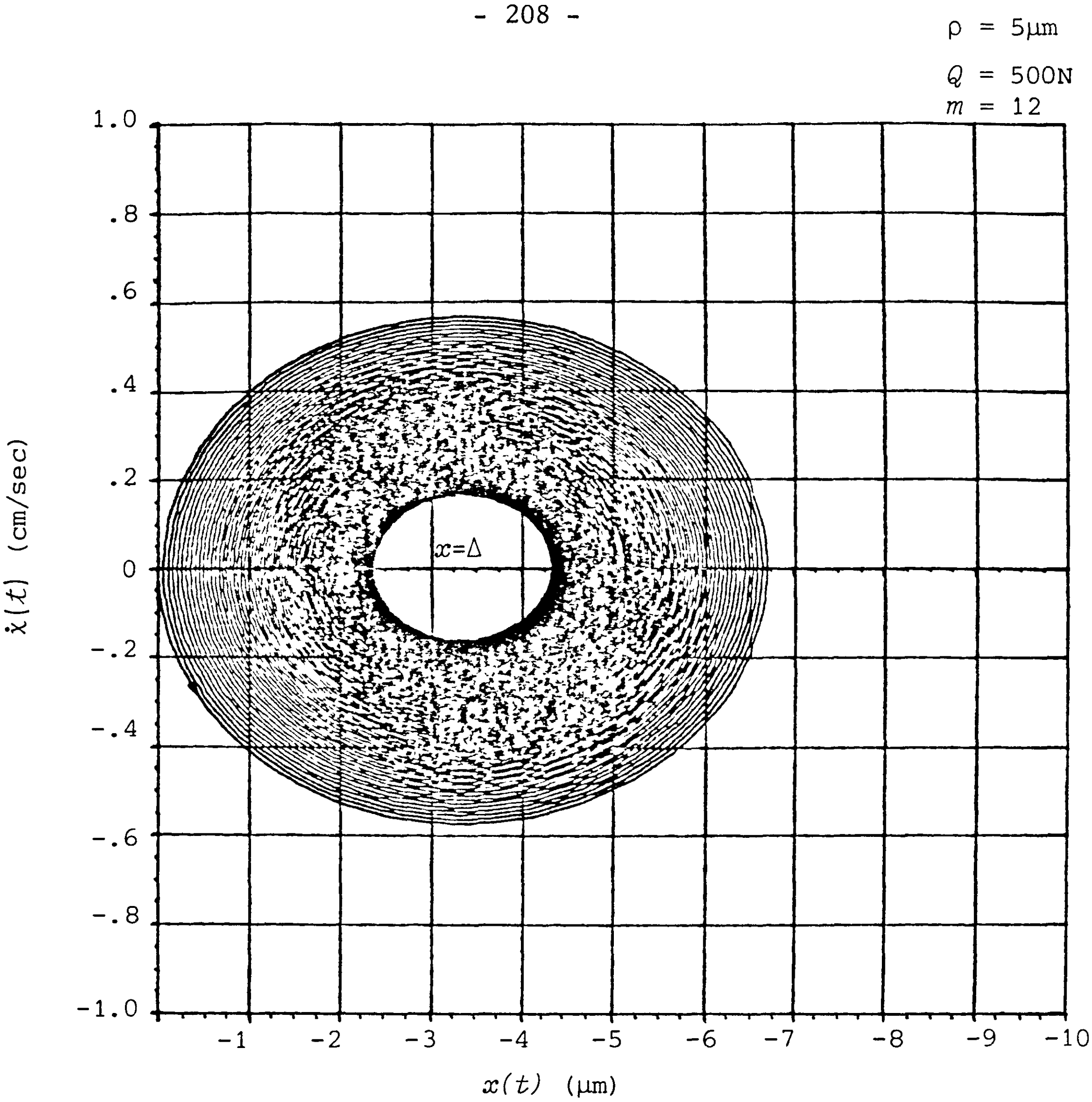

Fig 7.8 Phase plane trajectory $(x\text{-}\dot{x})$

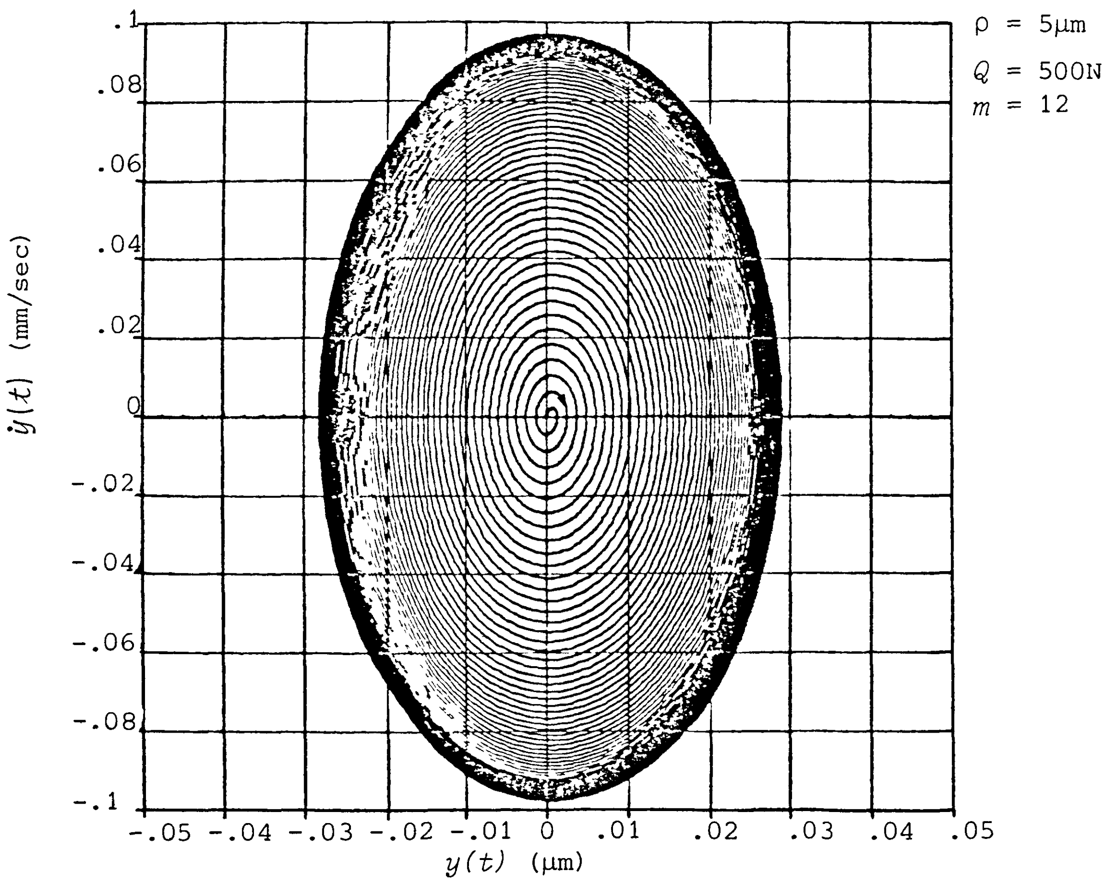

Fig 7.9 Phase plane trajectory $(y\text{-}\dot{y})$

major axis to the x-direction represents a larger phase-difference between x and y oscillation under lubricated conditions and is caused by the damping. Figures 7.11 and 7.12 show the elliptical (x-y) paths when the interference is reduced from 5μm to 3μm and 1μm respectively. The bearing effective stiffness reduces as the value of ρ decreases. Therefore, the ellipses increase in dimension, indicating larger residual oscillations. The corresponding damping contribution is more significant as ρ decreases, resulting in larger energy dissipation and higher decay rate of the x-oscillations (see figures 7.13 and 7.14, ρ = 3μm). Furthermore, the major axis of the(x-y)path trajectory has a larger angle of inclination to the x-axis showing more damping (by comparing figures 7.11 and 7.10).

This analysis indicates that reducing interference yields increasing ξ (section 7.14). On the other hand if the magnitude of the applied step load is increased, the bearing stiffness is increased and therefore the value of ξ is decreased. When the load is 2500N and ρ = 5μm, the amplitude of the residual x and y oscillations are approximately 5μm and 0.8μm respectively. This extent of equilibrium instability must be significant in most engineering applications such as in machine tool spindles [11]. However, in practice there are many additional sources of damping such as a small relative movement between the outer ring and housing in angular contact bearings, which is a major source of energy dissipation as well as the misalignment effect in rolling element bearings [12]. In machine tool spindle and bearing assemblies further damping is provided by the spindle joints as well as the oil seals, which may be used to reduce bearing chatter.

Note: Scales are different Q = 500N, m = 12

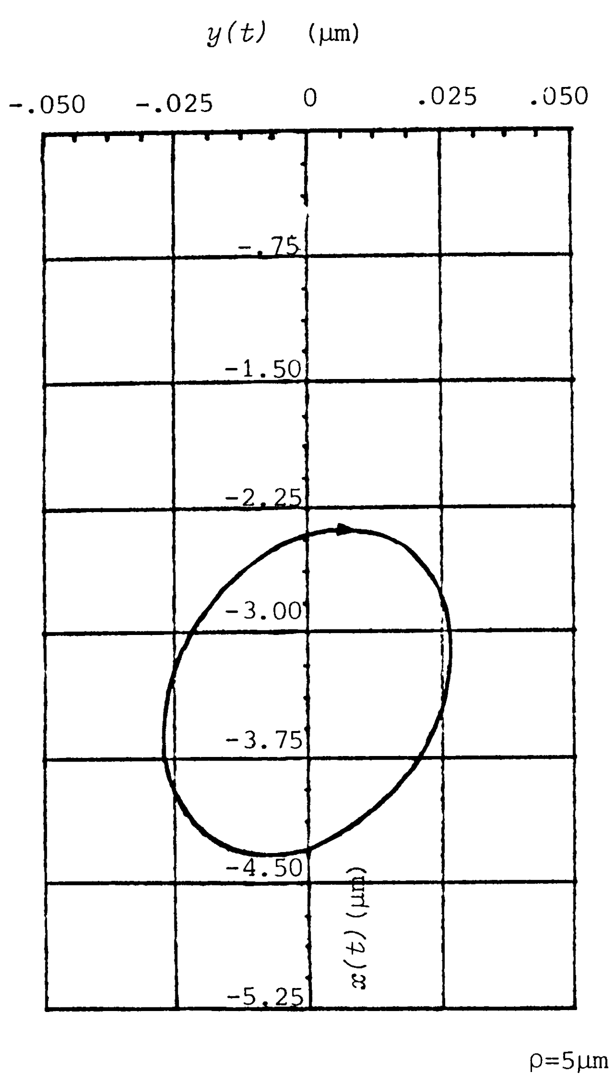

Fig 7.10 Shaft's centre locus

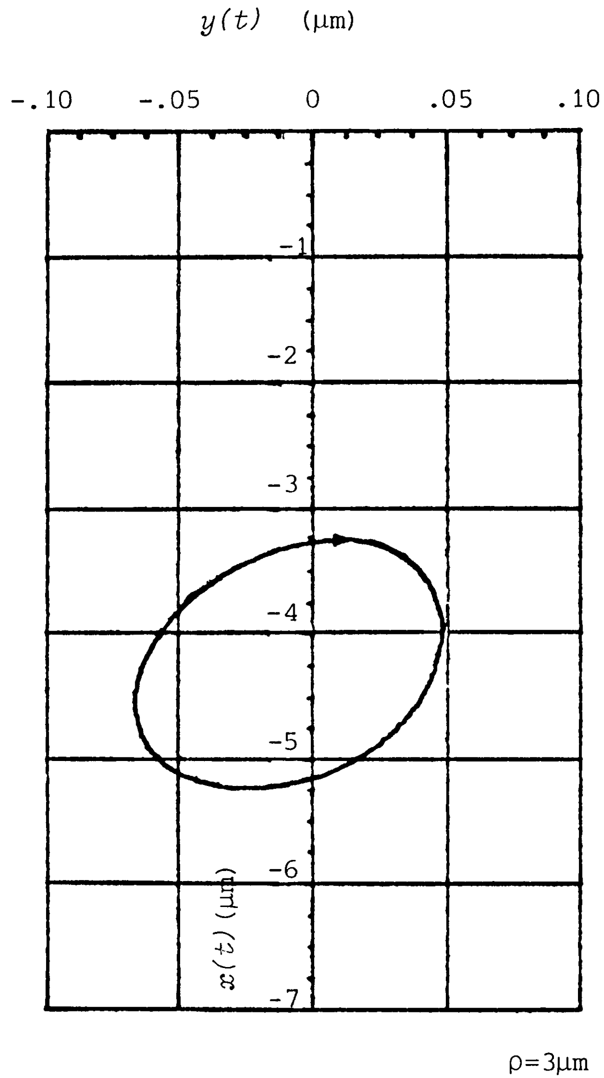

Fig 7.11 Shaft's centre locus

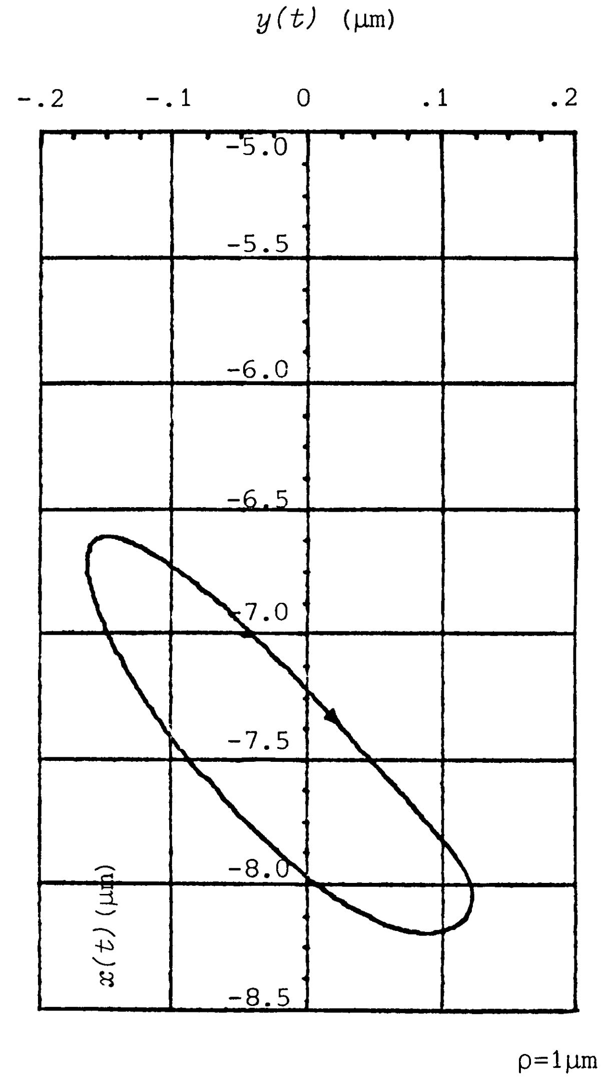

Fig 7.12 Shaft's centre locus

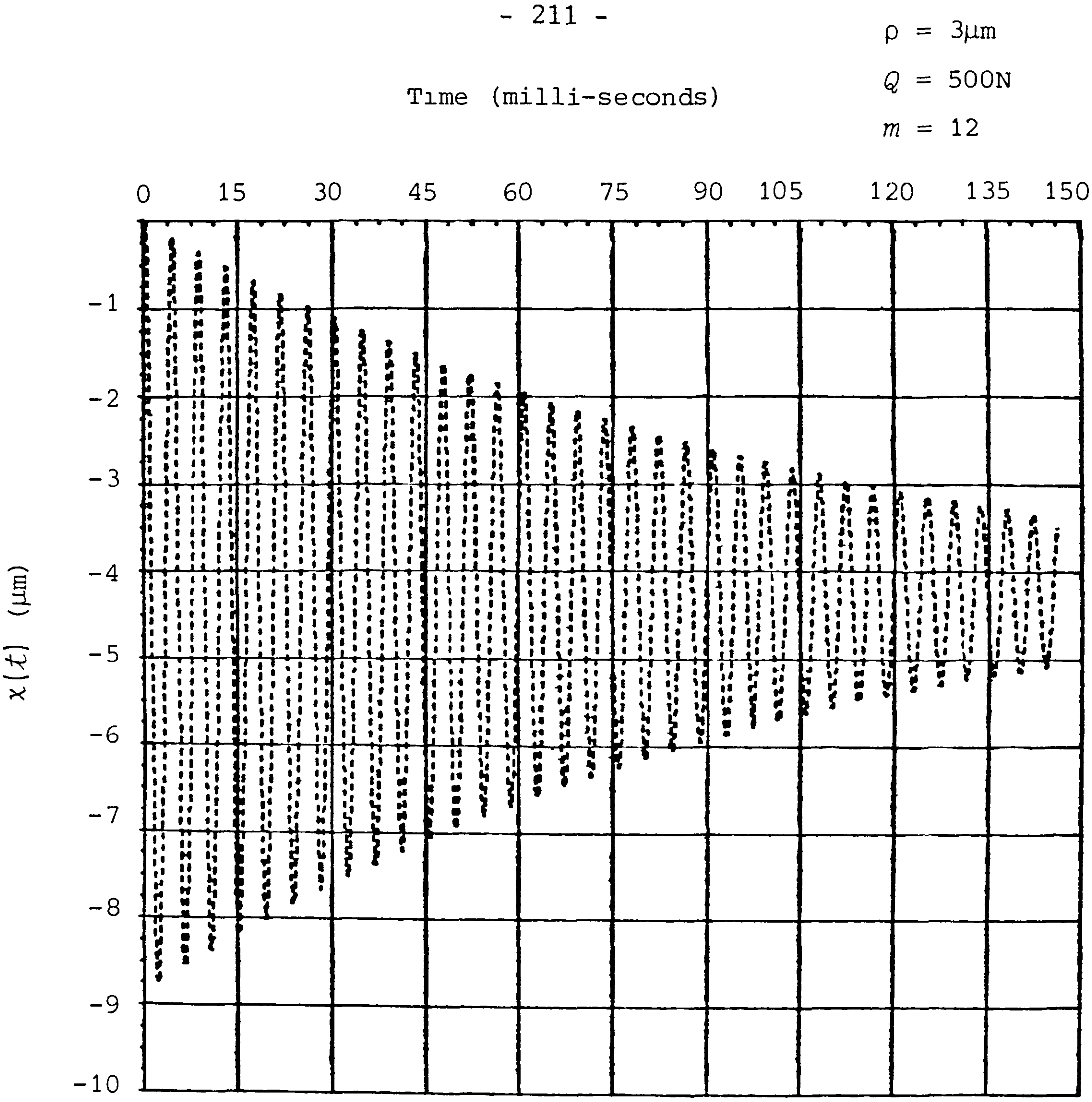

Fig 7.13 Shaft centre-line time history $x(t)$

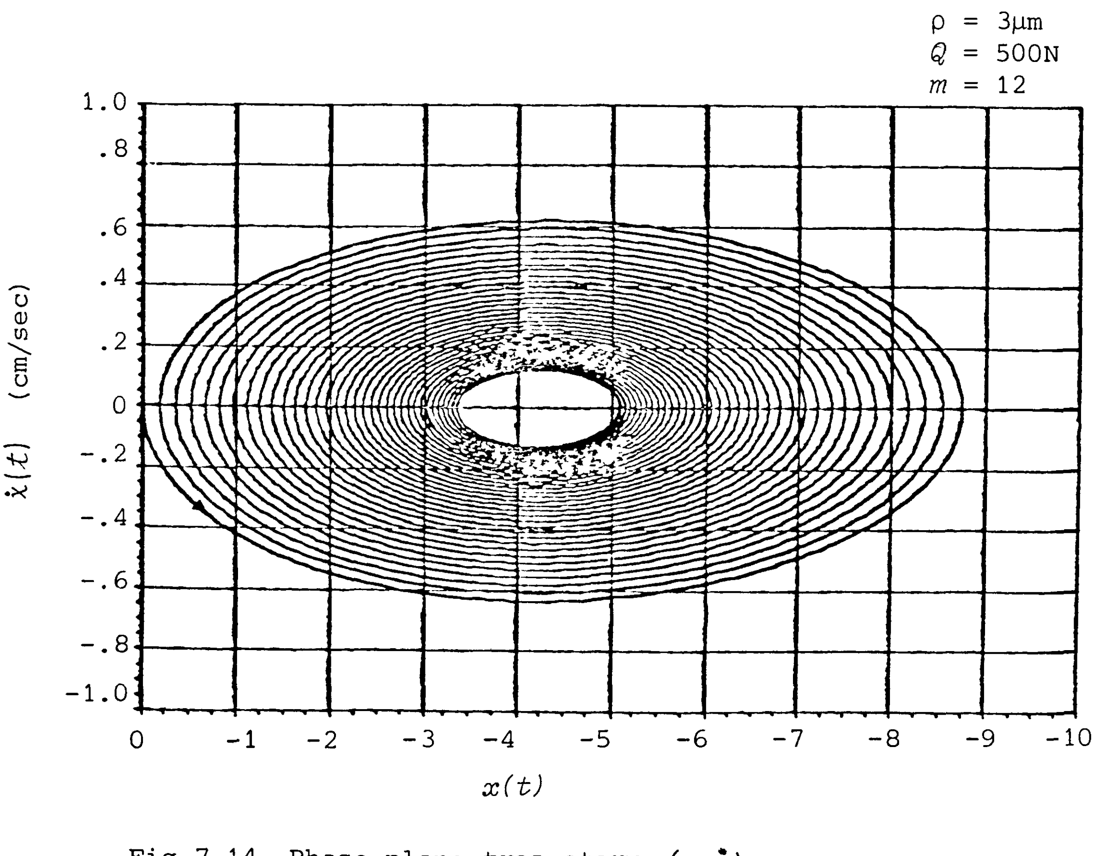

Fig 7.14 Phase plane trajectory $(x\text{-}\dot{x})$

7.13 Lubricant Film characteristics

The lubricant film history at any given contact (i) is illustrated by the steady-state limit cycle $(h-\dot{h})$ in figure 7.15. The limit cycle consists of two unequal portions of similar shape with a common point A. The larger segment, which is on the RHS of point A, represents the lubricant film behaviour in the unloaded regions of the bearing where there is a significant hydrodynamic contribution. The smaller part, on the LHS of point A, corresponds to the regions where the film is EHD and represents the more highly loaded areas of the bearing. There are five loops in each segment.

The period of one limit cycle corresponds to oscillations which commence and terminate at point A, describing all the trajectory loops in a to and fro motion, as outlined below:

The limit cycle trajectory goes from:

(i) outer to inner loops of the RH segment in a clockwise direction, then

(ii) inner to outer loops of the LH segment in an anticlockwise direction,

(iii) retraces the smaller part's loops from outer to inner in a clockwise direction,

(iv) retraces the larger part's loops from inner to outer in an anticlockwise direction.

Therefore, each of the trajectory loops are described twice. Here, $T_c = \frac{2\pi}{\omega_c}$ and is the period of the $(h-\dot{h})$ limit cycle, where ω_c is the cage set rotational speed. One loop traverse is the system natural frequency.

Figure 7.16 illustrates the corresponding steady-state $(x-\dot{x})$ limit cycle where its period here is $T = \frac{1}{20} T_c$ (the period is influenced by the bearing effective stiffness under a certain step gravity load). Therefore, the period to traverse each loop on the $(h-\dot{h})$ trajectory is equivalent to the limit cycle time of the $(x-\dot{x})$ trajectory. The points along the film axis (i.e. h-axis in fig 7.15) where $\dot{h} = o$, correspond to the positions $x = \Delta$, $\dot{x} = \pm\dot{x}_{max}$ and $\ddot{x} = o$. Furthermore, where $\dot{h} = \pm\dot{h}_{max}$ (on each loop), $x = \Delta\pm x_{max}$, $\dot{x} = o$ and $\ddot{x} = \pm g$.

The loops on the RHS of point A enclose larger areas than those on the LHS, indicating regions of greater energy dissipation. So squeeze film damping operates mostly in the region of thicker films.

Referring also to Fig 7.17 (and points B), the maximum load W_i occurs when $h = H_{min}$ (i.e. at the least oil film thickness) where the lubricant film has the greatest stiffness. The cyclic load distribution per ball (i.e. θ_i versus W_i) consists of 20 oscillations, corresponding to the 20 loops in the $(h-\dot{h})$ limit cycle. The maximum and minimum points on each oscillation in Fig 7.17 represent the positions $\dot{h} = \pm \dot{h}_{max}$ on the $(h-\dot{h})$ trajectory loops. The average value of W_i per oscillation describes the positions $\dot{h} = 0$ and $h = h_{min}$ or h_{max} within the respective loop of Fig 7.15. The points A_1 and A_3 relate to the ball transition into and out of the most loaded region of the bearing (i.e. the small segment of the $(h-\dot{h})$ limit cycle). Loading and unloading takes place during each oscillation with the average value of W_i increasing during the half cycle $A_0\ A_1\ A_2$ (see fig 7.17) and decreasing at the same rate during the remaining half cycle $A_2\ A_3\ A_4$.

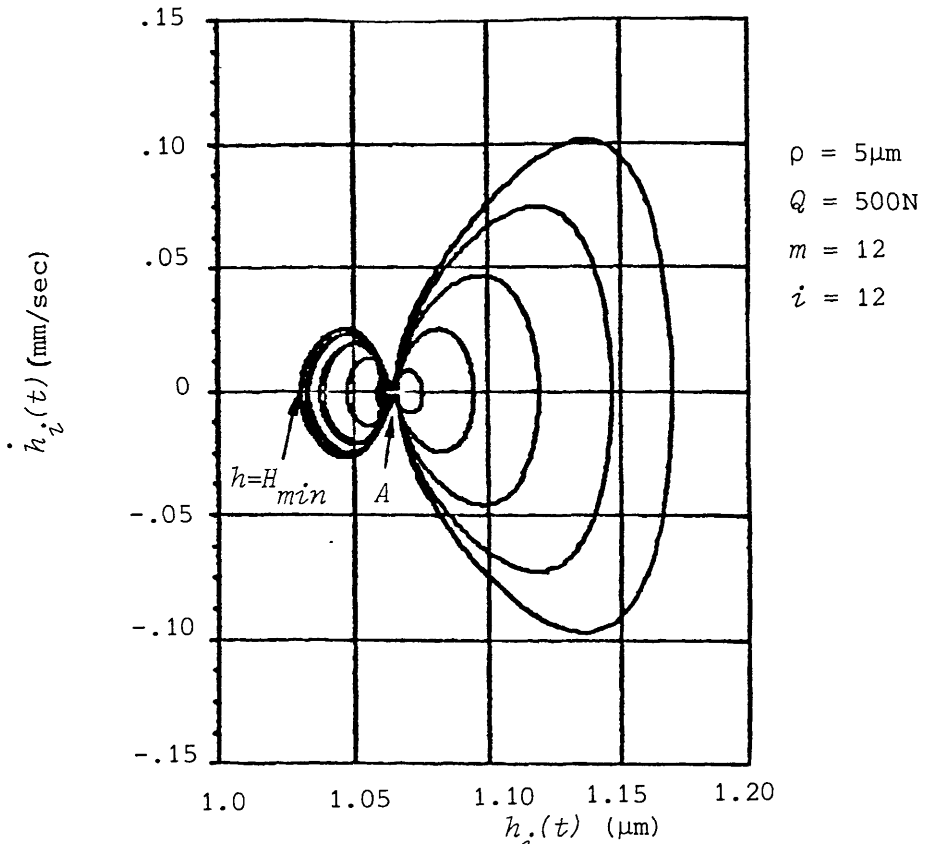

Fig 7.15 Steady-state limit cycle $(h\text{-}\dot{h})$

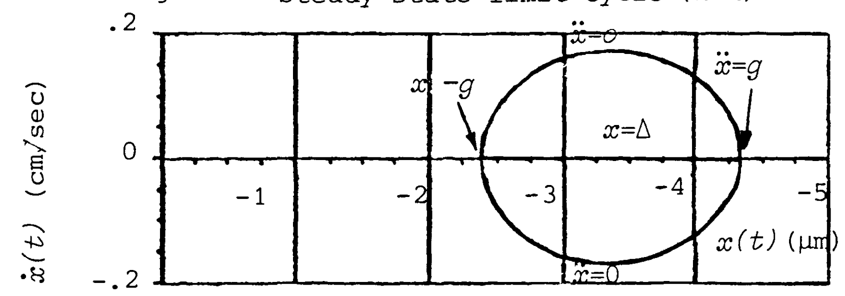

Fig 7.16 Steady-state limit cycle $(x\text{-}\dot{x})$

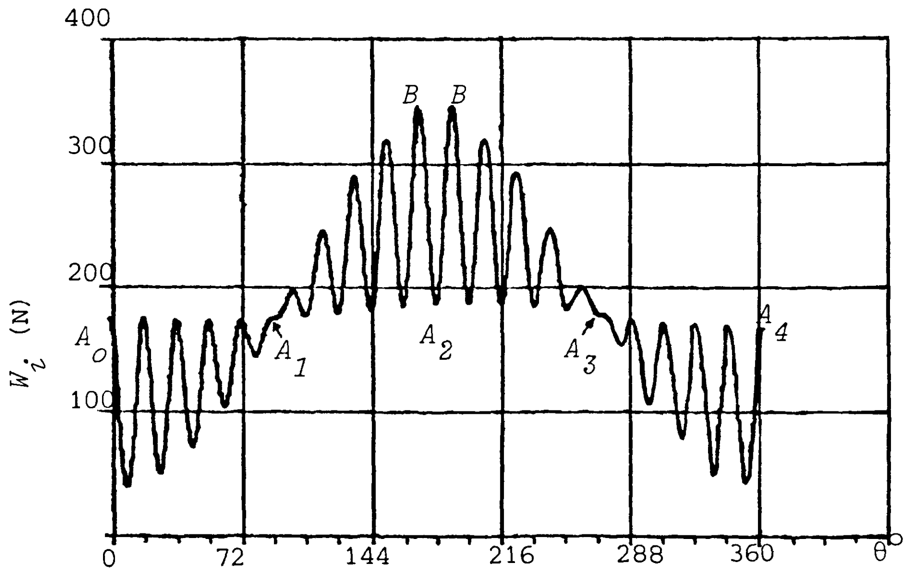

Fig 7.17 Steady-state cyclic load distribution per ball

7.14 Factors influencing the squeeze film damping

For a given bearing design the main parameters influencing the squeeze film damping are :

(i) The radial interference ρ,

(ii) The step gravity load Q,

and

(iii) The number of balls m.

The effect of each of these parameters on the system damping is obtained by progressively altering its value while keeping the remaining two constant. The resulting x direction oscillatory decay is analysed each time and the damping factor ξ is calculated. The ratio between two consecutive maxima is nearly constant. The oscillations' amplitude decrease in a geometric progression [13]. If x_n and x_{n+1} are the n^{th} and $n{+}1^{th}$ amplitudes respectively, then the logarithmic decrement $d = \ell n\left(\frac{x_n}{x_n+1}\right)$. For small damping [8]:

$$\frac{x_{n+1}}{x_n} = e^{-d} \doteq 1-d \quad . \tag{7.76}$$

Thus:

$$d = \frac{x_n - x_{n+1}}{x_n} \quad .$$

Therefore, by definition [8], the damping ratio $\xi = \frac{d}{2\pi}$. (7.78)

Fig 7.18 shows the variation of ξ with $\bar{\rho}(\bar{\rho} = \frac{\rho}{\delta_o})$. The initial film thickness is given by $h_o = \delta_o - \rho$. Therefore, $\bar{h}_o = 1-\bar{\rho}$ where $\bar{h}_o = \frac{h_o}{\delta_o}$. Point p on the graph corresponds to $\bar{\rho} = 1$ when $\bar{h}_o = 0$,

which is a hypothetical condition of zero film thickness. There is

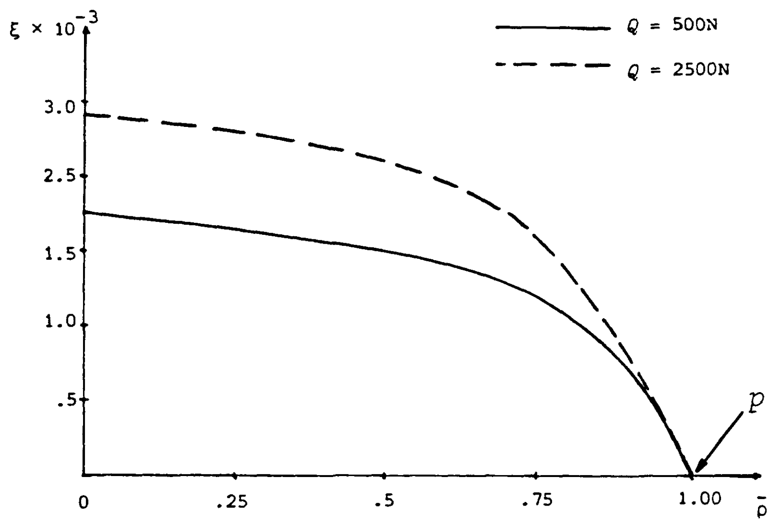

Fig 7.18 The influence of $\bar{\rho}$ on the damping factor ξ

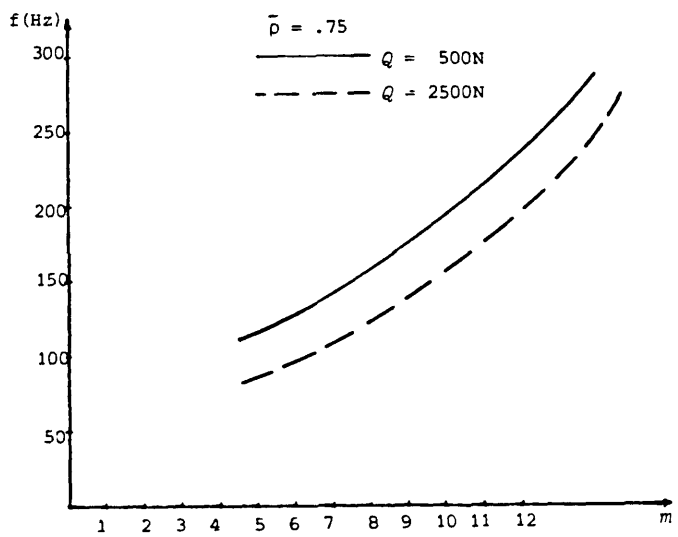

Fig 7.19 The influence of number of balls on the damped natural frequency

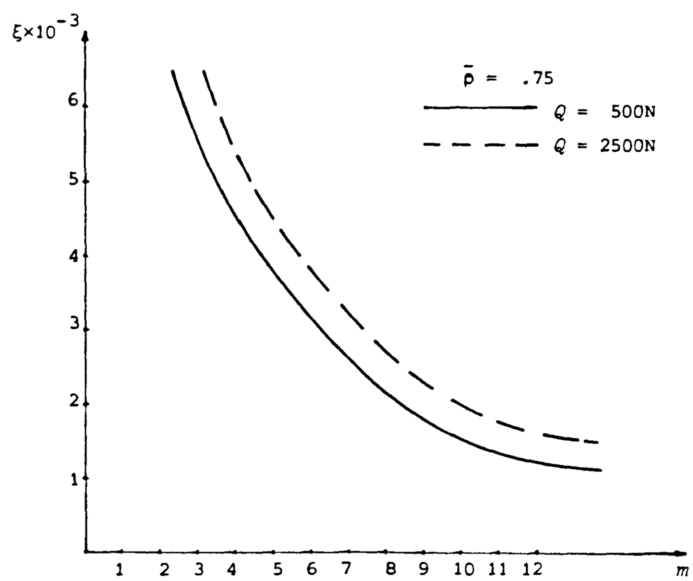

Fig 7.20 The influence of number of balls on the damping factor ξ

no damping under this condition (i.e. $\xi = 0$, Elastic Vibration).

When more balls are employed, the system stiffness is greater (see sections 6.9 and 6.10). Thus, both the initial static deflection and the subsequent dynamic oscillations are reduced. The damped natural frequency is therefore increased and so the damping factor ξ is reduced (see figures 7.19 and 7.20) respectively). Referring to Fig 7.19, when the value of step load Q is increased, the frequency is decreased (see section 6.11). The corresponding value of ξ increases as a result of larger gaps (divergence of bearing rings) which form in the lightly loaded regions and cause greater energy losses.

7.15 Vibrations of an unbalanced shaft

Fig 7.21 shows the $(x-\dot{x})$ cycle for an unbalanced shaft. It consists of two loops indicating a modulating response at two frequencies. One is the damped natural frequency of 260Hz (i.e. when Q = 500N, ρ = 5μm and m = 12) and the other relates to the ball-pass frequency of 159Hz. The unbalance frequency is $f_1 = \frac{\omega_1}{2\pi} = 33.3$ Hz.

Referring to Figure 7.22, the corresponding shaft's centre $(x-y)$ locus describes a complicated path. If the shaft is subjected to a step gravity load Q, $\omega_1 = 0$ and $e = 0$, the $(x-y)$ locus is a straight line along the x-axis, settling down to $x = \Delta$ in the steady-state condition. When $\omega_1 \neq 0$ and $e = 0$, this locus is an ellipse due to the residual x and y oscillations in the steady-state condition (see Figure 7.10). When $e \neq 0$, the out-of-balance force components in the x and y directions cause additional movements in these directions which are superimposed on the residual oscillations at the natural frequency. There are also stiffness changes in the x and y directions

ω_1 = 209 rad/sec

e = 25µm

ρ = 5µm

Q = 500N

m = 12

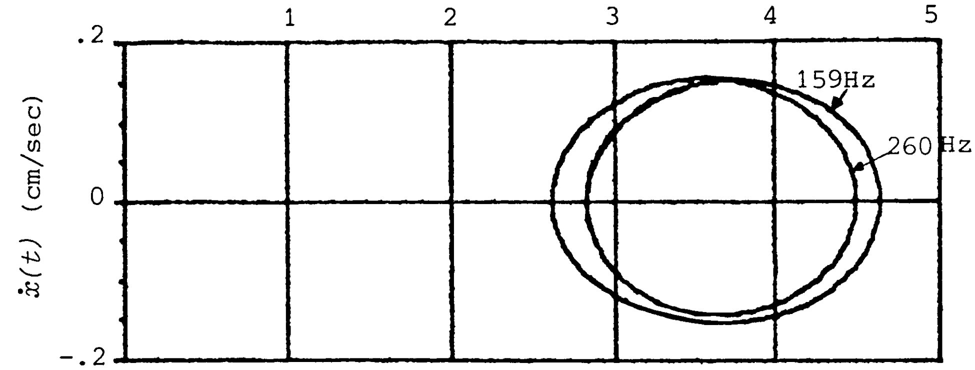

Fig 7.21 Steady-state $(x\text{-}\dot{x})$ cycle

ω_1 = 209 rad/sec

ϵ = 25µm

ρ = 5µm

Q = 500N

m = 12

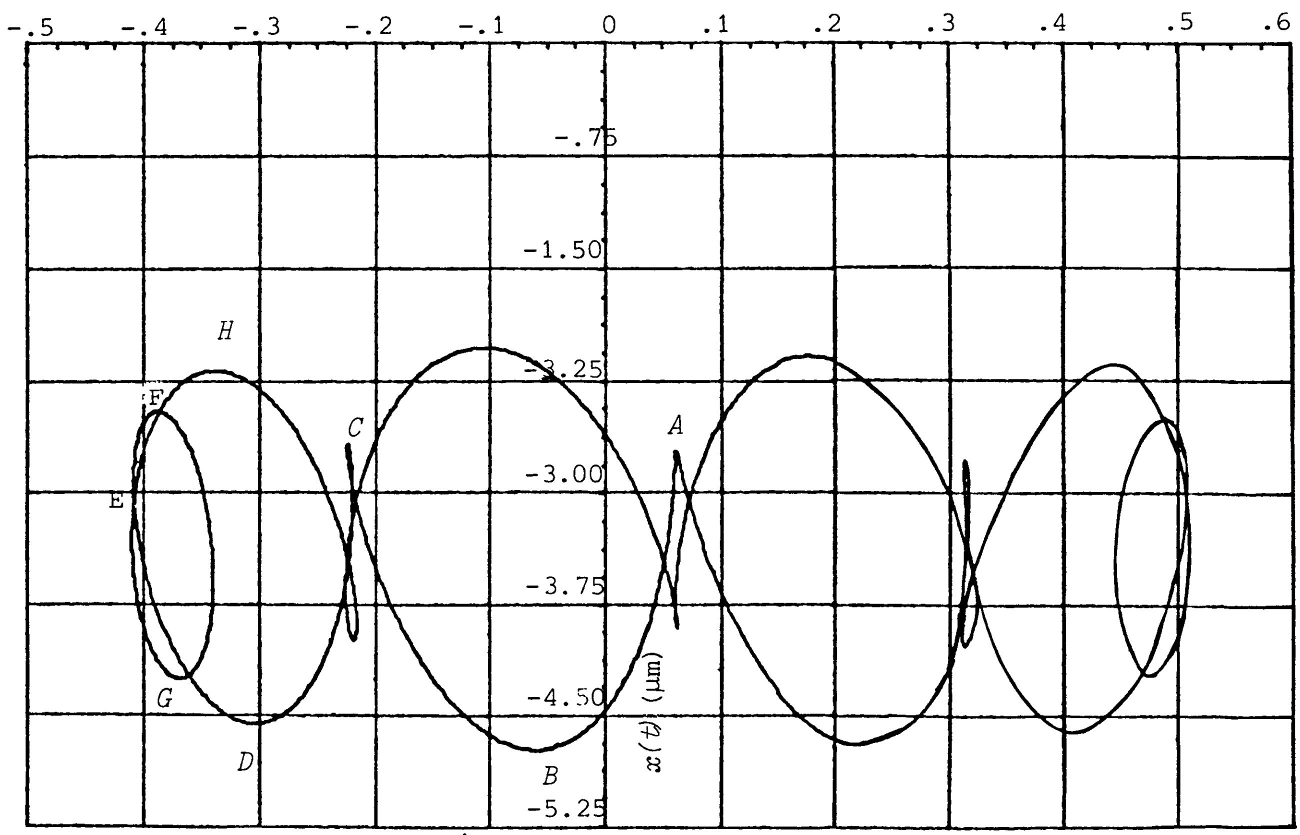

Fig 7.22 Shaft centre locus $(x\text{-}y)$

due to the orbital motion of balls introducing even further additional oscillation at the ball-pass frequency.

The $(x-y)$ path describes a closed loop in the steady-state condition. The period of one such loop is $T_1 = \frac{2\pi}{\omega_1}$. The period between any two successive cusp-like shapes (e.g. points A and B) corresponds to the ball-pass frequency (e.g. path ABC). $\ddot{x} = -g-\omega_1^2$, $\ddot{y} = 0$ at points A and C and $\ddot{x} = g + \omega_1^2 e$, $\ddot{y} = 0$ at point B. $\ddot{y} = \omega_1^2 e$ at a point almost 1/3 of the way along AB and $\ddot{y} = -\omega_1^2 e$ at a point almost 2/3 of the way along BC. The trajectory path DEFGEH and its mirror image along the positive y-axis corresponds to the motion at the damped natural frequency. $\ddot{x} = \pm (g + \omega_1^2 e)$ at points D and H respectively. $\ddot{x} = \pm g$ at points G and F correspondingly with $\dot{x} = 0$, $\ddot{y} = \pm\omega_1^2 e$ at point E.

7.16 Imperfections of rolling surfaces

The quality of a rolling bearing is described by the finish and the form of its surfaces. There are various types of surface defects generated during manufacture. These distributed features are usually defined in terms of their wavelength [1]. If the wavelength of the surface irregularities is longer than the width of a contact zone, the features are termed 'waviness' [3]. Other shorter wave length defects are termed 'roughness'.

The rolling motion can be considered continuous if the elements follow the surface terrain with their Hertzian contacts higher than the peak surface features. The peak curvatures are typically of order .05 - 2 μm (depending on the shaft diameter [14]), and the lubricant film thickness is usually between .3-1.5 μm depending on a number of governing parameters. These are principally the speed of the entraining motion, the amount of sliding between surfaces, the extent of preloading , the step load applied, and the squeeze film effect.

7.17 The EHD model with a wavy shaft

The model outlined in section 7.2 can be modified to include the shaft with a wavy periphery. Therefore, both wave distribution and the contact deformation features are allocated to the elastic non-bending shaft. When radial clearance is produced and the wave-length of surface irregularities is $\lambda_1 = \infty$ (i.e. no defects), the mutual convergence of rings is determined by $2(h_i - \delta_i)$, so there is radial clearance $2C_o$.

$$2(h_i - \delta_i) \quad x\cos\theta_i + y\sin\theta_i - 2C_o \quad . \tag{7.79}$$

If it is assumed that the shaft surface has a circumferential sinusoidal wave feature, the contact clearances are affected, and clearance is now a function of radial position θ'. So if $2C$ is the nett clearance at θ'

$$2C = 2C_o + 2C_p \sin\frac{2\pi\ell}{\lambda_1} \tag{7.80}$$

where C_o is now the initial radial clearance at the true shaft radius R_1 (see fig 7.23), C_p represents the waves amplitude, λ_1 the wavelength and $\ell = R_1\theta'$.

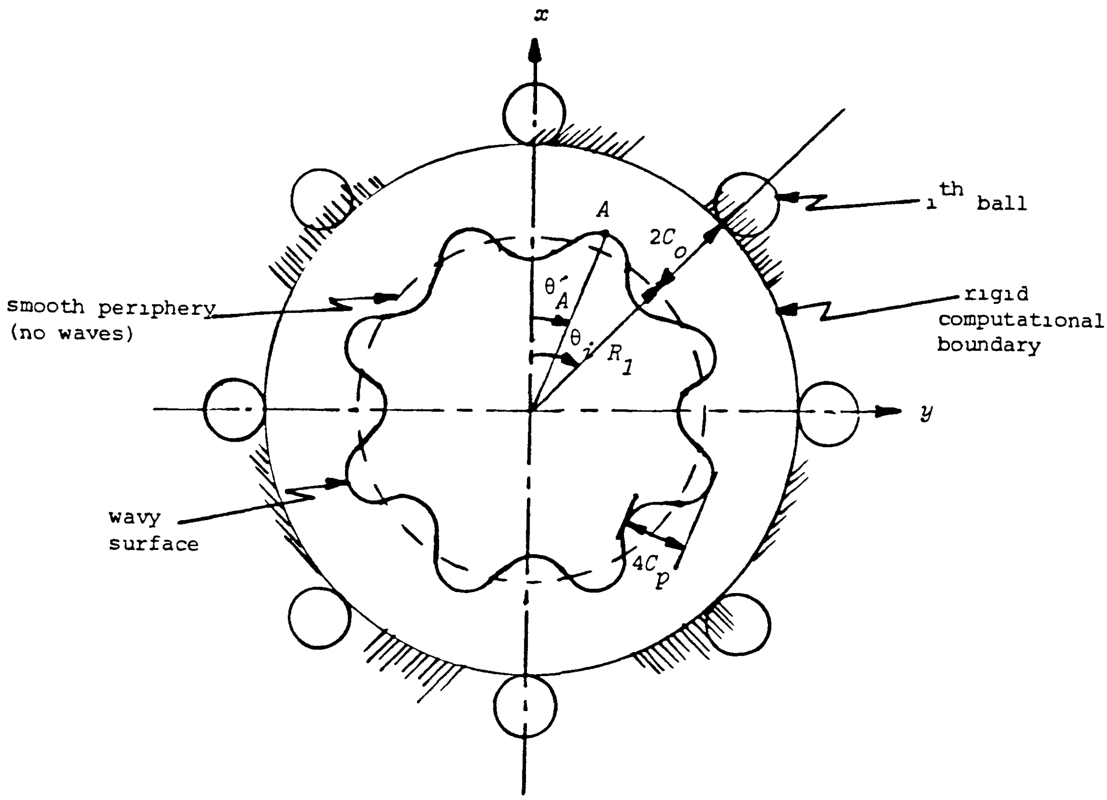

Fig 7.23 Shaft's wavy features

If $C_o = 0$, along a wavelength, radial interference takes place, as well as clearance. To provide a degree of overall interference initially, replace C_o by ρ_o : where $2C_o$ in equation (7.80) is replaced by $-2\rho_o$, and :

$$2\rho = 2\rho_o + 2\rho_p \, sin(\frac{2\pi\ell}{\lambda_1}) \; . \qquad (7.81)$$

If there are n waves describing the shaft's periphery, then :

$$\lambda_1 = \frac{2\pi R_1}{n} \; . \qquad (7.82)$$

The radial positions on each wave are defined by the angle θ'. The points of interest are when $\theta' = \theta_i$. Hence, the radial interference in the direction of the i^{th} contact is :

$$\bar{\rho}_i = \bar{\rho}_o + \bar{\rho}_p \sin(n\theta_i) \tag{7.83}$$

where $\bar{\rho}_i = \dfrac{\rho_i}{\delta o_i}$.

To reduce computing space allocation let $\delta_{o_i} = \delta_o$ (i.e. a universal initial contact deflection, no waves at $t = o$). The waves appear at $t = dt$ where $dt \lll 1$ milli-seconds.

The governing equations of the EHD model remain unaltered except for those describing the local deformation behaviour when $t > 0$:

$$2\bar{\delta}_i = 2(\bar{h}_o\ \bar{h}_i + \bar{\rho}_i) + \bar{x}\cos\theta_i + \bar{y}\sin\theta_i \tag{7.84}$$

and

$$\dot{\bar{\delta}}_i = \bar{h}_o\ \dot{\bar{S}}_i + \bar{\omega}_1\ \bar{\rho}_p n\cos n\theta_1 + \tfrac{1}{2}\{\dot{\bar{x}}\cos\theta_i + \dot{\bar{y}}\sin\theta_i + \bar{\omega}_c[\bar{y}\cos\theta_i + \bar{x}\sin\theta_i]\}. \qquad \ldots\ldots \quad (7.85)$$

where $\dot{\theta}' = \omega_1$ and $\theta' = \theta_1$.

The second term on the RHS provides the rate of change of radial interference $\bar{\rho}_i$ where $\dot{\bar{\rho}}_p = 0$ (i.e. the shaft's wavy contour is assumed to remain unaltered). Therefore, n must be chosen such that the contact width is considerably shorter than the wavelength of the waves. This ensures no change in the wavy features of the shaft (i.e. $\dot{\bar{\rho}}_p = 0$ and λ_1 = const). When a smaller number of waves is selected, a larger ρ_p may be considered. If the wavelength is of order of contact width it is only reasonable to assume $\dot{\bar{\rho}}_p \neq 0$. The implication of this might be to include a deformation rate function to describe the plastic behaviour of the contacts under load. This condition is not considered here.

7.18 Frequency Analysis Of The EHD Model With A Wavy Shaft

The value of ρ_p depends on the surface finish achieved by the machining process used. For a given surface finish the *r.m.s.* value of the wavy features can be correlated with the shaft diameter [14] (see Fig 7.24). When the shaft diameter, D = 40 - 50 mm, $\rho_{p\ r.m.s.} \doteqdot 1\mu m$. Therefore, the peak feature height is $\rho_p \doteqdot \sqrt{2}\mu m$.

Fig 7.25 shows the steady-state $(x-\dot{x})$ cycle when $n \doteq 48$. There are three loops which indicate a modulating oscillatory behaviour. The smaller inner loop corresponds to the forcing frequency introduced by the shaft's waviness. There are n waves which pass any given point on the stationary computational boundary (see Fig 7.23) as the shaft rotates once. Therefore, the 'waves-pass' frequency can be defined as the reciprocal of the period of time that elapses between two successive peaks passing a point on the computational boundary. Hence, $f_w = \frac{1}{T_w} = nf_1 \doteqdot$ 1596 Hz (T_w is the period to travel one wave length λ_1). The outermost loop represents the oscillations at the ball-pass frequency (often a component of the bearing frequency spectrum under forced vibration [3]) f_b = 159Hz. The middle loop corresponds to the system's natural frequency f = 260Hz.

Referring to figures 7.16 and 7.25, the static deflection position (i.e. $x = \Delta$) is unaltered since the waves do not affect the system stiffness characteristics (i.e. the position $x = \Delta$ is influenced by Q and m). The largest peak to valley oscillations are approximately of order of $2\rho_p$ and are independent of the number of waves. Fig 7.26 shows the $x-\dot{x}$ cycle for 24 waves. Comparing figure 7.26 with figure 7.25, the inner loop corresponding to the forcing frequency (i.e. waves frequency) is altered whilst the two remaining loops are unchanged.

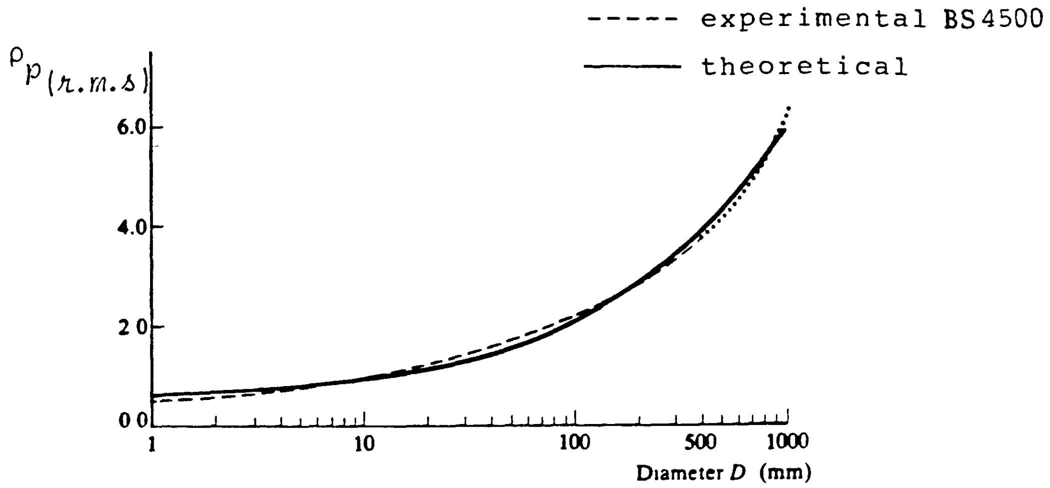

Fig 7.24 Feature variation with diameter [ref 14]

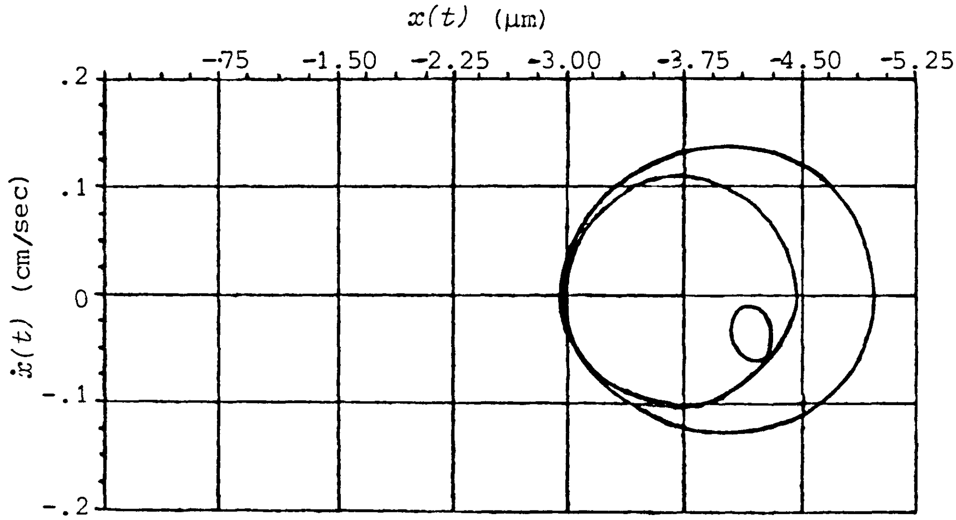

ρ = 5μm

ρ_p = √2μm

Q = 500N

ω_1 = 209 rad/sec

m = 12

Fig 7.25 Steady-state $(x\text{-}\dot{x})$ cycle n = 48

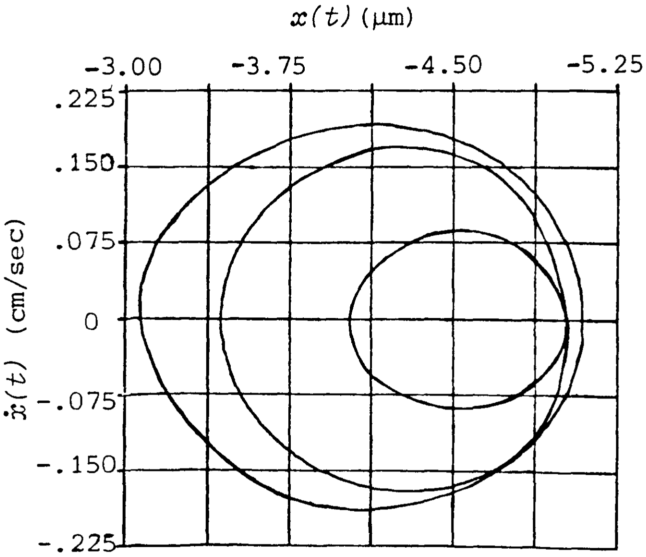

Fig 7.26 Steady-state $(x\text{-}\dot{x})$ cycle n = 24

The period to traverse the innermost loop of Fig 7.26 is $f_w = 24f_1 = 798Hz$.

7.19 REFERENCES

[1] RAGULSKIS, K.M., JURKAUSKAS, A. YU, ATSTUPENAS, V.V., VITKUTE, A. YU, and KULVEC, A.P.
"Vibration of Bearings",
Mintis Publishers, Vilnyus, 1974.

[2] GRAY, G.C., and JOHNSOM, K.L.
"The dynamic response of elastic bodies in rolling contact to random roughness of their surfaces",
Journal of Sound and Vibration, 1971, 22(3), pp. 323-342.

[3] WARDLE, F.P., and POON, S.Y.
"Rolling bearing noise - cause and cure",
CME, July/August 1983, pp. 36-40.

[4] DAREING, D.W., and JOHNSON, K.L.
"Fluid film damping of rolling contact vibrations",
J. Mech. Eng. Sci., 1975

[5] TIMOSHENKO, S. YOUNG, D.H., and WEAVER Jnr. W.
"Vibration problem in Engineering",
John Wiley & Sons, 4th Edition, 1974.

[6] HERTZ, H.
"Gesammelte Werke",
Volume 1, Leipzig, 1895

[7] BISHOP, R.E.D., and JOHNSON, D.C.
"The mechanics of vibration",
The syndics of the Cambridge University Press, 1960

[8] HARTOG, D.
"Mechanical vivrations"
Fourth edition, McGraw-Hill Book Company, 1956.

[9] PANOVKO, Ya.
"Elements of the applied theory of elastic vibration",
MIR publishers, Moscow, 1971.

[10] COLE, E.B.
"The theory of vibrations for engineers"
Crosby Lockwood and Sons Ltd., London, 1935.

[11] LACEY, S.J., WARDLE, F.P. and POON, S.Y.
"High speed bearings for CNC machine tool spindles",
CME, December 1983.

[12] ELSERMAN, M., HONGERLOOT, M., and SNOEYS, R.
"Damping in Taper rolling bearings",
Proc. 16th MTDR Conference, Manchester, 10.12 September 1975,
MacMillan, London , P. 223.

[13] THOMSON, W.T.,
"Vibration theory and application",
George Allen and Unwin Ltd, 1976

[14] THOMAS, T.R. (Ed.)
"Rough surface"
Longman, 1982.

CHAPTER 8

FURTHER DISCUSSIONS AND SUGGESTIONS FOR FUTURE WORK

The counterformal contact of two rolling discs (as in a disc machine) is meant to simulate the engagement of mating gear teeth. The effective contact stiffness in this simulation is provided by their crushing effect. However, the complete state of stress in a pair of contacting teeth is altered by another effect caused by tooth bending stresses as well as the direct contact stress which must be considered. Therefore, a general model of lubricated contact of gears must include non-linear elastic stiffnesses resisting bending as well as the corresponding elastohydrodynamic contribution along the line of common normal (see Figure 8.1). All the regression formulae employed in the thesis to describe the lubricant film behaviour under normal motion, assume a uniform squeeze velocity distribution over the contact area. In other words a universal surface deformation rate is assumed (i.e. all contact localities are distorted at the same rate) (see Figure 8.2). This assumption may be erroneous, especially when thin films are involved [1] (see Chapter3, Fig 3.3). Nevertheless, in the absence of any alternative formula they represent the only available tools that can be used to study the dynamic behaviour of normally approaching elements (i.e., crushing effect). It would be advantageous to vary the squeeze velocity W_s, keeping the remaining parameters constant, and thus obtain the corresponding values of W and h. The new squeeze form factor would include the effect of W_s on W as well as its effect on h. (Note that the present formulae were obtained for the effect of W_s on h alone, keeping W constant). Therefore the rate of change of local film thickness, $\dot{h}=W_s$ determines the local deformation rate $\dot{\delta}\propto\dot{W}$. It is not hard to imagine that whilst the surface at mid-contact may undergo a positive rate of deformation (i.e. move upwards), the local geometry at the end closures may suffer a corresponding negative

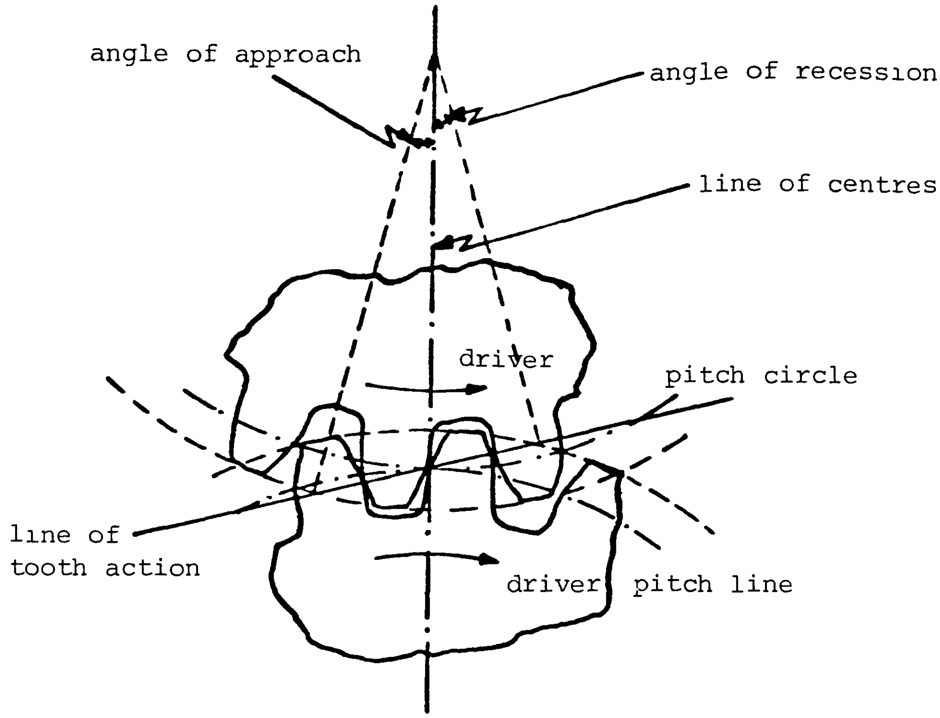

Fig 8.1 Involute gear teeth meshing

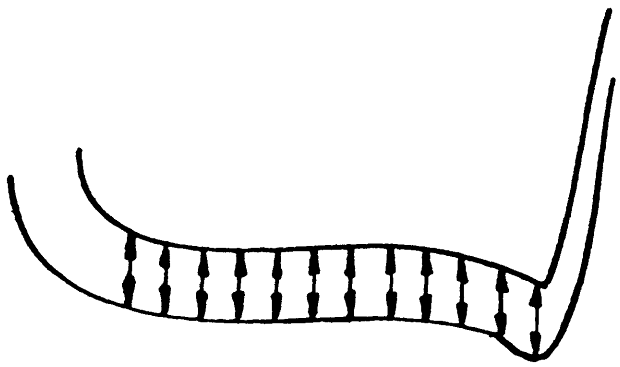

Fig 8.2 Uniform squeeze velocity profile
(elastic film shapes)

rate (i.e. downwards) (NB different h and $\dot{h}$ for the same value of W). Such considerations yields a general formula applicable for both $\dot{h} > 0$ or $\dot{h} \leq 0$.

In a recent work, Dowson et al [2] have considered the normal velocity variation along the contact length to be:

$$\frac{\partial h}{\partial t} = \frac{\partial h_o}{\partial t} + \frac{\partial \delta}{\partial t} \quad . \tag{8.1}$$

The term $\frac{\partial h_o}{\partial t}$ represents the rigid body squeeze-film action and the term $\frac{\partial \delta}{\partial t}$ is the local deformation rate. The authors compared the values obtained for the minimum oil film thickness which forms between the ring face and the cylinder liner in piston rings under the effect of (i) rigid body action (i.e. $\frac{\partial h_o}{\partial t}$) and (ii) local elastic deformation (i.e. $\frac{\partial h}{\partial t}$). The change in the lubricant film thickness was observed to be only 0.03 μm in 0.17μm.

Mostofi [3] considered the elastic film shape to be that given by equation (8.2) below:

$$h(x,y) = h(0,0) + (\delta(x,y)-\delta(0,0)) + P_r(x,y) \tag{8.2}$$

where $P_r(x,y)$ is the local profile.

However, he assumed that for the thin films found in EHL and high static loads, coupled with fairly high rolling speeds and low values of $\dot{h}$, the film shape is squeezed as $\dot{h} = \dot{h}_o$. Thus $\dot{\delta}(x,y) - \dot{\delta}(0,0) = 0$. The terms $\dot{\delta}(x,y)$ and $\dot{\delta}(0,0)$ are finite and have the same value across the film contour. Therefore, for rigid surfaces:

and
$$\left.\begin{aligned} \dot{\delta}(x,y) &= \dot{\delta}(0,0) = 0 \\ \dot{h}(x,y) &= \dot{h}_o \end{aligned}\right\} \tag{8.3}$$

and for elastic surfaces :

$$\left.\begin{aligned} \dot{\delta}(x,y) &= \dot{\delta}(0,0) \\ \text{and} \qquad \dot{h}(x,y) &= \dot{h}_o \end{aligned}\right\} \qquad (8.4)$$

If Mostofi's numerical model is used for one surface velocity at two different loads and the resulting films are of the same shape and equi-distant across the contact (e.g. Fig 8.2), his assumptions are justified. In any event, a new general regression formula which includes a squeeze form factor can replace the existing expressions both in EHD bearing and two discs models with minimal change.

The bearing model can be improved further by including a regime of traction as well as the existing contact normal reactions at the radial localities. Damping by sliding friction can then be studied as the slide-roll speed ratio varies. Furthermore, in rolling element/races contacts, the effect of misalignment can be included by incorporating it into Mostofi's solutions and amending the regression formula obtained in this thesis for the finite line contact condition (see Chapter 4). This effect is particularly observed in taper roller thrust bearings. It is found that the roller to rib contact geometry appears to critically determine the extent of misalignemnt [4] . Of course, misalignment can also be caused by mounting errors and shaft deflections. There are undesirable distributed defects such as race misalignment and off-sized rolling elements which cause additional vibrations of the bearing and also act as sources of energy dissipation [5].

The significance of fluid film damping has been studied by Dareing and Johnson [6]. They found that the fluid film damping is generated primarily by the squeeze film mechanism and that its contribution is a significant part of the total damping in a lubricated contact. This form of damping was found to be most effective under conditions of severe vibration. Compared with the dry contact conditions, the amplitude of vibration was reduced by nearby 50 per cent. Their findings conform closely to the behaviour of the EHD model outlined in Chapter 7. The extent of shaft oscillations in the loaded radial direction was found to decrease from 48μm (under dry elastic vibrations) to 2.5 μm (under EHD vibrations). when the step gravity load was 250Kg and the shaft angular velocity 83.5 rad/sec. The damping ratios obtained in reference [6] were in the range $\xi = 0.004 - 0.15$ and in the present model $\xi = 0.005 - 0.007$.

The damping characteristics of the lubricant film are dependent upon a number of governing parameters, one of which is the excitation frequency (see Section 5.1, Chapter 5). Using a servo-valve attachment and a signal generator, Smith [7] was able to introduce normal motion between two loaded rolling and sliding discs (see Section 4.1, Chapter 4) at different input frequencies. His aim was to establish a relationship between the input frequency and the contact load required to induce scuffing failure (keeping a constant slide-roll speed ratio). Unfortunately a pattern did not emerge from his results since a narrow range of frequencies (i.e. 0-60 Hz) was used. The numerical results obtained in Chapter 4 and the experimental work in reference [6] both show that in this range of excitation frequencies, the lubricant modal response is virtually unaltered.

To obtain a greater insight into lubricant behaviour it is possible to deposit a miniture pressure transducer [8,9] on a flat glass plate. A disc chamfered lightly at both sides (see Figure 3.4, Chapter 3) leaving a plane land in the middle can be loaded against the plate by a hydrostatic bearing. A piezo-meter or a servo-valve connected to this bearing and to a suitable signal generator can cause the disc to vibrate at a determined input frequency. If the plate was held firmly in a particular position the pressure profile in the region of its contact with the plane land could be monitored via the transducer signal. Fine movements of the glass plate relative to the disc would enable evaluation of the contact pressures at various sections. A three-dimensional finite line contact pressure distribution would result for each predetermined exciting frequency. If the disc was not rolling, pure squeeze effect would be observed. This effect can also be investigated by a moving indenter or piston instead of the disc, as suggested by Rohde et al [10]. It is expected that at the unblended edges of the plane land the pressures are higher in magnitude and end closure effects could be observed using interferometry to study the oil film contours [11]. The same principles can be applied to a two discs machine where the transducer is deposited on the mating unprofiled disc (running against the chamfered disc). In this case sliding motion may also be introduced. However, sliding may considerably reduce the life expectancy of the transducer. Safa [8] has studied the pressure and oil film profiles in the counterformal contact of mating discs under pure extraining motion using these principles.

REFERENCES

[1] HERREBRUGH, K.
"Elastohydrodynamic squeeze films between two cylinders in normal approach",
Trans. ASME. J. Lubn. Tech. April 1970.

[2] DOWSON, D, RUDDY, B.L. and ECONOMOU, P.N.
"The elastohydrodynamic lubrication of piston rings",
Proc. R. Soc. London, October 1982, pp. 409-430.

[3] MOSTOFI, A.
"Oil film thickness and pressure distribution in elastohydrodynamic elliptical contacts",
PhD Thesis, Imperial College of Science and Technology,
University of London, September 1981.

[4] RAHNEJAT, H. and GOHAR, R.
"Design of profiled taper roller bearings",
Tribology International, December 1979.

[5] MEYER, L.D., AHLGREN, F.F., and WEICHBRODT, B.Z.
"An analytic model of ball bearing vibrations to predict vibration response to distributed defects",
Trans. ASME, J. Mechanical Design, April 1980.

[6] DAREING, D.W. and JOHNSON, K.L.
"Fluid film damping of rolling contact vibrations",
J. Mech. Eng. Sci. 1975 (vol 17).

[7] SMITH, A.G.D.
"The effect of vibrational loading on gear scuffing",
PhD Thesis, University of London, October 1977.

[8] SAFA , M.M.A.
"Elastohydrodynamic studies using thin film transducers",
PhD Thesis, University of London, April 1982.

[9] JOHNS RAHNEJAT, P.M.
"Pressure and stress distribution under elastohydodynamic contacts",
PhD Thesis, to be submitted, University of London.

[10] ROHDE S.M., WHICKER, D. and BROWNE, A.L.
"Dynamic analysis of elastohydrodynamic squeeze films",
Trans. ASME, J. Lubn. Tech. July 1976.

[11] BAHADORAN, H. and GOHAR, R.
"End closure in elastohydrodynamic line contact",
J. Mech. Eng. Sci. 1974 (vol 16).

APPENDIX A1

The hydrodynamic reaction is considered to contain the effects of entraining and squeezing motions such that:

$$\bar{W}_i = \bar{W}_{SQ_i} + \bar{W}_{RL_i} \tag{A1.1}$$

where W_{SQ_i} is the contribution due to the squeeze effect and W_{RL_i} is the corresponding effect due to rolling. The latter term is available from reference [1].

$$W_{RL} = \frac{K_{c_1}}{h^{\frac{1}{2}}}$$

$$K_{c_1} = \frac{6\sqrt{2}\pi U\eta_o}{(1+2\bar{R})}\,(R_x^3/\bar{R})^{\frac{1}{2}} \tag{A1.3}$$

To obtain W_{SQ}, the pressure distribution in an elliptical contact under pure squeeze effect must initially be found using (A1.4) below:

$$\frac{\partial}{\partial x}\left(\frac{h^3}{\eta_o}\frac{\partial P}{\partial x}\right) + \frac{\partial}{\partial y}\left(\frac{h^3}{\eta_o}\frac{\partial P}{\partial y}\right) = 12\frac{\partial h}{\partial t} \tag{A1.4}$$

where the squeeze velocity term $W_s = \frac{\partial h}{\partial t}$, h is the film thickness, t is time, η_o and P represent lubricant viscosity and pressure respectively. Equation (A1.4) is made dimensionless by using the groups in (A1.5)

$$\bar{x} = \frac{x}{\sqrt{2R_x h}},\quad \bar{y} = \frac{y}{\sqrt{2R_y h}}$$

$$P^* = \frac{P h^2}{12R_x\eta_o\frac{\partial h}{\partial t}} \qquad \bar{h} = \frac{h}{h_o} \tag{A1.5}$$

$$\bar{R} = R_x/R_y$$

where h_o is the central oil film thickness and R_x and R_y represent the reduced radii in x and y directions respectively.

Thus:

$$\frac{\partial}{\partial \bar{x}}\left(\bar{h}^3 \frac{\partial P^*}{\partial \bar{x}}\right) + \bar{R} \frac{\partial}{\partial \bar{y}}\left(\bar{h}^3 \frac{\partial P^*}{\partial \bar{y}}\right) = 2 \tag{A1.6}$$

To obtain an expression for $\bar{P}$, let:

$$P^* = \frac{K}{(1+\bar{x}^2+\bar{y}^2)^2} \tag{A1.7}$$

substituting for $\bar{P}$ into (A1.6) from (A1.7) yields the value of k

$$k = -\frac{1}{2(1+\bar{R})} \tag{A1.8}$$

Thus:

$$P^* = \frac{1}{2(1+\bar{R})(1+\bar{x}^2+\bar{y}^2)^2} \tag{A1.9}$$

The instantaneous load W_{SQ} can be found by integrating the pressure distribution domain:

$$W_{SQ} = \int_{x=\infty}^{+\infty}\int_{y=-\infty}^{+\infty} P^* dxdy \tag{A1.10}$$

Using the dimensionless groups of equation (A1.5), it follows:

$$\frac{W_{SQ} \quad h \bar{R}^{\frac{1}{2}}}{24 R_x^2 \eta_o} \cdot \frac{\partial t}{\partial h} = -\frac{1}{(1+\bar{R})} \int_{-\infty}^{+\infty}\int_{-\infty}^{+\infty} \frac{d\bar{x}\, d\bar{y}}{(1+\bar{x}^2+\bar{y}^2)^2} \tag{A1.11}$$

Integrating with respect to $\bar{x}$, implementing the limits of integration, and using the principal of symmetry, the right hand side (R.H.S) reduces to:

$$\text{R.H.S.} = -\frac{\pi}{2(1+\bar{R})}\int_{o}^{+\infty}\frac{d\bar{y}}{(1+\bar{y}^2)^{3/2}} \tag{A1.12}$$

This is a standard integral solved by the substitution $\bar{y} = \tan\phi$.
Hence:

$$\text{R.H.S.} = -\frac{\pi}{2(1+\bar{R})}\int_{\phi=0}^{\pi/2}\cos\phi\, d\phi = \frac{\pi}{2(1+\bar{R})} \tag{A1.13}$$

substituting (A1.13) back into (A1.11) the instantaneous load W_{SQ} is obtained

$$W_{SQ} = -\frac{12\pi R_x^2 \eta_o}{(1+\bar{R})\bar{R}^{-\frac{1}{2}}h}\cdot\frac{\partial h}{\partial t} \tag{A1.14}$$

where $\frac{\partial h}{\partial t} = W_s$.

$$\bar{W}_i = \frac{W_i}{ER_x^2} \quad \text{and} \quad U^* = \frac{U\eta_o}{ER_x} \; .$$

Therefore, the total hydrodynamic load contribution in an elliptical contact is given by equation (A1.15).

$$\bar{W}_i = \frac{12\pi}{\bar{R}^{-\frac{1}{2}}h_o^{*\frac{1}{2}}}U^*\left(\frac{1}{\sqrt{2}(3+2\bar{R})\bar{h}_i^{\frac{1}{2}}} - \frac{W_s^*}{h_o^{*\frac{1}{2}}(1+\bar{R})\bar{h}_i}\right) \tag{A1.15}$$

If $\bar{R} = 1$ $$\bar{W}_i = \frac{12\pi U^*}{h_o^{*\frac{1}{2}}}\left(\frac{1}{5\sqrt{2}\bar{h}_i^{\frac{1}{2}}} - \frac{W_s^*}{2h_o^{*\frac{1}{2}}\bar{h}_i}\right) \tag{A1.16}$$

For the purpose of simple manipulation within the model it is desirable to approximate the expression (A1.15) by an equivalent exponential function of the form in (A1.17).

$$\bar{W}_i = \frac{C_{iso}(1-B_o e^{\bar{\lambda}\dot{\bar{h}}_i})^{\frac{1}{2}}}{\bar{h}_i^{\frac{1}{2}}} \qquad \text{(A1.17)}$$

Where B_o=.75,as obtained for the first term in equation (7.7). When $\dot{\bar{h}}_i = o, \bar{W}_i$ is the contribution due to pure rolling effect.

$$\bar{W}_i = \frac{C_{iso}}{2\,\bar{h}_i^{\frac{1}{2}}} \qquad \text{(A1.18)}$$

The pure rolling equation may be obtained from equation (A1.19).

$$\bar{W}_i = \frac{\sqrt{c}U^*}{\bar{h}_i^{\frac{1}{2}}} \qquad \text{(A1.19)}$$

thus:

$$C_{iso} = 2\sqrt{c} \quad U^* \qquad \text{(A1.20)}$$

Where:

$$\sqrt{c} = \frac{12\pi}{\sqrt{2}\bar{R}^{-\frac{1}{2}}\; h_o^{*\frac{1}{2}}(3+2\bar{R})} \qquad \text{(A1.21)}$$

The maximum percentage error between equations (A1.17) and (A1.15) when $\dot{\bar{h}}_i$=o, $\bar{R}$=1 and for any combination of U^* and $\bar{h}_i$,is found to be about 5%. The exponential coefficient $\bar{\lambda}$ is set such that both expressions (A1.15) and (A1.17) yield $\bar{W}_i$=o at the same value of $\dot{\bar{h}}_i = \dot{\bar{h}}_{\ell_2}$ Referring to equation (A1.15) if $\dot{\bar{h}}_i = \dot{\bar{h}}_{\ell_2}$ then:

$$\dot{\bar{h}}_{\ell_2} = \frac{(1+\bar{R})\bar{h}_i^{\frac{1}{2}}}{\sqrt{2}(3+2\bar{R})} \qquad \text{(A1.22)}$$

and equation (A1.17) :

$$\dot{\bar{h}}_{\ell_2} = -\frac{1}{\bar{\lambda}}\,\ell n B_o \quad . \tag{A1.23}$$

Equating (A1.22) and (A1.23) $\bar{\lambda}$ is found

$$\bar{\lambda} = -\frac{\sqrt{2}\,(3+2\bar{R})\,\ell n B_o}{(1+\bar{R})\;\bar{h}_i^{\frac{1}{2}}} \tag{A1.24}$$

but $\bar{\lambda} = \lambda\tau h_o$ (see equation 7.10 section 7.3).

Hence:

$$\lambda = -\frac{\sqrt{2}\,(3+2\bar{R})\,\ell n B_o}{(1+\bar{R})\,\tau h_i^{\frac{1}{2}}} \tag{A1.25}$$

If $\bar{R} = 1$ then :

$$\lambda = \frac{5\ell n B_o}{\sqrt{2}\,\tau h_i^{\frac{1}{2}}} \quad . \tag{A1.26}$$

References

[1] CAMERON, A.

"The Principles of Lubrication",

Longsmans Green & Company Limited, 1966.

APPENDIX A2

When $\dot{\bar{h}}_i > \dot{\bar{h}}_{\ell_2}$, equation (7.7) ceases to provide a real value for load $\bar{W}_i$. This condition does not usually occur under low to moderate loads (i.e. m=50-250kg) and when an interference fit of $\rho \geqslant 3\mu m$ is used. However, when $m>250$kg *and* $\rho<3\mu m$ the squeeze velocity term $\dot{\bar{h}}_i = \dot{\bar{S}}_i$ in equation (7.7) may exceed the hydrodynamic limit $\dot{\bar{h}}_{\ell_2}$ for a given number of balls and in a short period of time. To ensure continuity of the load regime, a hyperbolic function was used to describe the variation of $\dot{\bar{W}}_i$ with $\dot{\bar{h}}_i$.

$$\bar{W}_i = \frac{c_3}{\dot{\bar{h}}_i} + c_2 \tag{A2.1}$$

where c_2 and c_3 are constants to be evaluated. Note that

when : $\dot{\bar{h}}_i \longrightarrow \infty, \quad \bar{W}_i \longrightarrow c_2$

and $\dot{\bar{h}}_i = \dot{\bar{h}}_{co}, \quad \bar{W}_i = \bar{W}_{co}$

For a smooth load variation, equation (A2.1) and the hydynamic contribution of equation (7.7) must yield the same value at the change over point (co) where,

$$\dot{\bar{h}}_{co} = .999\ \dot{\bar{h}}_{\ell_2} \tag{A2.2}$$

Thus :

$$\frac{\Psi_2}{\bar{h}_i^{\frac{1}{2}}} \left[1-B_o e^{\bar{\lambda}\dot{\bar{h}}_{co}}\right]^{\frac{1}{2}} = \frac{c_3}{\dot{\bar{h}}_{co}} + c_2 \tag{A2.3}$$

The value of $\bar{h}$ is constant along any given graph of $\bar{W}_i$ versus $\dot{\bar{h}}_i$ (see fig 7.4). Furthermore, the slopes of equations (A2.1) and the second term of the equation (7.7) must coincide at $\dot{\bar{h}}_i = \dot{\bar{h}}_{co}$ when $\bar{h}_i$ = const. Using equation (7.7):

$$\frac{\partial \bar{W}_i}{\partial \dot{\bar{h}}_i} = -\frac{\psi_2 B_o \bar{\lambda}\, e^{\bar{\lambda}\dot{\bar{h}}_{co}}}{2\bar{\lambda}_i^{-\frac{1}{2}}} (1 - B_o\, e^{\bar{\lambda}\dot{\bar{h}}_{co}})^{\frac{1}{2}} \tag{A2.4}$$

and differentiating the hydrodynamic term of (A2.1) the slope is :

$$\frac{\partial \bar{W}_i}{\partial \dot{\bar{h}}_i} = \frac{C_3}{\dot{\bar{h}}^2_{co}} \tag{A2.5}$$

C_2 is then obtained by equating (A2.4) and (A2.5).

$$C_3 = \frac{\psi_2 B_o \bar{\lambda}\dot{\bar{h}}^2_{co}\, e^{\bar{\lambda}\dot{\bar{h}}_{co}}}{(1-B_o e^{\lambda\dot{\bar{h}}_{co}})^{\frac{1}{2}}} \tag{A2.6}$$

and replacing for C_3 from (A2.6) into (A2.3) C_2 can be obtained.

The new $\ddot{\bar{S}}_i$ term is formulated by equating the time differentials of (A2.1) and the equation (7.51), thus:

$$\ddot{\bar{S}}_i = \frac{-\nu\, \dot{\bar{\delta}}_i\, \bar{\delta}_i^{\nu-1} \dot{\bar{h}}_i^2}{C_3} \tag{A2.7}$$

Values of C_2 and C_3 are constant for a given value of $\bar{h}_i$. However, during the system dynamic response, these constants vary instantaneously because changes in $\ddot{\bar{S}}_i$ yield new values of $\dot{\bar{h}}_i = \dot{\bar{S}}_i$ and $\bar{h}_i = 1 + \bar{S}_i$. Therefore, as $\bar{h}_i$ varies, we move from curve to curve in Figure 7.4.

Design of profiled taper roller bearings

H. Rahnejat and R. Gohar*

Numerical solutions are given for the pressure distribution and footprint shape for a tapered roller. The effect of roller misalignment and its axial profile are investigated for a taper roller thrust bearing. A design procedure is described which indicates the value and whereabouts of the maximum pressure that will occur under equilibrium conditions

Cylindrical rollers of roller bearings having no reduction in diameter towards their ends (no axial profiling) can, when compressed between their races, suffer from high contact pressures which may lead to failure by fatigue spalling. Some recent papers[1,2] discuss the necessary axial profiling to reduce these untoward effects. The work reported below attempts to extend the theory for cylindrical rollers to taper rollers. Such an analysis is made more complicated because taper rollers are in equilibrium under three contact force vectors instead of two, a characteristic which must be accounted for in the design of their axial profiles.

Taper roller bearings allow for simultaneous high radial and thrust loads to be carried, normally at low to moderate speeds. This capability is advantageously exploited in helicopter gear boxes, car wheel bearings, and also on some mainshaft bearings of gas turbines. The rollers and raceways are truncated cones and it is important to ensure that their relative motion approaches true rolling. Thus, for the single row radial bearing in Fig 1 we see that the extensions of the lines of contact ideally all meet at a common apex situated on the bearing axis. A rib (guide flange) is necessary to ensure that when the tapered roller is subjected to a radial or thrust load, or a combination of both, a reaction force results between the rib and the roller. This force resists the tendency to squeeze the roller out of the bearing. Sliding friction at the rib makes this type of bearing normally unsuitable for high speed application. The magnitude of the axial load component determines the roller conical angle, α, which can vary typically between 5° and 19°. The larger α the more the distribution of pressure on the roller conical surface will differ from that on a cylindrical roller. These anomalies will be discussed in the work reported below.

Pressure distribution and footprint shape

Several recent papers have given results for pressure distribution and footprint shape (sometimes called planform shape) on radially loaded cylindrical rollers[1,2,3]. A boundary integral equation assembles a matrix of influence coefficients which are then used to find contact pressure distribution and the footprint dimensions for a roller of specified material geometry and applied load. The method employed for taper rollers is basically the same except

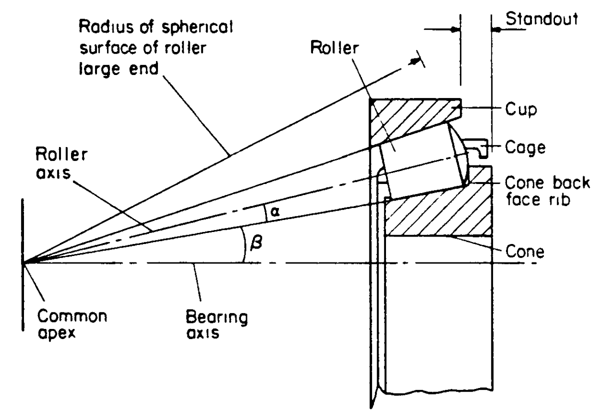

Fig 1 Terminology in taper roller bearings

that the varying roller radius throughout its length is taken into account. The problem is treated as one of elastostatics with no elastohydrodynamic film intervening anywhere, as static contact pressures are of similar magnitude. The following assumptions are also made:

(1) The contact surfaces of the rollers and their races are frictionless with all elements being considered as elastic half spaces.

(2) The maximum width of the footprint is small compared to the radius of curvature of the contiguous surfaces. The footprint dimensions are, in their turn, large compared with the elastic deflections and axial profile.

(3) The footprint length is smaller than the distance between the roller end faces. This is an important assumption, but quite valid when one considers that the rollers are generally profiled axially, so making them lose contact with the races before their ends are reached. The races are wider than the rollers with the cone rib geometry not considered to affect directly the radial pressure on the adjacent roller conical surface. The rib has, however, an indirect contribution by virtue of its reaction force vector with the roller end, being coincident with the cup and cone reactions in order to achieve equilibrium.

(4) Any small roller solid body rotation angle θ necessary for force equilibrium, ($< 0.1°$) is not considered to affect significantly the rib reaction vector direction or its point of application.

Department of Mechanical Engineering, Imperial College of Science and Technology, Exhibition Road, London SW7 2BX, UK

0301–679X/79/060269–07 $02.00 © 1979 IPC Business Press

(5) As in the case of cylindrical rollers[1,2], radial contact pressures vary elliptically in the transverse direction. This assumption appears justified because of the large ratio of footprint length to width and the circular arc shape of the transverse deflected profile.

(6) Again, because of the large aspect ratio of the footprint, for cylindrical rollers, the local contact width is assumed to be proportional to the local maximum pressure there[1,2], the constant of proportionality being found from Hertz's equation for an infinitely long cylindrical contact:

$$\frac{a_1(j)}{P_m(j)} = \frac{a_0}{P_0} = \frac{R}{2E_1} \tag{1}$$

A similar relation is assumed to apply for taper rollers except that the effect of varying roller radius must be included, that is:

$$\frac{a_1(j)}{P_m(j)} = \frac{a_0}{P_0} \times \frac{R(j)}{R_0} \tag{2}$$

Both Equations (1) and (2) depend additionally on the validity of assumption (3) Thus, for an unprofiled roller, the validity of Equations (1) and (2) would be questionable near the roller ends. Likewise excessive loads, sufficient to bring the footprint up to the roller ends, would invalidate assumptions (3) and (6). The possibility of this state of affairs occurring in practice seems unlikely.

Formulation of the equations

The numerical method employed calculates the deflection of an elastic half space due to a pressure distribution acting over part of its plane surface (the footprint). This is divided into a number of equal length overlapping rectangular based elements upon each of which is a pressure distribution formed of isosceles triangles longitudinally and ellipses transversely. A typical element is shown in Fig 2, and an assembly of such elements in the zy plane is shown in Fig 3. The lines joining the vertices of the triangles form a piecewise linear locus of maximum pressures which must fall to zero at the ends.

Using the elastic contact boundary integral equation[2], the deflection at any point $\bar{x}, \bar{y}$ on the footprint due to a single element of pressure acting on a base of area $4\,a_1c$, is given by:

$$\bar{d}\,(\bar{x}, \bar{y}) = I \tag{3}$$

where

$$I = \int_{-1}^{+1}\int_{-1}^{+1} \frac{(1 - \bar{x}_1{}^2)^{1/2}\,(1 - |\bar{y}_1|)\,d\bar{x}_1 d\bar{y}_1}{[(\bar{a}\bar{x} - \bar{a}_1\bar{x}_1)^2 + (\bar{y} - \bar{y}_1)^2]^{1/2}}$$

Nomenclature

xyz	Cartesian coordinates for deflection
$x_1y_1z_1$	Cartesian coordinates for a pressure element
a	Footprint width at y
a_0	Footprint width at $y = 0$
a_1	Footprint width at y_1
b	Maximum footprint half length
c	Pressure element triangle half base length
R	Roller radius at y
R_0	Roller radius at $y = 0$
L	Roller length between end faces
F	Straight length of axial profile
r	Profile crown edge radius
h	Height of roller to rib contact point above the lower race
d	Race deflection due to a pressure element
ω	Total race deflection at x, y
ω_r	Total roller deflection at x, y
Z_r	Roller axial profile
Z_{mr}	Misaligned roller
X_1, X_2	Distance of the roller top and bottom centres of pressures from the small end
θ	Roller solid body rotation angle
α	Roller conical half angle
ϕ	Inclination to the lower race of the contact normal to the roller and rib
n	Number of rollers in the bearing
P	Pressure at x, y
P_0	Pressure at o, o
P_m	Pressure at o, y
E_1, E_2	Young's moduli for race and roller
ν_1, ν_2	Poisson's ratios for race and roller
R_1, R_2	Reactions on the bottom and top of the roller
R	Reactions between rib and roller large end
M_1, M_2	Moments about roller small end due to bottom and top reactions
W	Total load on the thrust bearing.
$\bar{x}$	x/a
$\bar{x}_1$	x_1/a_1
$\bar{y}$	y/c (Measured from centre of pressure element)
$\bar{y}_1$	y_1/c (Measured from centre of pressure element)
$\bar{d}$	$\dfrac{d\pi E_1}{a_1 P_m(1 - \nu_1{}^2)}$
$\bar{P}_m$	P_m/P_0
$\bar{\omega}$	$\dfrac{\omega\pi E_1}{a_0 P_0(1 - \nu_1{}^2)}$
K	$\dfrac{1 - \nu_1{}^2}{1 - \nu_2{}^2}$
$\bar{Z}_r$	$Z_r\pi E_1/a_0P_0(1 - \nu_1{}^2)$
$\bar{Z}_{rm}$	$Z_{rm}\pi E_1/a_0P_0(1 - \nu_1{}^2)$
$\bar{R}$	R/R_0
$\bar{a}$	a/c
$\bar{a}_1$	a_1/c
$a_1{}^*$	a_1/a_0

and, in accordance with assumption (5), the pressure is elliptical transversely. Integration with respect to $\bar{y}_1$ can be done analytically. Integration with respect to $\bar{x}_1$ uses Simpson's rule where we need only solve I for $\bar{x} = 0$. The total deflection at any point along the $\bar{y}$ axis due to an assembly of elements can now be found. Expressed non-dimensionally this comes to:

$$\bar{\omega}_{(i)} = \sum_{i=1}^{n} \left(\frac{a_1(j)}{a_0}\right)\left(\frac{P_m(j)}{P_0}\right)\left(\frac{R(j)}{R_0}\right) I(i,j) \qquad (4)$$

$$(j = 1, n)$$

where $\omega_{(i)}$ is the dimensionless total deflection at the ith rectangular element due to all the elemental pressures. The set of equations $\omega_{(i)}$ can be expressed in matrix form as:

$$(\bar{\omega}) = [I'] \, (\bar{P}_m) \qquad (5)$$

where $(\bar{\omega})$ is the dimensionless deflection vector along the $\bar{y}$ axis, $(\bar{P}_m)$ is the vector of unknown maximum pressures, and $[I']$ is the matrix of influence coefficients, a typical element being.

$$I'(i,j) = a_1{}^*(j)\bar{R}(j)I(i,j) \qquad (6)$$

Deflection and roller profile

Fig 4 represents the contact region of a taper roller, having axial profile Z_r, and its race before and after deformation in the zy plane. At any y

$$(\omega(0,0) - \omega(0,y)) + (\omega_r(0,0) - (\omega_r(0,y)) = Z_r \qquad (7)$$

Assume that the ratio of deflection differences is inversely proportional to the ratio of the respective Young's moduli of the race and roller[2]. Thus,

$$\frac{\omega(0,0) - \omega(0,y)}{\omega_r(0,0) - \omega_r(0,y)} = \left(\frac{E_2}{E_1}\right)\left(\frac{1-\nu_1^2}{1-\nu_2^2}\right) \qquad (8)$$

or

$$\bar{\omega}(0,\bar{y}) = \bar{\omega}(0,0) - \bar{Z}_r \frac{E_2 K}{KE_1 + E_2} \qquad (9)$$

If $E_1 = E_2$ and $\nu_1 = \nu_2$, (which is usually the case) deflection differences on the race surface are half the undeformed axial profile. A similar equation applies in the $\bar{x}$ direction, where the undeformed roller profile is defined by its local radius, R. Equation (8) is one of those used in determining

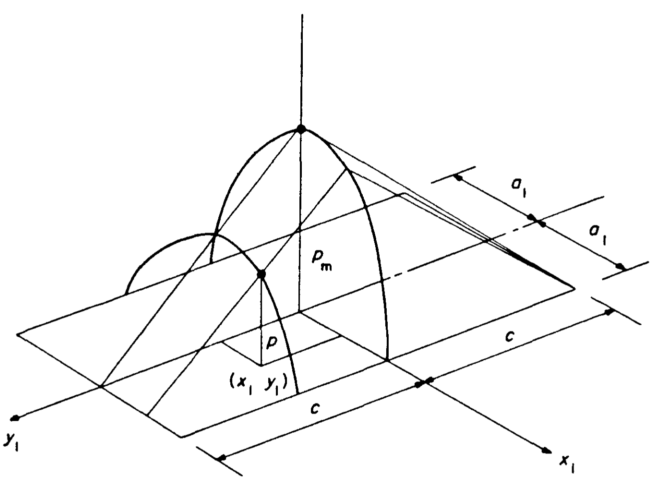

Fig 2 Pressure element shape

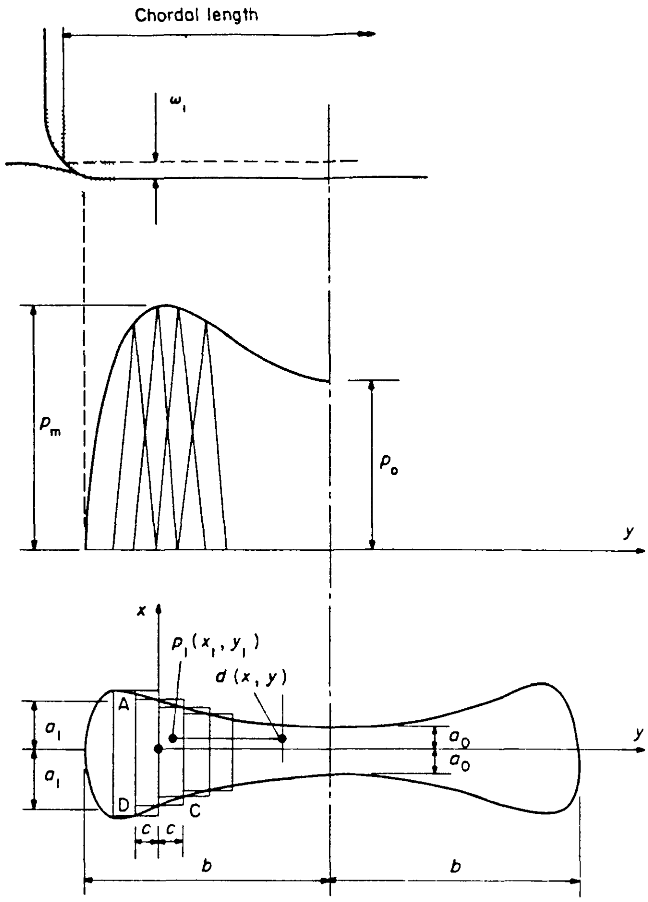

Fig 3 Assembly of pressure elements

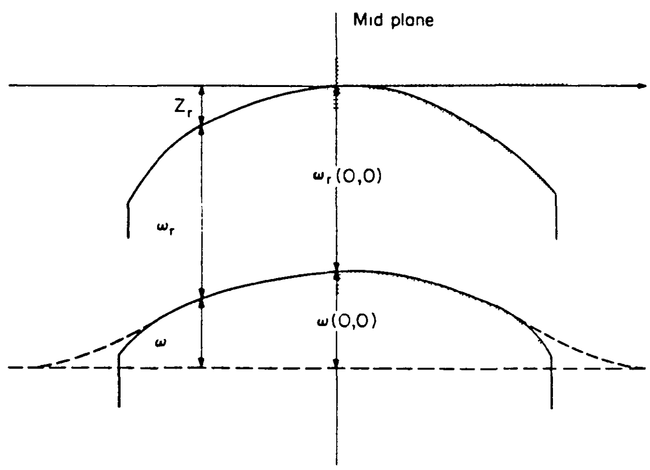

Fig 4 Deflections of the taper roller and a race

Hertz' equations for pressure distribution and footprint width for a long cylindrical roller. These are:

$$a_0 = \left(\frac{2R_{1,2}R_0}{bE_r}\right)^{1/2} \qquad (10)$$

where

$$E_r = \frac{1}{\pi}\left[\frac{1-\nu_1^2}{E_1} + \frac{1-\nu_2^2}{E_2}\right]$$

and

$$P_0 = \frac{R_{1,2}}{\pi b a_0} \qquad (11)$$

$R_{1,2}$ represent the bottom or top reactions on the taper roller. Equations (10) and (11) are used to find a_0 and P_0 at the taper roller mean radius R_0. They are needed in Equation (4), and are assumed to be accurate because R_0 is far from the roller ends where plane strain conditions can be assumed. A further equation is necessary in order to estimate the race dimensionless deflection at the footprint centre. This is given by Lundberg's expression:[2]

$$\bar{\omega}(0,0) = \pi\left(Ln\frac{4b}{a_0} + \frac{1}{2}\right) \tag{12}$$

The actual centre deflection $\omega(0,0)$ is kept constant throughout the iterative procedure described below, though a_0, P_0, b and $\bar{\omega}(0,0)$ may alter.

Calculation procedure for pressure distribution: radial load

1. For a roller and race of given geometry and material properties, a trial load is assumed with b taken as half the roller length, L. $\omega(0,0)$ is calculated from Equations (10), (11) and (12) and is kept constant thereafter.

2. Primarily, a rectangular footprint of length L is assumed and with the specified profile $\bar{Z}_r$, $\bar{\omega}(0,\bar{y})$ is found from Equation (9), thus yielding $[\bar{\omega}]$.

3. The integral I is evaluated from Equation (3) enabling $[I']$ to be assembled. For cylindrical rollers, $\bar{R}(j) = 1$ in Equation (6).

4. $(\bar{P}_m)$ is then calculated from Equations (5).

5. With the new $\bar{P}_m(j)$, a new footprint $\bar{a}_1(j)$ is determined from Equation (2).

6. The procedure is then repeated until the difference between corresponding pressures in successive iterations is within a specified limit.

7. The value of the load can then be found by numerical integration of the pressure distribution. By taking a new trial load, the relationship between it and $\omega(0,0)$ is obtained.

Misaligned rollers

As three reaction force vectors must act upon each roller, it may suffer a solid body rotation θ to come into equilibrium. In addition, a solid body rotation may be caused by terminal couples due to elastic shaft loading, or even by misalignment errors in the shaft and bearing assembly. Angle θ is simply taken as an independent variable in addition to the race central deflection $\omega(0,0)$. A modified equivalent taper roller undeformed axial profile is then determined, thus allowing the calculation procedure outlined above, to be followed as before. Fig 5 shows such a roller with some arbitrary profile, rotated through θ and pushed into a race. The modified profile Z_{rm} is taken relative to a tangential line through the roller to race undeformed contact centre. From elementary geometry, the modified profile at distance $(i-1)c$ from the centre is:

$$Z_{rm} = \frac{Z_r}{\cos\theta} - \sin\theta\,[Z_r\tan\theta \mp (i-1)c] \tag{13}$$

where (−) and (+) refer respectively to the lhs and rhs of the footprint centre.

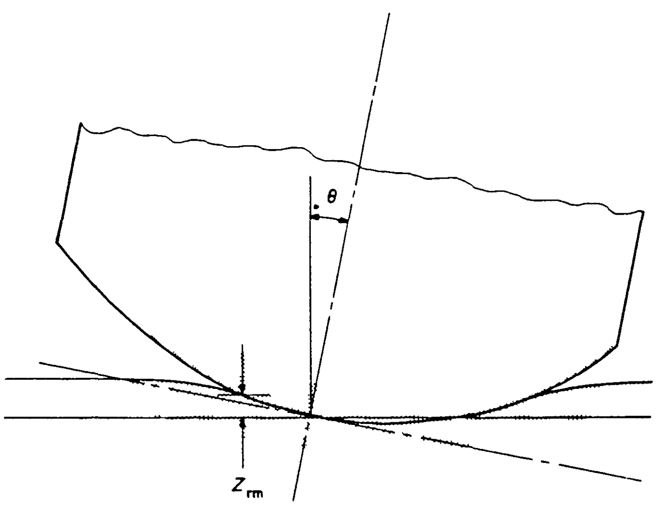

Fig 5 Misaligned roller axial profile

Forces on a taper roller

When a taper roller bearing is loaded, a reaction force results between the back face rib and the spherical end of the roller, the direction of which is normal to the roller end at the contact point. This force is in equilibrium with two normal reaction forces at the roller cup and roller cone contacts. The following analysis is confined for simplicity to a taper roller thrust bearing under a total applied load, W, though it can also apply with slight modification to a radial bearing of the type shown where the local load on each roller varies between the loaded and unloaded zones. A typical thrust bearing taper roller is shown in Fig 6 in equilibrium under three static force vectors, centrifugal, gyroscopic, gravity and viscous forces being neglected. Now there must be no precondition that the reactions R_1 and R_2 act at their footprint mid-points. They are different in magnitude, and their application points will depend upon their respective pressure distributions and footprint shapes. These in their turn are affected by the cone reaction vector R, Z_r, and θ. Derner has pointed out the existence of such factors in the discussion to reference 5. Referring to Fig 6, for equilibrium:

$$R_2 = \frac{R_1}{\cos 2\alpha - \sin 2\alpha\tan\phi} \tag{14}$$

and

$$W = nR_1 \tag{15}$$

ϕ depends upon the large end to cone geometry. Assuming that θ is less than 0.05°, ϕ can be considered constant as θ changes so that the vector R has constant direction.

We are now in a position to carry out a further calculation procedure to determine the force vectors and their application points on the roller in Fig 6. Knowing W, the number of rollers n, and their geometry, the force magnitudes can be determined from Equations (14) and (15). Another important roller property that is required is its axial profile, for this will be a factor in the determination of the pressure distributions caused by R_1 and R_2. The magnitude of the maximum pressure will decide whether the roller bearing is adequate for the applied load.

The calculation procedure described above, which determines the pressure distribution for a given Z_{rm}, θ, and $\omega(0,0)$, can be used to construct design charts for the roller top and bottom contacts. We take, as our example, a steel thrust bearing roller having the following characteristics:

Number of rollers, $n = 12$
Roller length, $L = 0.0128$ m
Crown edged radius, $r = 0.762$ m (the relevant definitions are shown in Fig 7).
Straight region, $F = 0.0076$ m
Taper roller conical angle, $2\alpha = 19.67°$
Large end diameter = 0.0089 m
Small end diameter = 0.0046 m
Angle between the common normal at the cone back-face rib and roller contact point, and the roller to cone axial contact line, $\phi = 0°$
Height of common normal application point above the bottom race, $h = 0.0016$ m.

The design charts for this roller are shown in Fig 8 (top and bottom reactions). They are for a clockwise rotation, θ, of the roller. This means that the top pressure distribution (causing R_2) will have greater deflections towards the roller small end as θ increases. The effect at the bottom race (causing R_1) will result in greater deflections towards the large end as θ increases. The charts relate θ to moments M_1 and M_2 about the roller small end, caused by the top and bottom pressure distributions, for various race centre deflections $\omega(0, 0)$. They also enable lines of contact force $R_{(1,2)}$ to be drawn.

The method of determining the equilibrium pressure distributions on a roller is as follows.
1. Assume that θ is zero and for a given W, calculate R_1, R_2, and R from Equations (14) and (15).

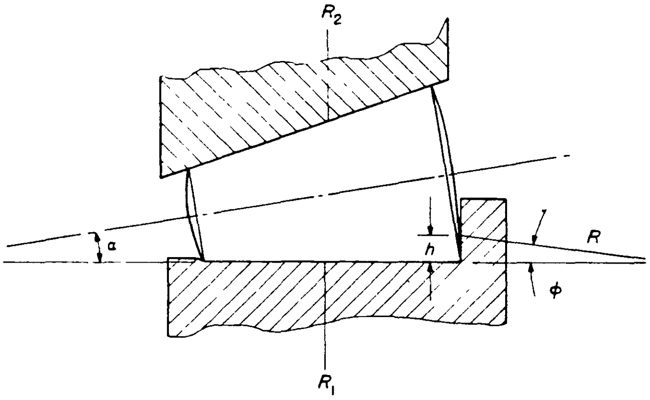

Fig 6 Forces on a taper roller in a thrust bearing

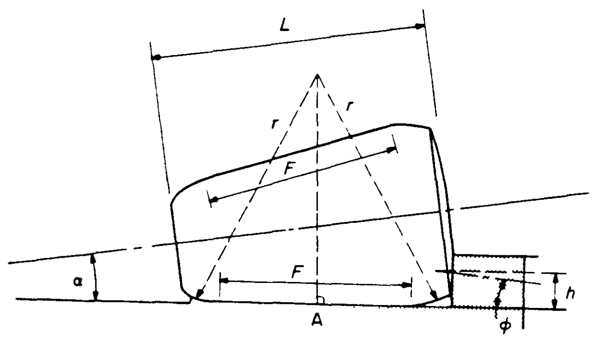

A is the mid point of the flat region

Fig 7 Taper roller with crown edge radii on its axial profile

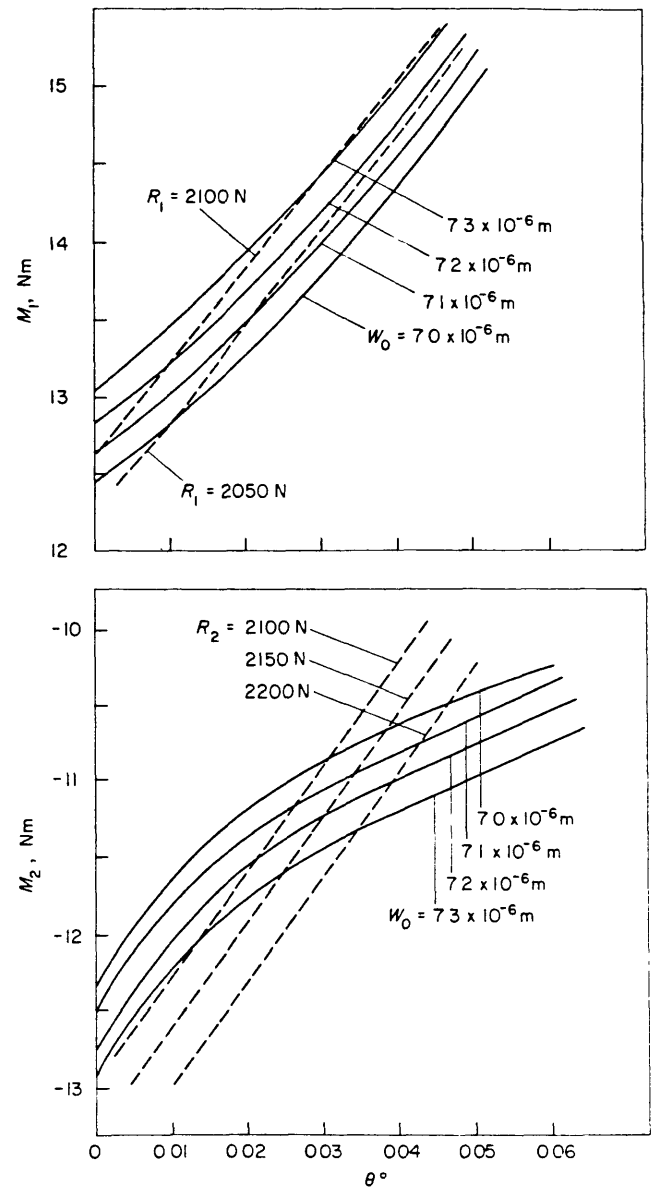

Fig 8 Design charts for a thrust bearing roller

2. Referring to the appropriate chart, find M_1 and M_2. Hence find $X_{(1,2)} = M_{(1,2)}/R_{(1,2)}$ where $X_{(1,2)}$ is the distance of $R_{(1,2)}$ from the small end.
3. Draw the roller to a large scale with the force vectors at their appropriate application points. If these vectors do not meet at a point, change θ by small increments ($\sim 0.01°$) and repeat the process until they do.
4. Knowing the correct θ and the magnitude of R_1 and R_2 enables their respective pressure distributions to be determined from the computer programme. If the maximum pressure anywhere exceeds some specified value, then W must be reduced and the process repeated.
5. If the three vectors never meet at any θ then this suggests that θ is anticlockwise. The same charts can be used again except that the chart which was for R_1 becomes that for R_2 and vice versa.

Results and discussion

If we take a total load, W, on the thrust bearing of 25 200 N, then $R = 750.6$ N, $R_1 = 2100$ N, and $R_2 = 2230$ N.

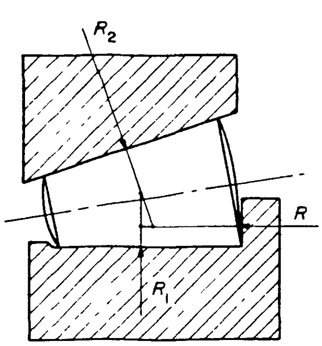

Fig 9 Forces on an aligned taper roller

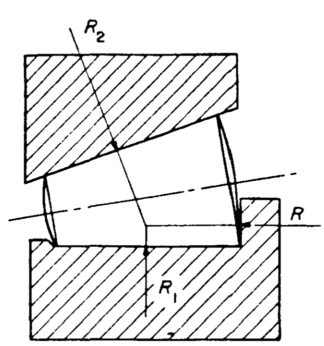

Fig 10 Forces on a misaligned taper roller $\theta = 0.015°$ (clockwise)

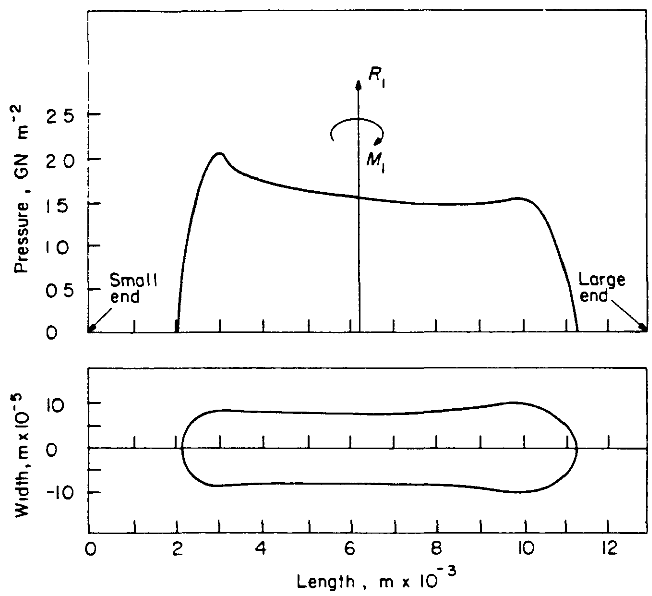

Fig 11 Pressure distribution on the bottom contact. $\theta = 0.015°$, $R_1 = 2100$ N

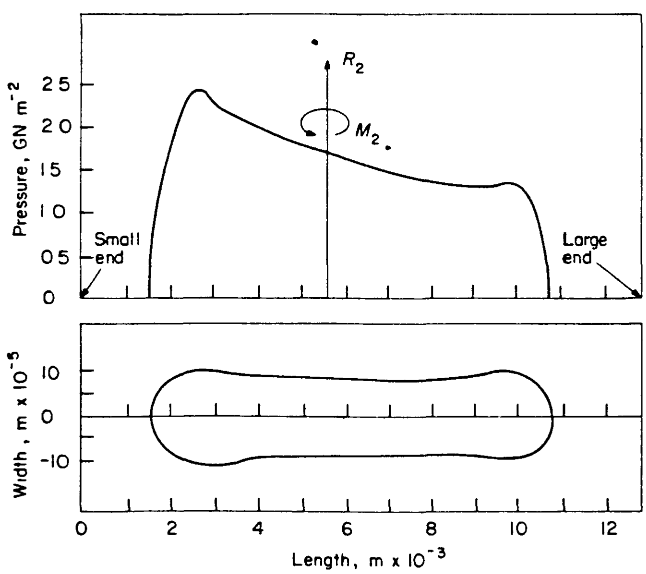

Fig 12 Pressure distribution on the top contact. $\theta = 0.015°$, $R_2 = 2230$ N

With $\theta = 0°$, $M_1 = 12.66$ Nm, $M_2 = 13.4$ Nm, giving $X_1 = 0.00602$ m, and $X_2 = 0.00601$ m. Fig 9 shows that for this roller position, the three force vectors do not meet. However, when $\theta = 0.015°$ (clockwise), $X_1 = 0.00629$ m, and $X_2 = 0.00574$ m. Fig 10 shows that the three force vectors meet at a point (within the accuracy of the diagram). The corresponding pressure distributions and footprints, for R_1 and R_2, are shown in Figs 11 and 12.

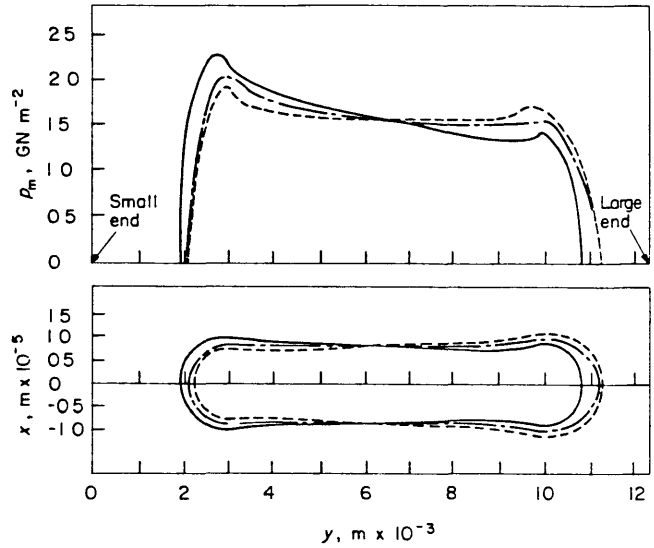

Fig 13 Effect of misalignment on pressure distribution. $\omega(0, 0) = 7.3 \times 10^{-6}$ m (Bottom contact)

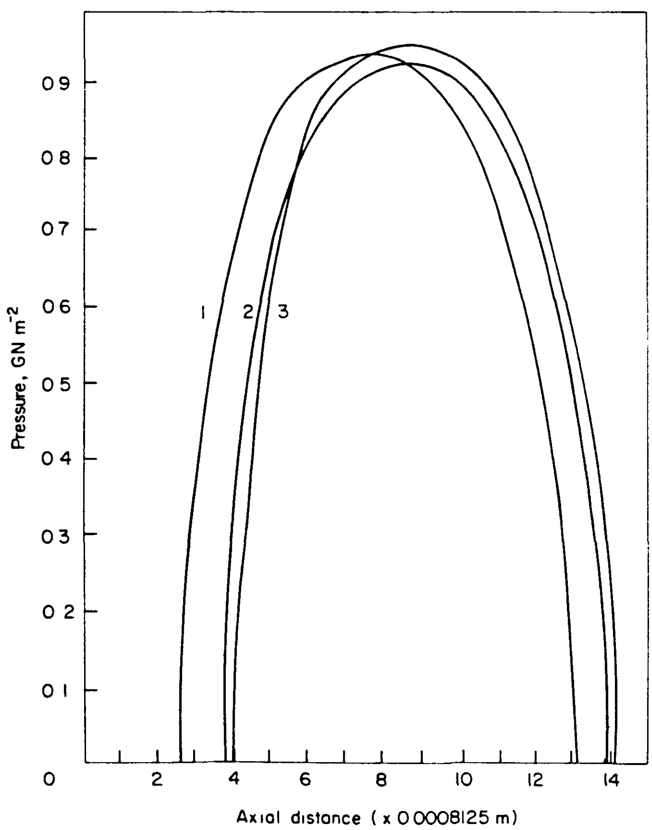

Fig 14 Pressure distribution on a crowned tapered roller, crown radius = 8.9 m, 1- aligned rollers, 2- 0.005° misaligned, 3- 0.01° misaligned

A maximum pressure of 2.425 GNm^{-2} occurs between the top race and the roller, 0.00285 m from its small end (Fig 12). This is an acceptable pressure if we assume that a taper roller can stand the same maximum radial stress as an equivalent cylindrical roller of radius R_0 [6]. Fig 13 shows how increasing misalignment for a constant centre deflection affects the pressure distribution and footprint. For a clockwise rotation θ and considering the contact between the bottom race and roller, the pressure peak moves from the small end towards the large end.
At $\theta = 0.05°$, the axial pressure is nearly uniform though the footprint is not. The roller to rib geometry appear then to be quite critical in determining the value of θ at equilibrium. Of course, misalignment can be caused also by mounting errors and shaft deflection. These factors are difficult to include in any design procedure. An axial profile which reduces stress concentrations is one given by a taper roller crowned over its whole length, a design which is being used by some bearing manufacturers. Typical pressure distributions for various misalignment angles are shown in Fig 14 for a roller having a crown radius of 8.9 m. Note that the maximum pressure is always near the contact centre. The pressure distribution simply moves bodily to the right as θ increases clockwise (bottom contact). A slight disadvantage of crowned rollers with spherical end faces, is that they can easily run skew during their orbits. Careful cage design can, however, mitigate this effect.

Conclusion

The paper has discussed the radial contact pressure distributions on tapered rollers in their bearing. The results suggest that they operate with some misalignment causing high contact pressures, but that careful axial profiling and rib design can reduce these untoward effects.

References

1. **Kannel J.W.** Comparison between Predicted and Measured Axial Pressure Distribution between Cylinders. *Trans ASME, July 1974, 508–514*
2. **Gohar R. and Heydari M.** Pressure Distribution on Radially Loaded Rollers. *To be published J. Mech Eng Sci, 1979*
3. **Goodelle R.A., Derner W.J. and Root L.E.** A Practical Method for Determining Contact Stresses in Elastically Loaded Line Contacts *Trans ASLE,* **13**, *269–277*
4. **Prescott T.** Applied Elasticity. *Dover, 1961*
5. **Zantapulos H.** The Effect of Misalignment on the Fatigue Life of Tapered Roller Bearings *Trans ASME, F, April 1972* **94** *(2)*
6. **Harris T.A.** Rolling Bearing Analysis *Wiley, 1966*